Report
R-16-14
May 2018

Modelling of bounding corrosion rates of reactor pressure vessels in SFR due to earth currents

Martin Löfgren
Magnus Sidborn

SVENSK KÄRNBRÄNSLEHANTERING AB

SWEDISH NUCLEAR FUEL
AND WASTE MANAGEMENT CO

Box 3091, SE-169 03 Solna
Phone +46 8 459 84 00
skb.se

ISSN 1402-3091
SKB R-16-14
ID 1569662

May 2018

Modelling of bounding corrosion rates of reactor pressure vessels in SFR due to earth currents

Martin Löfgren, Niressa AB

Magnus Sidborn, Kemakta AB

Extended summary

Fenno-Skan is a high voltage direct current (HVDC) transmission that transmits electrical current between Sweden and Finland. This is partly done through cables but to adjust for imbalanced currents in the cables, direct current can also be emitted, and picked up, at electrodes on the opposite shores of the Baltic Sea. By placing the electrodes in the water outside the shorelines, this enables current to be transmitted in the sea water and seabed. On the Swedish side, the Fågelsundet electrode is located about 25 km north of the SFR facility. Direct currents may impact buried metallic structures by way of increasing their corrosion rate, and questions have been raised whether HVDC transmissions may affect the long-term safety of SFR.

While a large part of the current will be transmitted in the sea water, a fraction will propagate down in the bedrock. As the current propagates in the ground on a regional scale, the term Earth currents is used. In the sea water, as well as in the bedrock, the direct current is carried by dissolved ions by electrolytic conduction. Most of the bedrock consists of insulating minerals. Accordingly, the current propagation is restricted to the rock's pore water (both in fractures and micropores). In crystalline rock, especially if it is sparsely fractured, this assures a high electrical resistivity of the bedrock. This will in turn limit the amount of current that can propagate down to the SFR underground facility.

If direct currents reach the SFR facility, this may increase the corrosion rate of its metallic waste, waste packages, and construction materials. While a small increase in the corrosion rate is inconsequential for most wastes, waste packages, and construction materials, the question has been raised if enhanced corrosion of reactor pressure vessels can be of consequence for the long-term safety. A reactor pressure vessel is a metallic vessel that surrounds the core of a nuclear power plant. Upon disposal its metal parts feature a significant amount of induced activity. When the vessels corrode, radionuclides incorporated in their metallic matrix may be released. It is important to note that the vessels in themselves are the waste and that they do not isolate other waste types. The corrosion situation is thereby different from that of copper canisters in the repository for spent nuclear fuel. In that situation, the main concern is that a hole will penetrate the isolating canister, enabling the release of radionuclide from the spent fuel. In the case of reactor pressure vessels, the radionuclides are fairly evenly distributed within the metal. Hence the impact on the radionuclide release is similar whether one kilogram of metal corrodes in a micrometre thin layer on the entire surface of the vessel, or on localised spots creating holes.

Even in the absence of Earth currents, the steel vessels will corrode. This occurs as the reaction between steel and water is thermodynamically spontaneous. However, under the anoxic and alkaline conditions that will prevail in the 1BRT vault, the corrosion rate is very small. On a planar carbon steel surface, the corrosion rate assumed in the safety assessment SR-PSU is 50 nm/yr. By accounting for the total surface area of the reactor pressure vessels, this corrosion rate can be translated to a corroded volume per year, and through the density to corroded mass per year. This mass equates to about 2.8 kg/yr.

The primary aim of this report is to estimate an upper bound for Earth current induced corrosion rates of reactor pressure vessels in the SFR repository. This is done by assuming that each electric charge carried to the vessel surfaces takes part in the corrosion reactions:

$$\mathrm{Fe(s)} \rightarrow \mathrm{Fe}^{2+} + 2\mathrm{e}^{-} \qquad \text{Equation E-1}$$

$$2\mathrm{H_2O} + 2\mathrm{e}^{-} \rightarrow \mathrm{H_2} + 2\mathrm{OH}^{-} \qquad \text{Equation E-2}$$

This is done by two approaches. In the more pessimistic approach the reaction rates of these reactions are assumed to be so fast that they pose no limitation on the Earth current induced corrosion rate. The current that propagates through the vessels can thereby be calculated by Ohm's law (in more or less complex models) without adding a polarisation resistance at the vessels' surfaces. This approach is called the charge-balance approach. In the more realistic approach, the rate constants of the reactions limit the Earth current induced corrosion rate. In this approach, called the kinetics limitation approach, the model incorporates activation polarisation at the vessels' surfaces. The current that enters a vessel is a function of the electrical overpotential at the surface, and is calculated by using the Butler-Volmer formulation. This formulation is derived from fundamental principles of reaction kinetics, and uses the corrosion rate assumed in SR-PSU, in the absence of Earth currents, as input data.

For each milliampere that propagates through a reactor pressure vessel, as calculated by either of the two approaches, this gives rise to an Earth current induced corrosion rate of about 9 g/year. To obtain the total corrosion rate of the vessels, the corrosion current leaving each vessel must be added. To achieve an Earth current induced corrosion rate of 2.8 kg/year, which matches the corrosion rate in the absence of Earth currents, a total corrosion current of about 300 mA needs to leave the vessels. To put this in perspective, 300 mA is about the current running in a 60W lightbulb at 220 V. For corrosion currents below this benchmark, Earth current induced corrosion will be a minor process.

The bulk of the modelling is done to represent a constant direct current output of around 1 280 A at the Fågelsundet electrode. For this current output there are empirical data on the local field strength in the SFR area. This output is close to the maximum output of electrode, which is 1 360 A for Fenno-Skan 1 and 1 670 A for Fenno-Skan 2. Under normal operating conditions, when both Fenno-Skan cables are in use, the current output at the electrode is smaller and sometimes close to zero. The modelling assumption of a high current output all around the year is judged to be pessimistic.

In this report, the Earth current induced corrosion is estimated in 1D, 2D and 3D models, with increasing degree of refinement. The 1D models are based on an electrical circuit analogue and have merits in their simplicity. Such models were also used in an earlier document that was submitted to the Swedish Radiation Safety Authority (SSM), dealing with Earth current induced corrosion at SFR. Unfortunately, an important error was made in this earlier document, which is now corrected. With the 1D model, the best estimate total corrosion current is in the range of 90 to 180 mA, which is still below the benchmark corrosion current of 300 mA.

In the 2D models, the 1BRT vault as well as simplistic representations of the access ramp and an access tunnel is confined to an inner cylinder. This inner cylinder is surrounded by an outer cylinder of host rock (Figure E-1). The model thereby uses cylindrical coordinates. The used software is COMSOL Multiphysics, which is a tool for finite element analysis that solves a coupled system of partial differential equations. The tool solves the electric field of the model volume, and the path and magnitude of the current (Figure E-1).

These models are used to gain understanding of how the engineered parts of the repository, having a lower resistivity than the surrounding rock, affects the large scale electric field. The engineered parts will provide a low resistivity path for the current, which will be diverted from the host rock and into the tunnels and 1BRT vault. The paths of current lines are also solved within the 1BRT vault, and the current entering each vessel can be calculated. In the 2D model this is done by both ignoring polarisation effects, as well as by acknowledging kinetics limitations. In the 2D base case, using the charge-balance approach, the total corrosion current is 104 mA, which is lower than the benchmark current. Here it should be noted that no parallel tunnels and vaults are accounted for, to where the current could be diverted. Results from modelling that incorporate kinetics limitations suggests that the charge-balance approach overestimates the Earth current induced corrosion rate by a factor of at least four.

In the 2D model, the impact of a presumptive segmentation of the pressure vessels is also investigated. This is done by the kinetics limitation approach. The results show that the segmentation will give rise to a diminished importance of Earth current induced corrosion. This is as the potential drop over each metallic object is reduced the shorter the object is. This in turn reduces the anodic corrosion current due to a non-linear dependence between the corrosion current and the overpotential.

To account for the effect of other vaults and access tunnels in SFR 3, the entire system has been modelled in a 3D model. This has been done using the charge-balance approach in COMSOL Multiphysics (Figure E-2). In the 3D base case, the total current of 75 mA enters SFR 3. Out of this 19 mA enters the 1BRT vault. The total corrosion current, for the nine vessels, summarises to 42 mA. This is a substantially lower corrosion current that the benchmark current of 300 mA, suggesting that Earth current induced corrosion will only contribute to 12 % of the total corrosion, at the most.

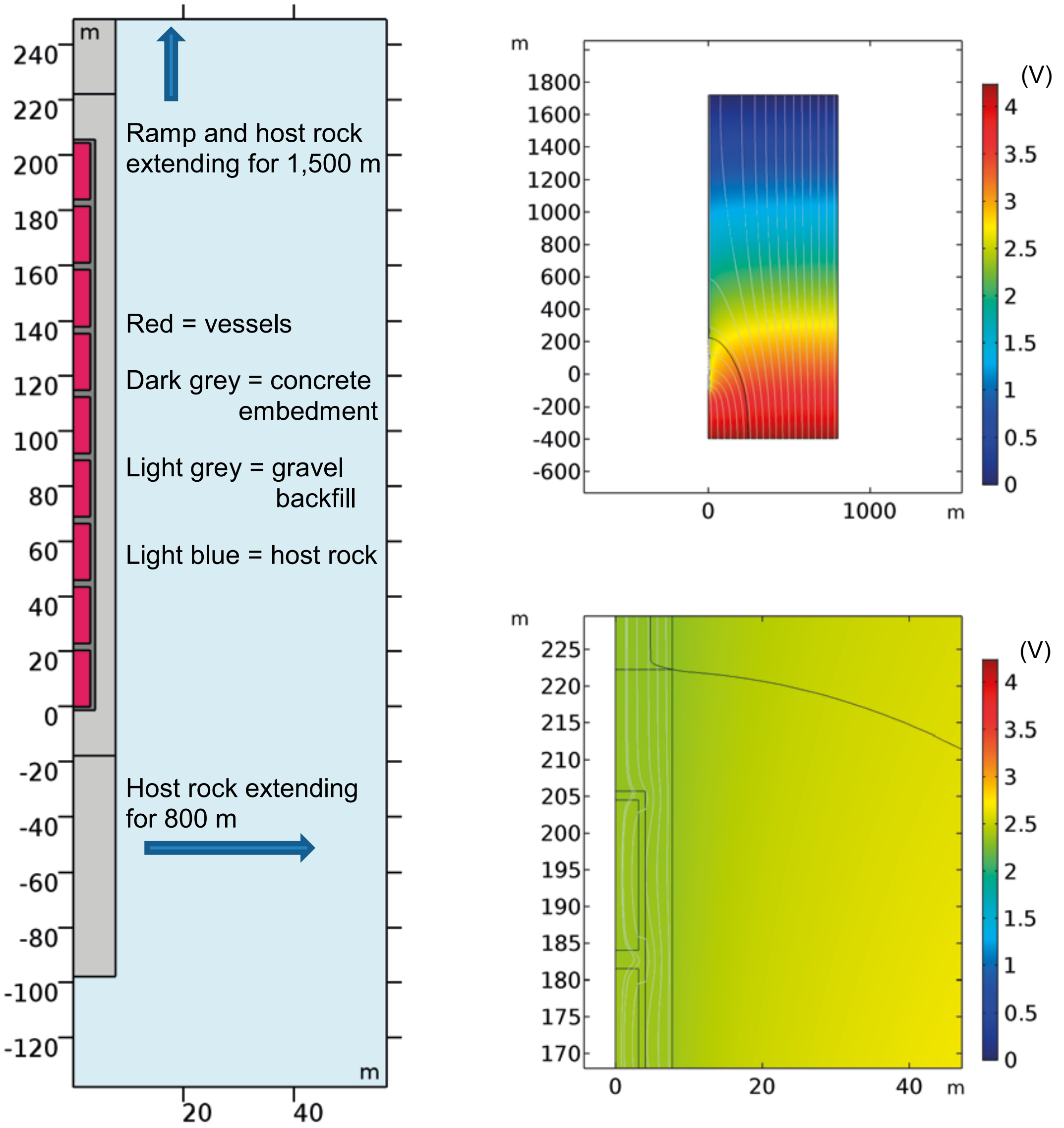

Figure E-1. *Results from the 2D cylindrical base case. Model components are shown on the left and results are shown on the right, at different degrees of zooming. Colour scale represent potential (V) and the lines represent the current lines in the system. All grey current lines to the left of the black current line will contact the 1BRT vault.*

In this report there are numerous of sensitivity cases relating to uncertainties in material properties, geometries, and the large-scale electric field. In no reasonable case Earth current induced corrosion will be the dominating corrosion process, even when disregarding kinetics limitations. This also applies for a future location of the HVDC electrode placed outside the Gräsö Island. As such, Earth current induced corrosion of reactor pressure vessels is judged to be within the range of insignificant to minor importance for the long-term safety of SFR. Moreover, the impact is quantifiable.

During operation, i.e. at relatively dry conditions, Earth currents from the Fenno-Skan transmission have an insignificant impact on the operational radiation safety of SFR.

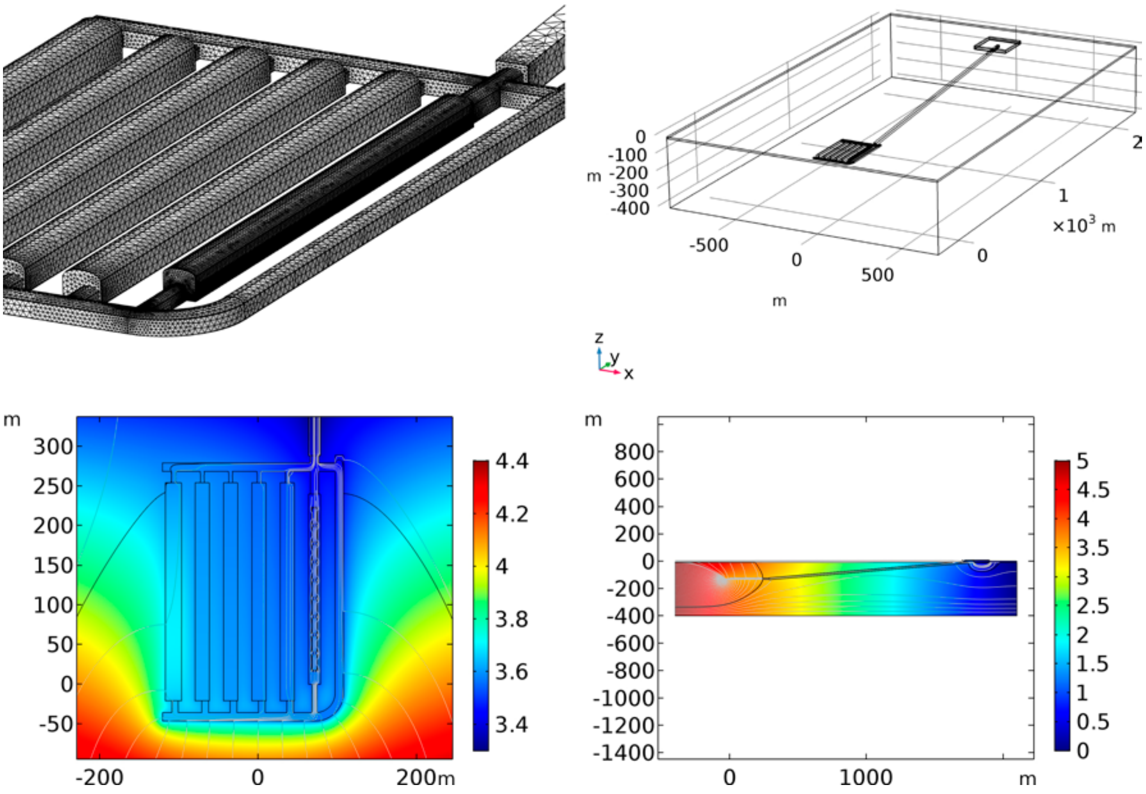

Figure E-2. *Results from the 3D repository base case. Model components are shown in the upper row at different degrees of zooming. Results are shown in the lower row, at different degrees of zooming and angles. The colours represent the potential (V) and the lines represent the current lines propagated through the system.*

Sammanfattning

Fenno-Skan är en likströmsöverföring mellan Sverige och Finland. Överföringen sker i huvudsak genom högspänningsledningar placerade under vattnet i Östersjön. Vid obalanserad drift sker dock strömöverföring även genom det elektriskt ledande havsvattnet med hjälp av elektroder placerade i vattnet utanför kustlinjen på var sida om Östersjön. På den svenska sidan är elektroden vid Fågelsundet placerad cirka 25 km norr om SKBs slutförvar för låg- och medelaktivt avfall, SFR. Likström genom deponerat metalliskt avfall kan öka korrosionshastigheten och frågan har därför väckts om HVDC överföringen kan påverka den långsiktiga säkerheten av förvaret.

Även om överföringen vid obalanserad drift i huvudsak sker genom havsvattnet kommer en andel av strömmen även ledas ner i berggrunden. Benämningen jordströmmar används för detta fenomen, då strömmen propagerar i marken på en regional skala. I havsvattnet och i berggrunden leds strömmen elektrolytiskt med hjälp av joner i lösning. Berggrunden består till största delen av elektriskt isolerande mineral och strömmen leds därför i huvudsak i porvattnet i berget (i sprickor och mikroporer). Detta medför en hög elektrisk resistivitet i kristallin berggrund, i synnerhet då sprickfrekvensen är låg, vilket i sin tur begränsar strömmen som kan nå SFR förvaret.

Likström som når förvaret kan öka korrosionshastigheten av deponerat metalliskt material. Även om en liten ökning av korrosionshastigheten saknar betydelse för det mesta av det metalliska avfallet, avfallspaketen och konstruktionsmaterialet, så har frågan väckts huruvida en ökad korrosion av deponerade reaktortankar kan ha betydelse för den långsiktiga säkerheten. Reaktortanken är det metalliska kärl som omger härden i ett kärnkraftverk och vid deponering innehåller metallen därför avsevärd inducerad radioaktivitet som frigörs i takt med att tankarna korroderar. Det ska noteras att reaktortankarna i sig är avfall, och alltså inte en omslutning av annat avfall. Korrosionsproblematiken skiljer sig därför från slutförvaret av använt kärnbränsle där avfallet ska isoleras av kopparkapslar som har en barriärfunktion, och där fokus ligger på korrosionsprocesser som kan penetrera barriären och därigenom frigöra radionuklider. I reaktortankarna är den inducerade aktiviteten någorlunda jämt fördelad i metallen och utsläppet av radionuklider är därför detsamma oavsett om ett kilogram metall korroderar i ett tunt skikt fördelat över hela metallytan eller om samma mängd korroderar lokalt fläckvis på ytan.

Reaktortankarna korroderar även i frånvaro av jordströmmar eftersom reaktionen mellan stål och vatten är spontan ur ett termodynamiskt perspektiv. I den anoxiska och alkalina miljön som förväntas i 1BRT efter förslutning är dock korrosionshastigheten långsam. Korrosionshastigheten på en plan yta av kolstål uppskattas i säkerhetsanalysen SR-PSU till 50 nm/år. Räknat på den totala ytan av deponerade reaktortankar kan volymen korroderad metall per år uppskattas och, med hjälp av metallens densitet, kan den totala massan korroderad metall per år beräknas. Denna motsvarar då cirka 2,8 kg/år.

Det huvudsakliga syftet med denna rapport är att uppskatta en övre gräns för den jordströmsinducerade korrosionshastigheten av reaktortankarna i SFR förvaret. Vid denna uppskattning antas att varje laddning som når metallens yta bidrar till korrosionsreaktionerna (ekvation E-1 och E-2).

Två angreppssätt används vid uppskattningen. I det mer pessimistiska angreppssättet antas reaktionerna ske så pass snabbt att de inte utgör någon begränsning av den jordströmsinducerade korrosionshastigheten. Strömmen som leds genom reaktortankarna kan då beräknas med Ohm's lag (med modeller av varierande komplexitet) utan att ta hänsyn till polarisationsmotstånd vid metallytan. Detta angreppssätt benämns i rapporten för ”charge-balance approach”. Ett mer realistiskt angreppssätt tar hänsyn till reaktionshastigheterna vilka kan begränsa den jordströmsinducerade korrosionshastigheten. Detta angreppssätt benämns i rapporten ”kinetics limitation approach” och inkluderar aktiveringspolarisation vid metallytorna. Strömmen som leds till en reaktortank är då en funktion av den elektriska överpotentialen vid ytan och beräknas med Butler-Volmer's ekvation. Denna härleds från grundläggande reaktionskinetiska principer och med den i SR-PSU antagna korrosionshastigheten i frånvaro av jordströmmar som indata.

Ström som leds genom en reaktortank ger upphov till en jordströmsinducerad korrosion om 9 g/år för varje milliampere, där strömmen beräknas enligt någon av de båda ovan beskrivna angreppssätten. För att uppskatta den totala korrosionshastigheten adderas korrosionsströmmen som lämnar varje reaktortank. För att uppnå en jordströmsinducerad korrosionshastighet om 2,8 kg/år, det vill

säga den korrosionshastighet som antas i frånvaro av jordströmmar, krävs att en total korrosionsström om 300 mA lämnar reaktortankarna. Detta motsvarar ungefär den ström som går genom en 60 W glödlampa vid 220V. Vid korrosionsströmmar som underskrider detta riktvärde kan jordströmsinducerad korrosion betraktas som en underordnad process.

Huvuddelen av modellerna representerar en situation med en konstant likström om 1 280 A vid elektroden i Fågelsundet. För denna utgående ström finns lokalt uppmätta fältstyrkor i området kring SFR tillgängliga. Denna ström är också nära den maximala kapaciteten för elektroden, som är 1 360 A för Fenno-Skan 1 och 1 670 A för Fenno-Skan 2. Under normala driftsförhållanden, när båda Fenno-Skan kablarna används, är utgående ström vid elektroden mindre och ibland nära noll. Modellantagandet om en konstant hög utgående ström vid elektroden under hela året bedöms därför vara pessimistisk.

Jordströmsinducerad korrosion uppskattas genom modellering i 1D, 2D och 3D och med en inkrementellt ökande detaljeringsgrad. Modelleringen i 1D baseras på analogier med elektriska kretsar och har fördelen med dess enkelhet. Denna typ av modeller har även använts vid tidigare dokumentation om jordströmsinducerad korrosion vid SFR som delgetts den svenska strålsäkerhetsmyndigheten (SSM). Detta tidigare dokument innehöll dock ett betydande fel som nu åtgärdats. Med 1D modellen uppskattas den totala korrosionsströmmen i intervallet 90 till 180 mA, vilket underskrider riktvärdet på 300 mA.

I 2D modellerna representeras 1BRT bergrummet, ramp, och en accesstunnel av cylindersegment i cylindriska koordinater som omges av ytterligare en cylinder som representerar berggrunden (se figur E-1). Modelleringsverktyget som används är COMSOL Multiphysics för lösning av kopplade system av partiella differentialekvationer i finita element. Verktyget löser för det elektriska fältet i modellvolymen samt ger magnitud och flödeslinjer för strömmen (figur E-1).

Dessa modeller i 2D används för att öka förståelsen för hur förvarsdelarna, med lägre resistivitet än det omgivande berget, påverkar det storskaliga elektriska fältet. Förvarsdelarna utgör en lågresistiv transportväg för strömmen som därmed avleds från berget genom förvarets tunnlar och också genom 1BRT. Modellerna löser även för strömlinjernas utbredning inom 1BRT och strömmen som passerar genom varje reaktortank kan därmed beräknas. Med 2D modellerna görs detta både med antagande om försumbara polarisationseffekter samt med hänsyn taget till kinetiska begränsningar. I 2D basfallet där kinetik försummas (”charge-balance approach”) beräknas den totala korrosionsströmmen till 104 mA, vilket underskrider riktvärdet. Det bör noteras att tunnlar och bergrum parallella med 1BRT, där ström skulle kunna ledas förbi 1BRT, inte räknas med i 2D basfallet. Modelleringsresultat då kinetikbegränsning inkluderas visar att ”charge-balance” ansatsen överskattar den jordströmsinducerade korrosionen med åtminstone en faktor fyra.

I 2D modellen undersöks även effekten av segmentering av reaktortankarna. Detta görs med kinetikbegränsning inkluderad. Resultaten visar att segmentering minskar betydelsen av jordströmsinducerad korrosion. Detta på grund av att potentialfallet över varje enskilt metallobjekt minskar ju kortare objektet är. Detta minskar i sin tur den anodiska korrosionsströmmen på grund av ett ickelinjärt beroende mellan korrosionsström och överpotential.

För att beakta också påverkan av andra bergrum och tunnlar i SFR 3 inkluderas hela systemet i en 3D modell i Comsol Multiphysics (Figure E-2) där ”charge-balance” ansatsen används. Resultaten visar en total ström om 75 mA som leds in i SFR 3, varav 19 mA leds in i 1BRT. Den totala korrosionsströmmen för samtliga 9 reaktortankar summeras till 42 mA. Detta är en väsentligt lägre korrosionsström än riktvärdet om 300 mA vilket tyder på att jordströmsinducerad korrosion bidrar med mindre än 12 % av den totala korrosionen.

I denna rapport inkluderas ett flertal känslighetsanalyser avseende osäkerheter i materialegenskaper, geometrier och det storskaliga elektriska fältet. Inget rimligt modelleringsfall visar på jordströmsinducerad korrosion som den dominerande korrosionsprocessen, även då kinetikbegränsning försummas. Detta gäller också för en framtida placering av en HVDC elektrod i vattnet utanför Gräsö. Jordströmsinducerad korrosion av reaktortankar bedöms vara obetydlig eller vara av mindre betydelse för långsiktig säkerhet av SFR. Dess påverkan är dessutom kvantifierbar.

Under drift av SFR, det vill säga vid relativt torra förhållanden, har jordströmmar från Fenno-Skan överföringen obetydlig påverkan avseende strålsäkerheten vid anläggningen.

Contents

1 Introduction

1.1 Background

On the 9th of January 2014, the Swedish Radiation Safety Authority (SSM) issued an injunction regarding the impact of Earth currents on SFR, originating mainly from the relatively closely located Fenno-Skan HVDC (high voltage direct current) electrode at Fågelsundet, about 25 km north of SFR at the Baltic Sea shoreline. SKB submitted a response later that year, in Swedish, which can be read in the publicly available document "*Svar på Föreläggande om redovisning rörande betydelsen av jordströmmar vid SFR*" (SKB 2014a). Appended to that document, in Appendix A, is an account of bounding corrosion calculations concerning the reactor pressure vessels, which are intended to be deposited in the extension of SFR. A significant error was made in these rather simplistic calculations, which is remedied in this present report. In the light of more realistic modelling, this report discusses the possible long-term impact of Earth currents on the reactor pressure vessels.

A reactor pressure vessel is a metallic vessel that surrounds the core of a nuclear power plant. As result of abundant radiation within the pressure vessel, its metallic parts will feature a significant induced activity at the time of dismantling. Accordingly, when deposited in SFR the pressure vessels constitute a radionuclide source term. The radionuclides will be incorporated in the matrix of the metallic parts and may be released upon corrosion. At repository closure the activity of the pressure vessels' radionuclide inventory will be 1.6 % of the total activity of the deposited waste in SFR (SKB 2013b, Section 5.3). Corrosion will occur upon repository closure, as the 1BRT vault becomes saturated with groundwater. This may occur both in the presence and absence of Earth currents, as the corrosion of iron in water is thermodynamically spontaneous. The impact of pressure vessel corrosion for the long-term safety of SFR, in the absence of Earth currents, has been analysed in the safety assessment SR-PSU. This process was judged to be a minor, although not an insignificant, contributor to radiological risk. In the main scenarios of SR-PSU, radionuclides from the pressure vessels contributed to less than 5 % of the peak annual effective dose (SKB 2015, Tables 9-1 to 9-2).

In the presence of Earth currents, the pressure vessel corrosion rate may be enhanced. In this report, we use the term Earth current induced corrosion, which is the corrosion that may occur in the presence of Earth currents minus the corrosion that would have occurred in their absence. The main question of this report is if Earth current induced corrosion may significantly increase the total corrosion rate, or if it likely has a minor contribution. The nature of this question allows us to make the analysis using overly-pessimistic assumptions on the Earth current induced corrosion and, if necessary, shave off the degree of pessimism as the analysis progresses. A simplistic analysis, using pessimistic assumptions, was made in SKB's response to SSM (SKB 2014a) where calculations relied on:

1) An electrical circuit analogy for calculating the electric current that propagates through the SFR repository, potentially contacting the pressure vessels;
2) A pessimistic charge-balance approach for calculating the bounding Earth current induced corrosion rates. This approach neglects reaction kinetics and other processes causing polarisation resistance. Here an error was made in not multiplying the assumed corrosion current with the number of pressure vessels; an error which is here remedied;
3) A simplified geometry of the 1BRT vault, as isolated from the remaining of the SFR repository.

Although using seemingly pessimistic assumptions, the simplicity of the calculations makes it less straightforward to justify that the resulting Earth current induced corrosion rates are indeed pessimistic. When using the electrical circuit analogy, one imposes certain limitations. A major limitation is that current propagation needs to be one-dimensional; resulting in parallel current lines through the system. In the real three-dimensional repository system, where different components have different electrical resistivities, the current lines will bend towards the components of the least resistivity. By doing this the cumulative resistance along the current line is minimised. As pressure vessels are metallic, current lines will bend towards them. This was compensated for in the previous calculations (SKB 2014a, Appendix A) by assuming that all current lines passing through the repository system, in some cases also including the surrounding host rock, may bend towards and contact the pressure vessels.

In this present report, we complement the one-dimensional electrical circuit model with more refined electric field modelling using the finite element computational tool COMSOL Multiphysics. In COMSOL Multiphysics there is no limitation in the three-dimensionality of the electric field. Accordingly, we may both obtain more accurate results, as well as investigate the degree of pessimism in the previous calculations.

Using a charge-balance approach to calculate the Earth current induced corrosion rate is, overall, considered to be the most pessimistic assumption that can be made, especially as one assumes no polarisation resistance at the pressure vessel surfaces. There are a number of processes and limitations that may lower the actual Earth current induced corrosion rate, compared to that calculated by the charge-balance approach, but we find no compelling arguments for the opposite. In one calculation case, activation polarisation is accounted for by using the Butler-Volmer formulation of electrode kinetics. This significantly lowers the corrosion rate compared to neglecting all polarisation resistance.

Concerning item three of the above list, the modelling described in this present report relies both on the simplified repository geometry used in SKB (2014a, Appendix A), as well as on 2D and 3D models based on the proposed layout of SFR 3. This allows for obtaining more reliable results, as well as to investigate the impact of using the simplified geometry in the previous calculations. The focus is on modelling the Earth current induced corrosion rates of intact reactor pressure vessels, as assumed in SR-PSU. However, the impact of segmentation of the pressure vessels is also investigated. In doing this, and especially if the segmentation is extensive, using the charge-balance approach becomes too pessimistic. This is handled by introducing a more realistic corrosion model, where the kinetics of the corrosion reactions is assessed through the Butler-Volmer equation.

The simplistic calculations presented in SKB (2014a, Appendix A) indicate that Earth current induced corrosion most likely occurs at subordinate rates compared to the corrosion occurring in their absence. This applies also after correcting for the error made in the previous calculations. Future possible locations of HVDC electrodes, as well as the impact of future groundwater compositions, were not investigated in SKB (2014a, Appendix A). Accordingly, this conclusion was not extended beyond present day conditions. In this present document we discuss the impact of possible future conditions regarding both the large-scale electric field and material properties.

1.2 Objectives and outline

The overall objective of this report is to investigate if Earth current induced corrosion of reactor pressure vessels could significantly add to the corrosion that would occur in the absence of Earth currents. This is done from the perspective of present day and possible future HVDC transmissions in the regional area, which transmit direct current over the Baltic Sea. This is mainly done for intact reactor pressure vessels, as accounted for in SR-PSU, but to some extent also for segmented pressure vessels. The objective is met in a number of steps that are reported in nine chapters of this report. The objective and scope of each of these chapters are summarised below.

Part 1: Introduction and prerequisites

Chapter 1. Provides the background to, and objectives of, this modelling task.

Chapter 2. Provides the basics of electric field theory applicable in fractured crystalline rock and other porous media. It also provides the basics of corrosion theory in terms of thermodynamics and kinetics of relevant corrosion reactions in the presence, or absence, of an external electric field.

Chapter 3. Provides the geometries and other initial state properties of the SFR facility and, in particular, the 1BRT vault hosting the reactor pressure vessels. It also justifies the large-scale electrical potential gradients and resistivities of the different media used in the modelling. Finally, it discusses the corrosion rate of intact pressure vessels in the absence of Earth currents, and the current needed to contact the pressure vessels to match this rate.

Part 2: Electrical circuit model

Chapter 4. Revisits the modelling performed in SKB (2014a, appendix A) with the electrical circuit model and adjusts for the error in the previous calculations.

Chapter 5. Further investigates the sensitivity of the electrical circuit model, in respect to input data and system boundaries.

Part 3: Numerical modelling in COMSOL Multiphysics

Chapter 6. Accounts for the 2D modelling of the 1BRT vault, and the added access ramp and tunnel, in cylindrical coordinates. This is done in the finite element tool COMSOL Multiphysics by modelling the electric field of the system, as well as the current that propagates through the pressure vessels. In this chapter much of the sensitivity analysis is done with regard to the used media's resistivities. The 2D model is also used to study the merits of the 1D electrical circuit model.

Generally, the current that is modelled to propagate through the pressure vessels is assumed to lead to corrosion, in the change-balance approach where polarisation resistance is neglected. However, at the end of the chapter (Section 6.7) the impact of a generic segmentation of the reactor pressure vessels is investigated. In doing this, limitations in reaction kinetics are acknowledged by using the Butler-Volmer equation. This lowers the Earth current induced corrosion rate, as compared to in the change-balance approach.

Chapter 7. Accounts for the 3D modelling of SFR 3 and the added access ramp, using the charge-balance approach. Here the layout of SFR 3 has been imported from SR-PSU. This allows for estimating the influence of parallel vaults and access tunnels on the current that propagates through the pressure vessels. It also allows for changing the direction of the electrical potential gradient. Furthermore, the impact of a reasonable, as well as a pessimistic, future HVDC electrode is investigated. This is done for both present day groundwater salinity and for a case where shoreline displacement has made the groundwater less saline.

Part 4: Impact on operational radiation safety

Relatively late in this project we were asked to draw conclusions on the operational radiation safety of SFR, based on experience from the performed modelling but without performing additional modelling.

Chapter 8. Discusses the impact of Earth current induced corrosion on the radiation safety of SFR during operation, i.e. when the underground openings are air filled.

Conclusions

Chapter 9. Summarises the main conclusions of this work.

This report also includes two appendices, where Appendix A presents the block-scale rock resistivity of fracture zones in the host rock. Appendix B discusses the correlation between the rock resistivity of the regional bedrock and the large-scale potential gradient, in cases with and without the Baltic Sea.

2 Theory

2.1 Earth currents and electric field theory

The nature of Earth currents, both natural and anthropogenic, is outlined in SKB (2014c, Section 5.12), Taxén et al. (2014), Thunehed (2017) and references therein. Earths current may be both direct and alternating. They may also fluctuate, both in magnitude and direction, over short or long timescales. This present report only focuses on direct Earth currents and disregards alternating as well as rapidly fluctuating Earth currents. The rational is that only direct currents may give rise to significant Earth current induced corrosion in a long-term perspective (cf. Section 2.2.3). At SFR, direct Earth currents are mainly induced by the Fenno-Skan HVDC electrode, located at the Baltic Sea shoreline about 25 km north of the site, and by more closely located power line installations at the Forsmark nuclear power plant (Thunehed 2017).

2.1.1 Electrical circuit analogy

In a repository system, there are large-scale components of different materials and electrical resistivities. This can be exemplified with an isolated vault, completely filled with gravel, deep within the host rock (cf. Figure 2-1). The resistivity of the gravel is much lower than of the host rock and in the real case, current lines from plane A to B will bend towards the vault. Simplistically explained, by bending toward and preferably into the least resistive component the current lines manage to minimise their total resistance along of their path from plane A to B. This is illustrated by the red current line in the figure, as compared to the blue current line that represents a case where the resistivity of the vault matches the resistivity of the host rock. While Figure 2-1 is only an imprecise illustration, its general features are confirmed by results from modelling with COMSOL Multiphysics in Chapter 6.

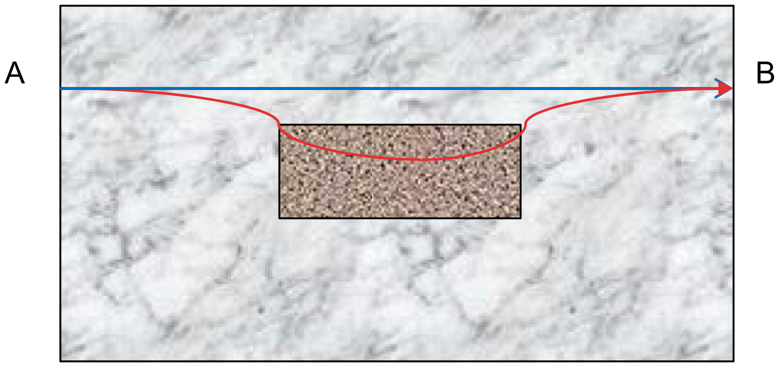

Figure 2-1. *Illustration of current lines in the host rock, from plane A to B, where the red current line bends towards a less resistive vault. The blue current line represents a case where the rock and vault have the same resistivity.*

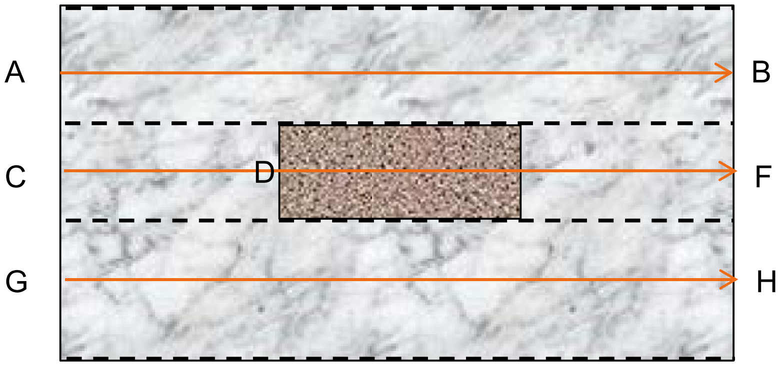

Figure 2-2. *Illustration of the same vault but with imposed internal no-flow boundaries (dashed lines). Current lines are shown by orange arrows.*

In using the electrical circuit analogy, one simplifies the true system by assuming one-dimensional current transport. Alternatively, one may say that the system is simplified by inserting internal no-flow boundaries. Such internal no-flow boundaries are marked by dashed lines in Figure 2-2. This creates three domains where, within each domain, all current lines would encounter the same electrical resistance. The no-flow boundaries effectively restrict the current lines from bending and thereby they all have parallel trajectories, as shown by the orange current lines in Figure 2-2.

As can be seen from Figure 2-2 the centre domain can be divided into three subdomains, from C to D, D to E and E to F, respectively. By doing this, we now have five homogenous domains, including the upper domain A to B and lower domain G to H. The resistance R (ohm) of each domain can be calculated by its resistivity ρ (ohm.m), length L (m) and cross section area A (m^2).

$$R = \rho \frac{L}{A} \qquad \text{Equation 2-1}$$

Figure 2-2 is represented by an electrical circuit diagram in Figure 2-3, where each domain is represented by a resistor. As can be seen, the resistors of the upper, centre and lower domain are connected in parallel while the three subdomains of the centre domain are connected in series.

The total resistance of the centre domain can be calculated by summarising the resistances of its three resistors, which are connected in series. The total conductance (with is the reciprocal of the resistance) of the upper, centre, and lower domains can be calculated by summing their individual conductances. To put this into an equation, the total resistance R_{tot} (ohm) of the system in Figure 2-3 becomes:

$$\frac{1}{R_{tot}} = \frac{1}{R_{A-B}} + \frac{1}{R_{C-D} + R_{D-E} + R_{E-F}} + \frac{1}{R_{G-H}} \qquad \text{Equation 2-2}$$

If having the potential drop ΔU (V) over the system, that is from left to the right planes in Figure 2-2, the total current I_{tot} (A) can be calculated by Ohm's law:

$$I_{tot} = \frac{\Delta U}{R_{tot}} \qquad \text{Equation 2-3}$$

Through basic equations it is easy to calculate the fraction of the current that is propagated through the domain of interest, which may for example be the 1BRT vault in SFR. What proves to be more challenging is compensating for the three-dimensionality of the current, as current lines in the real case bend towards the vault from the surrounding host rock. Pessimistic ways of doing this are discussed in Chapters 4 and 5.

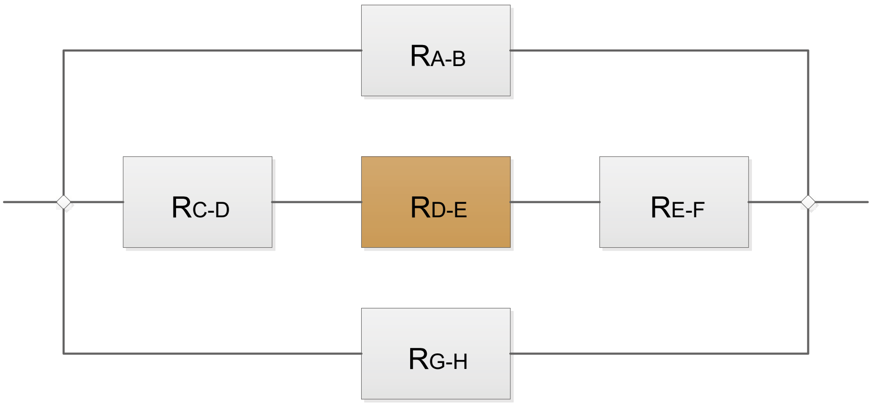

Figure 2-3. *Electrical circuit diagram representing Figure 2-2.*

2.1.2 Current propagation mechanisms in porous media

The propagation of electric current through a porous medium usually takes place by electrolytic conduction, electronic conduction, and dielectric conduction. If the pores are large enough and the water contains charged particles, electrophoresis may also contribute to the current propagation. Dielectric conduction requires an alternating or rapidly fluctuating electric field and is of no concern for the corrosion calculations in this report. Electrolytic conduction relates to the movement of electrical charge by means of mobile ions that are dissolved in water filled pores of the porous media. The transport mechanism is electromigration. Electronic conduction relates to the movement of electrons within the matrix of the porous medium. In the case of rock, this relates to movement of electrons in the crystal lattices of its constituting mineral grains.

In the host rock at the Forsmark site, a large fraction of the direct Earth currents is carried by ionic solutes in the water filled pore space of the intact rock matrix. A similar fraction is carried by solutes in free groundwater of open fractures on the decimetre scale or larger. Whether the free groundwater is stagnant or flowing is inconsequential for its electrical conductivity. The fraction of direct Earth currents that is carried by electronic conduction within mineral grains is minuscule at the Forsmark site (Löfgren 2015) and is of no consequence for this present report.

Electrolytic conduction is also the important current propagation mechanism for other porous media of concern for this report, namely: concrete; macadam backfill; and bentonite backfill of the SFR repository. Current propagation within the (non-porous) metallic parts of the pressure vessels occurs exclusively by electronic conduction.

2.1.3 Homogenous vs. heterogeneous media

The current density J (A/m^2) through a homogenous medium can be calculated from its resistivity ρ (ohm.m), or electrical conductivity κ (S/m), and the potential gradient over the medium. Equation 2-4 applies to one-dimensional current transport while Equation 2-5 applies for the three-dimensional case:

$$J = \frac{I}{A} = -\kappa \frac{dU}{dx} = -\frac{1}{\rho}\frac{dU}{dx}$$ Equation 2-4

$$J = \frac{I}{A} = -\kappa \nabla U = -\frac{1}{\rho}\nabla U$$ Equation 2-5

where I (A) is the current, A (m^2) is the cross-section area over which the current flows, and dU/dx (V/m) is the one-dimensional potential gradient. In Equation 2-5 we use the three-dimensional potential gradient ΔU (V/m) instead of the one-dimensional potential gradient. As noted from the equations the electrical conductivity is the reciprocal of the resistivity. In this report the abbreviation EC is often used for electrical conductivity.

Fractured rock

The fractured crystalline rock that surrounds the SFR repository is not a homogenous medium, but is in many aspects heterogeneous. On the millimetre scale, the rock is built from different mineral grains that are intersected and/or surrounded by water-filled pore space. On a larger scale, the host rock is built by a number of rock types and domains, and water-filled fractures cut through the intact rock (e.g. Crawford 2008).

When modelling the electric field in fractured or porous media, it may still be justified to use equations for a homogenous medium. A prerequisite is that the scale of the modelling is much larger than the scale of the heterogeneity (or at least the most consequential part of the heterogeneity). In sparsely fractured crystalline rock, existing for example at depth within the Forsmark lens, a large fraction of the electrical current propagates through the microporosity of the intact rock matrix. Only a smaller fraction propagates in open fractures on the decimetre scale or larger. In more fractured parts of Forsmark, for example in shallow rock and outside of the lens, a somewhat larger fraction of the current may be transported in open fractures than through the intact rock. This latter applies for the host rock surrounding SFR. Concerning the open fractures, it is estimated that the consequential part of their heterogeneity is on the metre or decametre scale. The scales of the rock models of this present report are typically on the decametre scale up to the kilometre scale. This justifies replacing the rightmost part of Equation 2-4 by:

$$J = -\frac{1}{\rho_r^{BS}} \frac{dU}{dx} \qquad \text{Equation 2-6}$$

where ρ_r^{BS} (ohm.m) is the block-scale rock resistivity of the fractured rock. The block-scale rock resistivity may be obtained from empirical observations, with the prerequisite that the observations are representative for the relevant scale. Alternatively, the block-scale rock resistivity may be estimated (or at least bounded) from a few simplistic equations, as discussed in the below sections.

Macadam, concrete and bentonite

Concerning the macadam backfill, it can be viewed upon as crushed rock with grain sizes of a few millimetres up to few centimetres. Current will be propagated by electrolytic conduction in the water-filled pore space between the rock grains, and not significantly within them. Accordingly, the scale of consequential heterogeneity is on the centimetre scale or less. Domains of SFR that are backfilled with macadam are meters or tens of meters long or more and accordingly, they may be treated as homogenous.

Concerning intact concrete, consisting of cement and ballast, the size of the ballast grains is typically less than 32 mm (SKB 2014d, Table 12-6). Current will mainly be propagated by electrolytic conduction in the water-filled pore space of the concrete, around the ballast and through the cement. Accordingly, the heterogeneity of interest is also on the centimetre-scale. For fractured concrete the fractures may span the entire modelled domain (i.e. they may intersect the entire concrete embedment surrounding the pressure vessel). Open fractures will only constitute the main routes for electrolytic conduction in severely fractured concrete. Such concrete may simplistically be viewed upon as a crushed material with grain sizes up to a few decimetres. By embracing this simplistic view, we chose to also model fractured concrete as a homogenous medium.

Concerning bentonite its heterogeneity is also assumed to be on the centimetre-scale or less, as bentonite mineral grains are typically small-scale. Accordingly, the bentonite, which only exists in the tunnel backfill at some distance from the pressure vessels, is modelled as homogenous.

2.1.4 Inert porous media

In this section, and the following sections, the tools for estimating the block-scale rock resistivity used in Equation 2-6 are provided. The equivalent equations can be used for estimating the resistivity of concrete, macadam, and bentonite. The quantification of the media's resistivities, used as input data to our models, is given in Chapter 3.

As discussed earlier the great majority of the direct Earth current is propagated by electrolytic conduction in the water-filled pore space of the host rock. One-dimensional current propagation in free water is calculated according to Equation 2-7:

$$I = -\frac{AF^2}{RT} \sum_i z_i^2 C_i D_{w,i} \frac{dU}{dx} \qquad \text{Equation 2-7}$$

Where R (J/mol × K), T (K), and F (C/mol) are the gas constant, temperature, and Faraday constant, respectively. C_i (mol/m^3), z_i (–), and $D_{w,i}$ (m^2/s) are the concentration, charge number, and diffusivity of each ionic solute in the free water, respectively. The Einstein relation between diffusivity and ionic mobility is a foundation for Equation 2-7 (e.g. Atkins 1994). Combining Equation 2-4 and Equation 2-7 gives Equation 2-8:

$$\kappa_w = \frac{F^2}{RT} \sum_i z_i^2 C_i D_{w,i} \qquad \text{Equation 2-8}$$

where κ_w is the EC of the free water. As expected, the electrical conductivity is (more or less, cf. Section 2.1.7) proportional to the ionic concentrations in the water, if also accounting for the ions' charge numbers. If current propagation takes place in an inert porous medium (IPM) that does not interact electrostatically with the current bearing solutes, its electrical conductivity κ_{IPM} (S/m) is reduced by a proportionality factor, as compared to κ_w. Within the field of geoscience this proportionality factor is often called the formation factor F_f (–):

$$\kappa_{IPM} = F_f \kappa_w \qquad \text{Equation 2-9}$$

The formation factor is proportional to the transport porosity ε_t (–) of the porous medium, wherein current bearing ions are propagated. If the pores are tortuous and constrictive, their constrictivity δ (–) and tortuosity τ^2 (–) need to be included in the formation factor (Neretnieks 1980):

$$F_f = \varepsilon_t \frac{\delta}{\tau^2} \qquad \text{Equation 2-10}$$

The formation factor of the porous medium can be measured in, for example, through-diffusion experiments using non-charged and non-sorbing tracers. In those experiments one measures the tracer's effective diffusivity D_e (m^2/s) and compares it to the diffusivity in free water D_w:

$$F_f = \frac{D_w}{D_e} \qquad \text{Equation 2-11}$$

This has been done for numerous of rock samples within the Forsmark site investigation (e.g. Selnertet al. 2008).

2.1.5 Charged porous media

In crystalline rock the surfaces of its constituting mineral grains are typically negatively charged and interact electrostatically with the current bearing solutes. As the surfaces are mostly negatively charged, cations are concentrated at the pore water/mineral surface interfaces. Some of these cations bind strongly to a specific sorption site, effectively prohibiting them to migrate and propagate current. However, a fair number are mobile along the mineral surfaces and can propagate direct current. Such current propagation is a well-known phenomenon that is called surface conduction (e.g. Waxman and Smits 1968, Stumm and Morgan 1996, Revil and Glover 1997, Löfgren 2015). Inlow-porous crystalline rock the surface conduction is often a significant factor for the overall electrical conductivity of the rock matrix κ_r (S/m), unless the pore water is highly saline. To account for this, Equation 2-9 needs to be modified by adding the surface conductivity κ_s (S/m):

$$\kappa_r = F_f \kappa_w + \kappa_s \qquad \text{Equation 2-12}$$

As can be seen from Equation 2-12, the rock matrix's electrical conductivity will approach the surface conductivity if the electrical conductivity of the pore water becomes sufficiently low (i.e. in much diluted waters).

Measurements of the surface conductivity on rock from the Oskarshamn and Forsmark site investigation areas (Ohlsson 2000, Löfgren 2004, Löfgren et al. 2009) suggest surface conductivities in the range of 7×10^{-6} to 7×10^{-5} S/m (cf. SKB 2010, Figure 6-72). This range, together with the ranges of measured in situ formation factors and groundwater ECs (cf. Chapter 3), indicates that the current propagation by anions and cations in the bulk part of the micropores matches the propagation by cations through surface conduction. Accordingly, cations carry significantly more current than anions through the rock. The resistivity of the intact rock matrix ρ_r (ohm.m) becomes:

$$\rho_r = \frac{1}{F_f \kappa_w + \kappa_s} \qquad \text{Equation 2-13}$$

2.1.6 Fractured porous media

At the Forsmark site, the undisturbed rock matrix is often regarded to be fairly isotropic in regard to solute transport in the microporous system (e.g. Penttinen et al. 2006, SKB 2010), and thereby also in regard to its rock resistivity. This would mean that the same rock resistivity can be used regardless of the orientation of the electric field. The same does not necessarily apply for current propagation in fractured rock, if there is a preferred direction of the open fractures. If so, the block-scale rock resistivity is lower in parallel with the preferred fracture direction and increases at increasing angles between the fracture direction and potential gradient.

In the following example, calculations are made for a much-idealised case of fractured rock where all fractures are planar and parallel. Assume that there is a large block of rock with the bases A, B, and C (m). Further assume that this volume is intersected by *n* planar fractures, as shown in Figure 2-4.

Let's assume that each fracture has a uniform volumetric aperture e_v (m). The rock matrix has a formation factor F_f and surface conductivity κ_s and the pore and fracture waters have the same electrical conductivity κ_w. Let's further assume that on two opposite planes of the block, there are uniform potentials V_1 and V_2 and that the current propagation is one dimensional. This is a simplification as in the real case current lines injected in the rock matrix would bend towards the less resistive fracture planes (cf. Figure 2-1). By applying this simplification, one effectively uses the electrical circuit analogy as discussed in Section 2.1.1. If the potential drop ΔU (V) is along the x-axis, that is parallel to the fracture planes, the current running through the block would be:

$$I = -\kappa_w n e_v C \frac{\Delta U}{B} - (\kappa_w F_f + \kappa_s)(A - n e_v) C \frac{\Delta U}{B}$$

Equation 2-14

In the equation the first term on the right hand side concerns electrolytic conduction in the fracture water (EC times free water volume times potential gradient) and the second right hand term concerns electrolytic conduction and surface conduction in the rock matrix (cf. Equations 2-7 and 2-12).

Although this is a much-idealised case one can still give reasonable values of the parameters in Equation 2-14, which is done in Table 2-1. If inserting these values in Equation 2-14, the total current becomes 53μA. In this idealised case, the resistivity of the intact rock matrix is 7.7×10^3 ohm.m and the block-scale rock resistivity is 1.9×10^3 ohm.m. One fourth of the current is propagated in the intact rock matrix while the rest is propagated in the fracture water. The red curve in Figure 2-5 shows the resulting block-scale rock resistivity if varying the fracture frequency (n/C) from 0 to 100 fractures per meter, which corresponds to a variation from intact rock to a crush zone. All other values, as well as the direction of the potential gradient, are kept the same.

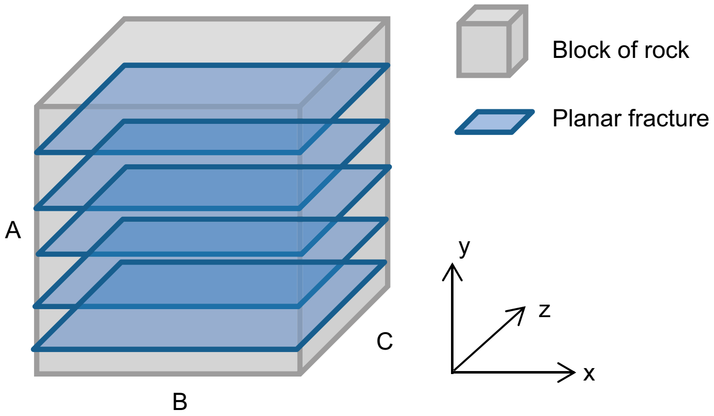

__Figure 2-4.__ Schematics of our much-idealised block of fractured rock. Fractures are blue and the rock matrix is grey.

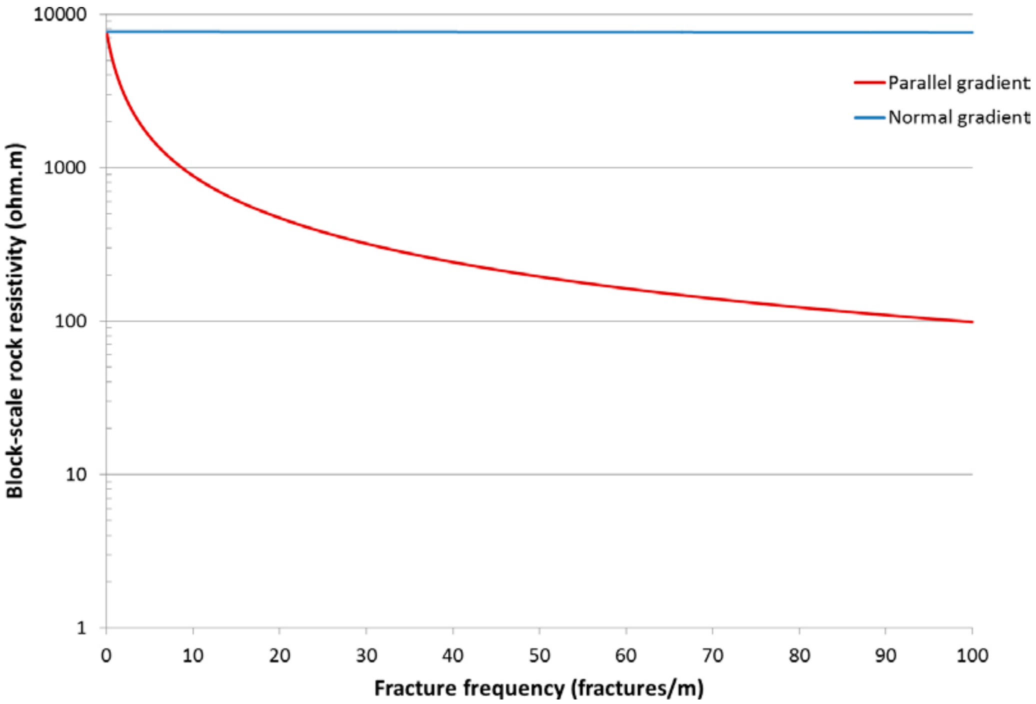

Figure 2-5. *The resulting block-scale rock resistivity if varying the fracture frequency of the idealised block of fractured rock for an electric potential gradient parallel and normal to the fracture planes.*

Table 2-1. Reasonable parameter values of our idealised block of fractured rock in Figure 2-4.

Parameter	Value	Comment
Arbitrary bases A, B, C of block	10 m	This value is arbitrarily chosen but is also inconsequential for the results.
Pore and groundwater EC, κ_w	1 S/m	This value roughly corresponds to present day groundwater composition in SFR (cf. Section 3.3).
Fracture frequency, n/A	4	In the drill core mapping of boreholes KFR105 and KFR102B at SFR, 473 m of drill core was mapped and 1 719 fractures were interpreted as open (Löfgren 2014, Section 4.2). This implies a fracture frequency of 3.6, which is rounded to 4.
Volumetric fracture aperture e_v	1×10^{-4} m	This value roughly corresponds to the median value in SKB (2010, Figure A-4).
Potential gradient $\Delta U/B$	1×10^{-3} V/m	This value roughly corresponds to the large scale gradient at Forsmark (Thunehed 2017).
Rock matrix formation factor, F_f	1×10^{-4}	This value roughly corresponds to the arithmetic mean of in situ rock matrix formation factors for boreholes KFR105 and KFR102B (Löfgren 2014).
Surface conductivity, κ_s	3×10^{-5} S/m	This value roughly corresponds to the only surface conductivity data point obtained with direct current in Forsmark (Löfgren 2015). Other data obtained with alternating current support this value (e.g. Ohlsson 2000, Löfgren et al. 2009).

If the potential gradient is normal to the fracture planes in Figure 2-4 (i.e. along the y-axis), the impact of the fractures is much less pronounced. This is as the resistive rock matrix becomes connected in series with the conductive fractures. The blue curve of Figure 2-5 shows the corresponding variation in the block-scale rock resistivity for the normal gradient, if varying the fracture frequency from 0 to 100 and keeping all other values constant. For this case, at a fracture frequency of 100 m^{-1}, the block-scale resistivity is only decreased by 1 % relative to the resistivity of the intact rock matrix.

In nature, fractures are not all aligned in parallel but are distributed in a three-dimensional network. Furthermore, they are not planar as they feature constrictions, fault gauge, splays, etc. that complicates matters even more. If distributing non-planar fractures in different types of dimensional networks, the block-scale rock resistivity would likely fall between the blue and red lines in Figure 2-5.

Realistic modelling of the influence of real fractures on the block-scale resistivity would be very difficult and require site specific information that is not available. Therefore, empirical data from geophysical downhole loggings have been used when evaluating a "best estimate" block-scale rock resistivity used as input data in the models (cf. Section 3.3 and Appendix A). The uncertainty in the block-scale rock resistivity has been further handled by sensitivity studies, using a range of rock resistivities. The above discussion has been used when assigning the resistivity range.

2.1.7 Temperature correction

The resistivity of a porous medium is influenced by the temperature of the electrolyte. In this report estimates of resistivities of different media have been made at the in situ temperature of SFR. Presently, the in situ temperature in the host rock, at repository depth, is about 10 °C (Nilsson 2011, Appendix 7).

If departing from Equation 2-8 it may be erroneously deduced from that the electrical conductivity is inversely proportional to the temperature. However, the diffusivity in water is also dependent of the temperature, as is shown by the Stokes-Einstein equation:

$$D_w = \frac{RT}{N_A}\frac{1}{6\pi\eta r}$$ Equation 2-15

where η (Ns/m^2) is the dynamic viscosity of the medium, N_A is the Avogadro number, and r (m) is the radius of the diffusing solute. If combining Equation 2-8 and Equation 2-15, the temperature will not cancel out, as also the dynamic viscosity is temperature dependent. Unless very high accuracy is demanded, a temperature compensation factor α (°C^{-1}) can be generally used in Equation 2-16 when making the temperature correction from 25 °C to the in situ temperature T (°C):

$$\kappa_{w,T} = \kappa_{w,25}(1 + a(T - 25))$$ Equation 2-16

Hayashi (2004) suggests a temperature compensation factor α of 0.019. The dynamic viscosity is also mildly influenced by the solute concentration in the water, but at SFR the groundwater is dilute enough for this to have little consequence. Mäntynen (2001, Table 8) measured the temperature compensation factor for groundwater taken from the Olkiluoto and Hästholmen sites in Finland. It varied between 0.018 and 0.02, where the value increased with decreasing ionic strengths. If instead relying on Arp's law (Arps 1953) the corresponding factor would be 0.0215.

From a practical point of view there are uncertainties in the extent to which the temperature influences the surface conductivity of the common rock types at the site (cf. Equation 2-13). This is even though the temperature is accounted for in the electrical double layer theory (e.g. Olin et al. 1997). Binley et al. (2010) have investigated the temperature dependence on electrical spectra in three sandstones by means of experimental observations. They suggest a correlation between effective relaxation length scales with the bulk tortuosity of the sandstone and highlight the need for a better mechanistic understanding of the processes involved and more complete models of electrical properties in porous media. In this report it is simply assumed that the temperature influences the mobility of ions in the electrical double layer (contributing to surface conduction) in the same way as for ions in the bulk pore water.

2.2 Basic corrosion theory

2.2.1 Corrosion reactions and thermodynamics

This section discusses the corrosion of iron in groundwater and concrete pore water. The great majority of the reactor pressure vessels consists of carbon steel, while only a small percentage consists of stainless steel. The specifics of the alloys will impact the corrosion on a level of detail that is outside the scope of this report. Instead this discussion departs from the assumption that the vessels are made from pure iron. In the corrosion of pure iron in groundwater under reducing conditions, metallic iron is typically oxidised to ferrous iron by:

$Fe(s) \rightarrow Fe^{2+} + 2e^-$ Equation 2-17

If the water is sufficiently oxidising, which may be the case directly upon repository closure, or during repository operation, ferric iron may be produced.

$Fe(s) \rightarrow Fe^{3+} + 3e^-$ Equation 2-18

The oxidation half-reactions in Equations 2-17 and 2-18 release two and three electrons, respectively, that need to be picked up by an accompanying reduction half-reaction. In the anoxic alkaline water assumed to contact the reactor pressure vessels in 1BRT after repository closure, the production of ferrous iron is expected. There are several conceivable reduction half-reactions that accompany iron corrosion in alkaline groundwater, where four straightforward ones are:

$\tfrac{1}{2}O_2 + 2H_2O + 2e^- \rightarrow 2OH^-$ Equation 2-19

$2H_2O + 2e^- \rightarrow H_2 + 2OH^-$ Equation 2-20

$2/x\ M^{x+} + 2e^- \rightarrow 2/x\ M(s)$ Equation 2-21

$Y(z)^{x-} + e^- \rightarrow Y(z-1)^{(x+1)-}$ Equation 2-22

Equation 2-19 involves the reduction of dissolved oxygen at oxic conditions. Equation 2-20 involves the reduction of water to hydrogen gas and hydroxyl ions. Equation 2-21 can be seen as an "electroplating reaction" where a dissolved metallic ion M, having the charge number x, is reduced to form a metal coating on the iron body. Equation 2-22 shows a generic reduction reaction with the anionic species Y; changing its overall oxidation number from z to $z-1$. The pickup of an electron may cause a reduction of the species' charge number, as indicated in Equation 2-22, but due to subsequent speciation reactions there is not necessarily a straight correlation between the studied element's oxidation number and the species' charge number.

In the groundwater at SFR, major dissolved cations are Na^+, Ca^{2+}, Mg^{2+} and to some extent K^+ (Román-Ross et al. 2014, Table A3-1, Auqué et al. 2013, Chapter 4). In concrete pore water, K^+ has relatively high concentrations (cf. Figure 3-19). The main anions in the groundwater and/or concrete pore water are Cl^- and OH^-. It should be noted that Cl(-I) cannot be further reduced and that reduction of OH^- cannot occur under the ambient conditions, as this would result in free oxygen radicals. The standard electrode potentials $e°$ (V) of reduction half-reactions involving the major cations are given in Table 2-2. The lower part of the table shows a few common reduction half-reactions involving no metals but more or less oxygenated water.

Table 2-2. Standard electrode potentials of a few reduction half-reactions. Upper part: common cations in concrete pore water. Lower part: half-reactions with water and oxygen. Data from Atkins (1994, Table 10.7) and Jones (1992, Table 2.1).

Reduction half-reaction	Standard potential e° (V) at 298 K
$Fe^{2+} + 2e^- \rightarrow Fe$	–0.44
$Na^+ + e^- \rightarrow Na$	–2.71
$K^+ + e^- \rightarrow K$	–2.93
$Ca^{2+} + 2e^- \rightarrow Ca$	–2.87
$Mg^{2+} + 2e^- \rightarrow Mg$	–2.36
$O_2 + 4H^+ + 4e^- \rightarrow 2H_2O$	+1.23 (at pH 0)
$2H_2O + 2e^- \rightarrow H_2 + 2OH^-$	–0.83 (at pH 14)
$O_2 + 2H_2O + 4e^- \rightarrow 4OH^-$	+0.401 (at pH 14)
$2H^+ + 2e^- \rightarrow H_2$	0 (by definition)

In Table 2-2, all reactions are given as reduction half-reactions by convention, although iron corrosion is an oxidation half-reaction. The standard electrode potential for the iron oxidation half-reaction is +0.44 V. Standard electrode potentials are given at unit activity for all species and deviations in their activities create deviating electrode potentials (e.g. Jones 1992). This is exemplified with the half-reaction:

$$aA + mH^+ + ne^- = bB + dH_2O \qquad \text{Equation 2-23}$$

The half-cell electrode potential e (V), at ambient temperature and electrolyte concentrations, can be calculated by the Nernst equation:

$$e = e^o - \frac{RT}{nF}\ln\frac{(\mathrm{B})^b(\mathrm{H_2O})^d}{(\mathrm{A})^a(\mathrm{H^+})^m} \qquad \text{Equation 2-24}$$

where the parentheses around the reactants and products denote their activity. In the studied system of pressure vessels in 1BRT, deviations from $e°$ are primarily caused by (relatively) low concentrations of the dissolved species, including deviating pH, and deviating ambient temperature and pressure (where the latter primarily relates to hydrogen gas production). From a thermodynamic point of view, the complete corrosion reaction (i.e. the sum of two half-reactions) should have a negative Gibbs free energy to be spontaneous. If not, and if no additional energy is added to the system, one can say that for the specific region of conditions, the metal has immunity to corrosion (Jones 1992). Such regions of conditions can, for example, be illustrated in Pourbaix diagrams. The Gibbs free energy is related to the cell potential E (V), which is the sum of the electrode potentials of the half-reactions. If the cell potential is positive, the Gibbs free energy is negative and the corrosion reaction is thermodynamically spontaneous. If the cell potential is negative, additional energy is needed to drive the reaction. Such additional energy may, in general terms, derive from Earth currents.

Even in the absence of Earth currents, the oxidation of iron is typically thermodynamically spontaneous in groundwater. Very high hydrogen gas pressures would be required for iron to be immune to corrosion in water, a situation not expected under realistic geological conditions. In pure[1] anoxic water the oxidation is accompanied by the reduction of the water molecule, as shown in Equation 2-20. If having unit activities, the cell potential E becomes –0.39 V, based on data in Table 2-2, indicating a positive Gibbs free energy. However, departures from unit activity change the cell potential which may, under many conditions, become positive. In the alkaline range and at room temperature and atmospheric pressure, the half-cell electrode potential of Equations 2-20 is dependent on the pH (Jones 1992):

$$e = -0.83 + 0.059 \times (14 - \mathrm{pH}) \qquad \text{Equation 2-25}$$

This means that the higher the pH-value is, the lower the driving force is for the reaction. The electrode potential of iron oxidation in Equation 2-17 is dependent on the Fe^{2+} activity by (Jones 1992):

$$e = -0.44 + 0.0295 \times \log_{10}(\mathrm{Fe^{2+}}) \qquad \text{Equation 2-26}$$

Equations 2-25 and 2-26 indicate that at low enough concentrations of Fe^{2+} and low enough pH-values (in the alkaline range), the cell potential is positive and the corrosion becomes spontaneous.

Similar considerations can be made for the other major constituent of the SFR groundwater and concrete pore water. As stated above the major anions are not reducible, while the main cations are listed in Table 2-2. As is easily deduced, the oxidation of Fe(0) to Fe(II), accompanied by the reduction of Na(I), K(I), Ca(II) or Mg(II) to its metallic form, is not thermodynamically spontaneous. In deducing this, it is worth noting that a sufficiently high Fe^{2+} concentration would be caused from the corrosion reaction with water (cf. Equations 2-25 and 2-26) to prevent a negative Gibbs free energy in the Fe(0) reaction with Na(I), K(I), Ca(II) or Mg(II). This can also be seen from mixed potential diagrams involving the reduction/oxidation of water and reduction/oxidation of iron and the major cation.

---

[1] Pure water with the exception of the alkaline agent, such as NaOH.

2.2.2 Corrosion kinetics

Activation polarisation

In this section a short account of electrochemical kinetics of corrosion is provided in the light of iron corrosion in aqueous solution. For a full introduction to the subject (Jones 1992, Chapter 3) is referred to. This discussion departs from the general redox reaction between an oxidised compound O and its reduced counterpart R:

$$\mathrm{O} + \mathrm{ne}^{-} \Leftrightarrow \mathrm{R} \qquad \text{Equation 2-27}$$

The net reaction rate R_{net} (mol/m$^2 \times$ s) is the forward reaction rate R_f minus the backward reaction rate R_b:

$$R_{net} = R_f - R_b = k_f C_{\mathrm{O}} - k_b C_{\mathrm{R}} = \frac{(i_c - i_a)}{nF} \qquad \text{Equation 2-28}$$

where k_f and k_b are the rate constants for the forward and backward reactions and C_{O} and C_{R} are the activities of the compounds O and R, respectively. The backward and forward reaction rates can also be described by forward and backward transfer of electrons. Before doing this, it is noted that the electron transfer can be expressed as an electrical current density, where the transfer of $1/F$ moles of electrons per second equals the current of 1 A. Here F is the Faraday constant (96 485 A.s/mol). By convention, in relation to corrosion reactions, the forward current density that gives rise to reduction is called the cathode current density i_c (A/m^2). The backward current density, giving rise to oxidation, is called the anode current density i_a (A/m^2). If the reaction is at equilibrium, i_c and i_a are equal but non-zero. At equilibrium, they also equal the exchange current density i_o (A/m^2):

$$i_o = i_a = i_c \text{ (at equilibrium)} \qquad \text{Equation 2-29}$$

It should be noted that the exchange current density correlates to the activation energy of the half-reaction at the corrosion surface, where a low activation energy gives a high exchange current density. When a net oxidation of metallic iron occurs, $i_a > i_c$. For sustained corrosion to occur, the net current density i_{net} (A) needs to be negative, where:

$$i_{net} = i_c = i_a \qquad \text{Equation 2-30}$$

The driving force of this net current density can be expressed as a overpotential η (V), which is the potential E (V) at the corrosion surface minus the equilibrium half-cell potential e in the Nernst equation (cf. Equation 2-24):

$$\eta = E - e \qquad \text{Equation 2-31}$$

The overpotential is also called polarisation and the anodic and cathodic overpotentials η_a and η_c relate to the anode and cathode current densities according to:

$$\eta_a = \beta_a \log_{10} \frac{i_a}{i_o} \qquad \text{Equation 2-32}$$

$$\eta_c = \beta_c \log_{10} \frac{i_c}{i_o} \qquad \text{Equation 2-33}$$

Where β_a and β_c (V) are the Tafel constants for the half-reaction. If applying a cathodic overpotential to the corrosion surface, the net current density becomes:

$$i_{net,c} = i_c - i_a = i_o exp^{\left(\frac{\alpha nF \eta_c}{RT}\right)} - i_o exp^{-\left(\frac{(1-\alpha) nF \eta_c}{RT}\right)} \qquad \text{Equation 2-34}$$

where the α and (1−α) are fractions of the cathodic overpotentials used for the forward and backward reaction. The similar expression as in Equation 2-34, if applying an anodic overpotential, is:

$$i_{net,a} = i_a - i_c = i_o exp^{\left(\frac{\alpha nF\eta_a}{RT}\right)} - i_o exp^{-\left(\frac{(1-\alpha)nF\eta_a}{RT}\right)} \qquad \text{Equation 2-35}$$

Equations 2-34 and 2-35 are consistent with the Butler-Volmer formulation of electrode kinetics. For high anodic overpotentials, the rightmost term of Equation 2-35 becomes insignificant and the equation simplifies to:

$$i_{net,a} = i_o exp^{\left(\frac{\alpha nF\eta_a}{RT}\right)} \qquad \text{Equation 2-36}$$

If comparing Equations 2-32 and 2-36, this suggests a β_a value of Equation 2-32 of:

$$\beta_a = \ln 10 \frac{RT}{\alpha nF} \qquad \text{Equation 2-37}$$

The corresponding cathodic Tafel constant becomes:

$$\beta_c = -\ln 10 \frac{RT}{\alpha nF} \qquad \text{Equation 2-38}$$

For a half-reaction that is symmetric (i.e. α = 0.5), involves the transfer of two electrons (as for metallic iron to ferrous iron), and occurs at standard conditions, β_a becomes 59 mV while β_c becomes –59 mV. If the half-reaction involves only one electrode, for the same set of conditions the Tafel constants would be ± 118 mV. Equations 2-32 and 2-33 can be plotted for both participating half-reactions in the same diagram, where the potential is on the y-axis and the current density is on the x-axis. This is illustrated in the Figure 2-6; but with this illustration follows a number of caveats.

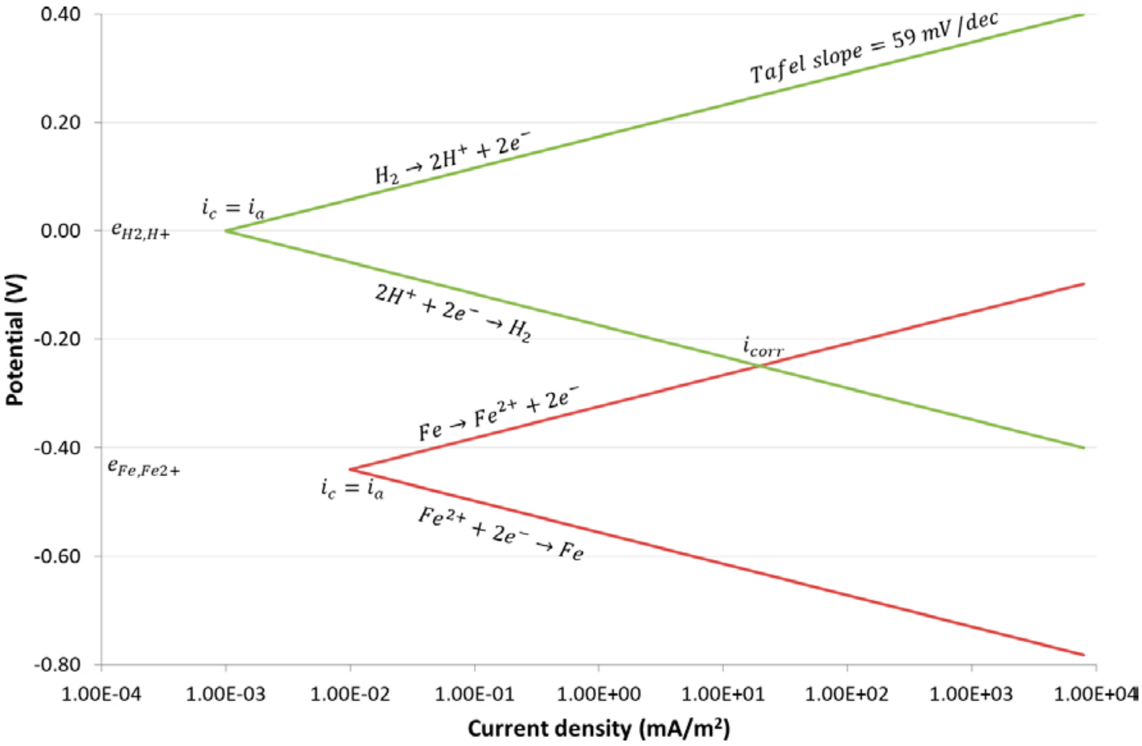

Figure 2-6. *Schematic illustration of a mixed potential diagram for the iron corrosion in an acidic solution. The exchange current densities of the reactions have been chosen arbitrarily, as they are unknown.*

The x-axis of Figure 2-6 represents the anodic and cathodic current densities i_a and i_c. However, as seen in Equations 2-32 and 2-33 the linear relationship between the overpotential is not versus $\log(i_a)$ or $\log(i_c)$ but versus $\log(i_a/i_o)$ or $\log(i_c/i_o)$. The exchange current densities i_o for the two half-reactions depend on their activation energies at the specific corrosion surfaces. If having a simple and well-defined system one may estimate (or measure) the exchange current densities (e.g. Jones 1992, Table 3-2) but this becomes increasingly difficult the more complex the actual corrosion system is. Accordingly, the current densities at equilibrium, e.g. when $i_a = i_c = i_o$, are unknowns. Accordingly, these points, together with their associated curves, may individually shift right or left in the plot.

The y-value at this point, for each half-reaction, is the half-cell electrode potential e, at equilibrium (cf. Equation 2-24). This value depends on the activities of the species of the half-reactions, which in Figure 2-6 corresponds to unit activity indicating a highly acidic solution. Moreover, the displayed mixed potential diagram applies under standard conditions. As such, $e_{\mathrm{H2/H+}} = e^{\circ}{}_{\mathrm{H2/H+}} = 0$ V. In a corresponding diagram for corrosion in alkaline solution, the half-reaction electrode potential at equilibrium would follow Equation 2-25. As ferrous iron would precipitate in an alkaline environment, its activity would be much lower than unity, decreasing its half-reaction electrode potential (cf. Equation 2-26). As such, in an alkaline system that it not under standard conditions, there is uncertainty in the half-reaction electrode potentials. Accordingly, the points where $i_a = i_c$ could also bedisplaced individually in the y-direction.

Moreover, there is uncertainty in the slope of the curves. A single reaction may follow a number of steps where any of these steps may be rate limiting. For example, it is suggested (Smart et al. 2001, Equation 8) that the rate limiting step in the reduction of water in an alkaline environment is $H_20 + e^- \rightarrow H(0)_{abs} + OH^-$. This reaction involves only one electron and this step of the reaction would, on its own, suggest a Tafel slope of 118 mV/dec. Moreover, the Tafel slopes are not only influenced by activation polarisation but also concentration polarisation, which tends to add to (observed) Tafel slopes. This creates uncertainty in all key parameters needed to draw a mixed potential diagram for corrosion at ambient conditions.

If being able to construct the correct mixed potential diagram, one could calculate the actual corrosion current density i_{corr} by the point where the upper red and lower green curves of Figure 2-6 intersects. At this point, the two curves share the same surface potential, also called the corrosion potential. This is a requirement as a single spot on a corrosion surface can only have a single potential. Due to the complexity of the system, the construction of reliable mixed potential diagrams for the corrosion process is outside the scope of this report. However, as shown in Section 2.2.5, if having an empirically obtained corrosion current density and Tafel slopes, one may construct the part of the mixed potential diagram that is consequential for the corrosion.

Concentration polarisation

The above discussion relates to activation polarisation, depending on the kinetics of the reactions at the corrosion surface. One may also speak of concentration polarisation. This relates to deviating concentration of reactants and reaction products at the metallic surface, as compared to in bulk of the aquatic solution surrounding the metallic object. This affects the equilibrium half-cell electrode potential e in Equation 2-24. Such deviating concentrations in turn relate to limitations in mass transfer of reactants and reaction products to, and from, the corrosion surface. Electromigration would, from a general perspective, enhance the mass transfer of ionic reactants and reaction products, as compared to the transport by diffusion. Such concentration polarisation effects are not further dealt with in this report but are neglected. However, their presence would give rise to lower corrosion rates, why neglecting them is pessimistic for the purpose of this study.

2.2.3 Impact of external electric fields

If placing an external direct electric field over the reactor pressure vessels, this may enhance the net corrosion rate. This is exemplified by an iron rod that is placed in an electrolyte over which there is an external potential gradient, as illustrated in Figure 2-7. The electrolyte includes the main current bearing cations and anions in concrete pore water. In the figure the dissolved anions migrate downward, towards the external anode, while cations migrate upward toward the external cathode. The solutes may migrate past the iron rod in the electrolyte, or they may react at its surface if they can be reduced or oxidised. When corrosion (i.e. the oxidation half-reaction) occurs at the metal surface it will release electrons that are propagated within the iron rod by electronic conduction. Thisoccurs locally even if there is no external electric field but if there is a field, relating to Figure 2-7, the electrons would preferentially propagate downward in the rod.

The excess of electrons either remains in the rod or the electrons leave (after reaction) through the surrounding electrolyte. Even a slight excess of negative charge in the rod would prevent further corrosion, which is often referred to as cathodic protection. For sustained corrosion the electrons need to leave the rod, which must be done by reduction of species (including H_2O) in the contacting electrolyte.

The external electric field can aid the iron corrosion by a number of mechanisms:

1. Bringing reducible anionic solutes to the anode side of the metal rod, at a higher rate than by Fickian diffusion and advection only.
2. Removing cationic corrosion products (i.e. Fe^{2+}) from the anode side of the metal rod, at a higher rate than by Fickian diffusion and advection only.
3. Bringing reducible cationic solutes to the cathode side of the metal rod, at a higher rate than by Fickian diffusion and advection only.
4. Removing anionic reduced water, i.e. the hydroxyl ion, from the cathode side of the metal rod, at a higher rate than by Fickian diffusion and advection only.
5. Bringing cations (both reducible and non-reducible) to the cathode, to balance the negative charge that is created in the water dissociation half-reaction (cf. Equation 2-20). This leads to sustained cathodic overpotential.
6. Bringing anions (both reducible and non-reducible) to the anode, to balance the positive charge that is created in the iron oxidation half-reaction. This leads to sustained anodic overpotential.

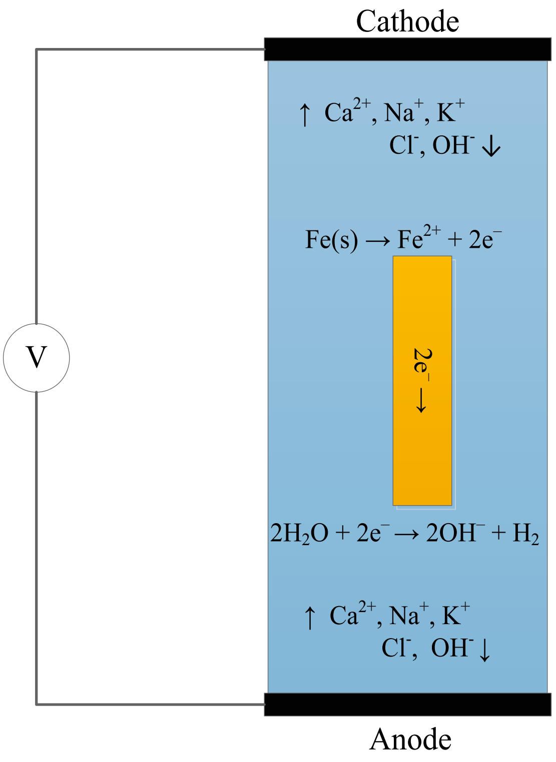

Figure 2-7. Illustration of an iron rod in an electrolyte subjected to an external electric field. Note that the released Fe^{2+} may precipitate in the high pH electrolyte.

Then there are a few less straightforward, but still conceivable, mechanisms:

7. Dissolving a formed iron precipitate, such as $Fe(OH)_2$.
8. Affecting the migration of anionic corrosion products involving iron, existing at high pH, such as $HFeO_2^-$.

Concerning the first item, that is bringing reducible anions to the metal rod, the most common anion in the groundwater at SFR is Cl^- (Auqué et al. 2013, Chapter 4). Chloride is already at its lowest oxidation state and cannot be further reduced. In concrete pore water there are also high concentrations of OH^- (cf. Figure 3-19), where its hydrogen can be reduced from oxidation state +1 to 0. However, the electromigration will not effectively increase the concentration of H(I) at the metal surface, as it is in contact with water. Also, further reduction of OH^- is unfeasible as it would result in oxygen radicals. Groundwater and concrete pore water may also contain small quantities of anions that may be reduced, such as sulphate. Bringing such anions to the surface at a higher rate (i.e. by electromigration and not only by diffusion) could in theory reduce the concentration polarisation. However, as the concentration of reducible anions is so low, this has little impact on the actual corrosion rate.

Concerning the second item, an increased removal rate of Fe^{2+} would perhaps increase the corrosion rate of iron (cf. Equation 2-26), as a lower ferrous iron concentration would be beneficial for the corrosion reaction in terms of its kinetics. Such electromigratory removal could, accordingly, reduce the concentration polarisation. However, as the rate limiting step in the overall corrosion reaction may relate to the reduction of water (Smart et al. 2001), the actual effect of this is uncertain and may depend on the magnitude of the local electric field.

Concerning the third item one can envision that metal cations of the electrolyte are reduced, facilitating the oxidation of iron. This can be exemplified by Na^+, which is often the most prominent current bearing cation in groundwater at depth:

$$Fe(s) + 2Na^+ \rightarrow Fe^{2+} + 2Na(s) \qquad \text{Equation 2-39}$$

As discussed in Section 2.2.1 this reaction and other reactions with major cations of the SFR groundwater are not thermodynamically spontaneous, unless there is a substantial added overpotential. If having an external electric field, one may envision a substantial potential drop over the metal/electrolyte interface that could match the negative cell potential of the reaction. On closer inspection, however, this mechanism becomes unfeasible for the studied system as:

- The energy would instead be spent on reducing water, in a half-reaction with a much lower half-cell electrode potential than of other half-reactions involving major current bearing cations.
- The required overpotential (at about 2 V) is not expected in the SFR repository system, as the large-scale potential gradients are in the mV/m range (cf. Section 3.2) and as the length of the reactor pressure vessels is about 20 m.
- The mantle of the reactor pressure vessels, and also the metal rod in Figure 2-7, is not insulated, allowing electrolytic conduction past the vessel. This prohibits the build-up of significant overpotentials.

Concerning the forth item, the corrosion of iron in an anoxic and alkaline concrete pore water is likely accompanied by the reduction of water according to the reaction in Equation 2-20. As stated previously, the driving force for this reaction is increased at lower pH-values (cf. Equation 2-25). If electromigration carries away the hydroxyl ions from the metal/electrolyte interface at enhanced rates, compared to diffusion and advection, this would decrease the concentration polarisation resistance and aid the corrosion. The away transport of OH^- may not be a straightforward process in the concrete matrix, as differences in pH would affect reactions with the concrete.

Concerning item 5 and 6, the iron rod's cathodic and anodic surfaces are separated by a significant distance (which is about 20 m in the case of reactor pressure vessels). The external field, upheld by the electromigration of ions in the surrounding electrolyte, creates anodic and cathodic overpotentials at the rod's anode and cathode side. These overpotentials affect the kinetics of the half-reactions. As such, there is an enhancement of iron corrosion at the anode side of the rod, but also a suppression of the corrosion rate at the cathode side. A similar process applies for the reduction of water. This creates a spatial separation in the net production of Fe^{2+} and OH^-. In case there (hypothetically) was no migration of current bearing ions in the surrounding electrolyte, the separated production of Fe^{2+} and OH^- would create a local electric field counteracting the external field. Accordingly, the electromigration of anions and cations in the surrounding electrolyte is needed to uphold the polarisation of the metal rod.

Concerning item 7, where corrosion occurs one can envision that large enough concentrations of Fe^{2+} build up at the metal surface for iron hydroxyl precipitates to form in the alkaline concrete pore water. If the precipitate is non-charged it will not be directly affected by the external electric field. However, at the precipitate/electrolyte interface the precipitate may dissolve in cases where the surrounding electrolyte's iron concentration is sufficiently low. Electromigration may then aid in the removal of dissolved iron species at the precipitate/electrolyte interface. This would aid the corrosion (by some degree of efficiency) by reducing the thickness of the protective iron precipitate layer. This layer could otherwise cause passivation.

Concerning the eight item, released Fe^{2+} at rod's anode side may react in the surrounding electrolyte to form anionic species, such as $HFeO_2^-$. These would be drawn back towards the corrosion surface and it is uncertain how this would impact the corrosion. One may speculate that there would be an up-concentration of the anionic iron species at the surface to the point where they would precipitate. According to Pourbaix diagrams (e.g. Jones 1992, Figure 2.11), $HFeO_2^-$ is only stable at low concentrations at the typical pH range of 12 to 13 in the concrete pore water (cf. Figure 3-19), and not stable at even lower pH-values.

Finally, it should be noted that in an alternating electric field, or in a rapidly fluctuating field under certain geometric constraints, ions in the electrolyte would move back and forth over short distances. This also applies to electrolytes in the film at the metal/pore water interface where capacitance effects would have a dampening effect on the alternating polarity. Moreover, the polarisation of the metal rod would switch back and forth, alternating between suppressing and enhancing the corrosion at a specific surface. As such, one may argue that an alternating electric field, at sufficiently high frequency, would not give a net increase in the corrosion rate.

2.2.4 The charge-balance approach

Due to the complexity of the 1BRT system, pessimistic assumptions need to be applied when modelling Earth current induced corrosion of reactor pressure vessels. The degree of pessimism is governed by the knowledge of the system and its uncertainty, but also by the assessment goal. In the charge-balance approach, both activation and concentration polarisations are neglected. As such, when modelling Earth currents being propagated through the reactor pressure vessels, no polarisation resistance is accounted for. The electrical current that is modelled to enter (and leave) each reactor pressure vessel is assumed to contribute fully to corrosion via the reaction $Fe \rightarrow Fe^{2+} + 2e^-$. The mass *m* (kg) of iron that becomes corroded per time unit *t* (s) is then:

$$m = \frac{Ita}{nF} \qquad \text{Equation 2-40}$$

where *a* is the atomic weight (kg/mol) of iron. For the corrosion to ferrous iron, if 1 A leaves the body, this gives rise to the corrosion of 9.1 kg of iron per year.

To investigate the merits of this approach, it is interesting to discuss the hypothetical case of a higher corrosion rate than warranted by the external electric field. In doing so, it is assumed that the reactor pressure vessel has insignificant resistance to electric transfer, due to the high electrical conductivity of steel and the neglecting of polarisation resistance. As such, the current that is transferred through the pressure vessel is governed by the large-scale electric field, as well as the dimensions and electrical properties of the surrounding materials in the engineered barrier and host rock. In this exercise it is assumed that the surrounding system allows for a potential drop of 1 V over the pressure vessel and that 1 A is fed into it. It is further assumed that the corrosion rate initially is above 9.1 kg iron per year, which suggests a corrosion current above 1 A. As discussed above, Fe^{2+} would predominantly be produced at one side of the pressure vessel while OH^- would predominantly be produced at the other side. If the charge production is at a higher rate than what can be carried away by Earth currents in the surrounding electrolyte, there would be a charge build-up at each side of the pressure vessel. This build-up would counteract the initial potential drop over the vessel. As the potential drop decreases, this lowers the anodic and cathodic overpotentials, which leads to slower kinetics of the iron oxidation (and water reduction). This reduces the corrosion current and the amount of charge separation per time unit in the vessel. Virtually instantly the system would stabilise and the corrosion current would correspond to 1 A and the potential drop over the vessel would be 1 V, as determined by the external electric field.

2.2.5 The kinetics limitation approach

Figure 2-8 is a modification of Figure 2-6 where the parts of the curves governing the iron oxidation and proton reduction are blackened. As in Figure 2-6, the mixed potential diagram applies for corrosion in an acidic solution. If there is no external field the corrosion current density and surface potential can be obtained from where the two black curves meet, if having a correct setup of the mixed potential diagram. If there is an external field, the iron body will become polarised and one end will function as its anode and the other as its cathode (cf. Figure 2-7). In Figure 2-8 an anodic overpotential η_a is indicated. As discussed previously where there is an anodic overpotential the oxidation and reduction reactions do not occur at equal rates, but the oxidation rate is enhanced while the reduction rate is supressed.

The slopes of Figure 2-8 suggest if one applies an anodic overpotential of 59 mV to a metal surface, this would increase its anodic current density by one order of magnitude. At the same time this would suppress the cathodic current density by one order of magnitude. The (absolute amount of the) net current transported to the anodic surface, i.e. the corrosion current, is the anodic current minus the cathodic current, if accounting for the surface area. In Figure 2-9 the anodic and cathodic current densities, as well as the absolute amount of the net current density, are plotted vs. the surface potential, based on the mixed potential diagram of Figure 2-8.

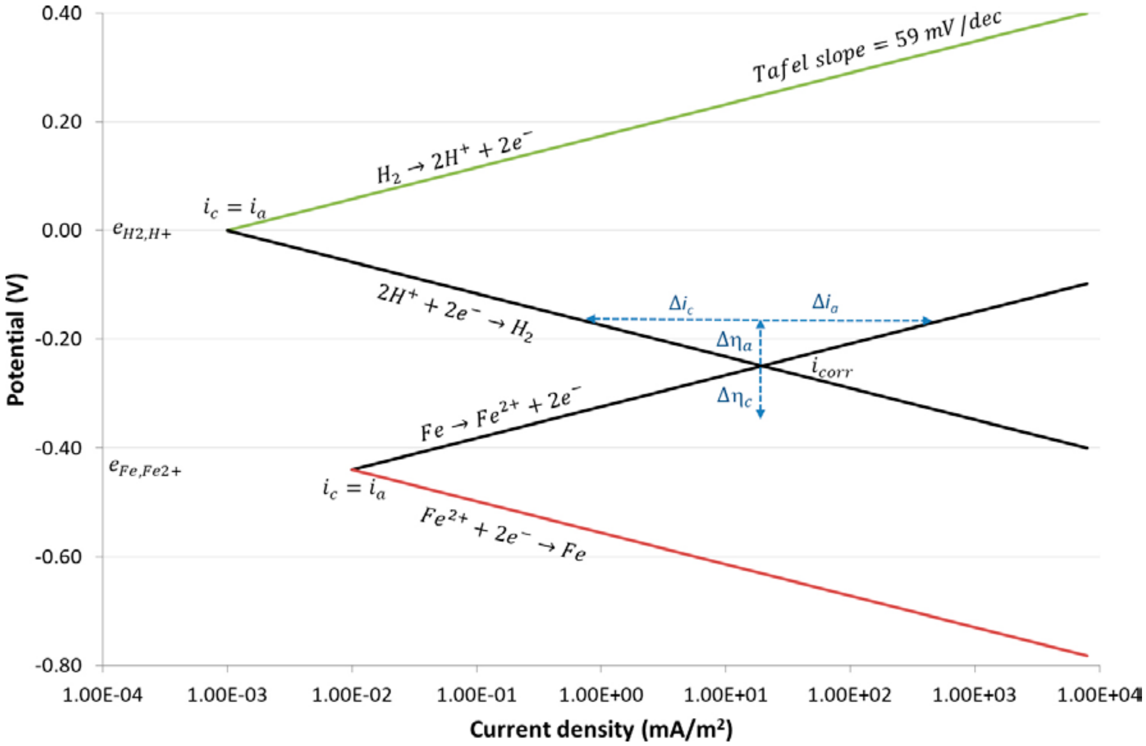

Figure 2-8. *Illustration of overpotentials created at the anode and cathode side of a metal body. Note that the mixed potential diagram reflects corrosion in acidic solution.*

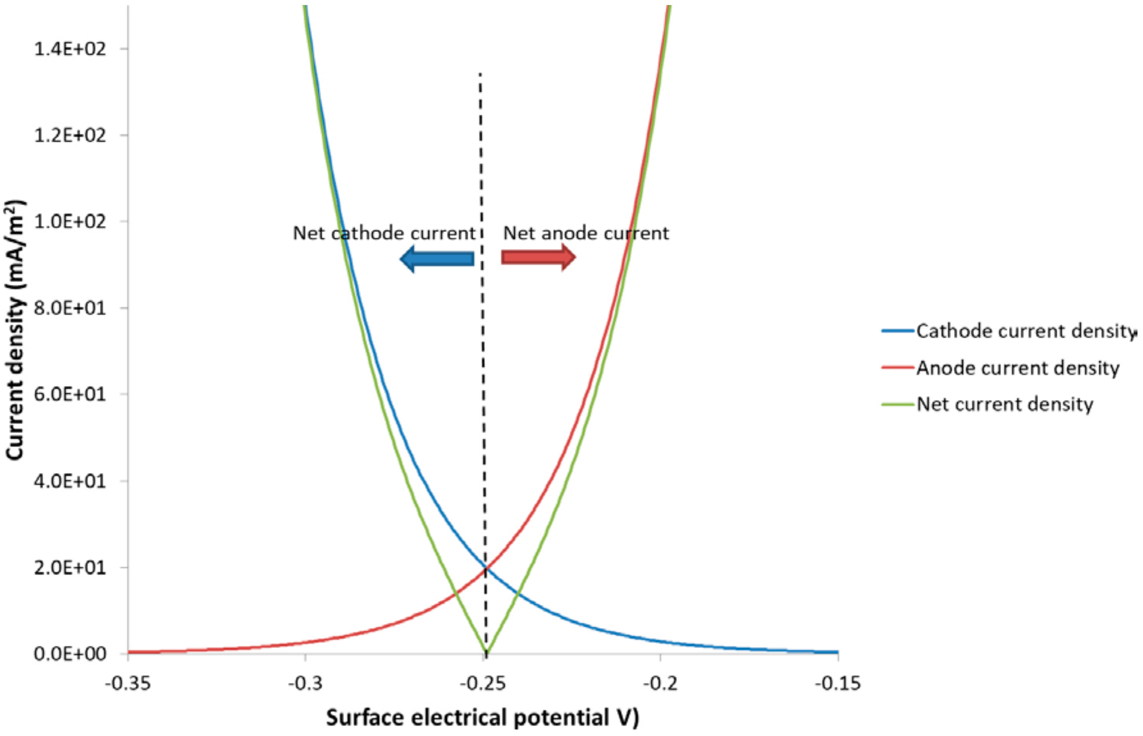

Figure 2-9. *The anodic and cathodic current densities, and the absolute amount of the net current density, vs. the surface potential, based on the mixed potential diagram of Figure 2-8. The dashed line separates the regions of net cathode current and net anode current.*

In Figure 2-9 the corrosion current density (20 mA/m^2) and corrosion potential (–0.25 V) correspond to the values where the black curves in Figure 2-8 meet. However, this point is neither determined in the x or y direction, as discussed above. Therefore, it is convenient to normalise the axes of Figure 2-9. For the y-axis this is done by dividing the current densities by the corrosion current density (i.e. 20 mA/m^2). For the x-axis this is done by calculating the surface overpotential, which is the actual surface potential minus the corrosion potential (i.e. –0.25 V). Here a positive overpotential corresponds to an anodic overpotential, while a negative overpotential corresponds to a cathodic overpotential. This is done in Figure 2-10. In the absence of an external field the metal body is not polarised and its surface has zero overpotential. As such, there is no net transport of charge to a corrosion surface. For Tafel slopes of 59 mV/dec, if having an overpotential of about 12 mV gives an increase in the corrosion current of a factor of two, compared to in the case of no overpotential (in the figure the net current density, normalised with the corrosion current density, is one). If increasing in the Tafel slopes, a higher overpotential is required to obtain the normalised net current density of one. This is shown in Figure 2-11, where the Tafel slopes are doubled to ± 0.118 mV/dec. In this case the required overpotential, to achieve a normalised net current density of one, is doubled to about 24 mV. For the same external electric field, one can thereby expect lower corrosion rates the higher the Tafel slopes are. Experimentally obtained Tafel slopes for iron oxidation may be higher than what is expected from Equation 2-37, due to the effect of concentration polarisation.

Figure 2-12 shows the case where the reduction reaction has a Tafel slope of –118 mV/dec and the oxidation reaction has the Tafel slope of 59 mV/dec. In this case, the overpotential required to achieve a normalised net current density of one is about 17 mV, which is 12 and 24 mV.

The same curves as derived above from the mixed potential diagram could be directly plotted if using the Butler-Volmer formulation of electrode kinetics (cf. Equations 2-34 and 2-35). These equations are, accordingly, adopted in the kinetics limitation approach when performing numerical modelling in Chapter 6.

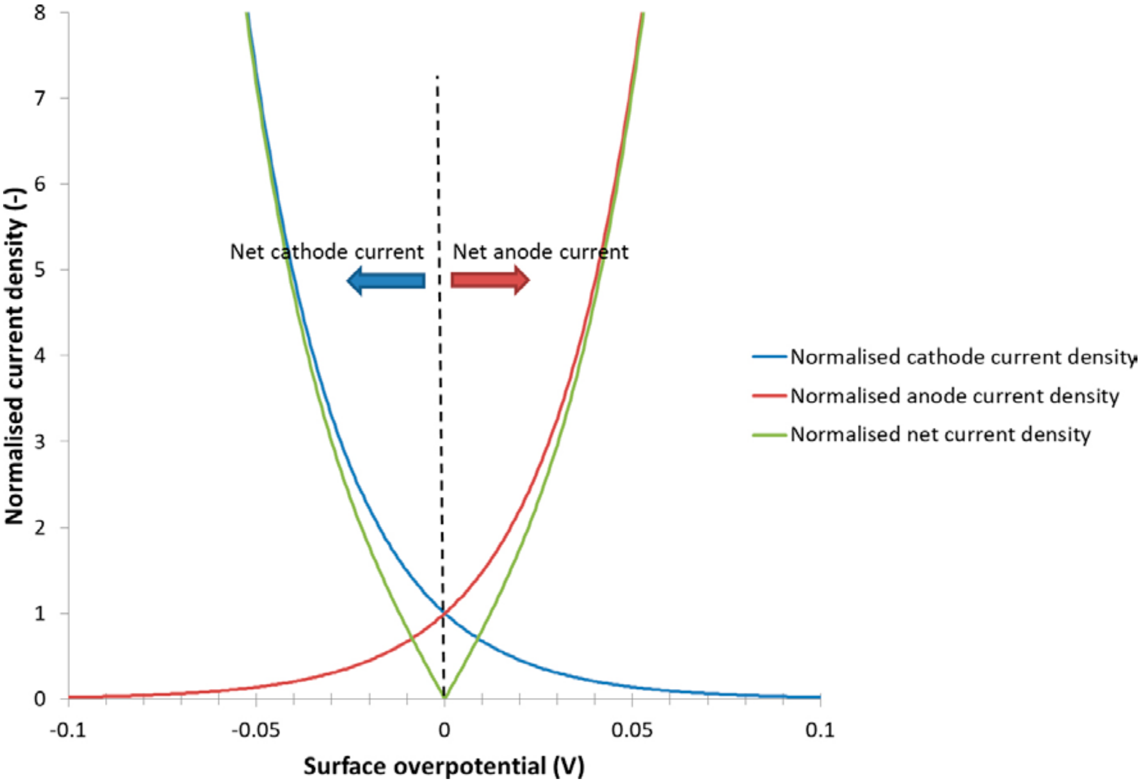

Figure 2-10. Normalised anodic and cathodic current densities, and the absolute amount of the normalised net current density vs. the surface overpotential. Tafel slopes are 0.059 and –0.059 mV/dec. The dashed line separates the regions of net cathode current and net anode current.

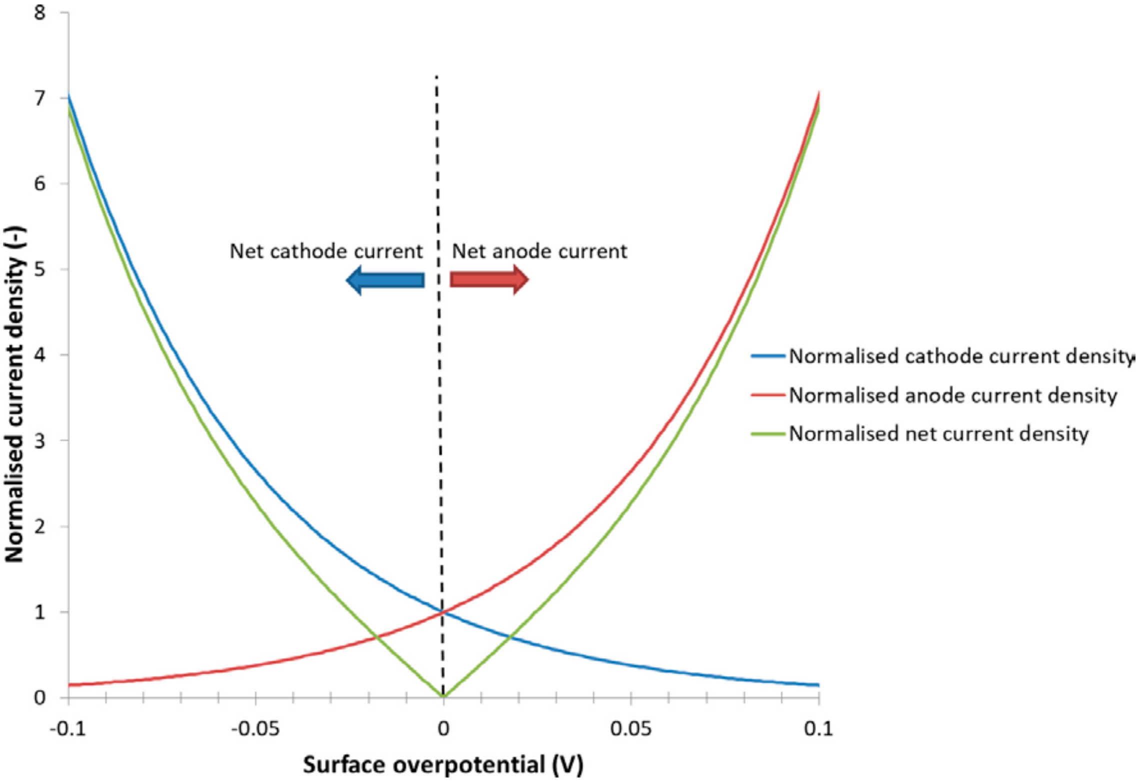

Figure 2-11. Normalised anodic and cathodic current densities, and the absolute amount of the normalised net current density vs. the surface overpotential. Tafel slopes are 0.118 and –0.118 mV/dec. The dashed line separates the regions of net cathode current and net anode current.

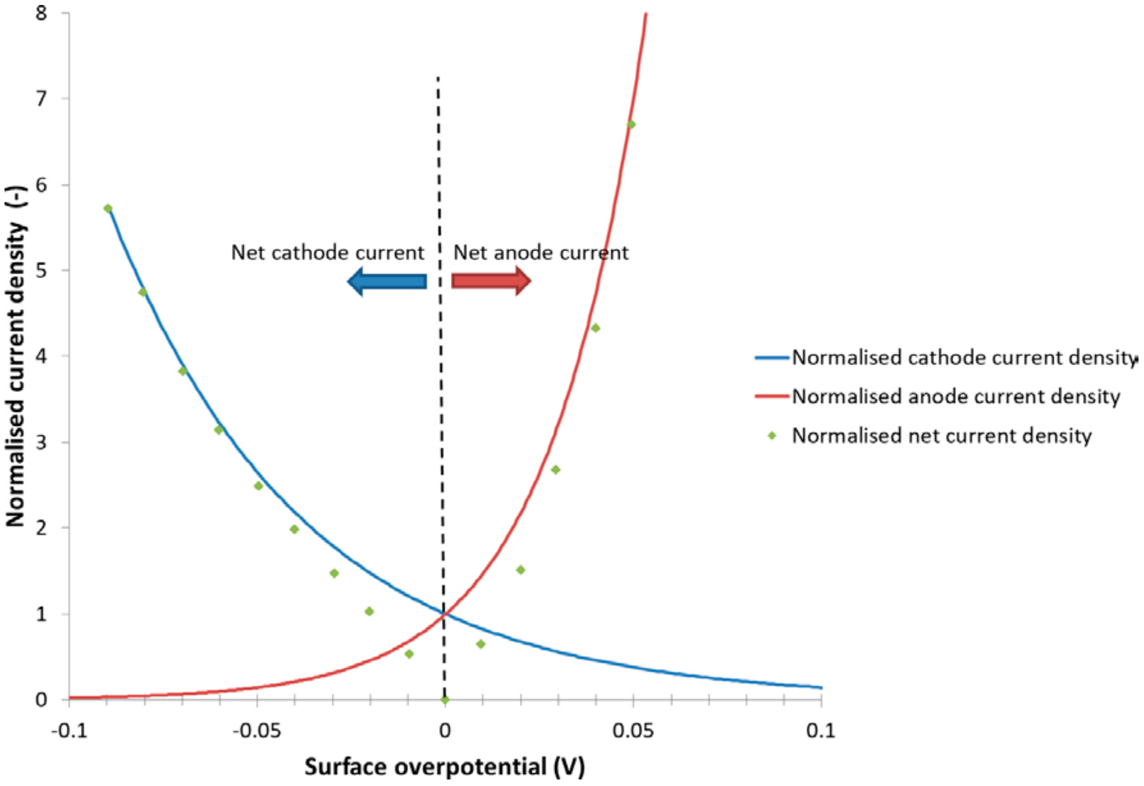

Figure 2-12. *Normalised anodic and cathodic current densities, and the absolute amount of the normalised net current density, vs. the surface overpotential. Tafel slopes are 0.059 and –0.118 mV/dec. The dashed line separates the regions of net cathode current and net anode current.*

3 Geometries and input data

3.1 Geometries

3.1.1 General layout of SFR

Figure 3-1 illustrates the general layout of the existing SFR and its planned extension, where the underground openings of blue colour represent the extension. The extended part consists of six vaults, access tunnels and an access ramp. The vault for reactor pressure vessels, 1BRT, is located in the centre part of SFR. The extension will be placed in the crystalline bedrock below the sea at a depth of approximately 120 m. This can be compared with the existing repository, where the vaults are located at a depth of about 60 m below the sea level and the silo extends between approximately 60–120 m depth. Figure 3-2 illustrates the extended repository from the side, where also a few depths are indicated. Again, the blue coloured parts represent the planned extension.

3.1.2 Layout of the extension

Figure 3-3 shows an overview of the six new vaults of the extension, the existing vaults, and the silo. In the SFR repository layout version 2.0, which has been used in this report, the length of the 1BRT vault is 240 m while the length of the 2–5BLA and 2BMA vaults is 275 m (SKB 2014d, Tables 5-1, 9-1 and 10-1). Between the 1BRT vault and the access tunnels 2TT and 2BST there are access paths that have the combined length of over 35 m. The vaults of the extension are between 15 to 20.4 m wide and between 13 to 16.4 m high. The rock pillars between the vaults roughly have the same widths as the vaults. Three ramps will create access to the repository from ground surface. The 1RTT ramp, wherein the pressure vessels will be transported from ground surface to the 1BRT vault, is the longest of the ramps with a length of about 1 700 m (Hellman and Winnerstam 2014). Note that there are passages between the three ramps. This is of importance for the modelling of Earth currents in SFR as these connections enable low resistivity paths for the electrical current from the vaults of the extension to the existing access ramps.

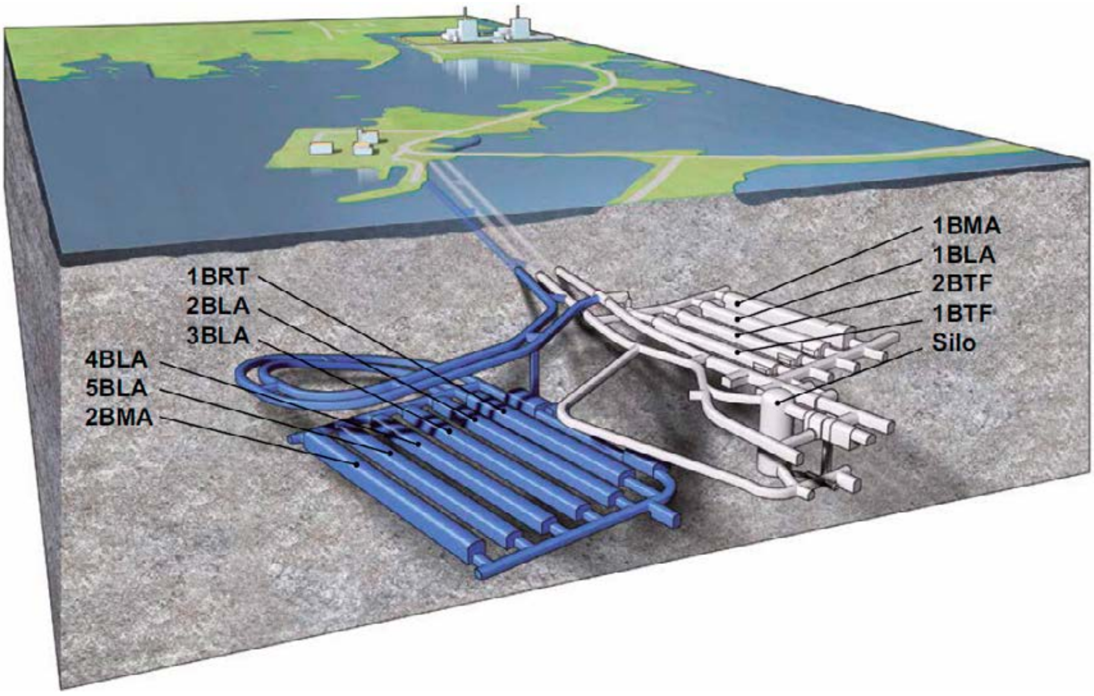

Figure 3-1. *Illustration of the extended SFR repository. The existing SFR is shown in grey on the right and the extension on the left is in blue. The different vaults are indicated where 1BRT is the vault for reactor pressure vessels. Reproduced from SKB (2015, Figure 1-2).*

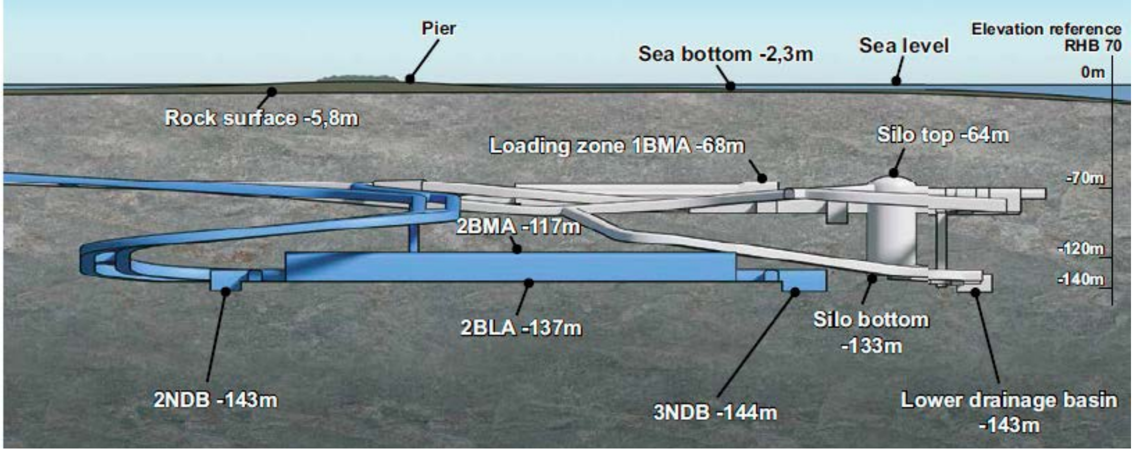

Figure 3-2. *Illustration of the extended SFR repository from the side. Designated levels are in RHB 70. Reproduced from SKB (2015, Figure 4-3).*

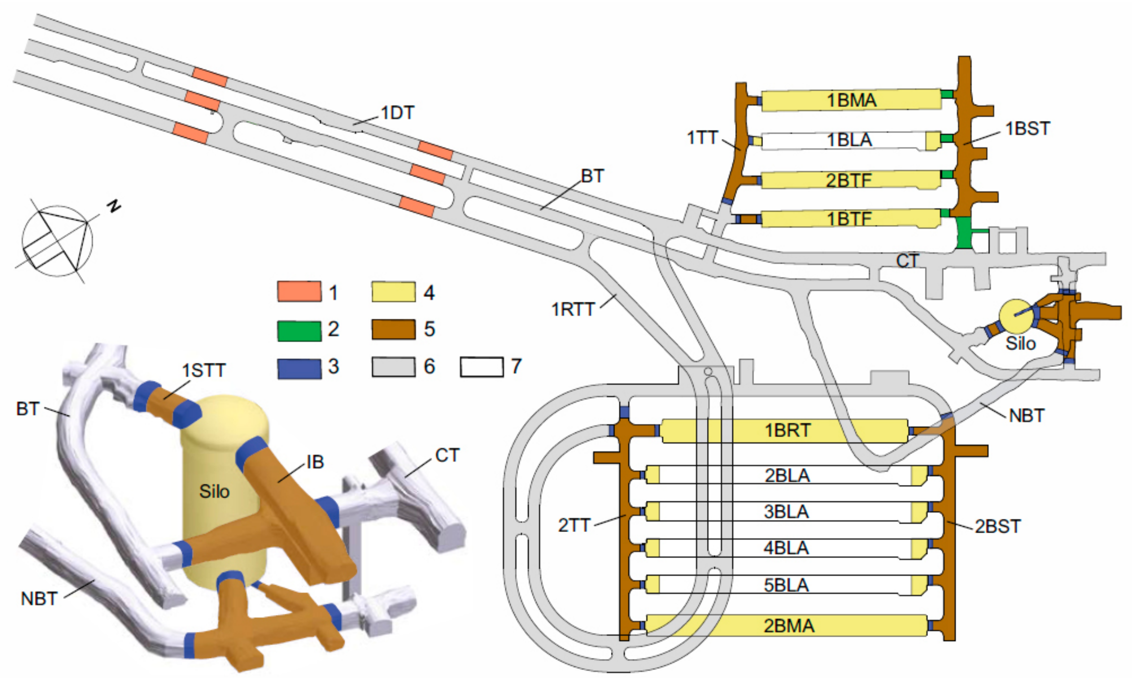

Figure 3-3. *The new and existing vaults, silo, access tunnels and ramps of SFR. Yellow colour indicates vaults that are backfilled with macadam. Brown colour indicates access tunnels backfilled with bentonite. Reproduced from SKB (2014d, Figure 11-1).*

3.1.3 Geometries of the 1BRT vault

This section is written under the prerequisite that intact reactor pressure vessels are deposited in 1BRT, which was the assumption in SR-PSU. The impact of Earth currents on segmented pressure vessels is studied in Section 6.7.

The dimensions and inventories of the 1BRT vault and its pressure vessels are described in SKB (2013b, 2014d). Figure 3-4 shows an illustration of the 1BRT vault during operation. Nine pressure vessels will be deposited in a vault where the roof and walls are lined with shotcrete. The floor of the vault will be made of reinforced cast concrete on a bed of macadam. It is stated in Hellman and Winnerstam (2014, Figure 5-11) that the pressure vessels will be placed on stands of concrete. At closure, all nine pressure vessels have been placed in a row on the floor. Their void space will be filled with concrete or cementitious grout. Thereafter all pressure vessels will be embedded in a concrete grout. The remaining space of the vault will be filled by macadam, i.e. crushed rock. Schematic illustrations of the vertical cross section areas of the 1BRT vault are provided in Figure 3-5 and

Figure 3-6. Key dimensions of the 1BRT vault are given in Table 3-1. Key dimensions of the pressure vessels, and their metal inventory, are given in Table 3-2 and Table 3-3. A great majority of the reactor pressure vessels consist of carbon steel, although their insides are lined with a stainless steel layer of at least 3 mm (e.g. Anunti et al. 2013, SKB 2013b).

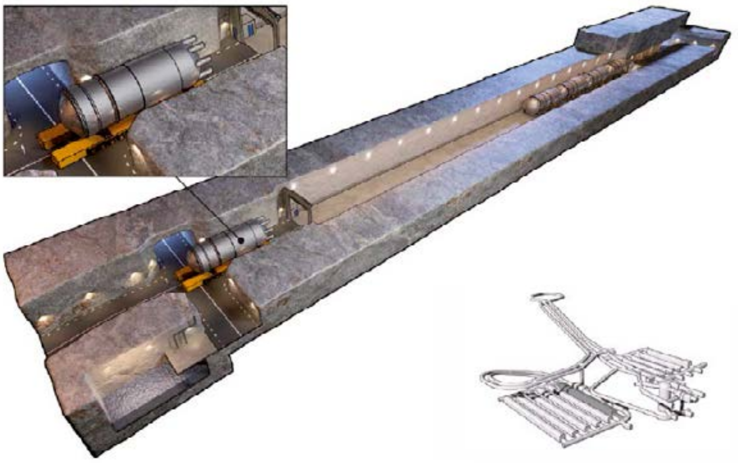

Figure 3-4. *Illustration of 1BRT during the operating phase. Reproduced from SKB (2014d, Figure 10-1).*

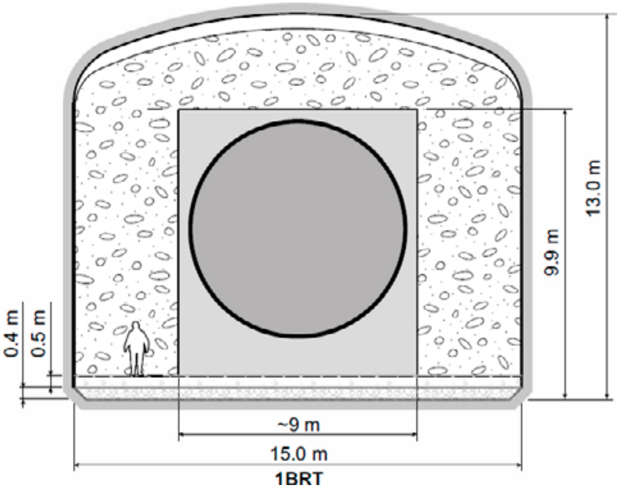

Figure 3-5. *Schematic cross-section of 1BRT after closure. Reproduced from SKB (2014d, Figure 10-2).*

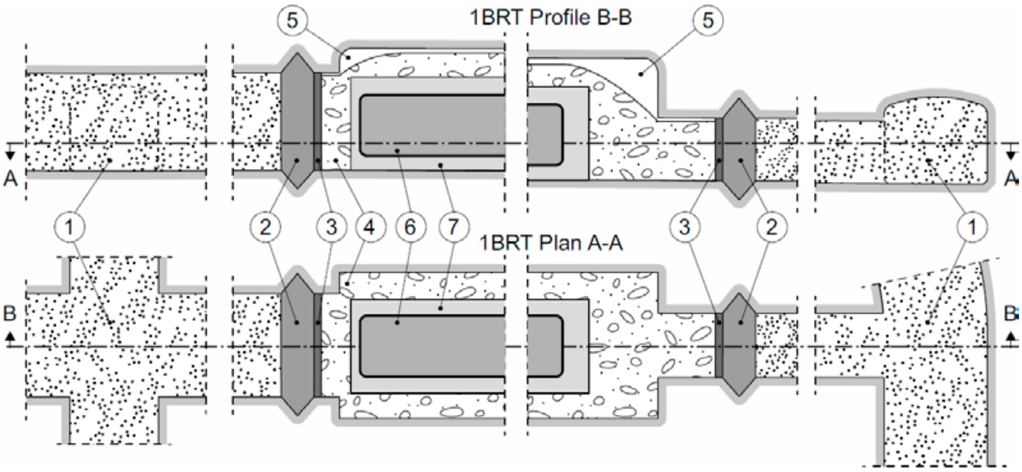

Figure 3-6. *Schematic profiles of 1BRT after closure. Key to numbering: 1) bentonite 2) concrete plug 3) supporting wall and mould for casting 4) macadam 5) open gap between macadam and tunnel roof 6) reactor pressure vessel filled with concrete 7) concrete embedment. Reproduced from SKB (2014d, Figure 10-3).*

Table 3-1. Dimensions of 1BRT. Data reproduced from SKB (2014d, Table 10-1)

Geometries of 1BRT (Layout 2.0)	Values
Length of vault	240 m
Width of vault	15
Maximum height of vault	13 m
Average height of vault	12.5 m
Vertical cross section area	188 m^2
Thickness of shotcrete	5 cm
Length of concrete embedment	207 m
Width of concrete embedment	8.6 m
Height of concrete embedment	9 m
Thickness of reinforced concrete floor	0.5 m
Thickness of macadam under concrete floor	0.4 m

Table 3-2. Dimensions of the pressure vessels. Data reproduced from SKB (2013b, Sections E2, E19, E32 and E44).

Pressure vessel	Length/height (m)	Outer diameter (m)
O1	18	5.3
O2	20.2	5.5
O3	21.4	6.75
F1	21.5	7.2
F2	21.5	7.2
F3	21.4	6.75
R1	20.2	6.2
B1	20.0	5.9
B2	20.0	5.9

Table 3-3. Corrosion area and metal inventory of pressure vessels. Data reproduced from SKB (2013b, Table 5-2).

Description	Value
Total surface area of the nine (non-segmented) pressure vessels: so-called corrosion area	7.240 m^2
Total weight of the nine pressure vessels' steel parts	5.55×10^6 kg
Main steel type	Carbon steel

The representative thickness of the concrete embedment that surrounds the pressure vessels' mantel area has not been specified in studied reports. In Figure 3-5 the outer width and height of the embedment are given as ~ 9 m and in Table 3-1 they are specified to 8.6 and 9.0 m, respectively. As the pressure vessels have different outer diameter (cf. Table 3-2) this suggests a minimum concrete thickness between 0.7 and 1.9 m. The thickness of the concrete layer covering the vessels' mantel area is of no consequence for the electrical circuit model, but for the COMSOL Multiphysics model we have adopted the baseline value 0.9 m. This was calculated from the ~ 9 m width and height specified in Figure 3-5, minus the outer diameter of the largest vessel (F1 and F2), divided by 2. In sensitivity calculations with COMSOL Multiphysics the impact of the concrete embedment is investigated by modifying the concrete's resistivity, as well as by setting its thickness to zero (cf. Section 6.4).

3.2 Large-scale electric field

3.2.1 Present day field

The electric field in the Forsmark area is described in Thunehed (2017). The regional field is mainly in response to the Fenno-Skan HVDC electrode at Fågelsundet, located about 25 km north of SFR. Field strength measurements have been performed when Fenno-Skan 1 was in use close to its maximum rating and Fenno-Skan 2 was out of operation, making the Fågelsundet electrode emit a direct current of around 1 280 A into the Baltic Sea. Under such conditions the regional field would, on its own, create horizontal and vertical potential gradients of about 0.7 and 2 mV/m, respectively, at Forsmark (Thunehed 2017). However, at the Forsmark site there is a large-scale anomaly in the electric field that is caused by grounding of power line installations close to the Forsmark nuclear power plant. Figure 3-7 shows a conceptual illustration of the regional situation with regard to Fenno-Skan, as reproduced from Thunehed (2017). The illustration shows the Fenno-Skan cable from Sweden to Finland (solid blue line); the current lines at the Fågelsundet electrode when used as anode (red arrows); the iso-potential contours around the electrodes (green lines); and the network of power lines from the high-voltage AC sub-station at the power plant (dashed blue lines). These power lines are grounded at the site.

Figure 3-8 shows conceptual illustrations of the electric field at the Forsmark site. The left illustration shows the regional iso-potential contours caused by the Fågelsundet electrode by black dashed lines (compare with green solid lines in Figure 3-7) and the local iso-potential contours (green solid lines) caused by local grounding of the power lines. The red current lines illustrate that the power lines pick up current emitted from the Fågelsundet electrode and carry it inland. The right illustration shows the resulting iso-potential contours if superimposing the regional and local fields. Note that the distance between the contours is inversely proportional to the field strength. The right illustration indicates that the field strength close to the AC sub-station may be significantly higher than further away.

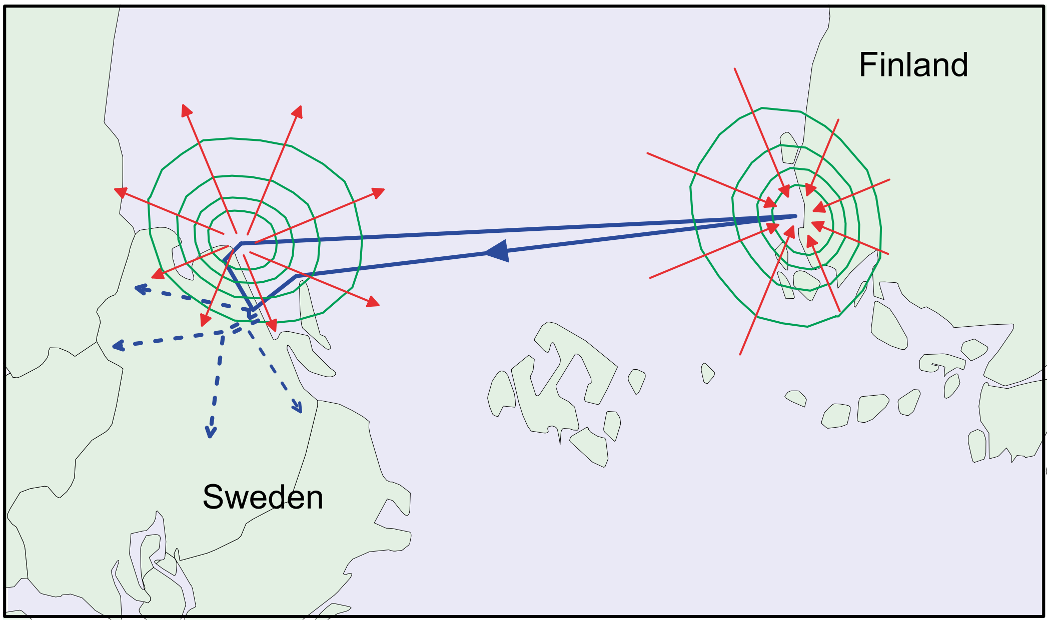

Figure 3-7. *Map illustrating the principal current flow of the Fenno-Skan HVDC link, assuming current flow from Finland to Sweden (Fenno-Skan 1 in use) and the use of the Fågelsundet electrode as an anode. The solid blue line shows the HVDC cable and the electrode line. Red arrows illustrate the current direction in the ground. Green lines are (sketched) potential contours. Dashed blue lines are high-voltage AC lines connected to the Swedish power grid and with top and earth conductors grounded at Forsmark. Reproduced from Thunehed (2017, Figure 7-1).*

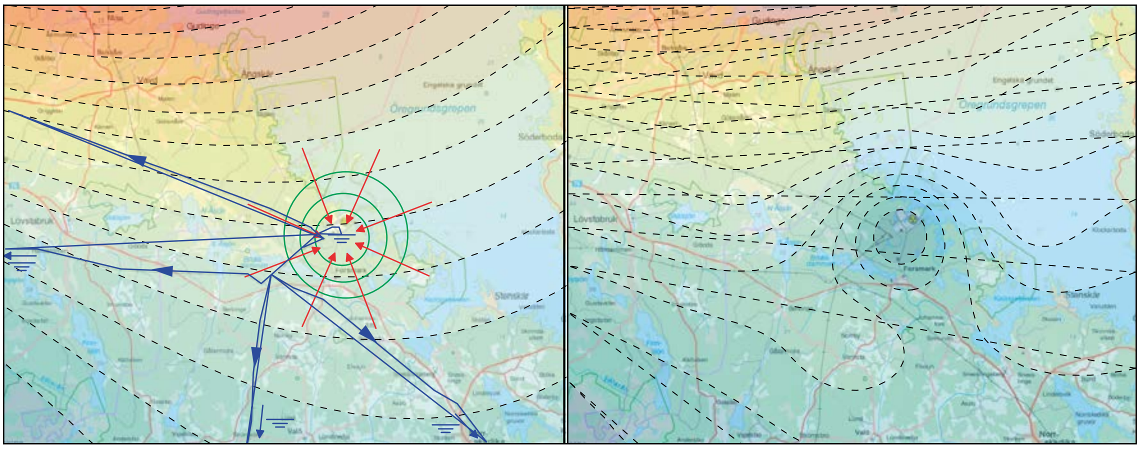

__Figure 3-8.__ Map of the Forsmark area with sketched iso-potential contours due to current injection at Fågelsundet and current transmission along grounded AC line top conductors. The solid blue lines represent the high-voltage AC lines connected to the Swedish power grid. Reproduced from Thunehed (2017, Figures 7-2 and 7-4)

These conceptual illustrations are backed by the potential measurements at the site, performed at a time when the Fågelsundet electrode was switched on emitting around 1 280 A. Figure 3-9 shows the measurement data as well as the extrapolated electric field at the local site. The position of SFR in relation to the measurement points can be deduced from comparisons with Figure 3-10. The layout of the extension, shown in Figure 3-10, is preliminary but no major changes have been done in later layouts with regard to the general positions and alignments of the vaults.

The largest measured potential gradient in Figure 3-9 is between the data points 2 441 and 1 611 mV. The Euclidian distance between these two points is about 300 m, making the potential gradient 2.8 mV/m. The alignment of the local field is roughly along the access ramps of SFR. At SFR, further away from the AC sub-station, the potential gradient is somewhat lower and the large-scale gradient of 2 mV/m has been used in most of the modelling in this study.

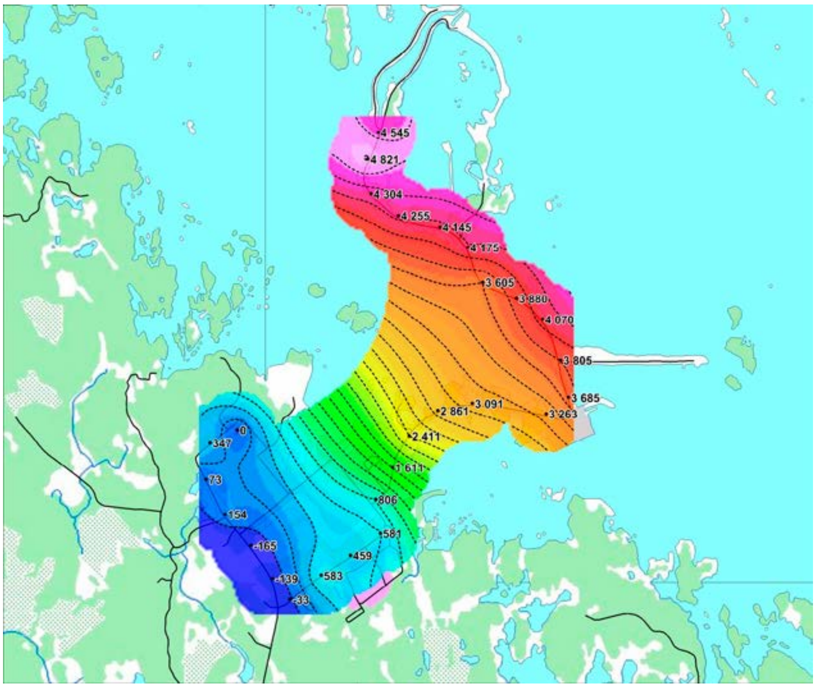

__Figure 3-9.__ Potential measurements in mV with a reference by the Forsmark 3 power plant (redrawn from Sandberg et al. 2009). The measurements were carried out during injection of around 1 280 A current at Fågelsundet. Interpolated contours are shown with dashed black lines. The contour interval is 200 mV. The SFR vaults are located just to the right of the coloured field. Reproduced from Thunehed (2017, Figure 6-10).

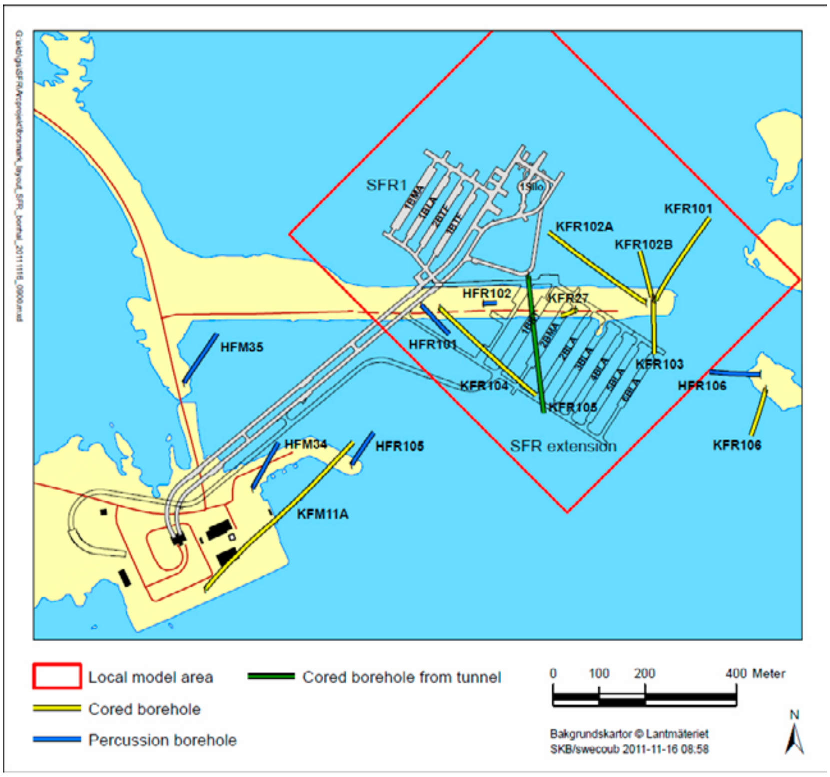

***Figure 3-10.** Preliminary layout of the extension relative to the existing SFR 1. The image also indicates boreholes drilled at the site by coloured tubes. Reproduced from SKB (2013a, Figure 2-10).*

The maximum power ratings of Fenno-Skan 1 and Fenno-Skan 2 is 1 360 A and 1 670 A, respectively (Taxén et al. 2014, Section 4.1). It should be noted, however, that the Fågelsundet electrode is not always switched on, as there are two cables between Sweden and Finland. The Fågelsundet electrode is only used to even out occasional imbalances of the currents running through the cables. Such imbalances occur when one cable is taken out of operation, or when the current flowing in one cable outweighs that flowing in the other. Accordingly, the local electric field may vary both in direction and magnitude. On an annual basis, at least if averaged over a decade or so, the current emitted at the Fågelsundet electrode is significantly less that maximum possible value of 1 670 A. In this modelling exercise, the fluctuating electric field is handled by using different field strengths and directions in different sensitivity cases. Furthermore, it is pessimistically assumed that the Fågelsundet electrode is always switched on at a constant and high-power output.

3.2.2 Possible future fields

It is very speculative to predict future electric fields, and here the discussion is limited to future fields emanating from HVDC cables. In Taxén et al. (2014, Section 3.2) it is anticipated that the DC output of future HVDC cables may increase to 2 500 A. This is less than a doubling of the maximum output from Fenno-Skan. Similar reasoning applies to the voltage at the electrode.

Reasonable future field

The purpose of a future HVDC cable with a sea electrode would reasonably be to transmit current over the Baltic Sea to the opposite shore. This means transmission to the Finland mainland, Åland, or the Baltics. The closer the HVDC electrode is to SFR, the higher the field strength will be. However, if placing the electrode directly off the shore in Öregrundsgrepen, at SFR, the Gräsö Island would shield the current's path to Finland, Åland, and the Baltics. The shielding effect of the Gräsö Island is illustrated in Figure 3-11, which also shows the 15 km perimeter to SFR by the dashed circle.

From this we deduce that about 15 km is about the shortest distance[2] from SFR to a reasonable future HVDC electrode.

If assuming the minimum distance of 15 km between a future electrode and SFR, as compare to the present-day distance of about 25 km, this would lead to a relatively small increase in the field strength. If somewhat simplistically assuming that the electric field around the HVDC electrode is perfectly hemispherical (cf. Figure 3-12), the ratio of the electric field strengths at 15 km and 25 km from the electrode is $25^2/15^2 = 2.8$.

The presence of the Baltic Sea, as well as the large-scale heterogeneity in the rock resistivity, will skew the electric field; causing deviations from the hemispherical case. In Thunehed (2017, Figure 3-2) electric fields at different distances from the electrode are calculated using different resistivity models for creating deviations from the hemispherical field. With these models, the ratios of the field strengths at 15 and 25 km from the electrode vary between about two and four.

Figure 3-11. Map of the regional area showing directions to the closest part of the mainland in Finland, Åland, and Estonia. The shortest distance to a presumptive future HVDC electrode outside Gräsö is 15 km, as marked by the dashed circle.

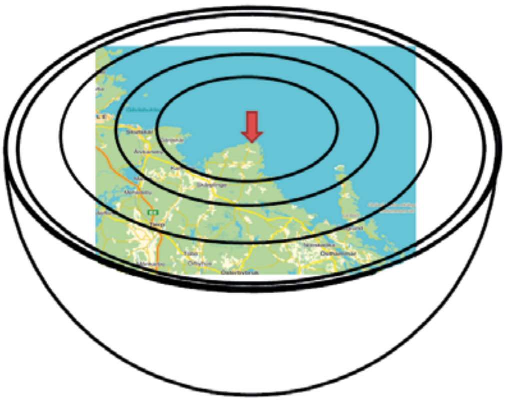

Hemispherical variant of Equation 2-4.

$$J = \frac{I}{2\pi r^2} = -\frac{1}{\rho}\frac{dU}{dr}$$

$$I = -\frac{2\pi r^2}{\rho}\frac{dU}{dr}$$

Figure 3-12. Illustration of a perfectly hemispherical field around the Fågelsundet electrode, as marked by the red arrow. Equations for the current I (A) and current density J (A/m²) are shown as a function of the potential gradient dU/dr (V/m), rock resistivity ρ (ohm.m) and radial distance r (m) from the current source.

---

[2] Here it is neglected that the electrode needs to be placed a few kilometres off shore for various reasons. The Fågelsundet electrode, for example, is placed 2.3 km off the shoreline (Taxén et al. 2014).

Based on the above it is reasonable to assume that the future regional electric field at SFR would be within a factor of 10 larger than presently. That would give a maximum regional horizontal gradient about 7 mV/m and a vertical gradient of about 20 mV/m. At present day conditions at SFR, a locally increased potential gradient is seen as result of the grounding of power lines from the AC sub-station at Forsmark (cf. Figure 3-8). The relatively large distance to the assumed future electrode does not prohibit the placement of a future AC sub-station in the area. The highest measured horizontal field strength close to SFR is about 2.8 mV/m. Increasing this value by a factor of 10 would give a bounding horizontal potential gradient of about 30 mV/m.

Pessimistic future field

In Taxén et al. (2014) a more pessimistic approach was taken, where the shielding effect of the Gräsö Island was not discussed and where the electrode was placed at only a short distance (2 km) from the repository for spent nuclear fuel, in a worst-case scenario. Pedersen (2016) deemed that situation as improbable. Furthermore, Öregrundsgrepen is a rather shallow water body except for at the Gräsö Island (Taxén et al. 2014, Figure 4-13) that may not be suitable for current injection for environmental reasons, for example due to the formation of chlorine gas at the electrode. The worst-case scenario in Taxén et al. (2014) relates to a rise in sea level due to global warming, which may make it less far-fetched.

In this report a pessimistic scenario is created by assuming the highest measured horizontal field strengths at the shore facing the Fågelsundet electrode, at maximum power output. The distance between the Fågelsundet electrode and the shoreline is 2.3 km; a distant (roughly) adopted in the pessimistic scenario. This is done by assuming that the distance is sufficiently large, compared to the depth of the 1BRT vault, to assume that the field is horizontal. The highest measured field strength is 200 mV/m. Higher field-strengths than this, at the shoreline, are unreasonable as they would create a significant risk to human health and the environment.

On the probability of future electrode locations

It is outside the scope of this report to quantitatively assess probabilities of the two future electrode scenarios. Qualitatively one may say that the placement of a future electrode outside the Gräsö Island has a fairly low probability. Although power transmission over the Baltic Sea will probably exist in the future, such transmissions could be placed at other locations along Sweden's long shoreline. Also, such transmissions may not necessarily involve a sea electrode. Alternatively, the occasions of imbalanced transmission may be very rare. The closer the assumed distance is between the electrode and SFR, the lower the probability of its future location becomes. The probability of a location only 2 km from SFR is judged to be very low, where also the shielding effect of the Gräsö Island comes into effect.

Relation to climate domains

The above reasoning applies to the temperate climate domain. During the glacial climate domain, the ice sheet is likely to prevent power installations. One can envision a need for power transmissions from the Forsmark area to the opposite shore of the Baltic Sea during the periglacial climate domain. This may however require technical solutions that deviate from those of present day HVDC transmissions in sea water. Accordingly, it is outside the scope of this report to assess the impact of future anthropogenic Earth currents during the periglacial climate domain.

3.2.3 Field strengths used in modelling

In the previous calculations in SKB's response to SMM (SKB 2014a, appendix A), using the electrical circuit analogy, it was assumed that the large-scale electric potential gradient of 2 mV/m is parallel with the axis of the 1BRT vault. This alignment should give the greatest electric current running through the vault. By the assumptions made this field alignment should, accordingly, give rise to the highest Earth current induced corrosion rates. In addition, this alignment corresponds with the general direction of the observed potential gradient at the SFR site (cf. Figure 3-9).

Most calculation cases in this report use the horizontal potential gradient of 2 mV/m at SFR, which implies that the Fågelsundet electrode emits around 1 280 A into the Baltic Sea on an annual average basis. In the base case the potential gradient is aligned[3] with the 1BRT vault and access ramp. In sensitivity studies the impacts of 1) rotating the horizontal field by 90° and 2) using a vertical field are also investigated (cf. Section 7.3).

For future cases where the SFR is still located beneath the seabed, the horizontal potential gradients of 30 and 200 mV/m are used, in parallel with the 1BRT vault and ramp. For a future case, where isostatic rebound has made SFR an inland repository, the potential gradients of 30 mV/m is used, in parallel with the 1BRT vault and ramp (cf. Section 7.6). The choice of not using the 200 mV/m field strength for this case is that the isostatic rebound makes SFR more distant to the shoreline, and also a future electrode.

3.3 Resistivities

In this section the resistivities of the different media used in our modelling is estimated. These media are:

- Groundwater and pore water
- Fractured rock on the block scale
- Macadam backfill
- Concrete embedment
- Bentonite backfill
- Metal parts of the pressure vessels

Estimations are presented both for present day conditions, when the repository is submerged beneath the Baltic Sea, and for a future case when the repository is an inland repository. This latter means that the shoreline has retreated, due to isostatic rebound, to a point where the repository is beneath ground and infiltration of meteoric water gives a dilute groundwater. Only the temperate climate domain is considered.

3.3.1 Groundwater and pore water resistivity

Present day conditions

Presently the SFR repository is beneath the Baltic Sea. This gives a brackish groundwater at shallow depths and a brackish-saline groundwater at and below repository depth. Expected groundwater compositions after repository closure have been modelled in Auqué et al. (2013) and Román-Ross et al. (2014). For the first 500 years after repository closure, before the shoreline retreats past the repository, no major changes in groundwater composition are expected (Román-Ross et al. 2014). During this period the main anion of the groundwater is expected to be chloride, with a proposed concentration of 3 500 mg/L (Auqué et al. 2013, Table 4-2, Román-Ross et al. 2014, Table A3-1).

At relatively high salinities, the electrical conductivity of groundwater at Forsmark is well correlated with the chloride concentration. This is seen in Figure 3-13, displaying site investigation data from a multitude of boreholes at the Forsmark site. The electrical conductivity corresponding to a chloride concentration of 3 500 mg/L is about 0.9 S/m at 25 °C. This corresponds to a groundwater resistivity of 1.6 ohm.m at the in situ temperature of 10 °C, as calculated by Equation 2-16 with an α of 0.019 $°C^{-1}$.

A similar image can be made based on groundwater composition data obtained in the SFR site investigation only (Nilsson 2011). This is done in Figure 3-14 but with the difference that the temperature correction has been made prior to the plotting. Here the chloride concentration of 3 500 mg/L corresponds to a groundwater resistivity, at the in situ temperature, of 1.3 ohm.m.

---

[3] According to Layout 2.0 the central lines of the 1BRT vault and of the access ramps are not exactly parallel. This deviation is disregarded when setting up our models, which is a pessimistic approach.

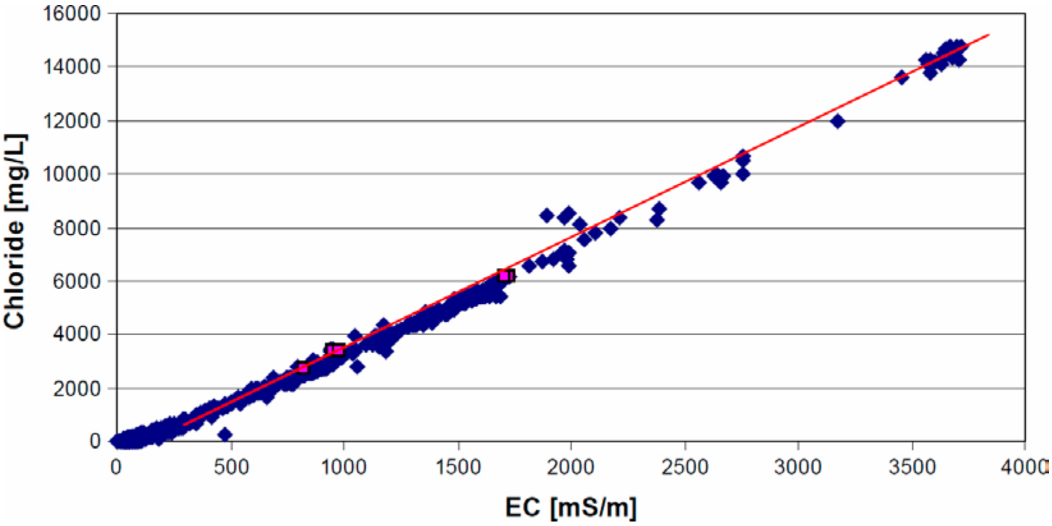

Figure 3-13. *Chloride concentration versus electrical conductivity at 25 °C for groundwaters at different depths within the Forsmark site investigation area. Reproduced from Berg and Nilsson (2007, Figure 8-2).*

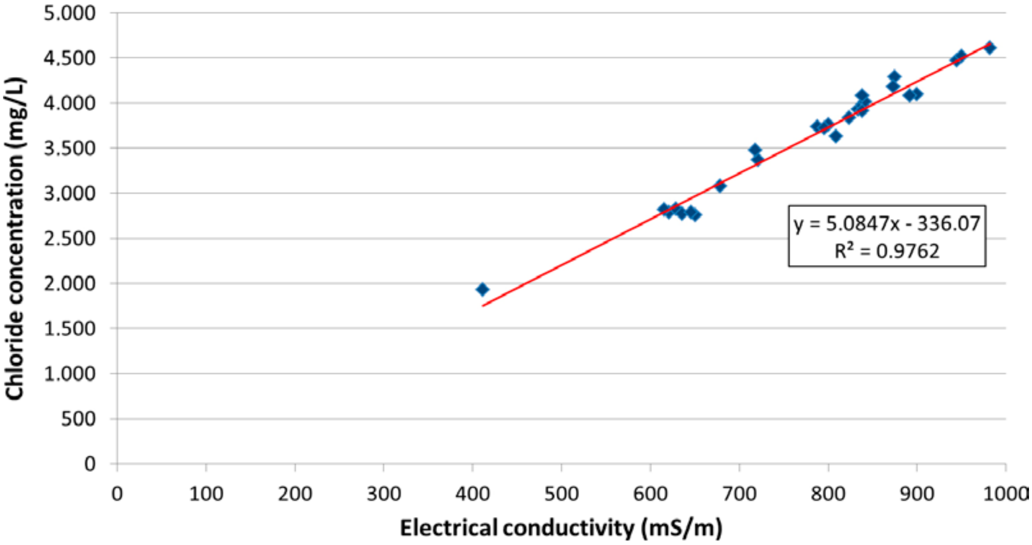

Figure 3-14. *Chloride concentration versus electrical conductivity at in situ temperature (~ 10 °C) for groundwaters at different depths at SFR. Data from 13 boreholes from very shallow depth to borehole length up to 341 m. Data prior to temperature correction are found in Nilsson (2011, Appendix 7).*

Based on these two groundwater resistivities, we promote uniform present-day groundwater and pore water resistivities for the entire SFR repository and host rock:

- Present day groundwater and pore water resistivity: 1.5 ohm.m.

This water resistivity is later used for estimating the present day resistivities of different porous media.

Future conditions within the temperate climate domain

In the base case for the temperate climate domain modelling in Román-Ross et al. (2014), the ionic concentration in the groundwater decreases with time. This is as isostatic rebound makes the repository's ground surface emerge above the sea level. This causes infiltrating meteoric water to govern the groundwater composition to an increasing degree. Figure 3-15 shows the concentrations the main cations, chloride, carbon (carbonate), and sulphur (sulphate) as function of time during the uplift, according to the groundwater evolution modelling in Román-Ross et al. (2014, Table A3-1). Prior to 2500 AD, the groundwater composition is assumed to be represented by present day conditions.

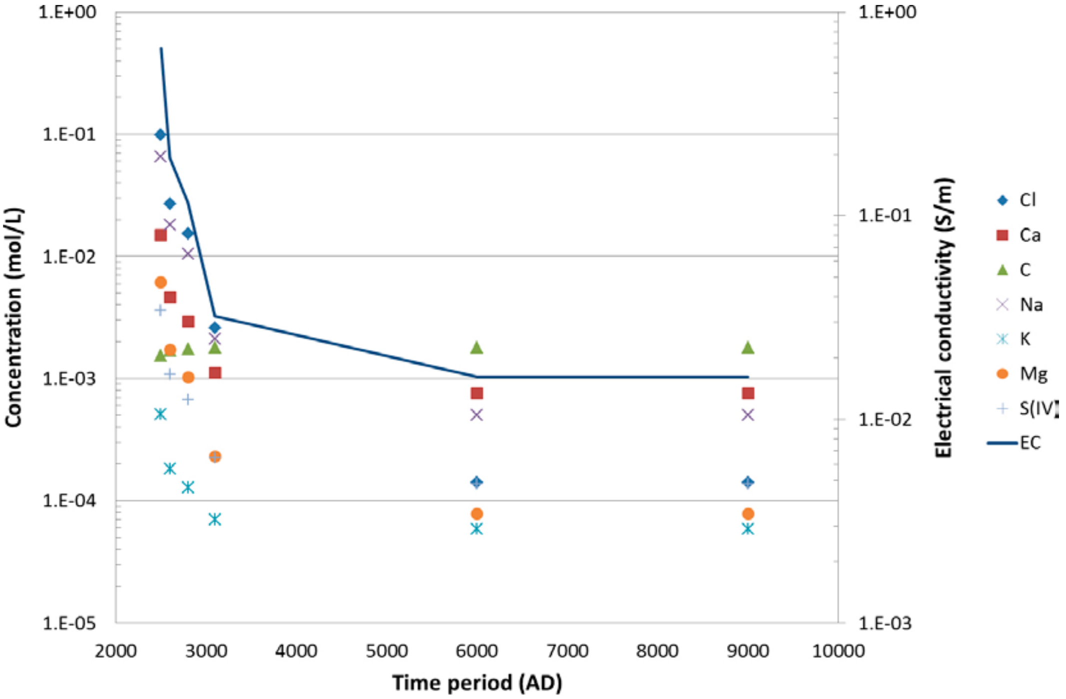

Figure 3-15. *Concentrations of the main solutes in SFR groundwater as function of time. Based on data in Román-Ross et al. (2014, Table A3-1). Electrical conductivity is calculated by Equation 3-1.*

If having all ionic concentrations of the future water, its electrical conductivity can be calculated by using Equation 2-8. As the full set of data is not available we instead scale the future EC based on the present-day EC. In doing this we use the ionic concentrations C_i (mol/L) we have at 2500 AD and later times (cf. Figure 3-15), the ions' charge number z, and the EC of the present day groundwater, $\kappa_{w,PD}$ (S/m), in Equation 3-1.

$$\kappa_{w,t} = \kappa_{w,PD} \frac{\sum C_{i,t} {z_i}^2}{\sum C_{i,2500} {z_i}^2} \qquad \text{Equation 3-1}$$

In the calculation all carbon is assumed to be HCO_3^- while all S(VI) is assumed to be SO_4^{2-}. The resulting decrease in electrical conductivity with time is shown by the blue line in Figure 3-15. The electrical conductivity value at time beyond 6000 AD becomes 0.015 S/m, corresponding to a resistivity of 67 ohm.m. Based on this we promote uniform future groundwater and pore water resistivities for the entire SFR repository and host rock of:

- Future ground- and pore water resistivity of inland repository: 67 ohm.m

This resistivity is later used for estimating the future resistivities of different media, related to a repository situated well inland. For future situation where the SFR repository is still beneath the sea, e.g. due to rising sea levels due to global warming, the present-day resistivity can be used.

- Future ground- and pore water resistivity of submerged repository: 1.5 ohm.m

3.3.2 Resistivity of the host rock

Fractured rock between deformation zones – present day

In the SFR site investigation, the apparent rock resistivity has been measured in downhole geophysical surveys (e.g. Nielsen and Ringgaard 2009 a, b) which is used as an approximation for the true resistivity of the rock. The in situ resistivities reflect the in situ conditions, mainly relating to the groundwater salinity and in situ stresses and temperatures. These measurements, made by a focused resistivity tool, delivers high resolution logs of the apparent rock resistivity and the data can be processed statistically. Histograms of the measured apparent resistivities have been produced in Löfgren (2014) for borehole KFR105 (Figure 3-16) and KFR102B (Figure 3-17). Borehole KFR105 is drilled sub-horizontally from the SFR underground facility in a direction so that it intersects the rock mass intended to host SFR 3 (cf. Figure 3-10). Borehole KFR102B is drilled from ground surface down to an elevation of 143 m. Arithmetic means of the measured apparent resistivities in boreholes KFR105 and KFR102B are 8 308 and 15 811 ohm.m, respectively (Löfgren 2014).

The apparent resistivities at the high end of the histograms in Figure 3-16 and Figure 3-17 were obtained in rock sections that had a relatively low frequency of open fractures, while those at the low end were obtained in heavily fractured rock volumes. In analogy with the discussion in Section 2.1.6, the fractures or fracture zones may (simplistically) be represented by planar low resistivity volumes. If assuming that all fractures are parallel to the current lines being injected from the geophysical logging tool, the anisotropic block-scale rock conductivity normal to the borehole axis could be obtained from the arithmetic mean of all measured conductivities. The corresponding block-scale rock resistivity could thereafter be obtained from the invers of the block-scale rock conductivity. For boreholes KFR105 and KFR102B, this results in block-scale rock resistivities of 4 487 and 6 572 ohm.m, respectively[4]. If, again in analogy with the discussion in Section 2.1.6, assuming that all fractures are normal to the injected current lines, the arithmetic mean of the measured apparent rock resistivities (i.e. 8 308 and 15 811 ohm.m) better reflects the anisotropic block-scale rock resistivity normal to the borehole axis. As the high and low resistivity zones are distributed in a three-dimensional pattern, probably on a larger scale than detected by the geophysical downhole tool, a proper block-scale rock resistivity is likely somewhere between these data. It should also be noted that the downhole tool is more sensitive to fractures normal to the borehole axis in real systems with fractures distributed in a three-dimensional pattern.

In the geophysical downhole measurements, alternating current has been injected into the rock at a fairly high frequency. When measuring the rock resistivity by alternating current, the frequency should be low enough to avoid dielectric conduction and induced polarization (Löfgren 2015). This is not necessarily the case in the measurements and, accordingly, there is a risk that they somewhat underestimate the actual rock resistivity.

Based on the above, we deem it appropriate to use a round number of the block-scale rock resistivity of 1×10^4 ohm.m as the baseline in our modelling, representing present day conditions. In sensitivity cases (cf. Section 6.5) this rock resistivity is varied over two orders of magnitude, from 1×10^3 to 1×10^5 ohm.m. This range also encompasses increased rock resistivities in response to changes in groundwater composition, as discussed below.

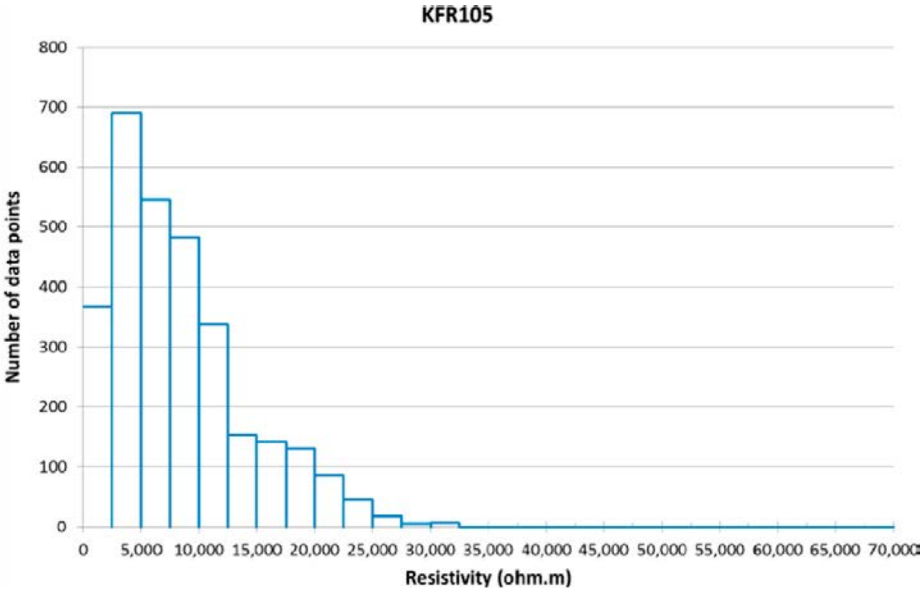

***Figure 3-16.** Distribution of apparent rock resistivities in KFR105. Reproduced from Löfgren (2014, Figure 4-1).*

---

[4] Based in site investigation raw data taken from SICADA: DATA DELIVERY Sicada_12_091.

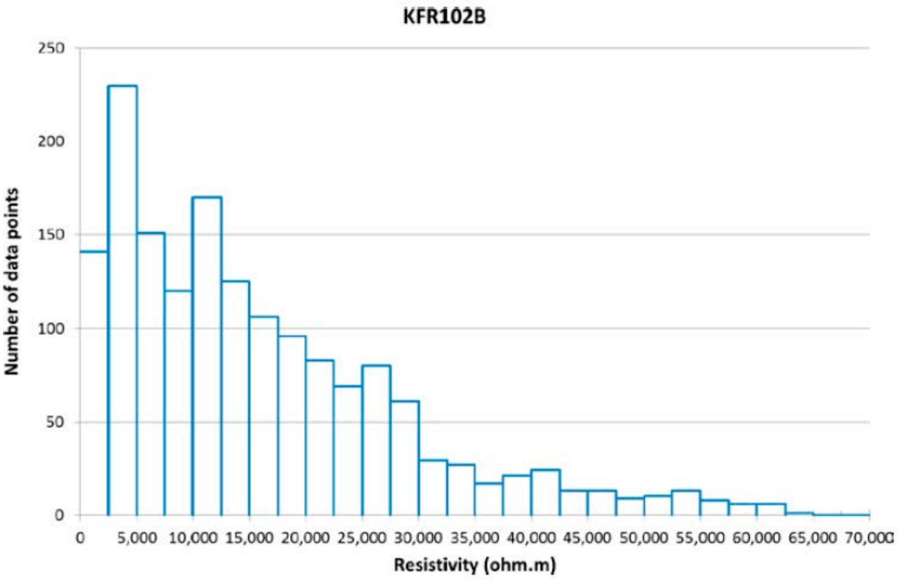

Figure 3-17. *Distribution of apparent rock resistivities in KFR102B. Reproduced from Löfgren (2014, Figure 4-4).*

Fractured rock between deformation zones – future conditions

As is indicated in Figure 3-15, the electrical conductivity of the groundwater will decrease significantly a few thousand years after repository closure, as response to the shoreline displacement. Here we assume that the bulk part of the rock matrix's pore water becomes fairly well equilibrated with the groundwater, through matrix diffusion, within a relatively short time span (say within a few thousands of years). If so, one can make the á priori assumption that the majority of the current will be propagated through the rock by surface conduction. The one data point existing on the surface conductivity of Forsmark rock comes from a laboratory measurement using direct current, with a surface conductivity of 3.25×10^{-5} S/m (Löfgren 2015, Figure 4-2). The median value of all surface conductivities from the Forsmark, Laxemar and Äspö sites (displayed in SKB 2010, Figure 6-72) is 2.2×10^{-5} S/m. This can be compared to the part of the rock conductivity that is contributed by electrolytic conduction in the bulk part of the pore water. If assuming the recommended formation factor for the intact rock in SR-PSU of 1.8×10^{-4} (Löfgren 2014, Table 6-1) and a future pore water EC of 0.015 S/m for a well inland repository (cf. Section 3.3.1), the term $F_f \kappa_w$ of Equation 2-12 becomes 2.7×10^{-6} S/m. This is about ten times less than the surface conductivity. We may also calculate the contribution to the rock conductivity solely from current conduction in the free groundwater in open fractures, in analogy with Equation 2-14. Here we assume fractures that are parallel with the electric field, which gives the highest conductivity. Furthermore, we assume a fracture frequency of four and a uniform volumetric fracture aperture of 0.1 mm (cf. Table 2-1). If again using the groundwater EC of 0.015 the "open fracture" conductivity becomes 6×10^{-6} S/m, which is a factor of about five lower than the surface conductivity.

Based on the above discussion, we judge that a reasonable value of the future block-scale resistivity is about 3×10^4 ohm.m.

Fractured rock in deformation zones – present day

In the early part of this work, prior to doing modelling with COMSOL Multiphysics, it was seen as a possibility that deformation zones could have a significant impact on the current flow through the repository. Hence it was attempted to assign reasonable, as well as pessimistic, rock resistivities to minor and major fracture zones. Later on, the modelling showed that deformation zones have less impact on the electrical current flow than was originally thought. Accordingly, the underlying discussion on block-scale rock resistivities of deformation zones has been placed in Appendix A, while only the suggested values are presented in Table 3-4.

Table 3-4. Assumed parameters of deformation zones used in modelling.

Description zone	Block-scale rock resistivity	Thickness
Realistic zone in the SFR host rock	1 000 ohm.m	10 m
Intense zone (such as regional zones in the area)	100 ohm.m	10 m
Extreme zone (not existing in the area)	10 ohm.m	10 m

The thickness of the zone in Table 3-4 does not represent the thickness of the entire deformation zone, which could be significantly larger. It aims to roughly represent the combined thickness of fracture zones within the deformation zone for which these low resistivity values can be expected. Many large-scale deformation zones have cores that are relatively sparsely fractured, with higher degree of fracturing at their outer planes. In addition, it is not the separate values of Table 3-4 that areof interest but the zone's conductance, which involves the product of the block-scale rock conductivity and zone thickness. As such, an alternative parameterisation of an extreme zone could have been, for example, a block-scale resistivity of 50 ohm.m and a zone thickness of 50 m.

Comparison with rock resistivities of similar works

In Thunehed (2017) the impact of the Fenno-Skan HVDC electrode on the electric field at Forsmark is modelled. In doing this, a rock resistivity model is set up (Thunehed 2017, Figure 4-3), where different resistivities represent what is in this report called the block-scale rock resistivity. Three different rock resistivities are used. In the shallow inland, the resistivity is set to 14 300 ohm.m. In shallow rock under the Baltic Sea, and in more deeply lying inland rock, the resistivity is set to 3 000 ohm.m. In very deeply lying rock, the resistivity is set to 1 250 ohm.m.

Taxén et al. (2014) performed similar modelling of the corroding capacity of Earth currents, but for the KBS-3 repository. They varied the rock resistivity from 3 000 to 20 000 ohm.m in the upper 1 000 m of the rock (Taxén et al. 2014, Figure 4-14).

It is noted that there is a range of assumed block-scale rock resistivities in different works. As stated before, in the present report this is handled by varying the rock resistivity in sensitivity studies. According to Figure 3-12, the resistivity of the regional rock volume impacts the large-scale field strength for a given current output at the Fågelsundet electrode. The large-scale interplay between the field strength and rock resistivity is preliminarily investigated in Appendix B, for a field that is not hemispherical but skewed due the presence of the Baltic Sea.

3.4 Resistivity of macadam backfill

In SKB's response on Earth current to SSM (SKB 2014a, appendix A), the resistivity of the macadam backfill was set to 3.75 ohm.m. This was based on a groundwater resistivity of 1.5 ohm.m (cf. Section 3.3.1), a macadam porosity of 40 %, and an effective tortuosity of 1. Here the effective tortuosity (e.g. Vilks et al. 2005) is the ratio between the porosity and formation factor (cf. Equation 2-10). This means that even if the local current lines in the macadam are tortuous, as the current tries to avoid being transported in the highly resistive rock grains, this was ignored in the previous parameterisation. In the new modelling the same baseline macadam resistivity is kept as in SKB (2014a). This is justified as using a relatively low macadam resistivity á priori is judged to be pessimistic. However, the macadam resistivity is varied in COMSOL Multiphysics modelling to confirm this assumption in models (cf. Section 6.4). Below a reasonable range of macadam resistivities at both present day and future groundwater compositions is discussed.

The electrical resistivity of a fully saturated unconsolidated porous medium ρ_{pm} (ohm.m) can be obtained from an empirical relation by Archie (Archie 1942); if knowing the medium's porosity ε (–) and pore water resistivity ρ_w (ohm.m):

$$\rho_{pm} = \rho_w \varepsilon^{-m} \qquad \text{Equation 3-2}$$

where an appropriate value of m is 1.3 for unconsolidated sand. This value is assumed also for the unconsolidated macadam. It is cautioned that Equation 3-2 is only valid if surface conduction is of no consequence (i.e. it should not be used for granitic rock). This prerequisite is fulfilled in the highly porous macadam. In Section 3.3.1 it was argued for using pore water resistivities of 1.5 ohm.m at present day conditions and 67 ohm.m at future inland conditions.

SKB (2014d) does not provide specifics, such as the porosity, of the macadam intended to be used as backfill. It is, however, indicated that there will be a very small fraction of fines with particle sizes below 2 mm. In Freeze and Cherry (1979, Table 2.4) porosity ranges are given for non-consolidated geological media, with gravel 25–40 %; sand 25–50 %; silt 35–50 %; and clay 40–70 %. In Parkhomenko (1967) the typical porosity range of sand is given as 20–35 %.

The macadam will likely be taken from the rock mass that has been excavated from underground openings in the area. The total rock volume that should be excavated from SFR is approximately 400 000 m^3 and the approximate volume of the excavated crushed rock is estimated to be 770 000 m^3 (SKB 2014d, Section 11.4). This indicates a porosity of the excavated crushed rock of 48 %. However, this rock may be further processed (crushed and sieved) before used as backfill material, so it is uncertain to what extent this porosity represents that of the macadam backfill. The value perhaps points at the upper end of the porosity range for gravel in Freeze and Cherry (1979). As Figure 3-6 indicates, there will also be an open gap between the macadam backfill and the tunnel roof. Based on the above, we assume a possible porosity range of the backfill from 20–50 %. At present day groundwater composition, this gives a macadam resistivity range between 3.9 to 12 ohm.m, as calculated by Equation 3-2. To also encompass the macadam resistivity value used in SKB's response to SSM (SKB 2014a, Appendix A), we expand this range to:

- Range of present day macadam resistivity: 3.75 to 12 ohm.m.

As the repository becomes an inland repository with a more dilute groundwater, for which a resistivity of 67 ohm.m is assumed, the macadam resistivity range becomes:

- Range of future (inland) macadam resistivity: 1.7×10^2 to 5.4×10^2 ohm.m.

3.5 Resistivity of the concrete embedment

At repository closure, the pressure vessels are planned to be embedded in concrete and/or cementitious grout. The details of the cementitious material and its installation are yet to be determined. It is not explicitly stated in SKB (2014d) whether or not reinforcement bars are intended to be used in the embedment, but we assume that they will not be used. However, reinforcements will be used in the concrete floor.

The specifics of the used material will not only determine its initial state, but also the degradation pattern. Accordingly, there is some remaining uncertainty on the electrical properties of the embedment concrete, which are explored by sensitivity studies in Chapter 6.

3.5.1 Concrete embedment without reinforcements

The resistivity of the concrete can be estimated if knowing the formation factor of the intact concrete matrix, the degree of fracturing, the electrical conductivity of the pore water, and the surface conductivity. It is judged that there is too much involved uncertainty to predict an evolution of the resistivity of the concrete embedment in the 1BRT-vault. However, bounding values can be estimated. The concrete embedment generally functions by creating a barrier for electrical current; reducing the amount of current in the 1BRT vault that actually contacts the metallic pressure vessels. As such, one is less interested in an upper limit for the concrete resistivity and much more interested in a lower limit.

In calculating the lower resistivity limit for non-reinforced concrete, it is assumed that the embedment has the same properties as the concrete of 1BMA. In SKB (2014b, Table 9-5) the upper bound of the block-scale effective diffusivity $D_{e,BS}$ (m^2/s) for BMA concrete is provided as function of time. This effective diffusivity takes into account both the transport capacity in the intact concrete matrix and in fractures, and is further justified in Höglund (2014) and references therein. Figure 3-18 shows the evolution of this effective diffusivity. The pressure vessels are planned to be embedded at repository closure and the time in Figure 3-18 can be taken to be relative to this embedding.

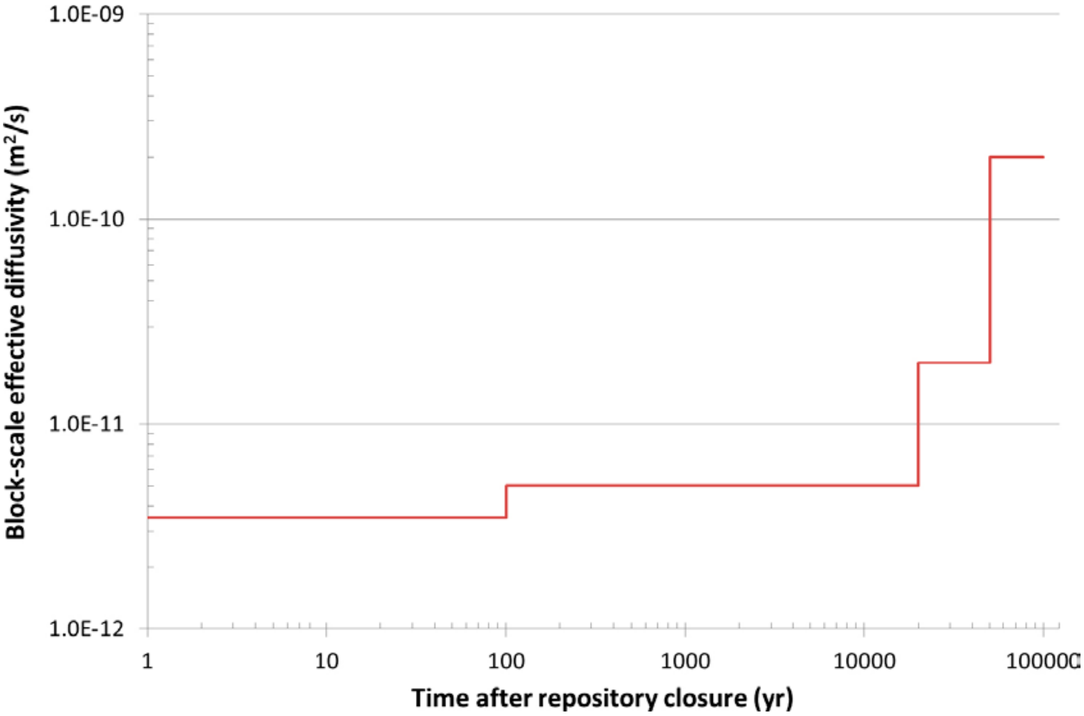

Figure 3-18. *The upper bound of the block-scale effective diffusivity in BMA. Data from SKB (2014b, Table 9-5).*

The influence of fracturing on the block-scale effective diffusivity can be illustrated if assuming that the increase in diffusivity is only due to fracturing and not due to alteration of the microporous network in the ageing concrete.

In Figure 3-18 the initial value represents a concrete matrix that is free of larger fractures with an effective diffusivity D_e of 3.5×10^{-12} m^2/s. For the purpose of illustration, planar fractures are added to this concrete matrix, where each fracture has a uniform volumetric aperture e_v of 1 mm and is parallel with the transport direction. This is in analogy with Figure 2-4 and Equation 2-14. The block-scale effective diffusivity can be calculated by Equation 3-3, where n/B is the fracture frequency (m^{-1}). D_w is assumed to be 1×10^{-9} m^2/s.

$$D_{e,BS} = D_w \frac{ne_v}{B} + D_e \left(1 - \frac{ne_v}{B}\right) \qquad \text{Equation 3-3}$$

By using Equation 3-3 the fracture frequency needed for obtaining the block-scale effective diffusivity of Figure 3-18 can be calculated. In this example, 100 years after repository closure the fracture frequency increases from zero to 1.5/m. In 20000 years after closure the fracture frequency increases to 7/m and in 50000 years after closure it increases to 200/m. At such high fracture frequency, the concrete embedment can be visualised as crushed concrete.

To assess the block-scale electrical resistivity of the concrete embedment, one also needs the electrical conductivity of the concrete pore water and, formally, the surface conductivity. Concerning the latter, it is assumed that surface conduction will have no significant impact on the current flow, due to the relatively high porosity of the concrete and (at least initially) high ionic strength of its pore water. An example of a possible evolution of the concrete pore water is provided in Höglund (2014, Figure 7-14), as reproduced in Figure 3-19. Although this is only an example, it provides the expected ranges of different solutes over time.

The ions constituting the majority of the ionic charges in the pore water are OH^-, Na^+, K^+, Ca^{2+}, and Cl^-. Figure 3-20 shows a simplified representation of Figure 3-19, regarding these ions, as well as the estimated electrical conductivity of the pore water.

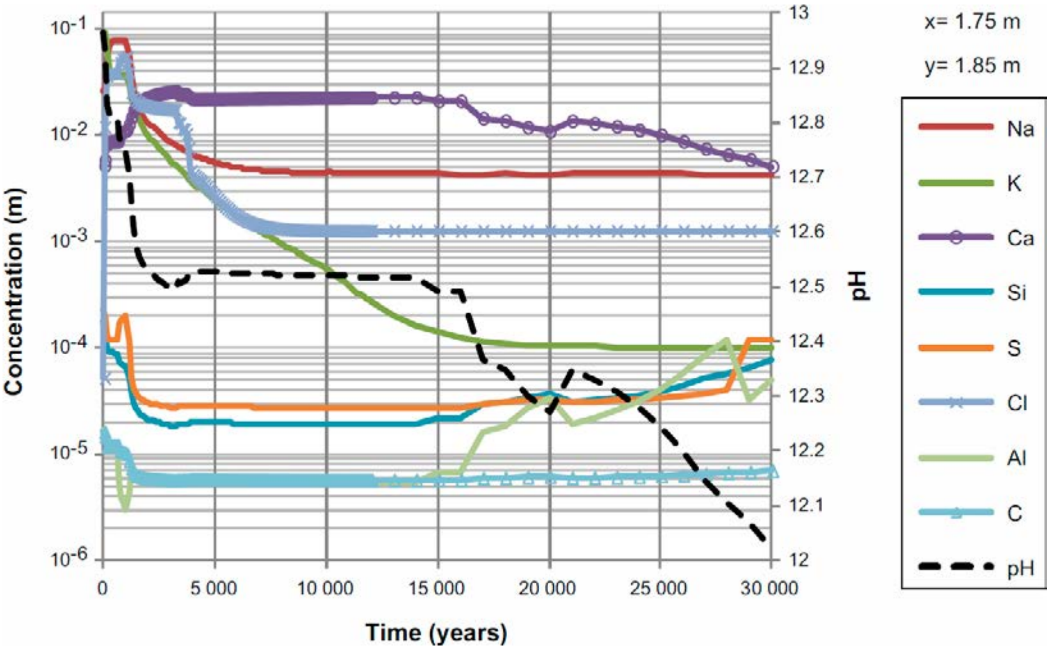

***Figure 3-19.** Evolution of dissolved components (molar concentrations) in the concrete pore water during the first 30 000 years at position GH in 2BMA. Reproduced from Höglund (2014, Figure 7-14).*

For times between 30 000 and 100 000 years after repository closure, the pore water is assumed to be equilibrated with the inland groundwater (under temperate conditions), which is assumed to have an electrical resistivity of 67 ohm.m (cf. Section 3.3.1). Prior to 30 000 years after closure, the electrical conductivity is calculated based on the ionic concentrations, using Equation 2-8. In doing this, D_w is assumed to be 1×10^{-9} m^2/s for all species. With the same assumption, the concrete's effective diffusivity in Figure 3-18 can be converted to the formation factor (cf. Equation 2-11). If multiplying the formation factor with the pore water EC of Figure 3-20 and taking the inverse, one obtains a rough estimate of the concrete's block-scale resistivity evolution (cf. Figure 3-21).

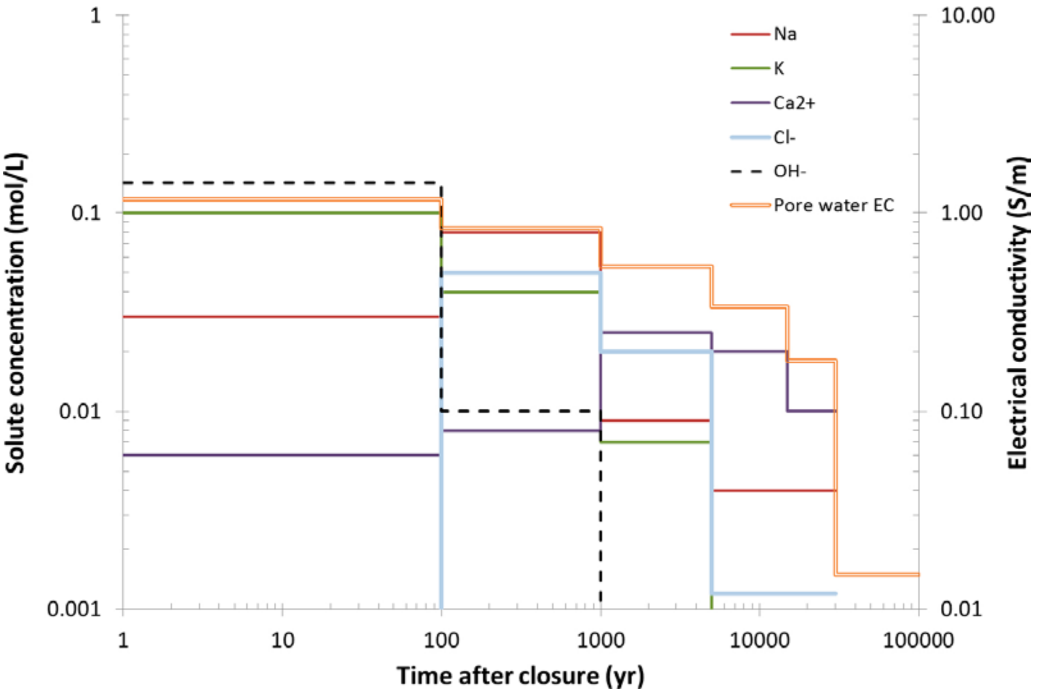

***Figure 3-20.** Idealised evolution of concrete pore water in term of major ions and electrical conductivity, intended to represent the concentrations of Figure 3-19.*

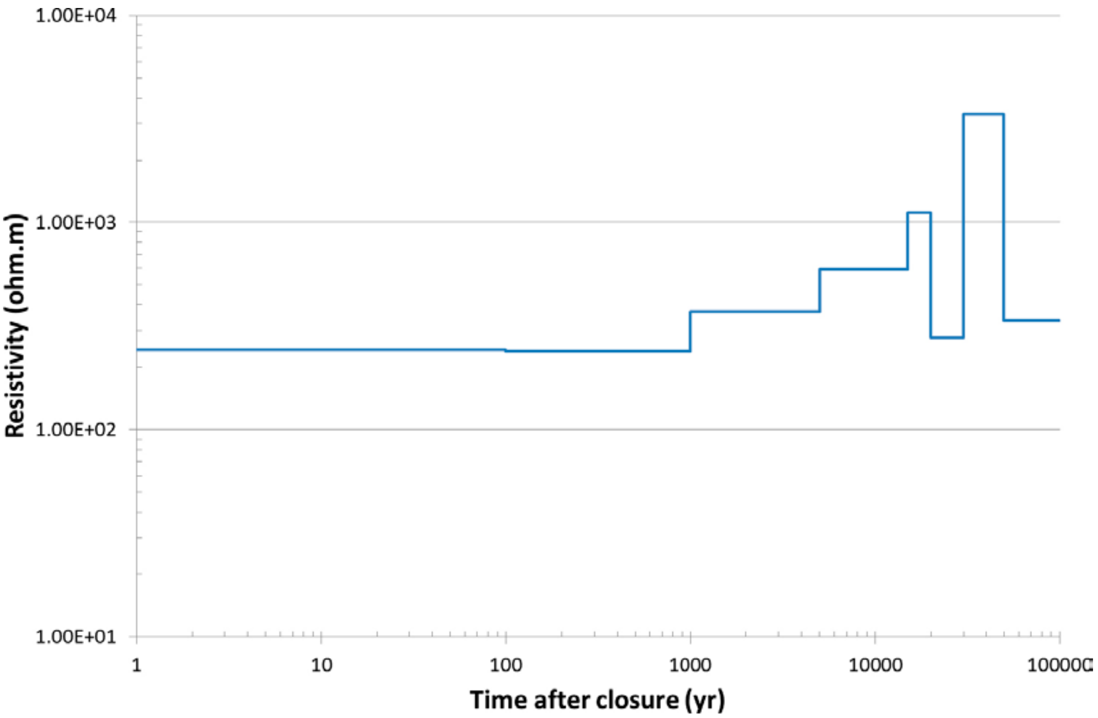

Figure 3-21. *Idealised evolution of the concrete's block-scale resistivity.*

Although the general trend in the evolution of the concrete's block-scale resistivity in Figure 3-21 is plausible, it relies on too many assumptions to be included in detail in the modelling. As stated before, one is rather interested in the lower resistivity limit of the concrete. This lower limit is judged to be 100 ohm.m, which encompasses the data in Figure 3-21 by a margin. This resistivity also agrees fairly well with empirical data for non-site-specific concrete (Keyvani 2013).

To account for additional uncertainty, sensitivity cases in COMSOL Multiphysics are set up where properties of the concrete embedment are varied (cf. Section 6.4).

3.5.2 Concrete with reinforcement bars – reduced thickness

If the concrete is reinforced with metallic reinforcement bars this may have two effects. Firstly, the reinforcements may short-circuit part of the concrete embedment, effectively reducing its thickness. Secondly the network of reinforcements would create a Faraday's cage around the pressure vessels, preventing current from reaching their surfaces. This latter effect can be pessimistically ignored, while the former effect may need to be investigated if one plans to use reinforcement in the embedment. No documentation has been found indicating that reinforcements will be used in the embedment, although it will be used in the concrete floor. Moreover, the pressure vessels will not be placed directly on the floor but on stands of concrete. No dedicated modelling has been made that requires data on the thickness of the remaining embedment that is not short-circuited by reinforcement bars (should such occur). Such a case instead encompassed by the sensitivity case where the embedment thickness is assumed to be zero, and the 1BRT vault is completely filled will macadam backfill.

3.6 Resistivity of bentonite

The access tunnels connecting the 1BRT vault with other vaults and access ramps will partly be filled with bentonite (cf. Figure 3-3). The bentonite backfill has a significant impact on the groundwater flow, due to its low hydraulic conductivity. However, the electrical conductivity of bentonite is quite high, due to a high porosity. Even highly compacted bentonite has a diffusion available porosity of ~ 40 % for cations and ~ 20 % for anions (SKB 2010, Table 5-14). This indicates similar current conducting properties as of the macadam backfill. In Taxén et al. (2014, Table 6-2), for example, the resistivity of the fully saturated bentonite buffer surrounding deposition holes in a KBS-3 repository is set to 1.9 ohm.m. As justified by the limited importance of the bentonite plugs and backfill on the electrical current through 1BRT, the assumption is made that the bentonite has the same resistivity as the macadam backfill in all calculation cases. Accordingly, volumes that are backfilled with bentonite are not separated from volumes backfilled with macadam in the modelling in Chapter 7.

3.7 Resistivity of the reactor pressure vessels

In the electrical circuit model, the resistance due to electronic conduction in the pressure vessels is pessimistically set to zero. Furthermore, no polarisation resistance is accounted for at the pressure vessels' surfaces. When using COMSOL Multiphysics, a zero resistivity for electronic conduction causes numerical problems and a resistivity of of 0.01 ohm.m is used. If a current line is propagated through 2 mm of concrete and 20 m of pressure vessel in series, the two components would contribute with about matching resistances. Hence, using this relatively high resistivity for steel (i.e. 0.01 ohm.m) only invokes an insignificant error in the modelling.

3.8 Compilation of used resistivities

Table 3-5 lists the resistivities used in modelling in Chapters 4 to 7, both for present day conditions and future inland conditions. For each condition a baseline value is provided. This value may be pessimistic and may not reflect the best estimate of the medium's resistivity. For present day conditions, a lower and upper resistivity may be given, if utilised in sensitivity studies. The range of resistivities used these in sensitivity studies may be larger than recommended in the above sections.

Table 3-5. Resistivities (ohm.m) suggested for modelling.

Medium	Present day repository	Future inland repository	Sensitivity cases, lower	Sensitivity cases, upper
Baltic Sea[a]	1.5	–	–	–
Block-scale rock	10 000	30 000	1 000	100 000
Block-scale rock, deformation zone	–	–	10	1 000
Concrete	100	100	3.75	540
Macadam backfill	3.75	170	3.75	4 000
Bentonite[b]	3.75	170	3.75	4 000
Pressure vessels[c]	0 or 0.01	0.01	–	–

[a] The resistivity of Baltic Sea water is set to match that of the groundwater beneath the seabed.

[b] The resistivity of bentonite is set to always match that of the macadam backfill.

[c] Zero resistivity is used in the electrical circuit model and 0.01 ohm.m is used in COMSOL Multiphysics.

3.9 Corrosion rates

3.9.1 Corrosion rates in SR-PSU

The reactor pressure vessels will corrode, at some rate, even if not subjected to Earth currents. For carbon steel, the corrosion rate used in SR-PSU, under alkaline and anoxic conditions, is 0.05 μm/yr (SKB 2014b, Table 5-3). The corresponding value for stainless steel is 0.01 μm/year (SKB 2014b, Table 5-4) but only a fraction of the reactor pressure tanks consists of stainless steel. To be on the conservative side, one may assume that the entire reactor pressure vessel surface corrodes with the corrosion rate 0.05 μm/yr.

The total surface area of all nine reactor pressure vessels is (at least initially) 7 240 m^2 (cf. Table 3-3), referring to the deposition of intact pressure vessels. If assuming that the pressure vessels corrode by the rate of carbon steel and multiplying the corrosion rate with the total surface area, 0.36 L of the reactor pressure vessels would corrode per year (at least initially). With a typical carbon steel density[5] of 7.86 kg/L (Lide 2003), this implies that about 2.8 kg would corrode per year. If simplistically assuming that all steel consists of pure iron, this weight corresponds to 51 mol Fe/yr.

If, hypothetically, assuming that the reactor pressure vessels are entirely made of stainless steel and corrodes by the rate 0.01 µm/year, 0.072 L would corrode per year. If assuming a density[6] of 7.89 kg/L (Lide 2003), this gives a corrosion rate of 0.57 kg/yr. Under the simplification that pure iron makes up stainless steel, the corrosion rate would be 10 mol Fe/yr.

3.9.2 Benchmark corrosion current

In the charge-balance approach, it is assumed that all current leaving the pressure vessel gives rise to corrosion according to the reactor $Fe(s) \rightarrow Fe^{2+} + 2\ e^-$ (cf. Section 2.2). The summarised current that needs to leave the pressure vessels to corrode 51 mol Fe per year is 313 mA (cf. Equation 2-40). This is rounded down to 300 mA and used as a benchmark corrosion current, to which sum of the modelled current propagated through the reactor vessels is compared.

- Benchmark corrosion current: 300 mA.

The corresponding benchmark corrosion current for (hypothetical) stainless steel vessels is 63 mA.

When using the kinetics limitation approach in Section 6.7, the corrosion current density i_{corr} is needed for a case where there is no external electric field, i.e. at zero overpotential. This is estimated from the total corrosion current of 313 mA, divided by the total corrosion surface of 7240 m^2.

- Corrosion current density at zero overpotential: 4.3×10^{-5} A/m^2

---

[5] Plain carbon steel AISI-SAE 1020 (not necessarily used in pressure vessels).

[6] Stainless steel type 304 (not necessarily used in pressure vessels).

4 Revisiting the previous modelling in SKB's response

4.1 General considerations

In this chapter we revisit the previous calculations of Earth current induced corrosion made in SKB's response to SSM regarding Earth currents (SKB 2014a, Appendix A) using the electrical circuit analogy approach. In that response, an error was made and in this present chapter, revised numbers are given. By using the charge-balance approach, the previous erroneous assumption was that for each charge that enters the control volume including the 1BRT vault, this give rise to the corrosion of in total half an iron atom (cf. Equation 2-17). In the revised approach, each charge entering the control volume gives rise to the corrosion of half an iron atom per reactor pressure vessel. Consequently, for the system analysed in SR-PSU, the Earth current induced corrosion rate is increased by a factor of nine.

The electrical circuit analogy is a useful tool for making scooping calculations of the electrical current that may contact the pressure vessels. It also gives a tool for understanding the importance of different domains and features of the repository and host rock, in terms of current propagation. This may contribute to a better understanding of the numerical 3D-modelling made in COMSOL Multiphysics in Chapter 6 and Chapter 7.

Five different calculation cases are reported in SKB (2014a, Appendix A) using the electrical circuit model:

- 1a, 1b, 2a, 2b and 3

These can, more or less, all be seen as variations of calculation case 2a. Accordingly, calculation case 2a is described first, with its geometries and boundary conditions. This case is also used to describe the setup of the electrical circuit model. The other calculation cases are thereafter described in the light of case 2a.

4.2 Calculation case 2a

Calculation case 2a uses four categories of homogenous components to represent the 1BRT vault of the SFR repository:

- The steel pressure vessels.
- The concrete embedment surrounding the pressure vessels.
- The macadam backfill (divided on two components).
- The host rock surrounding the 1BRT vault (divided on two components).

All of these components can be represented by coaxial cylinders, as shown in Figure 4-1.

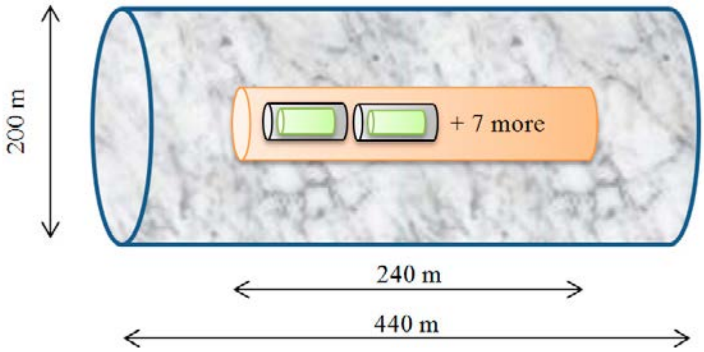

Figure 4-1. *Illustration of the 1BRT vault with surrounding rock, as conceptualised in calculation case 2a. Only two out of the nine pressure vessels are shown. Note that in this conceptualisation the vault is isolated from the rest of the underground openings.*

The representation in Figure 4-1 suggests that the 1BRT vault is isolated from the remaining underground openings of SFR, which is of course a simplification. Furthermore, it implies that the concrete embedment is made as separate units for each pressure vessel. Moreover, the pressure vessels are illustrated to be evenly distributed along the axis of the 1BRT vault with even spacing in-between the embedment units. This spacing is filled with macadam backfill. This description does not comply with the proposed technical solution and the separation into embedment units should be seen as artificial. This artificial separation is allowed for in the used 1D-representation and does not impact the results.

There are in total nine reactor pressure vessels with varying length and diameter (cf. Table 3-2). However, the simplification was made to assume that all pressure vessels have equal length. The assumed geometries of the 1BRT vault components, as well as their assumed resistivities, are tabulated in Table 4-1:

Table 4-1. Dimensions and properties of components in calculation case 2a.

Pressure vessel

Length: 21.5 m (cf. Table 3-2).
Outer radius: *Inconsequential parameter in model.*
Cross section area: *Inconsequential parameter in model.*
Total electric resistance, including the polarisation resistance = 0 ohm (pessimistic assumption).

Concrete embedment unit

Total length: 23.5 m.
Length not occupied by pressure vessel: 2 m (assumed data).
Cross section area including the pressure vessel: 81 m^2 (based on Figure 3-5, deviates ~ 5 % from Layout 2.0).
Outer radius: 5.08 m (derived from the cross-section area).
Thickness of concrete embedment at mantel area: *Inconsequential parameter in model.*
Electric resistivity of concrete: 100 ohm.m (cf. Section 3.5).

Macadam backfilled 1BRT vault

Total length: 240 m (cf. Table 3-1).
Length not occupied by concrete embedment: 28.5 m (deviates ~ 10 % from Layout 2.0).
Cross section area including concrete embedment: 188 m^2 (from Table 3-1).
Outer radius: 7.74 m (from cross section area).
Cross section area excluding concrete embedment: 107 m^2.
Electric resistivity of gravel: 3.75 ohm.m (cf. Section 3.4).

Host rock

Total length: 440 m (assumed data).
Large-scale potential gradient: 2 mV/m (cf. Section 3.2).
Potential drop over system: 0.88 V (calculated from above values).
Length not occupied by 1BRT vault: 200 m.
Outer radius: 100 m (assumed data).
Cross section area including 1BRT vault: 31416 m^2.
Cross section area excluding 1BRT vault: 31228 m^2.
Electric resistivity of rock: 10000 ohm.m (cf. Section 3.3.2).

This system has been simplified by the electrical circuit model in Figure 4-2, featuring six different electrical resistors. Resistor 1 signifies the 200 m of rock upstream and downstream of the 1BRT vault, which poses an electric resistance of 63.7 ohm. Resistor 2 signifies the rock surrounding the 1BRT vault's mantel area with a resistance of 76.9 ohm. Resistor 3 signifies the gravel backfill that surrounds the inner model cylinder of the vault. This resistor corresponds to the backfill between the inner and second inner dashed lines in Figure 4-3 and has the resistance of 8.5 ohm, which is significantly less than that of the surrounding rock. The inner cylinder, as encircled by the inner dashed lines in Figure 4-3, is represented by three resistors connected in series. Resistor 4 signifies the total length of the concrete embedment units that are found on the top and bottom of each of the nine pressure vessels (i.e. length of embedment unit minus length of pressure vessel, times nine).

Resistor 5 comprises the pressure vessels and the concrete embedment surrounding their mantel area. This part is assumed to pose no resistance to electric current, as all current will be propagated in the metallic pressure vessel. Resistor 6 signifies the total length of macadam gravel backfill in-between the concrete embedment units. The total resistance of resistors 4, 5, and 6 is 23.5 ohm, where the majority is due to the concrete in resistor 4.

Assumptions made when setting up this electrical circuit model are illustrated in Figure 4-3. The fact that resistor 1 is connected in series with the system of resistors 2–6 suggests a plane on either side of the 1BRT vault in which current can flow freely, i.e. with no resistance. This is illustrated by the semi-transparent blue cross-section areas on each side of the vault in Figure 4-3.

The electrical circuit model suggests that electric current can only flow horizontally, except for in the above-mentioned planes, and not over the horizontal dashed lines (i.e. the internal boundaries) in Figure 4-3. This would conceptually mean that there would be discontinuities in the electric potential field over these dashed lines.

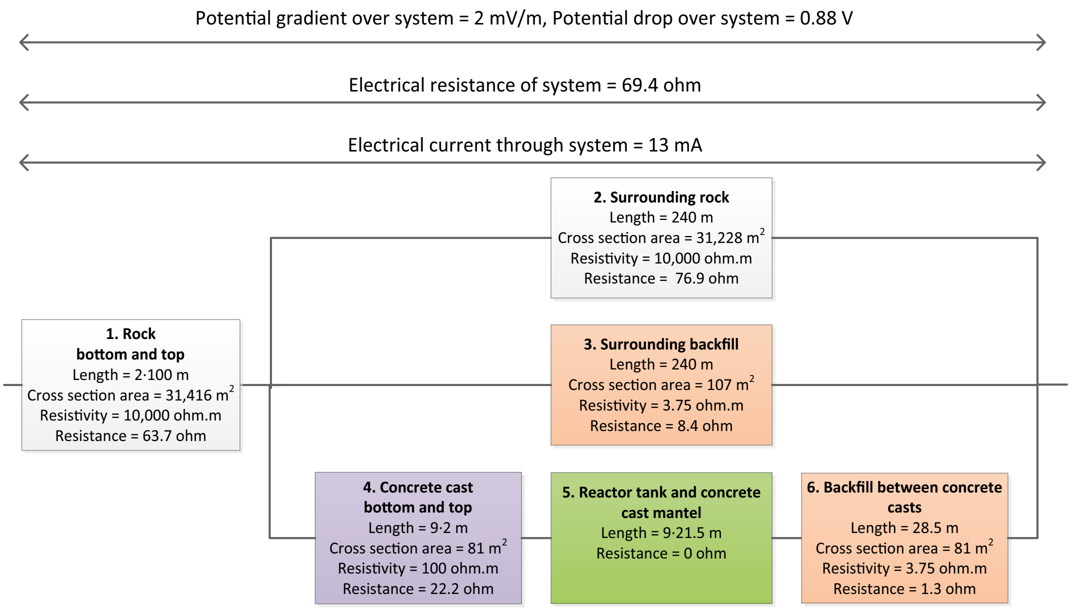

Figure 4-2. *Electric circuit model of the system in calculation case 2a. The term "reactor tank" is here, and in corresponding figures, used synonymously with reactor pressure vessel.*

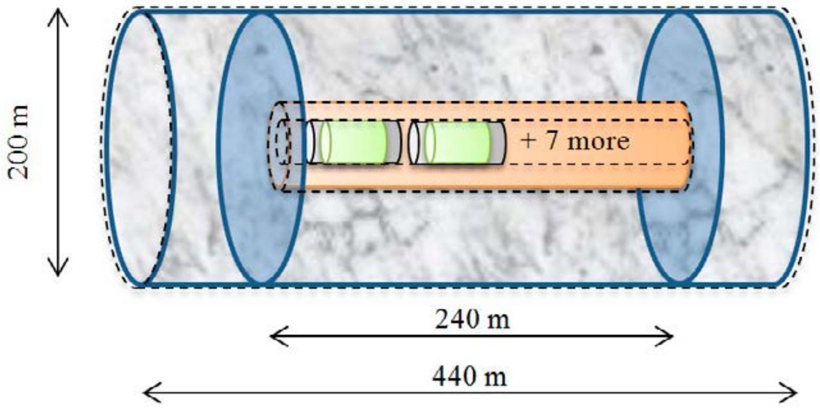

Figure 4-3. *Illustration of assumptions made when setting up the electrical circuit model. Horizontal dashed lines represent no-flow boundaries for electric current. There may also be a discontinuity in the electric potential over the dashed lines. The light-blue circles represent planes over which current can flow freely.*

With these assumptions, the results of calculation case 2a are as follows. The potential drop over the 440 m long system is 0.88 V. The resistance of the entire system is 69.4 ohm, whereof the highest contribution (92 %) comes from the upstream and downstream rock in resistor no.1. By using Ohm's law, one can calculate that a total current of 13 mA runs through the system of Figure 4-3, including the current that runs through the host rock and backfill. The model does not allow for the current lines to bend towards the pressure vessels and this is compensated for by pessimistically assuming that all current in the system contacts all nine pressure vessels. This makes the vessel contacting current 117 mA (13 mA multiplied by the nine vessels), which is less than the benchmark corrosion current of 300 mV used in this report for comparison with corrosion in the absence of Earth currents (cf. Section 3.9.2). This indicates that, for this calculation case, Earth current induced corrosion is a minor corrosion mechanism.

If looking at the individual resistances of Figure 4-2, that of resistor no. 1 is the largest. This resistance is proportional to the length of the upstream and downstream rock, as well as the radius of the cylinder. In the model these are assumed parameters. This is a weakness of the models presented in SKB (2014a, Appendix A) that is further explored in Chapter 5.

Another weakness of the model is that the Earth current induced corrosion rate increases linearly with the number of disposed metallic objects. This is as all current in the system, including the host rock, is pessimistically assumed to be propagated through each object. This can be handled in a more realistic manner using a finite element tool (cf. Chapter 6 and Chapter 7) where one can track the amount of current propagated through each object.

4.3 Calculation case 2b

Calculation case 2b of SKB (2014a, Appendix A) is identical to calculation case 2a except for one variation concerning the concrete embedment. It is pessimistically assumed that the thickness of the concrete at the top and bottom of the pressure vessel, corresponding to resistor 4 in Figure 4-2, is 0.1 m thick instead of 1 m as in calculation case 2a. As a consequence, this gives a total length of the macadam backfill in-between the concrete embedment units of 44.7 m (resistor 6).

This variation has a very limited impact of the results, under the assumptions made. The total resistance of the system decreases to 66.4 ohm and the total current increases to 13.3 mA, which is an increase of ~ 5 % compared to in calculation case 2a. As for calculation case 2a, the vessel contacting current is lower than the benchmark corrosion current of 300 mA.

It is interesting to note that in this case, the fraction of the total resistivity that resides in the upstream and downstream host rock increases to 96 %. This indicates that the host rock is the limiting factor for the amount of current that can be transported to the vault, and that changes in the design of the engineered barrier only affect the amount of inflowing current to a mild degree.

4.4 Calculation case 1a and 1b

Calculation cases 1a and 1b of SKB (2014a, Appendix A) are not very realistic cases in the sense that they disregard the host rock. This makes them very sensitive to assumptions made concerning the engineered barrier. This fact was used in SKB (2014a, Appendix A) for justifying the inclusion of the host rock in calculation cases 2a, 2b and 3.

In case 1a, the system was limited to a slice of the 1BRT vault that only includes one 21.5 m long pressure vessel, its 23.5 m long embedment unit and the corresponding backfill that surrounds the mantle area of the embedment unit. The same material properties were used as in calculation case 2a.

In Taxén et al. (2014), concerning the impact of Earth currents on a KBS-3 repository, a result was that the potential gradient within a deposition tunnel is about 10 % of the large-scale potential gradient in the surrounding host rock. This result was directly transferred to the 1BRT vault and it was assumed that the local potential gradient within the vault was 0.2 mV/m. The electrical circuit model for this system is shown in Figure 4-5, where it is also indicated that the components relating to the host rock and backfill in-between of the embedment units are disregarded. This model setup produces a total current through the system of 7.6 mA, whereof 1.9 mA goes through the concrete embedment.

In calculation case 1b the same simple system was maintained, but the length of the concrete embedment and corresponding slice of backfill was reduced to 21.7 m. This means that the pressure vessel was only protected by 0.1 m of upstream and downstream concrete. The current running through the entire 1b system becomes 23 mA, whereof 18 mA runs through the concrete embedment.

If taking the largest of the above mentioned current, i.e. 23 mA, and multiplying it by the number of vessels, the vessel contacting current becomes 207 mA. This is below the benchmark corrosion current of 300 mA.

If using the electrical circuit of Figure 4-5, but assuming no concrete on top and at the bottom of the pressure vessel, the current would become infinite. This shows the severe limitations of this approach, and point to the need of including the surrounding rock in the calculations, as the rock will limit the amount of current that can reach the 1BRT vault.

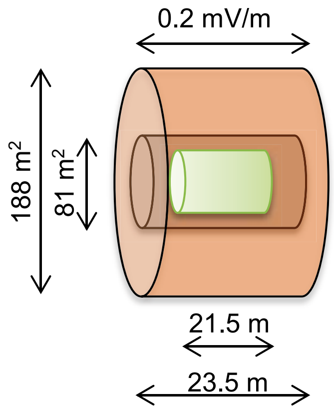

Figure 4-4. *Illustration of the limited system of case 1a only consisting of one pressure vessel (inner cylinder), its embedment unit, and a slice of the surrounding backfill (outer cylinder).*

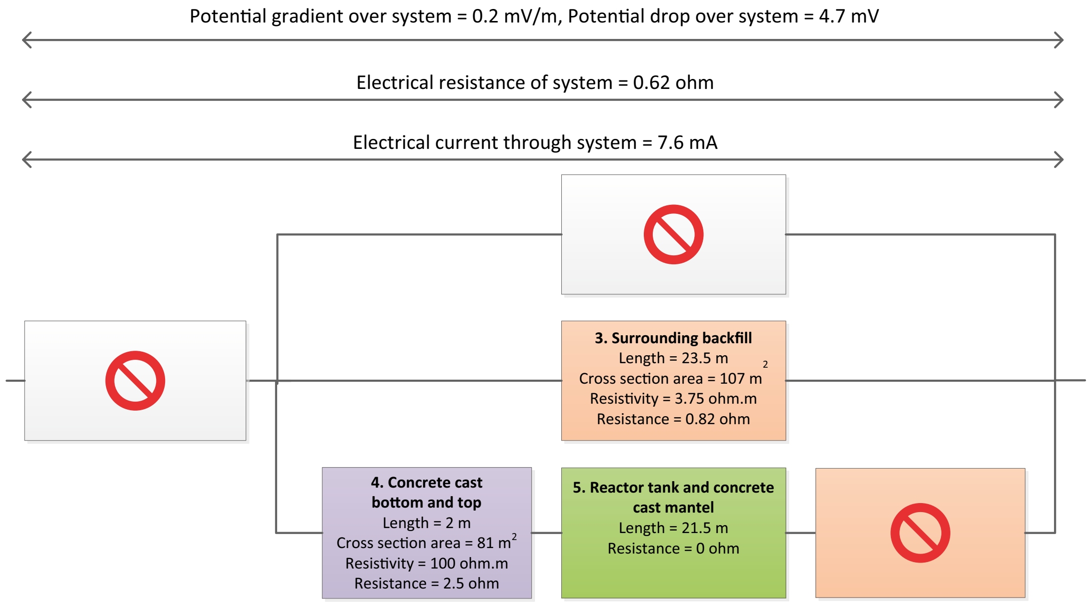

Figure 4-5. *Electrical circuit model of the system in calculation case 1a.*

4.5 Calculation case 3

Calculation case 3 of SKB (2014a, Appendix A) is a simplification of case 2a, where the upstream and downstream host rock of the 1BRT vaults is disregarded (i.e. resistor 1 of Figure 4-2). This creates a system where the current is governed by the 1BRT vault, as oppose to in calculation case 2a and 2b where it is governed by the upstream and downstream host rock. Accordingly, the potential gradient within the 1BRT vault was reduced to 0.2 mV/m, as in calculation case 1a and 1b. However, in the host rock surrounding the vault's mantle a potential gradient of 2 mV/m was kept. According to Figure 4-3, a discontinuity in the electric potential along an internal boundary is acceptable in the electrical circuit analogy.

Figure 4-6 shows the resulting electrical circuit model where a total current of 14 mA runs through the system. The pressure vessel contacting current then becomes 126 mA. This resulting current is similar to that of calculation case 2a. In calculation case 3 the limiting factor of the upstream and downstream bedrock is disregarded, which in turn is compensated for by reducing the potential gradient in the vault. Due to these simplifications the importance of this similarity should not be overstated.

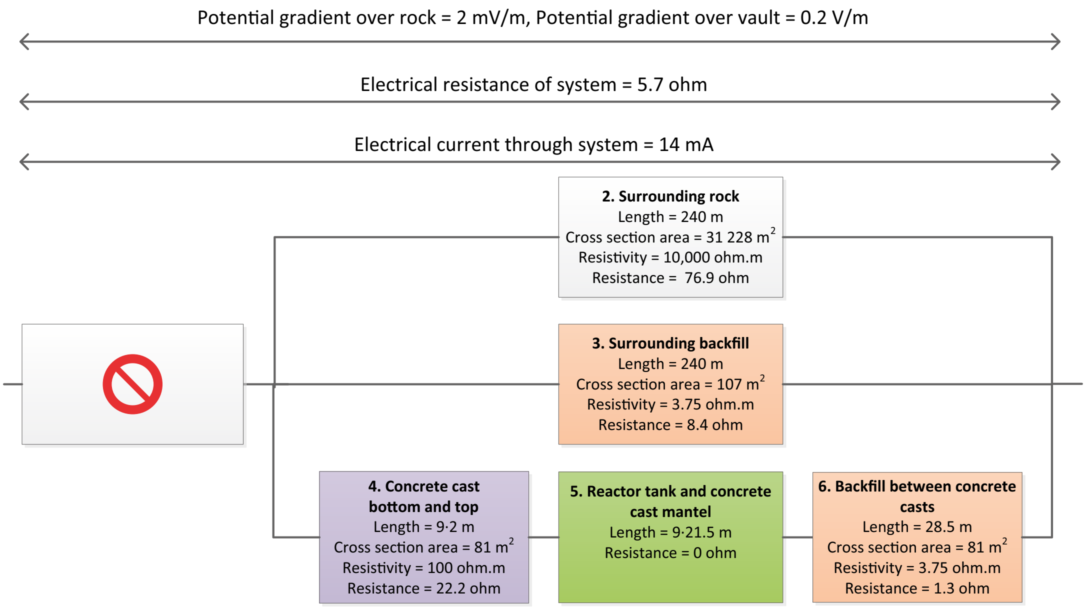

***Figure 4-6.** Electrical circuit model of the system in calculation case 3.*

5 Sensitivity studies

5.1 General considerations

In this chapter a few sensitivity studies are made with the electrical circuit model, by starting from calculation case 2a and varying various parameters. Three parameters are studied. Firstly, the block-scale rock resistivity is varied as there are uncertainties associated with its magnitude. In one calculation case the rock resistivity and the large-scale potential gradient are taken to be uncorrelated. In the other calculation case a correlation is assumed between the entities, as described by the hemispherical variant of Equation 2-4.

Secondly, the large-scale potential gradient is varied independently of the rock resistivity. This is done to include cases of higher gradients stemming from a possible future Fenno-Skan type electrode located at closer distance to SFR, and/or with higher power output.

Thirdly, a weakness of the electrical circuit model is explored by introducing a parameter which we call the "current deviation angle"; and vary this angle. As is detailed in Section 5.4, this is roughly the angle by which current lines in the host rock can bend towards the vault.

The objective of this chapter is merely to define bounding cases and to promote understanding of the system. From a quantitative point of view, the sensitivity studies of Chapter 6 and Chapter 7 that better incorporate the 3D-nature of the system, as well as account for other parts of SFR such as the ramp and parallel vaults, should be favoured over the ones made here.

5.2 Varying the rock resistivity

To accommodate a rather large range of plausible rock resistivities (cf. Section 3.3.2), two new calculation cases are set up where the rock resistivity is varied between 1 000 and 100 000 ohm.m. In one case the rock resistivity is varied independently of the large-scale electric field. In the other case, it is assumed that the Fenno-Skan electrode sends out a perfectly hemispherical electric field (cf. Figure 3-12) and that the large-scale potential gradient is correlated to the rock resistivity by the hemispherical variant of Equation 2-4. As is indicated in Appendix B, in the real case the presence of the Baltic Sea, and the proximity to the shoreline, skews the electric field so that it resembles, but still clearly deviates from, the hemispherical field.

5.2.1 Independent variation of the rock resistivity

This calculation case equals calculation case 2a in all aspects except for the block-scale rock resistivity, which is varied between 1 000 and 100 000 ohm.m. Regardless of the used rock resistivity, a large-scale potential gradient of 2 mV/m is used.

Figure 5-1 shows the resulting current through the entire system, as function of the used block-scale rock resistivity. This current varies by almost two orders of magnitude over the varied rock resistivity range. In fact, on log-log scale the relation between rock resistivity and total current is almost linear, as shown by the right plot in Figure 5-1. This supports the hypothesis that it is not the specifics of the repository, such as the conducting properties of the backfill and concrete, that governs the current flowing through the system. Instead the upstream and downstream rock governs how much current can be fed into the repository system, at least for a specified potential gradient. Mind, though, that part of this hypothesis is contradicted in Section 5.2.2.

5.2.2 Dependent variation of the rock resistivity

Figure 5-1 indicates that it may be of great importance to use a proper block-scale rock resistivity in the modelling. However, this is under the prerequisite that the electric field is independent of the rock resistivity, which is not the case. If the Fenno-Skan electrode sends out a perfectly hemispherical field, the large-scale potential gradient is inversely proportional to the rock resistivity (cf. Figure 3-12).

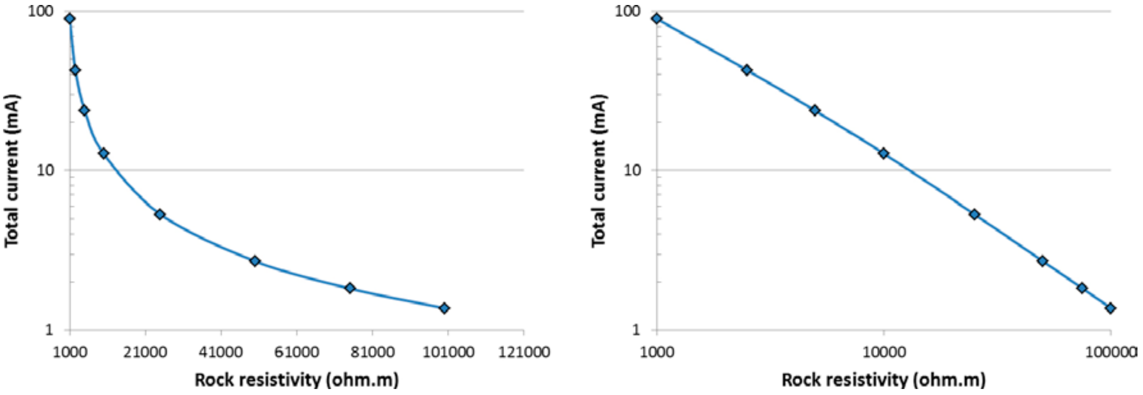

***Figure 5-1.** Results showing the total current running through the system as function of the block-scale rock resistivity. The large-scale potential gradient is assumed to be independent of the rock resistivity. Note that the images display the same results, but that the x-axis in the left plot is in linear scale and in the right plot is in logarithmic scale.*

If departing from calculation case 2a and assuming an unchanged current output at the Fågelsundet electrode; decreasing the rock resistivity from 10000 to 1000 ohm.m would not significantly influence the current fed to the repository system. This is as a lower potential would be required at the Fågelsundet electrode, resulting in a large-scale potential gradient at SFR that would decrease from 2 to 0.2 mV/m.

If the electrical circuit model was correctly tuned, in respect of the dimensions of the surrounding host rock, the current running through the system would be practically constant irrespectively of the assumed rock resistivity. This is not really the case, as is shown in Figure 5-2, indicating that too little surrounding host rock has been included in calculation case 2a.

5.3 Varying the large-scale potential gradient

Future HVDC electrodes may both be placed at a closer location to SFR and be more powerful. In Section 3.2.2 it is suggested that the horizontal field strength from a future HVDC electrode located just outside the Gräsö Island may be high as 30 mV/m at SFR.

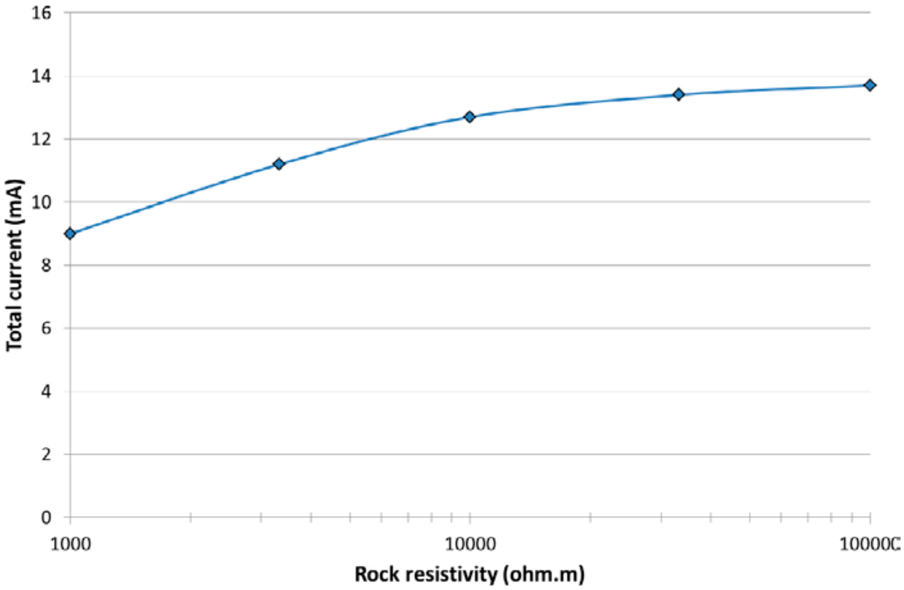

***Figure 5-2.** The total current running through the repository system when departing from calculation case 2a by varying the rock resistivity. Here the assumptions of a hemispherical electric field and an unchanged current output at the Fågelsundet electrode are used.*

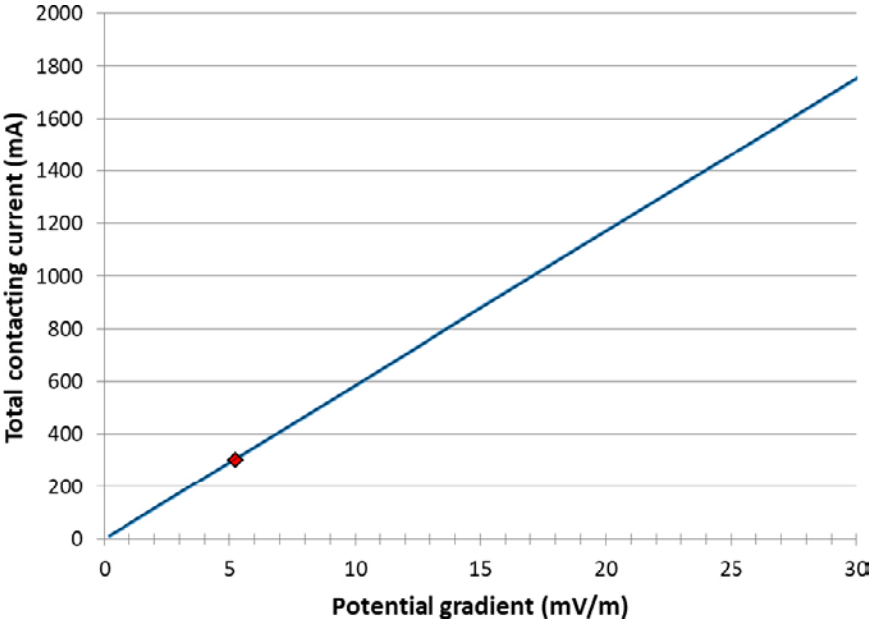

***Figure 5-3.** The vessel-contacting current assumed to give rise to Earth current induced corrosion, departing from calculation case 2a (with a contacting current of 117 mA at a potential gradient of 2 mV/m) by varying the large-scale electric potential gradient. The benchmark corrosion current of 300 mA is displayed by the red diamond.*

The vessel-contacting current that may give rise to Earth current induced corrosion is proportional to the large-scale potential gradient, as shown in Figure 5-3. In the figure the benchmark corrosion current of 300 mA is highlighted by a red diamond. With this simplistic approach, Earth current induced corrosion seems to dominate in the potential gradient range above about 5 mV/m. However, this assumes that all current running through the system is led to all nine reactor pressure vessels, which may not be the case, and that there is no polarisation resistance. Figure 5-3 suggests, however, that the impact of Earth currents from a possible future HVDC electrode needs to be investigated by more realistic modelling, which is done in Chapter 6 and Chapter 7 of this report.

5.4 Varying the current deviation angle

The lower resistivity of the 1BRT vault, compared to the surrounding rock, will impact the current lines by way of bending them towards the vault. This is a feature that the electrical circuit model cannot capture and as a result, it is pessimistically assumed that all current lines that run through the system may bend to the extent that they contact the pressure vessels. This begs the question of how large the system should be. In calculation case 2a it was subjectively assumed that the length of the cylinder representing the host rock should be 200 m longer than the isolated 1BRT vault. It was further subjectively assumed that its radius should be 100 m. If these assumptions are off, the estimate of the current that runs through the system will be off.

Before estimating the needed size of the system, let’s imagine an infinitely large rock volume of homogenous resistivity. At the middle of this rock volume is a vault, which can be seen as a low-resistivity anomaly (cf. Figure 5-4). Over this rock volume there is a uniform and horizontal potential gradient, except for at the vault where the current lines bend towards the low-resistivity anomaly. At some distance upstream and downstream of the vault, the anomaly does not significantly affect the current lines in the host rock which are accordingly parallel. These upstream and downstream locations are indicated by the left and right edges of the inner rock cylinder in Figure 5-4. The distance from these edges to the centre point of the vault (assuming a symmetrical vault) is 120 + L m, where 120 m is half of the vault length.

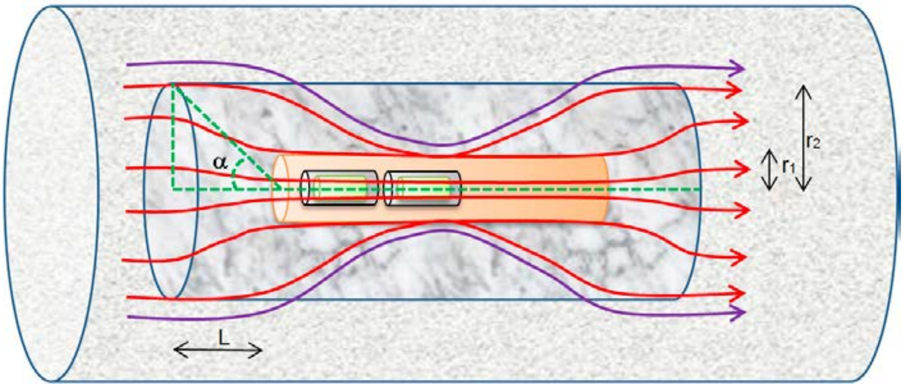

***Figure 5-4.** Illustration of how current lines bend towards the vault, and description of the parameters L, r_1, r_2 and α.*

Only current lines entering the edges of the inner rock cylinder, with the radius r_2 (m), are assumed to enter the vault. In this report the radius r_2 is called the influence radius and current lines beyond this radius will not be drawn towards to the vault to the extent that they enter. This situation is sketched in Figure 5-4 where the purple current lines do not touch the vault, but where the red current lines do.

For this influence radius, a bounding value can be estimated. In doing this a rock cylinder of arbitrary length is used. As in calculation case 2a the vault length is 240 m and vault radius r_1 (m) is 7.7 m. In Figure 5-5 two current lines, one purple and one red, flow past the vault. The purple line never enters the inner rock cylinder and will not affect the vault. The red current line, however, utilises the maximum pathway of the low resistivity vault. For this bounding case a zero resistivity within the vault is assumed and the paths of the studied current lines are not restricted by adjacent current lines (i.e. they can bend in 90° angles). In Figure 5-5 the purple line will have to travel through 440 m of resistive rock before exiting the system. For the red current line to travel the same distance within the resistive rock, or less, the radius r_2 would need to be 127.7 m or less. Accordingly, the value 127.7 m is adopted as a bounding influence radius for this particular system.

Next the parameter *L* of Figure 5-4 is varied, using the bounding influence radius of 127.7 m. In practice this is done by introducing a new parameter that we call the current deviation angle and denote α (°), as defined in Figure 5-4 and Figure 5-6.

This calculation case departs from calculation case 2a, but has a modified influence radius of the host rock cylinder (127.7 m) and a varying length of the upstream and downstream host rock (cf. Table 5-1). As such, the values of resistor 1 and 2 in Figure 4-2 are modified. The current deviation angle α is varied from 0° to 90°, where the 90° case corresponds to the red current line in Figure 5-5. As in calculation case 2a, the large-scale potential gradient of 2 mV/m is kept. The total current running through the system, at different α-values, is presented in Table 5-1 and the results of the case are plotted by the blue curve in Figure 5-7.

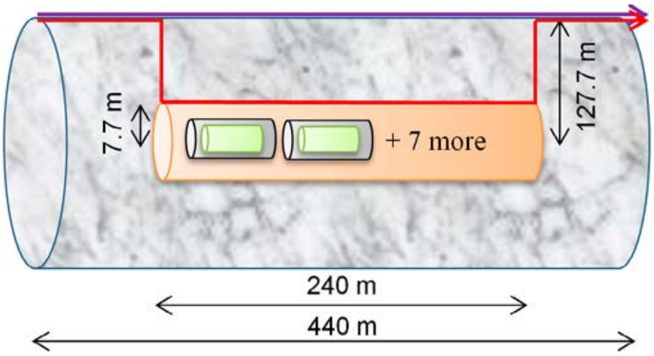

***Figure 5-5.** Illustration of the bounding influence radius for current lines that may bend and enter the vault.*

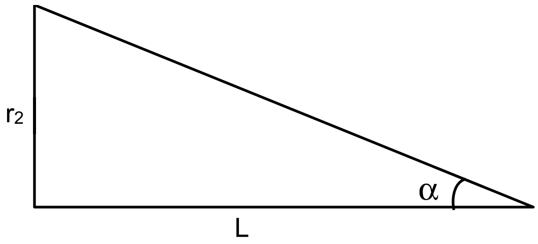

Figure 5-6. Definition of the current deviation angle α. See context in Figure 5-4.

Table 5-1. Resulting total current for different current deviation angles α and lengths *L* of upstream and downstream host rock. The radius of the host rock cylinder is set to 127.7 m. Otherwise data from calculation case 2a are used.

α (°)	L (m)	Total current (mA)
0	∞[a]	10
10	726	12
20	352	13
30	222	15
40	153	17
45	128	18
50	107	19
60	74	23
70	47	28
80	23	40
85	11	53
90	0	88

[a] Value 1×10^{16} used in calculation.

The blue curve in Figure 5-7 implies that the model is fairly insensitive to α at low values. Between 0 and 50° the change in total current is under a factor of two. Using higher angles gives a more rapid increase in the current, and at 90° the current is about nine times higher than at 0°. The α-value of 45° was used in calculation case 2a but in this present calculation case the influence radius of the host rock cylinder is increased from 100 to 127.7 m. Thereby, the total current in Table 5-1, at α = 45°, is increased by a factor of 1.4 compared to in calculation case 2a.

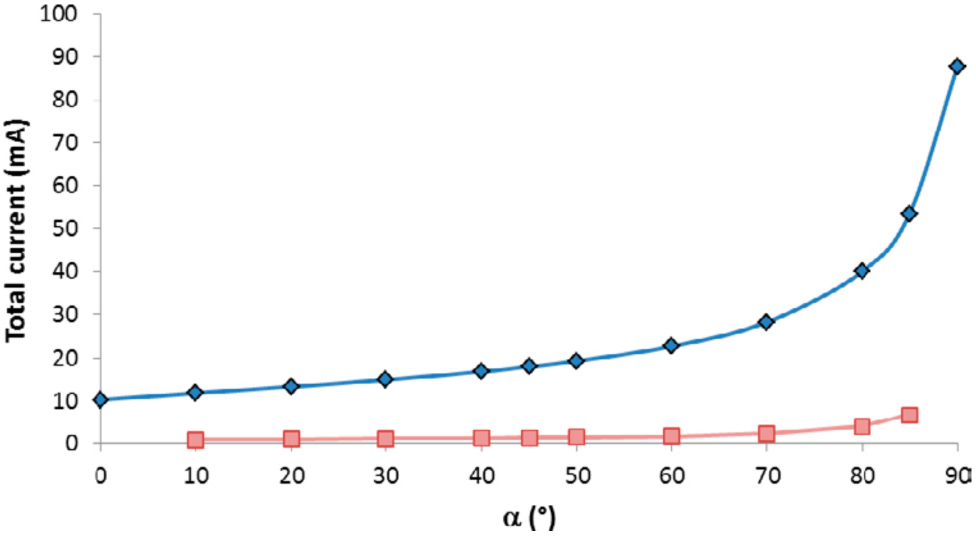

Figure 5-7. Total current running through the system versus current deviation angle (blue curve). The pink curve refers to the case using truncated funnels.

The above pessimistic approach can be compared with a non-conservative approach where current lines that enter the inner rock cylinder of Figure 5-4 are constrained to a truncated funnel before entering the 1BRT vault. Upon exiting the vault the current lines are constrained by another truncated funnel. These truncated funnels are illustrated in Figure 5-8 by green dashed lines. By this approach, no current lines in the rock outside these funnels may contact the 1BRT vault.

The resistance R (ohm) of a truncated funnel can be calculated according to Equation 5-1:

$$R = \frac{\rho L}{\pi r_1 r_2} \qquad \text{Equation 5-1}$$

Departing from calculation case 2a, the resistance of resistor 1 in Figure 4-2 can be replaced for the resistance of two truncated funnels. Moreover, the current path over resistor 2 is disregarded, as no current outside of the funnels is assumed to enter the vault. By using the same radii as above, that is r_1 = 7.7 m and r_2 = 127.7 m, and varying the length L according to Table 5-1 (exempting the 0° and 90° cases) the current through the system can be calculated. This current is plotted versus α by the pink curve in Figure 5-7. As can be seen, the current that enters the vault is, in this approach, lower than the corresponding current shown by the blue curve. In reality, current lines that affect the vault are not restricted to entering by its edges but may also enter through the vault's mantle area. Accordingly, one may expect the truncated funnel model to under-predict the entering current. If so, the true current that enters the 1BRT vault would be somewhere between the blue and pink curves in Figure 5-7.

If only having access to the electrical circuit model there is no way of knowing the appropriate current deviation angle. By revisiting calculation case 2a with COMSOL Multiphysics in Chapter 6 (cf. Figure 6-5) one can see that for this case, the corresponding current deviation angle is roughly 45°. This is within the α-range of Figure 5-7 where the angle's impact on the total current is limited. At an α-value of 45°, the currents entering the 1BRT vault are 1.2 mA and 13 mA, for the pink and blue curves respectively. Note that from the perspective of Earth current induced corrosion, and for comparisons with the benchmark corrosion current of 300 mA, the currents discussed in this section should be multiplied by nine to account for the number of reactor pressure vessels. Multiplying the highest of these total current, i.e. 13 mA, with nine gives 117 mA, which is still lower than the benchmark corrosion current.

With the introduction of the current deviation angle, and also the truncated funnel, the electrical circuit model has been pushed to its limits. For more accurate calculations, one must turn to more complex models, which has been done with COMSOL Multiphysics in Chapter 6 and Chapter 7 of this report.

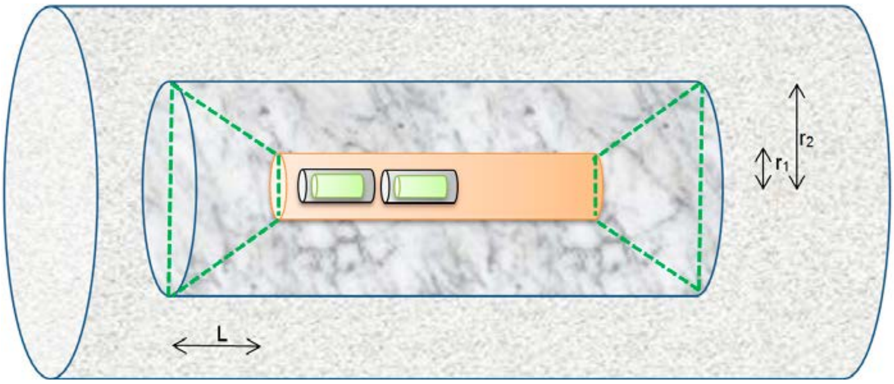

Figure 5-8. *Illustration of truncated funnels (in green dashed lines) to which the current lines entering the inner rock cylinder are constrained. No current lines carried within the rock outside the funnels enter the vault.*

6 2D axisymmetric representation

6.1 Use of COMSOL Multiphysics

COMSOL Multiphysics is a commercial software for finite element analysis that may be used to solve coupled systems of partial differential equations. Generally, a system of chosen geometries and material properties can be constructed and represented by a fine mesh of tetrahedral elements. The system is thereafter subjected to constraints including boundary conditions, and solved numerically. In the post-processing of the numerical results, a variety of variables and entities within the system can be analysed numerically.

6.1.1 Charge-balance approach

In all calculation cases of Chapters 6 and 7, except for in Section 6.7, Earth current induced corrosion is estimated by using the charge-balance approach. This is done by building a more or less complex system of components of different geometries and electrical resistivities, which should represent the SFR repository. Typical components are the reactor pressure vessels; the concrete embedment; the backfill of the 1BRT vault; parallel vaults; and other underground openings of SFR. For each component a material is assigned, having a specified electrical resistivity. In the 2D axisymmetric representation, all components are made of cylinders sharing the same axis. The outer cylinder represents the host rock and the mantel area of this cylinder has a non-flow boundary criterion, meaning that no electric current can pass over this area. At one of the edges of the outer cylinder the electrical potential is set to zero, while at the other edge a non-zero value is set. This creates a large-scale potential gradient over the cylindrical model volume and a two-dimensional electric field is solved for each tetrahedral element by a version of Equation 2-5, in cylindrical coordinates.

Within the cylindrical model volume there are boundaries between the different components. Electric current can flow in both the axial and radial directions over these component boundaries, and there can be no (significant) discontinuities in the electric field. This latter condition may create numerical problems if the meshing at the boundary is too coarse. Accordingly, a finer mesh is typically used at such boundaries. This is illustrated in Figure 6-1a, showing the meshing of an excerpt of the model volume representing the 1BRT vault (cf. Figure 4-1), below the symmetry line. As can be seen, the mesh is rather course at some distance from the reactor pressure vessels, as compared with the mesh inside and close to the 1BRT vault.

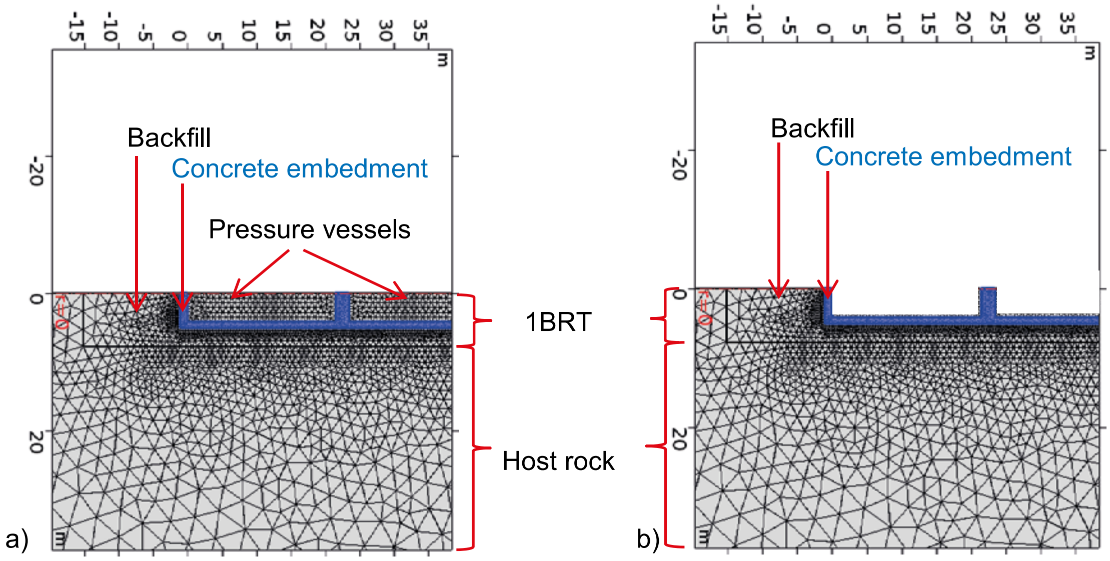

Figure 6-1. Illustration of the meshing in the a) charge-balance approach and b) kinetics limitation approach. A courser mesh is seen distant from component boundaries and a very fine mesh is used at the reactor pressure vessels. Vault is viewed from the side.

In the system, current lines will bend towards the least resistive components, which are the reactor pressure vessels. Current may enter, and leave, through the mantel area of the pressure vessels, as well as through their edges. At each tetrahedral element, facing the boundary between the pressure vessel and the concrete embedment, a specific value of the current density is calculated. The total amount of current that leaves a specific pressure vessel is calculated by integrating the absolute amount of the ingoing and outgoing current density over the vessel's surface, and dividing the outcome by two[7]. In the charge-balance approach, this current equals the corrosion current.

COMSOL Multiphysics allows for assigning surface impedance to a component boundary, which could be used to mimic a polarisation resistance. However, as it is more pessimistic to neglect such a polarisation resistance, no surface impedance has been implemented when using the charge-balance approach in this report.

In Chapter 7 the modelling is not restricted to cylindrical coordinates, but is performed in full 3D. As a consequence, the model volume is typically a cuboid and the components can have any shape and placement within it. Apart from this, the above description is valid also for the modelling in Chapter 7.

6.1.2 Kinetics limitation approach

When evaluating the effects of kinetically constrained corrosion, as done in cylindrical coordinates in Section 6.7, the corrosion rate is estimated by a different approach. In the model, the components of the host rock; backfill; concrete embedment; and other underground openings share the same setup as in the charge-balance approach. However, the reactor pressure vessels (or segments of the vessels) are treated differently. In practice it is assumed that the electrical conductivity of the metallic pressure vessels is infinite, forcing the electrical potential at each part of a vessel's surface to be the same. This creates a potential discontinuity between this uniform electrical potential and the potentials of tetrahedral elements within concrete embedment that faces the vessels. This discontinuity translates to the surface overpotential, which is used to calculate the kinetically controlled anodic and cathodic current densities. In doing this, the Butler-Volmer formulation (cf. Equations 2-34 and 2-35) is used. As discussed in Section 2.2.5, this can be illustrated by converting a mixed potential diagram to a diagram showing the anodic and cathodic current density as function of the overpotential. In doing this, the corrosion current density is needed for conditions where there is no external electric field. This corrosion current density at zero overpotential was calculated in Section 3.9.2 to be 4.3×10^{-5} A/m^2. The resulting plot is shown in Figure 6-2.

For a specific overpotential at each element facing the boundary, the anodic current density, as well as the cathodic current density, can be obtained. This is shown in Figure 6-3, where the length of the arrows that emanate from the vessel surface signifies the magnitude of the anionic and cathodic current density. The corrosion current of the vessel is evaluated by surface integration of the anionic current density. The total corrosion current for all vessels in 1BRT is obtained by summing the corrosion currents of each individual vessel, or segment.

In this approach, the pressure vessels are not treated as meshed volumes. Instead a vessel is treated as a "void" in the model, having a surface over which current flow is allowed (cf. Figure 6-1b). This surface has a uniform electrical potential, which absolute value directly relates to the overpotential and the net current entering the vessel. Accordingly, the vessel's surface potential and the local electric field in the vessel's surroundings are coupled. The absolute value of the vessel's potential is therefore evaluated by iteration, using the constraint that the surface integral of the net current density (that is $i_c - i_a$) should be zero.

---

[7] As no current is created in the vessel, the ingoing current must equal the outgoing current. Only the outgoing current contributes to corrosion. Accordingly, the surface integral result is divided by two.

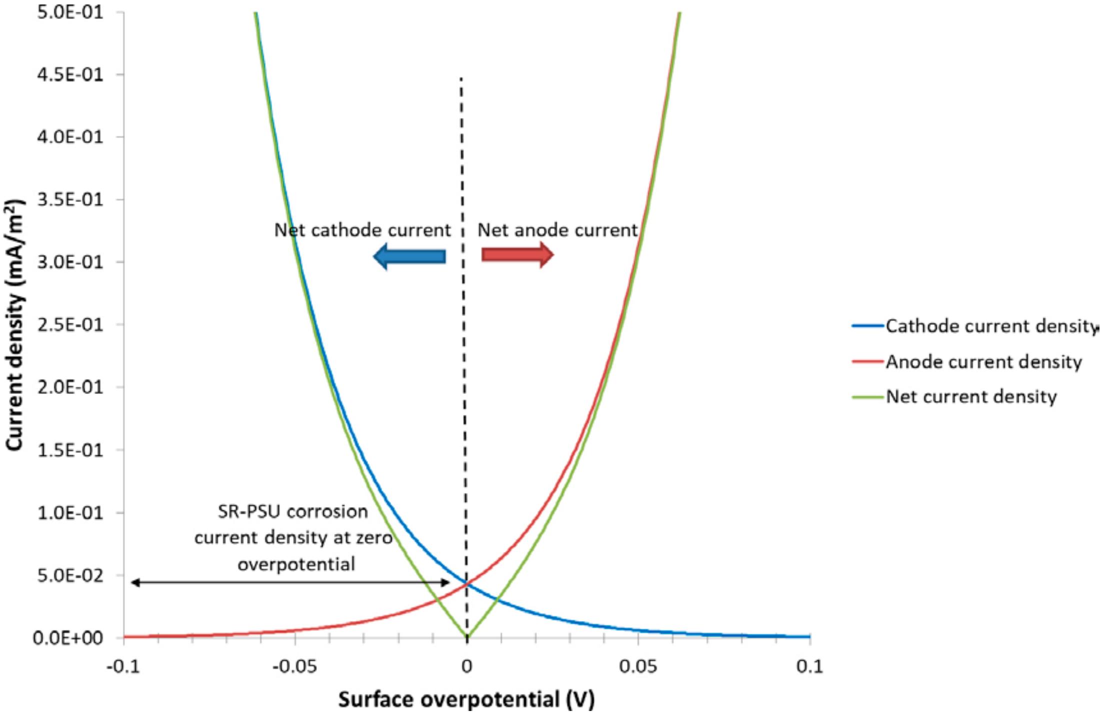

Figure 6-2. *Anode and cathode current density vs. surface overpotential, using the SR-PSU corrosion current density at zero overpotential and Tafel slopes of 59 mV/dec.*

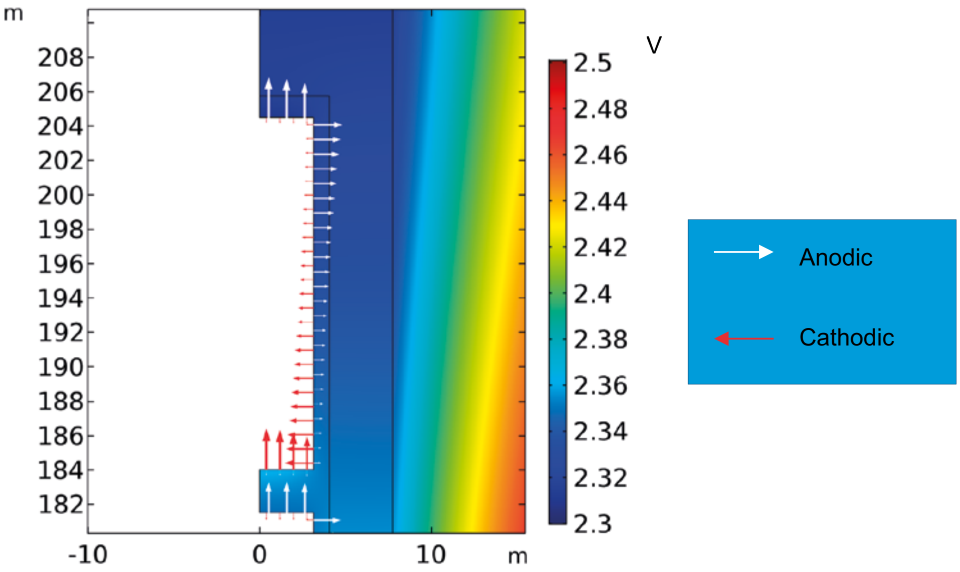

Figure 6-3. *Image of a reactor pressure vessel, represented by the white "void" in the electric field, and arrows showing the direction and magnitude of anodic and cathodic current densities.*

6.2 Revisiting calculation case 2a

In this section the conceptualisation and parametrisation presented for calculation case 2a (Section 4.2) is implemented in COMSOL Multiphysics. This is done with the main purpose of illustrating the influence of assumptions used in the 1D model in Chapters 4 and 5. Furthermore, it highlights the differences between the current in the total system; the current entering the 1BRT vault; and the current propagated through the reactor pressure vessels. Finally, the numerical implementation of the model in COMSOL Multiphysics is tested.

A simplified representation of the 1BRT vault, with data from Table 4-1, is implemented in a 2D axisymmetric model with a symmetry axis at r = 0. As in calculation case 2a the vault is isolated and the influence of neighbouring vaults, access tunnels, and ramp is neglected (cf. Figure 4-1). The different material domains represented in the model are the granitic rock surrounding the 1BRT vault; the macadam backfill of the 1BRT vault; and 9 concrete embedded reactor pressure vessels. In calculation case 2a, each pressure vessel was visualised as being embedded in a separate unit. This is a deviation from the planned method for embedment but in the 1D electrical circuit model this deviation is inconsequential. In the 2D and 3D COMSOL Multiphysics modelling of this report, a single continuous concrete embedment is assumed to surround the pressure vessels, which is according to plan (SKB 2014d).

Each domain has a uniform electrical resistivity as in the following (cf. Section 3.8):

- Block-scale rock: 10.000 ohm.m
- Backfill: 3.75 ohm.m
- Concrete: 100 ohm.m
- Metal of pressure vessels: 0.01 ohm.m
- Polarisation resistance at pressure vessel surface: 0 ohm.m^2

Concerning the resistivity of the metal, the value used is significantly higher than typically reported for carbon steel. This is to avoid the need to a very fine mesh at the reactor pressure vessels, which would require much computational power. The chosen value is, however, low enough not to impact the results in a significant way.

The different material domains are shown in Figure 6-4 represented on a plane in 2D (where the symmetry axis is shown as a red line at r = 0), viewed from above.

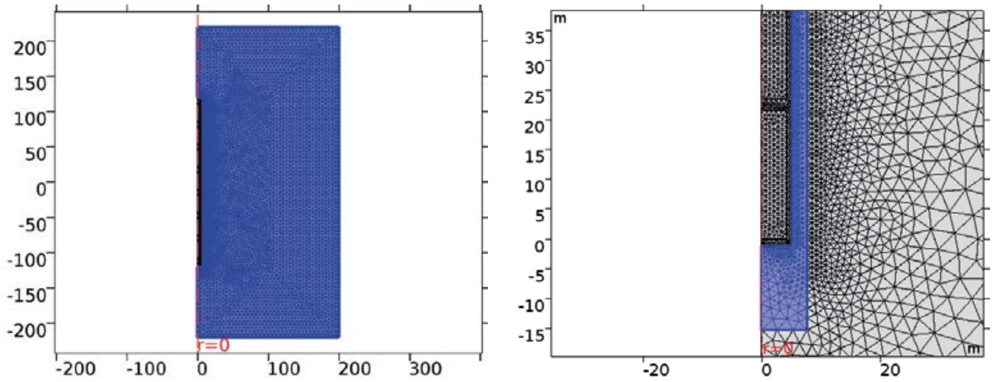

a – Granitic rock

b – Gravel backfill

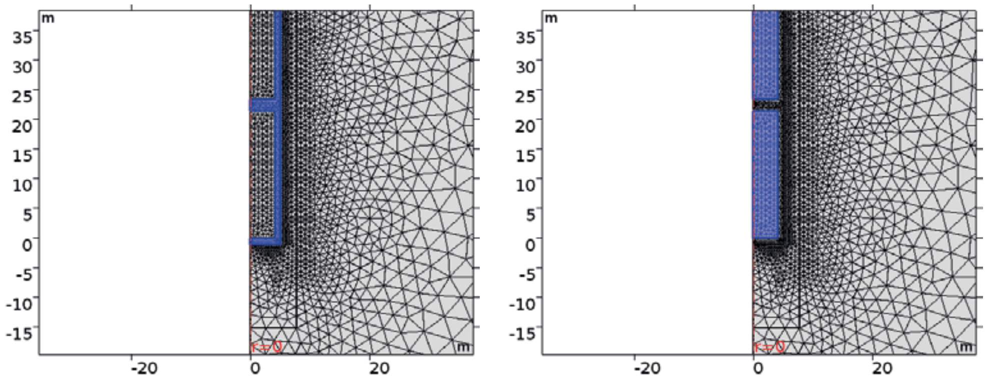

c – Concrete embedment

d – Pressure vessels

Figure 6-4. *Model domain (note the red dashed cylindrical symmetry line at r = 0) and finite element mesh at different zoom levels to visualise (in blue colour) the different material domains having different electrical conductivities, (a) granitic rock surrounding the 1BRT vault, (b) gravel backfill in the vault, (c) concrete embedment, (d) pressure vessels.*

A specified large-scale potential gradient (2 mV/m) is imposed over the modelled domain by fixed potentials at the top and bottom boundaries in Figure 6-4a. The main difference between this modelling and that performed in Chapter 4 is that current lines may bend towards less resistive domains. Importantly, one can separate the current that bends towards, and run through, the pressure vessels from the current that runs past them in the vault or host rock. One can also estimate the influence radius in the host rock, wherein all current lines bend toward, and also contact, the 1BRT vault. This has bearing on the discussion in Section 5.4.

The 2D results are illustrated in Figure 6-5 where upper left image shows the cylindrical symmetry results after revolution in 3D. The colour represents the electrical potential (V) and grey and black streamlines represent current conduction path lines. In the remaining of this report, these lines will simplistically be called current lines. As is seen in Figure 6-5, most current lines that enter the concrete embedment will contact at least one of the pressure vessels.

Concerning the influence radius (cf. Section 5.4), it is about 80 m in this case, as can be seen by the black current line that barely touches the 1BRT vault in Figure 6-5 (lower left). This is somewhat lower than what was assumed in calculation case 2a, i.e. 100 m. It is also lower than the theoretical upper limit of the influence radius, as evaluated in Section 5.4 (i.e. 127.7 m). At roughly 80 m upstream the end of the 1BRT vault, the current lines are virtually parallel and unaffected by the presence of the vault. If using this distance and the influence radius of 80 m to calculate the current deviation angle α (for comparison with Section 5.4) it becomes about 45°.

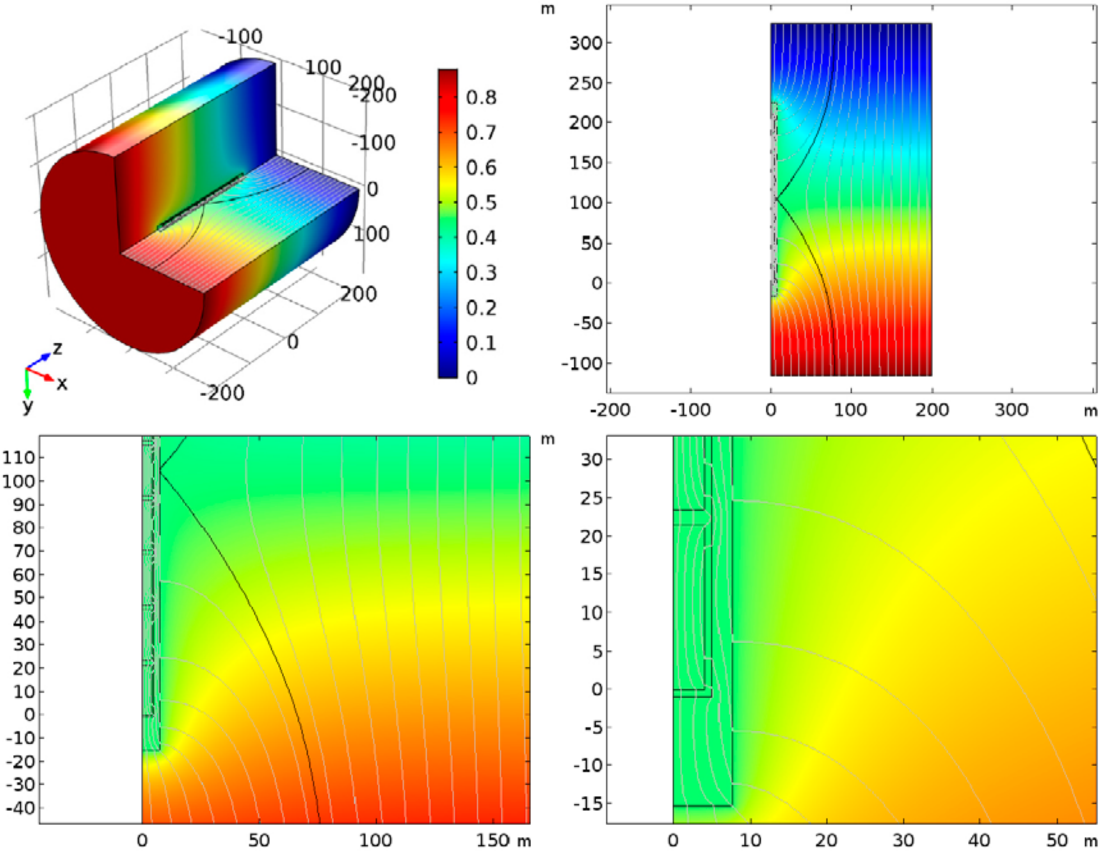

Figure 6-5. *Electric potential (V) and grey current lines in 3D and 2D axisymmetric plane. The black current line indicates the influence radius of ~ 80 m. The 1BRT vault is located at the centre of the cylinder in the 3D representation and at the left-hand side of the domain in the 2D representation. The bottom row of figures shows the 2D axisymmetric plane at two different zoom levels.*

By integrating the current density of different objects (as explained in Section 6.1.1), the following outgoing currents are evaluated:

- The outgoing current from the entire system (i.e. the model volume).
- The outgoing current from the 1BRT vault.
- The outgoing current from each pressure vessel,
- The sum of the outgoing currents from all pressure vessels, i.e. the total corrosion current.

Where applicable, these currents are compared to the corresponding current of calculation case 2a and also of a variant of calculation case 2a with a current deviation angle of 45° (cf. Table 5-1). The comparison is provided in Table 6-1.

Table 6-1. Comparison of currents running through different components in the calculation cases, and the total corrosion current.

Component	2D representation (mA)	Calculation case 2a (mA)	Calculation case 2a variant with α = 45° (mA)
Entire system	7.2*	13	18**
1BRT vault	4.6		
Vessel 1	1.3		
Vessel 2	1.8		
Vessel 3	2.1		
Vessel 4	2.3		
Vessel 5 (middle)	2.4		
Vessel 6	2.3		
Vessel 7	2.1		
Vessel 8	1.8		
Vessel 9	1.3		
Total corrosion current	17	117	162**

* The entire 2D model domain has the radius of 200 m. The tabulated value only reflects the current entering the inner cyliner with a radius of 100 m, for comparison with calculation case 2a.
** The radius of the model domain is 127.7 m in the 2a variant case.

From the results in Table 6-1, it appears that the 1D modelling overestimates the current running through the entire system. In the 1D model it is assumed that all current lines entering the host rock can reach the 1BRT vault, and thereby find a low resistivity path. Figure 6-5 shows that this is not the case, as many current lines never enter the low resistivity vault, although they bend towards it. Out of the current in the entire 2D model volume, only about two thirds enter the vault. Furthermore, some of these current lines only travel a short distance in the vault.

In the 2D representation, between 18 and 33 % of the current in the entire 2D model volume enters the reactor pressure vessel. Out of the current that enters the 1BRT vault, only about half is carried through the pressure vessels. As a result, the total corrosion current is not nine times the current in the entire system, as assumed in the 1D model. Instead this ratio is only 2.4. This reduced the total corrosion current in the 2D model to merely 17 mA, which is 15 % of the assumed corrosion current in calculation case 2a. This is of course much smaller than the benchmark corrosion current of 300 mA (cf. 3.9.2). Accordingly, Earth current induced corrosion has, for this case, a very minor influence on the total corrosion rate.

6.3 2D cylindrical base case

In Section 6.2, the 1BRT vault is represented as being isolated in the host rock. For the 2D cylindrical base case, structures that extend in the axial direction from the 1BRT vault (i.e. parts of access tunnels and ramps) are added to the 1BRT vault, in a stylistic manner (see Figure 6-6). Structures in parallel with the 1BRT vault (i.e. the other repository vaults and some access tunnels) may provide shortcuts that direct current past the 1BRT vault, without contacting its pressure vessels.

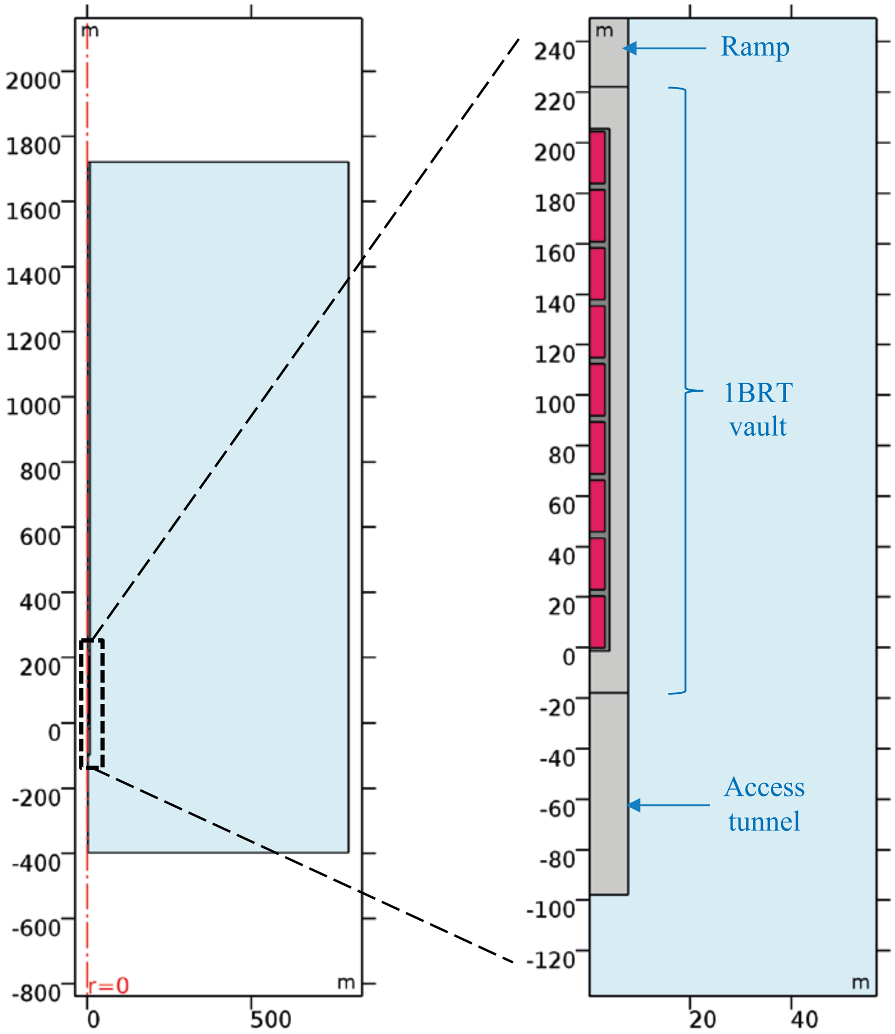

***Figure 6-6.** Model domain for 2D cylindrical base case with symmetry line at the centre of the 1BRT vault, access tunnel and ramp at r = 0. The 1BRT vault, access tunnel, and part of the ramp is indicated in zoomed inset image along with pressure vessels (red), concrete embedment (dark grey) and macadam backfill (light grey).*

These parallel structures are therefore pessimistically neglected in the 2D cylindrical base case. Current is expected to be directed along structures of least resistance, and with a potential gradient perfectly aligned with these structures this will enhance the current through the 1BRT vault. Note that a more realistic representation of SFR, which includes also parallel structures, requires a full 3D analysis. Such modelling is presented in Chapter 7.

The ramp, providing a conductive path for current down to (or up from) the repository, is expected to be one of the most important structures in addition to the 1BRT vault. In fact, three ramps connect the SFR repository with the ground surface (see Section 3.1), where the longest of the ramps (1RTT, cf. Figure 3-3) is 1 680 m long and has a cross-section area of 102 m^2 (Carlsson et al. 2014, Table 3-1). This ramp is spiralling down to repository depth, whereas the other ramps (1DT and BT) are straighter and therefore significantly shorter. The combined effect of these ramps is cautiously taken into account by assuming a single ramp of simplified geometry. This simplified ramp is straight and coaxial with the 1BRT vault; has a uniform cross section area that coincides with that of the 1BRT vault (i.e. 188 m^2); and extends for 1 500 m in the tangential direction from the 1BRT vault. This simplified ramp pessimistically neglects the curved geometry of the actual ramps but still utilises almost the entire length of the longest ramp as a conductive structure. It should be noted that the longest Euclidian distance is less than 1 km between the ramp entrance at ground surface and exit at the vaults (cf. Figure 3-10). The ramp is also assumed to extend all the way to the model boundary. With the specified potential gradient direction, the consequence is that current leaves (or enters) the ramp mainly through its cross-sectional surface at the model boundary, as this is the path with least resistance. This may be conceived as the ramp exiting in the sea (rather than on dry land) and is deemed to be a pessimistic assumption. This also incorporates the possible short-circuiting of the ramp and the Baltic Sea by the Singö zone.

At the opposite end of the 1BRT vault, an access tunnel of 80 meters in length and 188 m^2 in cross section area is assumed (see SFR 3 design in Figure 3-3). This access tunnel pessimistically represents the access tunnel 2BST with its appendix facing the 1BRT and 2BLA vaults. The possible influence of relatively less conductive concrete plugs in the backfilled ramp, as well as in the assumed access tunnel and the 1BRT vault, is pessimistically neglected as such plugs would decrease the current running through these structures.

A potential gradient of 2 mV/m is assumed over the modelled domain by specifying fixed potentials at the top and bottom boundary in Figure 6-7.Accordingly, the potential gradient is aligned along the 1BRT and ramp direction. The ramp and access tunnel are assumed to be backfilled by the same macadam gravel (or bentonite) as in the 1BRT vault. To avoid any undesired effects of the model boundaries, the model domain is extended to 800 metres in the radial direction (as compared with 200 m in Section 6.2). Other modifications are that the length and radius of the pressure vessels are set to 20.5 m and 3.15 m, respectively. These are average dimensions based on data Table 3-2. As a result of shortening the pressure vessels, as compared to in Section 6.2, the concrete filled spacing between the vessels is increased to 1.25 m.

The resulting potential field and current lines are shown in Figure 6-7. The black current line is the outermost current line that touches the 1BRT vault; in this case the part closes to the ramp. This suggests an influence radius of ~ 247 m. As expected, current entering from a larger area of the model boundary is directed through the vault and ramp, providing a path with lower resistance. Acknowledging that the 1BRT vault is not isolated, but connected to ramps and other tangential parts of the repository, increases the amount of current propagated through 1BRT to about 49 mA[8]. The current that propagates through each pressure vessel is provided in Table 6-2, together with the total corrosion current of this case. The vessels closest to the ramp are subjected to the highest Earth current induced corrosion rate.

Table 6-2. Corrosion currents of reactor pressure vessels 1 to 9, and total corrosion current. The vessels are ordered by proximity to the access tunnel.

Component	2D Base case (mA)
Entire system	461*
1BRT vault	49
Vessel 1 (at access tunnel)	7.8
Vessel 2	8.9
Vessel 3	9.9
Vessel 4	11
Vessel 5 (middle)	12
Vessel 6	13
Vessel 7	13
Vessel 8	14
Vessel 9 (at ramp)	15
Total corrosion current	104

* Entire model domain has the radius of 800 m.

As can be seen from Table 6-2 the total current in the system is increased to 461 mA, which is significantly larger than when revisiting calculation case 2a. This is partly due to the inclusion of the ramp and access tunnel and partly due to the increase in model volume radius, from 100 m to 800 m.

---

[8] This value is obtained by surface integration at the 1BRT boundaries. The current that enters the entire model volume inside the area bounded by the influence radius is 47 mA. This suggests that in this case, a small fraction of the current lines exit and re-enter the 1BRT vault. This fraction is thereby accounted for more than once in the integration. This creates the deviating 2 mA.

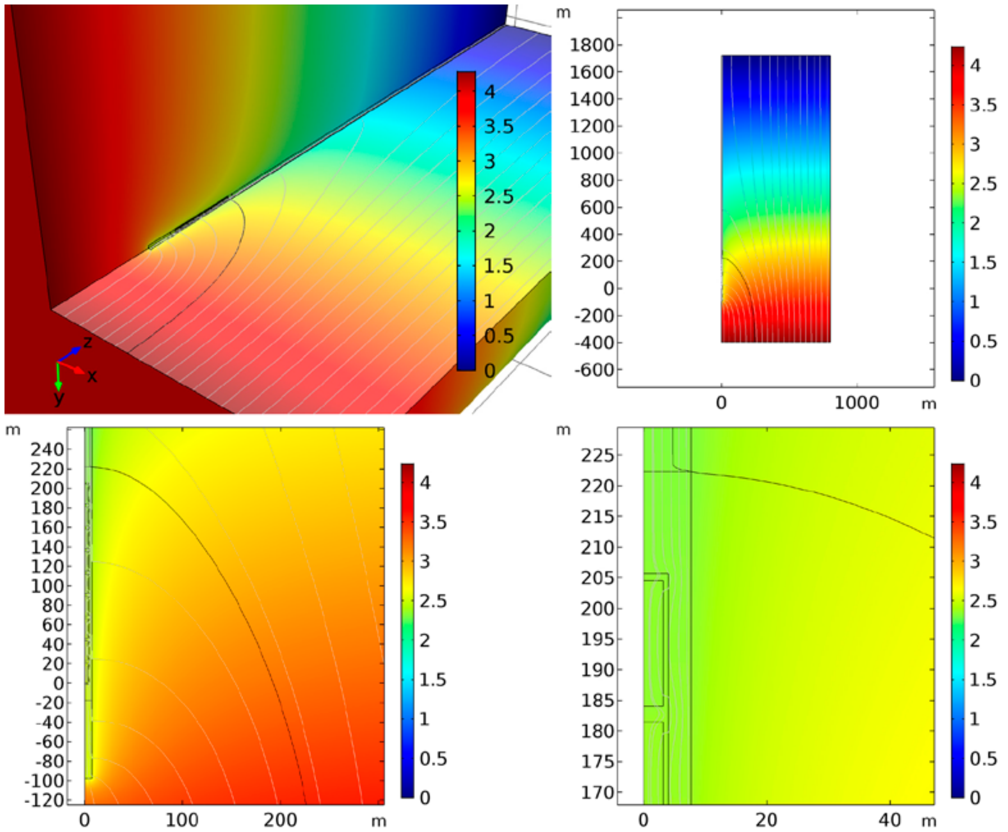

Figure 6-7. Electric potential (V) and grey current lines in 3D and 2D axisymmetric plane for the base case. The black current line indicates an influence radius of ~ 247 m. The 1BRT vault is located along the axis of the cylinder in the 3D representation and at the left-hand side of the domain in the 2D representation. The bottom row of figures shows the 2D axisymmetric plane at 2 different zoom levels.

The inclusion of the ramp and access tunnel gives a tenfold increase in the current that propagates through the 1BRT vault, as compared to the isolated vault case.

This results in a total corrosion current to 104 mA, which is still lower than the benchmark corrosion current of 300 mA. This suggests that for this case, the Earth current induced corrosion is minor but still significant. This total corrosion current is expected to decrease when also accounting for kinetics limitations in Section 6.7. It is expected to further decrease when accounting for parallel structures in Chapter 7.

6.4 2D cylindrical variation case A – backfill and embedment properties

In this set of variation cases, different properties of the concrete embedment and backfill that surround the pressure vessels are evaluated. The variation spans from a vault with no concrete embedment, entirely backfilled with macadam gravel of low resistivity, to a vault entirely backfilled with concrete of high resistivity. The variation also includes the impact of non-saline groundwater for a future location of the shoreline, due to isostatic rebound. The aim is to evaluate the effect of the materials surrounding the pressure vessels. Moreover, the variations encompass uncertainties in construction dimensions discussed in Section 3.1.3 and 3.5.2 (i.e. the thickness of the concrete embedment). All input data of the model are the same as in the 2D cylindrical base case (Section 6.3), except for the electrical resistivities of the backfill and embedment.

In the first set of analyses the resistivity of the concrete embedment is left unchanged at 100 ohm.m, while the resistivity of the backfill is modified. Used backfill resistivities are 12, 170 and 540 ohm.m (from Section 3.4), as well as 100 ohm.m. The first three variation cases (A:1, A:2, and A:3) correspond to uncertainty in the macadam resistivity due to uncertainty in its porosity and pore water salinity. In these cases, the resistivity is also varied for the ramp and access tunnel. The fourth case (A:4) concerns a hypothetical situation where the entire 1BRT vault is filled with concrete. Here it is assumed that the ramp and access tunnel are backfilled with macadam.

In a second set of analyses the resistivity of the macadam backfill is left unchanged at 3.75 ohm.m, while the resistivity of the concrete embedment is modified. Used embedment resistivities are 3.75, 200, and 3 000 ohm.m. In the first case (A:5) the resistivity of the embedment coincides with that of the macadam backfill; illustrating a hypothetical case where no concrete embedment is used. In the other cases (A:6 and A:7) the embedment resistivity roughly corresponds to the lowest and highest concrete resistivities of Figure 3-21.

The results from the variation cases are shown in Table 6-3, both in terms of the current entering the 1BRT vault as well as the total corrosion current leaving the reactor pressure vessels. For comparison the values from the 2D cylindrical base case are shown.

Table 6-3. Current entering the 1BRT vault and the total corrosion current for different resistivities of the embedment and backfill.

Calculation case	Embedment resistivity (ohm.m)	Backfill resistivity (ohm.m)	Current entering 1BRT (mA)	Total corrosion current (mA)
Base case	100	3.75	49	104
Variation A:1	100	12	23	101
Variation A:2	100	170	5.4	40
Variation A:3	100	540	3.8	27
Variation A:4	100	100/3.75*	28	155
Variation A:5	3.75	3.75	52	313
Variation A:6	200	3.75	48	61
Variation A:7	3000	3.75	47.5	4.8

* The resitivity of the 1BRT backfill is 100 ohm.m, while that of the ramp and access tunel is 3.75 ohm.m.

When increasing the resistivity of the backfill in variation case A:1, A:2 and A:3, the current propagated through the 1BRT vault rapidly decreases. With a backfill resistivity of 540 ohm.m only 3.8 mA is propagated through 1BRT. This is a decrease with a factor of about thirteen, as compared to in the base case. With a higher backfill resistivity, however, the Faraday's cage aspect of the backfill is diminished. As such, the total corrosion current of variation case A:3 is about one fourth of that in the base case. The Faraday's cage aspect is highlighted in variation case A:4. In this case the current is drawn towards the axis of the cylindrical model, as the resistivity of the access tunnel and ramp is kept low. As a result, a relatively high amount of current seeks to propagate into the edges of the concrete filled 1BRT vault (which is still less resistive than the surrounding host rock). In total 28 mA reaches the 1BRT vault in this variation case. As can be seen, most of this current propagates through the majority of the reactor pressure vessels, and aids the corrosion. The ratio between the total corrosion current and the current entering 1BRT is 5.5. The same number is 2.1 for the base case.

In variation case A:5 the concrete embedment is replaced for macadam backfill. As such, the current that enters the 1BRT vault is to a great majority propagated in the pressure vessels, and only a small part is propagated past (some of) the vessels. In total 52 mA reaches the 1BRT vault, which is only marginally more than in the base case. The total corrosion current is, however, increase to 313 mA which is in parity with the benchmark corrosion current. Moreover, in this particular variation case one may suspect that the used electrical resistivity of the vessel's metal of 0.01 ohm.m, which is unusually high, affects the results. Having a lower metal resistivity would probably increase the total corrosion current somewhat.

Increasing the concrete resistivity in variation case A:6 and A:7 leads to decreased corrosion currents, as expected.

The modelled electric fields, zoomed in at the 1BRT vault, are shown for three of the above variation cases in Figure 6-8, as compared to the 2D cylindrical base case. For the different cases one can see the different tendencies for current lines to bend towards, or away from, media of varying resistivity.

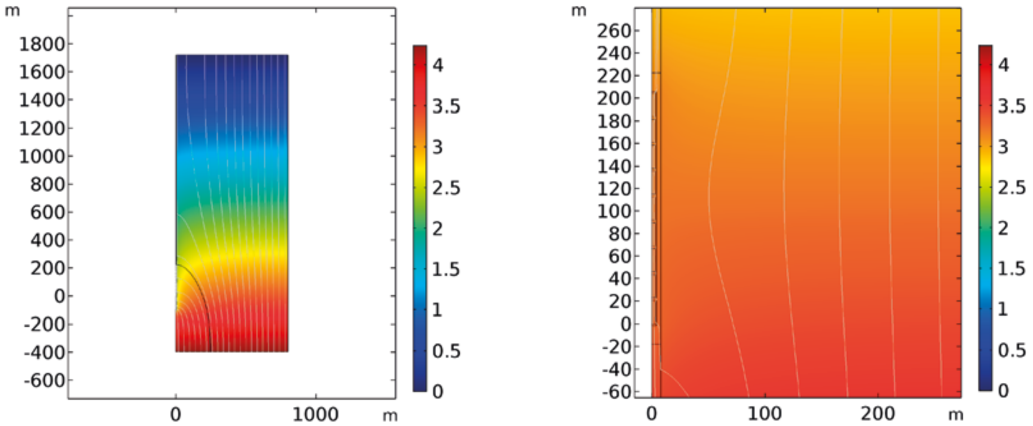

Base case (3.75, 100 ohm.m)

A:2 (170, 100 ohm.m)

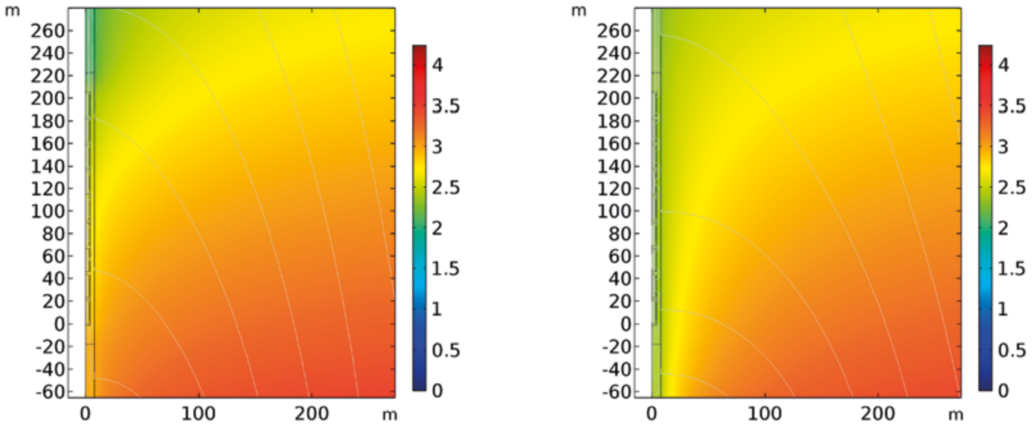

A:4 (100/3.75, 100 ohm.m)

A:5 (3.75, 100 ohm.m)

Figure 6-8. *The electric fields, and current lines, in the base case and variation cases A:2, A:4, and A:5.*

6.5 2D cylindrical variation case B – variable rock resistivity

In this set of variation case the sensitivity to the assumed host rock resistivity is explored. Apart from the values of the rock resistivity and large-scale electrical potential gradient, the variation cases are reproductions of the 2D cylindrical base case (Section 6.3). For a high contrast in the host rock resistivity and the engineered barrier resistivity, the current is expected to be diverted from the host rock through the 1BRT vault and the ramp of lesser resistivity. On the other hand, with a relatively low rock resistivity it is expected that a larger portion of the current remains in the host rock without being diverted through the 1BRT vault and the ramp. In varying the rock resistivity, one may, or may not, correlate the large-scale potential gradient with the rock resistivity. This correlation is discussed in Section 3.2, where a simplified theoretical relation is derived between the parameters, assuming a perfectly hemispherical field, (see Figure 3-12). The hemispherical field assumption implies that the potential gradient scales linearly with the rock resistivity.

In Section 3.2, deviations from the hemispherical field are also discussed. These are partly caused by the local grounding of power lines at the Forsmark nuclear power plant, and partly by the presence of the Baltic Sea shoreline. In Appendix B, it is further investigated to what extent the field around the HVDC current electrode may be skewed as result of the shoreline (although the investigation is preliminary in nature). Deviations from the hemispherical field indicate that the potential gradient should not scale linearly with the rock resistivity, but that the entities are correlated in a more complicated (although probably monotonic) manner.

Due to the complexity of the situation, the set of cases includes both hemispherically correlated and non-correlated variations. The justification is that the different approaches should include the upper corrosion currents at different ends of the rock resistivity spectrum. The estimation of the potential gradient in the correlated cases uses the 2D cylindrical base case rock resistivity and potential gradient as input data.

The results from the variation cases are shown in Table 6-4, both in terms of the current entering the 1BRT vault as well as the total corrosion current leaving the reactor pressure vessels. For comparison the values from the base case are shown. In the correlated high resistivity cases it is assumed that there is no limitation in the power rating of the electrode, and that it can emit a high amount of current into the highly resistivity bedrock, which may not be reasonable.

Results are shown for the correlated variation cases in Figure 6-9, in terms of the electric field and current lines. Going from variation case B:5 to B:8, the contrast between the vault resistivity and rock resistivity increases. This is seen by a larger fraction of current lines bending towards the cylinder axis in variation case B:8, compared to in B:5.

For the correlated case, the total corrosion current in Table 6-4 is at its highest for the highest rock resistivity where it reaches 273 mA. For the uncorrelated case, the corrosion current is at its highest, at 213 mA, for the lowest rock resistivity. Both these currents are lower than the benchmark corrosion current. It should be noted that the higher rock resistivities (50 000 and 100 000 ohm.m) may be valid for the intact rock matrix, especially for rock types of very low porosity. For fractured rock and its block-scale rock resistivity, values at 10 000 ohm.m and lower should apply.

An underlying assumption for the correlated case is that the current output from the electrode is unaffected by the rock resistivity. As the correlated case assumes a hemispherical field, there is also the assumption of a homogenous medium. If emitting a large current into very resistive rock, one would need an unreasonably high potential at the electrode. If one would instead assume a constant effect output (or power rating) at the electrode, the current entering the 1BRT vault would be significantly lower for high rock resistivities than shown in Table 6-4.

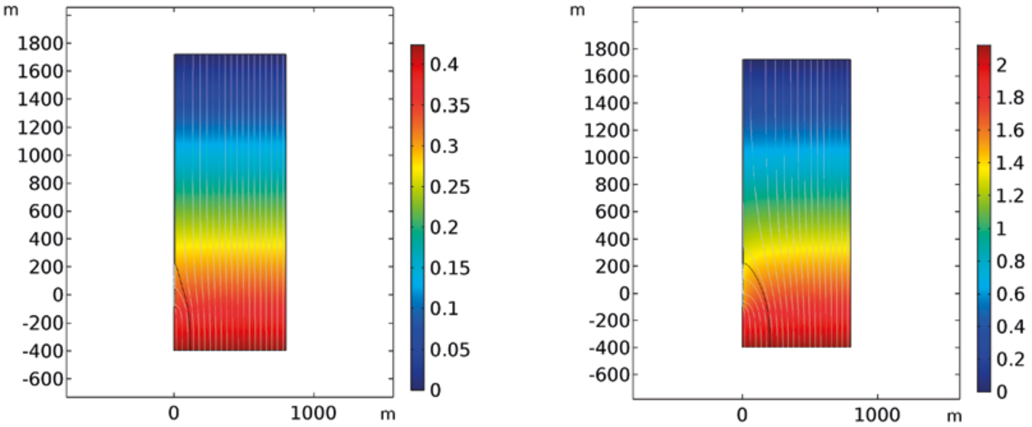

B:5 (1,000 ohm.m, 0.2 mV/m)

B:6 (5,000 ohm.m, 1 mV/m)

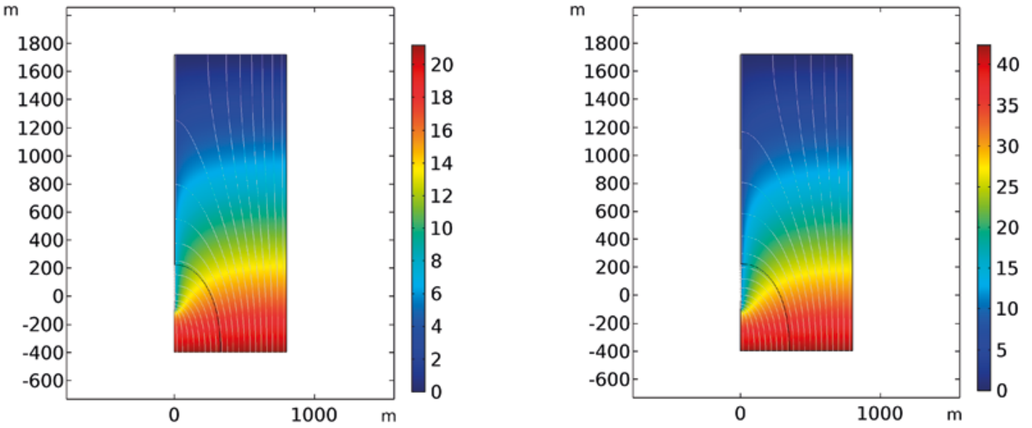

B:7 (5,000 ohm.m, 10 mV/m)

B:8 (100,000 ohm.m, 20 mV/m)

Figure 6-9. *Electric potential (V) and grey current lines in 2D axisymmetric plane for various rock resistivities assuming a potential gradient proportional to the resistivity, based on a hemispherical potential field. The black current lines indicate the influence radii. The 1BRT vault is located on the left-hand side of the 2D domain.*

Table 6-4. Current entering the 1BRT vault and the total corrosion current for different host rock resistivities of potential gradients. Upper panel shown non-correlated case and lower panel correlated case.

Calculation case	Rock resistivity (ohm.m)	Potential gradient (mV/m)	Current entering 1BRT (mA)	Total corrosion current (mA)
Variation B:1	1 000	2	87	213
Variation B:2	5 000	2	61	135
Base case	10 000	2	49	104
Variation B:3	50 000	2	22	45
Variation B:4	100 000	2	13	27
Variation B:5	1 000	0.2	8.7	21
Variation B:6	5 000	1	31	68
Variation B:7	50 000	10	109	225
Variation B:8	100 000	20	133	273

It is noteworthy that the influence radius is affected by the contrast of the assumed rock resistivity and the resistivity of the engineered repository parts, but not affected by the magnitude of the potential gradient (cf. Figure 6-9).

6.6 2D cylindrical variation case C – conductive zone in the rock volume

In this set of variation cases a vertical fracture zone of enhanced electrical conductivity transects the host rock and connects to the far end of the access tunnel (cf. Figure 6-6). The zone extends in the radial direction throughout the model domain. The conductive zone is expected to direct current towards the underground openings; increasing the influence radius. Accordingly, a larger portion of the total current in the system should be directed through the 1BRT vault and further on through the ramp, as compared to in the 2D cylindrical base case. The sensitivity to different zone properties (e.g. zone width and fracture intensity) is evaluated by using a range of electrical resistivities, while keeping the zone width constant at 10 m (cf. Appendix A). The zone resistivity ρ_{zone} (ohm.m) is set to 10, 100, and 1 000 ohm.m in variation cases C:1, C:2, and C:3, respectively (cf. Table 3-4). Except from the inclusion of the zone, the variation cases are reproductions of the 2D cylindrical base case.

The expected effect of current being directed through the zone and towards the underground openings is confirmed by the model results, as shown in Figure 6-10 for different zone resistivities. The lower the zone resistivity is, the larger the influence radius becomes. Results from the different variation cases are shown in Table 6-5, both in terms of the influence radius, current entering the 1BRT vault, as well as the total corrosion current leaving the reactor pressure vessels. For comparison the values from the base case, involving no zone, are shown.

Even for variation case C:1, with an extremely low zone resistivity, the influence area (based on the influence radius) is only about doubled compared to the base case with no zone. This result in an, about, doubling of the current entering the 1BRT vault. However, in the C:1 case virtually all current lines within the influence radius enters the 1BRT vault through its edge (at the access tunnel). Thereby, all pressure vessels are influenced by these current lines, and the total corrosion current is increased to 267 mA. This is a factor of 2.5 more than in the base case. For a realistic zone (in variation case C:3), the total corrosion current is 55 mA, which is an increase by 12 % compared to in the base case.

In all variation cases C:1 to C:3, the zone is in direct contact with the vault. In the process of analysing the impact of deformation zones, the location of the zone was adjusted to either contact the vault, or to be separated from it by 10 m of host rock. This was done for the isolated vault case of Section 6.2, where one zone was assumed on either side of the vault. Separating the zones from the vault gave rise to a significant reduction in the influence radius, as compared to the case of direct contacting the zones to the vault. Based on this observation, it was decided on pessimistic grounds to only model zones contacting the access tunnel in variation case C, even though this may be a less plausible case.

In conclusion, plausible zones have a very limited impact on the current that can be drawn towards the repository, and can be ignored. Accordingly, in no other calculation case the impact of zones has been incorporated. Intense or extreme zones may have a minor impact on the Earth current induced corrosion current, should they contact the vault or nearby underground openings. This is, however, not the case in SFR.

Table 6-5. Current entering the 1BRT vault and the total corrosion current for different zone resistivities.

Calculation case	Zone resistivity (ohm.m)	Influence radius (m)	Current entering 1BRT (mA)	Total corrosion current (mA)
Variation C:1	10	280	95	267
Variation C:2	100	273	77	208
Variation C:3	1 000	256	55	127
Base case	10 000	247	49	104

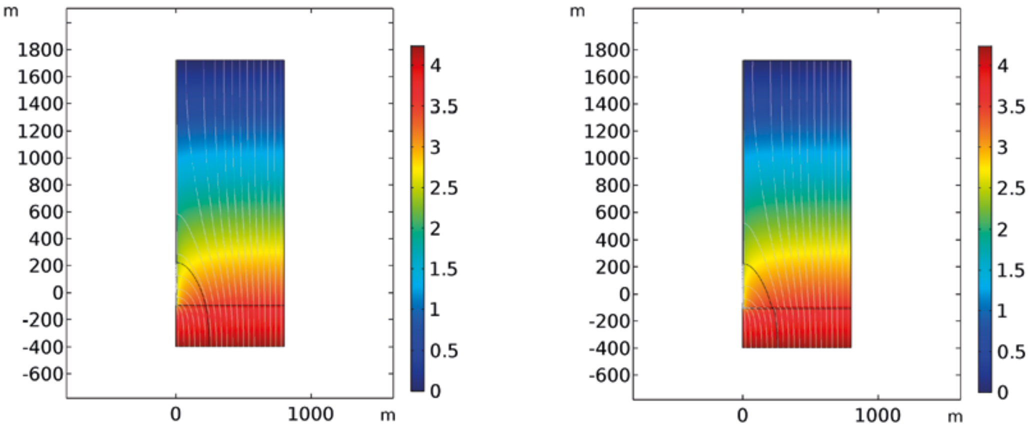

Base case - no zone, ρ_{zone} = 10,000 ohm.m

C:3 - realistic zone, ρ_{zone} = 1,000 ohm.m

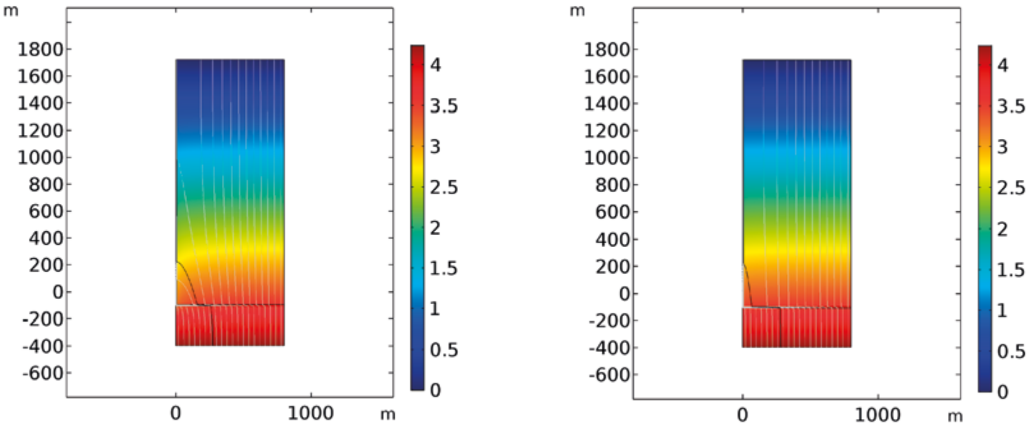

C:2 - intense zone, ρ_{zone} = 100 ohm.m

C:1 - extreme zone, ρ_{zone} = 10 ohm.m

Figure 6-10. *Electric potential (V) and grey current lines in 2D axisymmetric plane for various zone resistivities (the zone is indicated by black horizontal lines at about –100 m). The black current line indicates the influence radius. The 1BRT vault is on the left-hand side of the 2D domain.*

6.7 2D cylindrical variation case D – vessel segmentation

6.7.1 Background

In the 2D cylindrical base case, where no polarisation resistance is accounted for, it is shown that current lines that exit one reactor pressure vessel typically enter the downstream vessel (cf. Figure 6-7). Imagine slicing each vessel (normal to the axis) into, say, 100 closely stacked segments that are separated by thin slices of concrete, which prohibits metallic contact. If not accounting for polarisation resistance, the current that enters this stack of segments would need to be multiplied by (roughly) 100 to achieve the corrosion current.

Such an increase in the corrosion current may not be "affordable" from the perspective of a long-term safety assessment. Accordingly, when analysing the effect of extensive segmentation, one needs more realistic modelling that incorporates polarisation. This is done by incorporating activation polarisation, while still pessimistically neglecting concentration polarisation (cf. Section 2.2.2).

6.7.2 Used input data and model setup

As described in Section 6.1.2, the model calculates the overpotential at each tetrahedron element facing at the pressure vessel surface. This overpotential is used to calculate the anodic current density by the Butler-Volmer approach. The surface integral of the anodic current density is thereafter calculated to obtain the anodic current. This anodic current is subsequently divided by the surface area of the vessel, to achieve an averaged anodic current density. In doing this, three input data relating to the activation polarisation are required according to the theory in Section 2.2.5. These are:

- The anodic current density at zero overpotential.
- The anodic Tafel slope for the oxidation reaction Fe → $Fe^{2+} + 2e^-$.
- The cathodic Tafel slope for the reduction reaction $2e^- + 2H_2O \rightarrow 2OH^- + H_2$.

The used data in variation cases D:1 to D:6 are shown in Table 6-6 and justified below.

Table 6-6. Input data in variation cases of the kinetics limitation approach.

Variation case	Anodic current density at zero overpotential (A/m^2)	Anodic Tafel slope (mV/dec)	Cathodic Tafel slope (mV/dec)	Number of segments
D:1	4.3×10^{-5}	59	–59	9
D:2	4.3×10^{-5}	118	–118	9
D:3	4.3×10^{-5}	59	–59	18
D:4	4.3×10^{-5}	59	–59	27
D:5	4.3×10^{-5}	118	–118	18
D:6	4.3×10^{-5}	118	–118	27

The anodic current density at zero overpotential equals 4.3×10^{-5} A/m^2, as derived in Section 3.9.2. The anodic Tafel slope depends on the number of electrons involved in the reaction and the symmetry factor α (cf. Equation 2-37). With a reaction involving two electrons, the anodic Tafel constant becomes (at standard conditions) $29/\alpha$ mV. The anaerobic corrosion of carbon steel was investigated by Smart et al. (2001) with resulting anodic Tafel slopes of about 60 mV/dec, depending on the method (e.g. Smart et al. 2001, Table 4). This suggests a symmetry factor close to 0.5. In this present study the best estimate anodic slope of 59 mV/dec is used (deviations from standard conditions are disregarded).

The cathodic Tafel slope was in the same report measured to be about –50 mV/dec (Smart et al. 2001, Table 4), although it is suggested that the theoretical Tafel slope should be about 118 mV/dec. This is based on the suggested rate limiting reaction:

- $H_2O + e^- \rightarrow H(0)_{abs} + OH^-$,

where $H(0)_{abs}$ signifies a proton sorbed on the metal surface. As seen in Figure 2-12, a smaller Tafel slope gives a lower net current density. In this study, the cathodic Tafel slope of –59 mV/dec is used as best estimate value.

To test the model's sensitivity to the used Tafel slopes, in variation case D:2 the anodic and cathodic Tafel slopes are set to ± 118 mV/dec. In the modelling, the Tafel slopes of ± 200 mV/dec have also been used. Such high slopes would suggest concentration polarisation and therefore, we chose not to present the results with the following exception. As expected, the modelled anodic current density is decreased when increasing the Tafel slopes from ± 59 to ± 118 mV/dec, and further decreased when using Tafel slopes of ± 200 mV/dec.

Due to the need for extensive computational power (and very fine meshing) we only managed to solve a limited system when $\beta_a + \beta_c \neq 0$ (cf. Equations 2-32 and 2-33). When solving the entire system, as reported below, $\beta_a + \beta_c = 0$.

6.7.3 Variation cases

Variation cases D:1 and D:2 are reproductions of the 2D cylindrical base case, with the exception of how current flows over the boundary between the concrete embedment and pressure vessels, and how the Earth current induced corrosion current is calculated. Variation case D:1 uses Tafel slopes of ± 59 mV/dec while D:2 uses slopes of ± 118 mV/dec.

Cases D:3 to D:6 are reproductions of case D:1 or D:2 (depending on the Tafel slope) in all aspects except that each vessel is segmented into two parts (D:3 and D:5) or three parts (D:4 and D:6) reducing the length of each segment along the direction of the main potential gradient. Apart from the segmentation, the repository layout geometries are identical to the 2D cylindrical base case. This is only a mild segmentation, as compared to an extensive segmentation of a vessel into hundreds of pieces. The aim is to show a monotonic decrease in total Earth current induced corrosion current with decreasing length of the segments along the main potential gradient. If this aim is fulfilled, and if coupled with an understanding that the monotonic response will also be valid for a larger degree of segmentation, it is judged that no further modelling is required. The Tafel slopes and number of segments are shown in Table 6-6 for each variation case.

6.7.4 Results

Figure 6-11 shows the different potential profiles in the system for variation case D:1. The red line is the electric potential at the interface between the 1BRT vault and the host rock. The blue lines represent potentials in the concrete embedment for elements facing the nine reactor pressure vessels. The peaks and dips in the blue lines, at the ends of the pressure vessels, correspond to the cross-section areas of the vessels. The green lines represent the calculated uniform potentials at the vessel surfaces. The anodic or cathodic overpotentials can be calculated from the differences between the potentials shown by the blue and green lines. The largest overpotentials are found at the edges of the vessels, where they amount to about 10 to 20 mV, depending on the vessel. For comparison, an anodic overpotential of 20 mV would result in an anodic current density of about 9.6×10^{-5} A/m^2, according to the diagram of Figure 6-2. This would about double the corrosion rate for that particular surface, compared to the corrosion rate at zero overpotential. As can be deduced from Figure 6-11, much of the anodic side of the vessel will be subjected to much lower overpotentials than 20 mV, and half of the vessel will be on the cathodic side where corrosion is suppressed.

The anodic and cathodic current densities of different parts of the vessels' surfaces are shown in Figure 2-12 for variation case D:1. In the figure the length of the arrows represents the magnitude of the current density. White arrows represent anodic current densities while red arrows represent cathodic current densities. Note that at the same patch of the vessel surface, both anodic and cathodic current densities occur, but at different magnitudes (if there is a nonzero overpotential).

By taking the surface integral of the anodic current density, the anodic current of each vessel can be calculated. In the model, each reactor pressure vessel is modelled as a solid body, and as such only the outer surface is subjected to corrosion. In the real case, both the inner and outer areas of the pressure vessel count as corrosion surfaces. As such, the total corrosion surface of the nine actual vessels was estimated to be 7 240 m^2 in SR-PSU (cf. Table 3-3). The total corrosion area of the nine modelled vessels is only 4 213 m^2. When comparing the results with the 2D cylindrical base case, comparisons are better made in terms of corrosion current densities. Moreover, it should be noted that the anodic current density is 4.3×10^{-5} A/m^2 at zero overpotential. To obtain the (Earth current) induced corrosion current density, this value must be subtracted from the averaged anodic current density. This is done in Table 6-7, for variation case D:1 and D:2. The corresponding induced corrosion current densities are shown for the 2D cylindrical base case, under the assumption that the surface area of a vessel in the base case is 7 240 m^2 divided by nine.

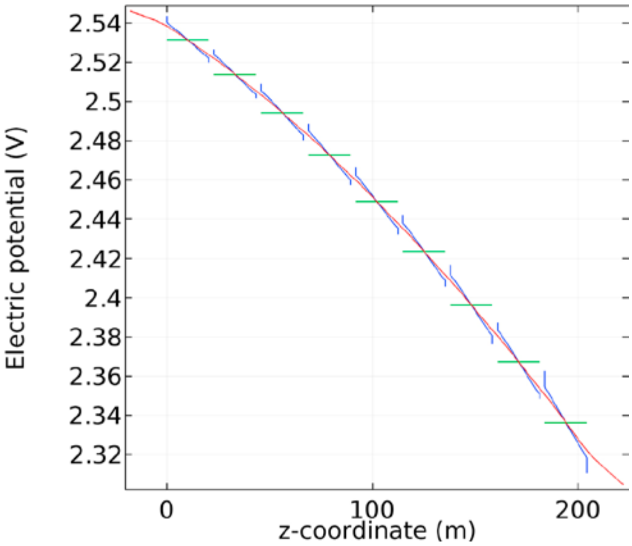

Figure 6-11. *Potentials for variation case D:1. Red line: potentials at the rock/vault interface. Blue lines: potentials at the concrete/vessel interface, in the concrete. Green lines: uniform potentials of vessels' surfaces.*

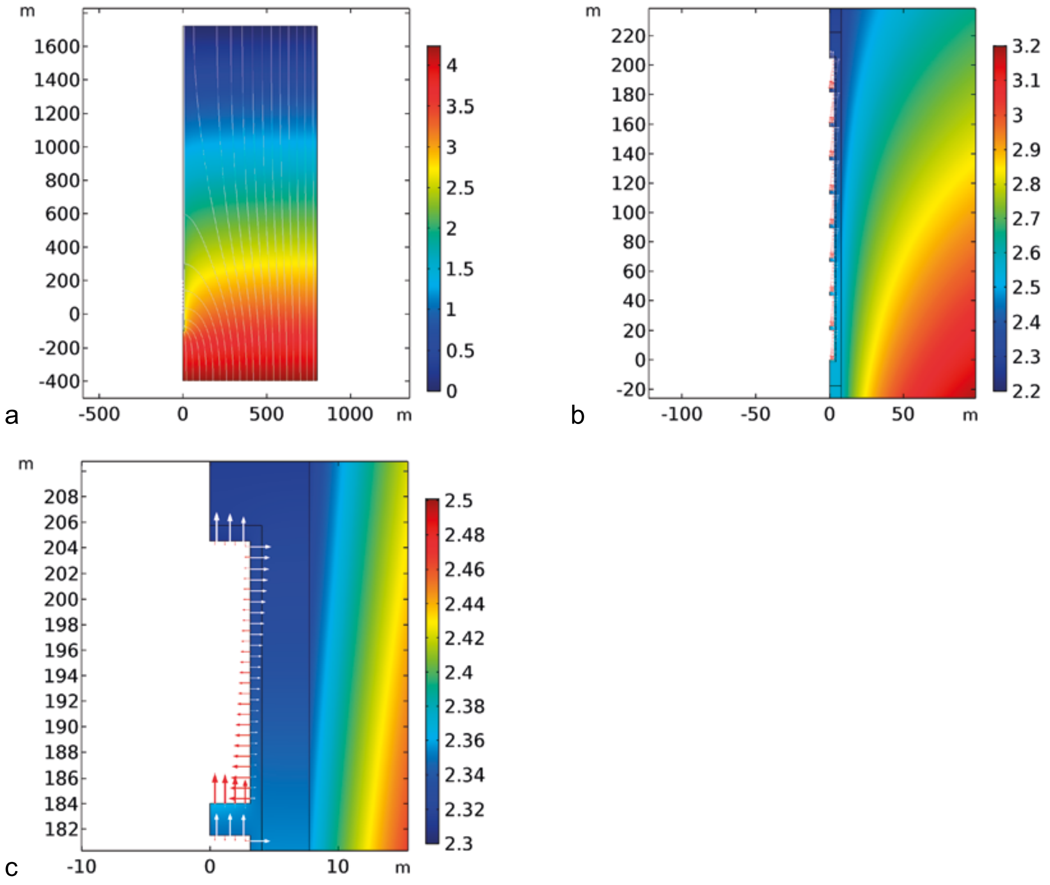

Figure 6-12. *a) Electric potential (V) and current lines in 2D axisymmetric plane. b) Zoom-in on the 1BRT vault. White "holes" in the model represent pressure vessels. White arrows represent the anodic current density and red arrows the cathodic current density. c) Further zoom-in on a pressure vessel, showing the varying magnitude of the current densities at different parts of the vessel surface.*

Table 6-7. Induced corrosion current densities of reactor pressure vessels 1 to 9, in variation case D:1 and D:2, as well as the corresponding value for the 2D cylindrical base case.

Component	2D base case (μA/m²)	Variation case D:1 (μA/m²)	Variation case D:2 (μA/m²)
Vessel 1 (at access tunnel)	9.7	1.3	0.23
Vessel 2	11	1.6	0.28
Vessel 3	12	2.1	0.35
Vessel 4	14	2.5	0.42
Vessel 5 (middle)	15	3.0	0.49
Vessel 6	16	3.4	0.56
Vessel 7	16	4.0	0.64
Vessel 8	17	4.3	0.71
Vessel 9 (at ramp)	19	5.7	0.85
Total corrosion current density	14	3.1	0.50

Data in Table 6-7 indicate that by introducing kinetic limitations, the Earth current induced corrosion rate can be reduced to about a quarter of the value in the 2D cylindrical base case, for the average vessel. This is for the case of using Tafel slopes of ± 59 mV/m. If using Tafel slopes of ± 118 mV/m, the effect is even more pronounced.

In variation case D:3 and D:4, each vessel is segmented into two and three segments respectively. This should create smaller overpotentials at each segment, which should reduce the averaged anodic current density. On the other hand, this would create more corroding bodies and, hence, larger corroding surface. Table 6-8 shows the total corrosion surface of the segments, the induced corrosion current density (as averaged over all segment's surfaces), and the total induced corrosion current for the segments. The latter data is the product of the two former data in the same row.

Table 6-8. Results for segmented vessels in variation case D:3 and D:4, in comparison with results for non-segmented vessels.

Case	Segments per vessel	Tafel slopes (mV/dec)	Total corrosion surface* (m²)	Induced corrosion current density (μA/m²)	Total induced corrosion current (mA)
D:1	1	± 59	4212	3.1	13.1
D:3	2	± 59	4774	0.83	4.0
D:4	3	± 59	5335	0.48	2.6
D:2	1	± 118	4212	0.50	2.1
D:5	2	± 118	4774	0.15	0.73
D:6	3	± 118	5335	0.09	0.48

* The corrosion surface is calculated assuming solid cylindrical segments, $A = 2\pi r(L + r)$.

As can be seen in Table 6-8, when increasing the number of segments per vessel, the total (Earth current) induced corrosion current for all segments in 1BRT decreases. This is valid both for Tafel slopes of ± 59 and ± 118 mV/m.

6.7.5 Concluions from using the kinetics limitation approach

By introducing kinetics limitation in variation case D:1 and D:2, the overall corrosion current is reduced compared to in the 2D cylindrical base case, which ignores activation polarisation. The reduction becomes more significant the larger the Tafel slopes are. This is understandable as high Tafel slopes indicate large polarisation effects. The overall takeaway from the study of intact vessels is that the charge-balance approach overestimates the corrosion current by a factor of at least four (base on variation case D:1), if having a large-scale external field of 2 mV/m (or less). As such, corrosion currents from the change-balance approach in this chapter and in Chapter 7 may be reduced by a factor of four, for present day external electric field. If having larger field strengths, this may increase the overpotentials at the pressure vessel surfaces to the point where the results from the kinetics limitation approach edge closer to the results from the change-balance approach.

The main objective of this section is to study the impact on the Earth current induced corrosion rate from a presumptive segmentation of the reactor pressure vessels. The results of Table 6-8 show a beneficial impact from the segmentation. Basically, the shorted the segments become the less the Earth current induced corrosion will be. To extrapolate these results to more extensive segmentation, one must take process understanding into consideration.

By cutting a vessel in half, this roughly cuts the potential drop over each segment in half. This in turn reduces the overpotentials by a factor of about two. As can be seen from Figure 6-2, there is not a linear, but exponential, relation between the anodic current density and overpotential. As such, reducing a rather high overpotential (say 30 mV) by a factor of two would reduce the anodic current density by a factor larger than two. In such a case, even if the segmentation leads to a doubling of the corrosion surface, the total Earth current induced corrosion current would decrease (under the prerequisite that all of the corrosion surface is subjected to the same high overpotential). The dotted purple line in Figure 6-13 shows the slope where a doubling of the anodic overpotential gives a doubling of the anodic current density. At small anodic overpotentials, in the range 0 to about 10 mV, the exponential curve almost coincides with the dotted line. At extensive segmentation, the anodic part of the segment will likely have overpotentials in this low range. If so, cutting the segment in half will cut the anodic corrosion current density in (about) half. If this segmentation leads to a doubling of the corrosion surface, the Earth current induced corrosion current will remain at about the same value.

The larger the large-scale electric field is, the larger is the chance that overpotentials at parts of the vessels' surfaces (or segments' surfaces) is larger than 10 mV. Therefore, segmentation should have the largest effect at high large-scale field strengths. This is shown in Figure 6-14. Here the large-scale potential gradient has been swept over 0, 0.5, 1, 1.5 and 2 mV/m for calculation case D:1, D:3 and D:4. As can be seen, the decrease in Earth current induced corrosion current density is larger at higher field strengths, when going from 9 to 18, and further to 27 segments.

If should be noted that for most geometries, cutting an object in half does not double the corrosion surface. Furthermore, if increasing the corrosion surface by segmentation, the general corrosion, i.e. the one taking place in the absence of overpotentials, will occur at a higher rate. With this in mind, one can conclude that the influence of Earth current induced corrosion on the total corrosion rate will diminish when segmenting the reactor pressure vessels.

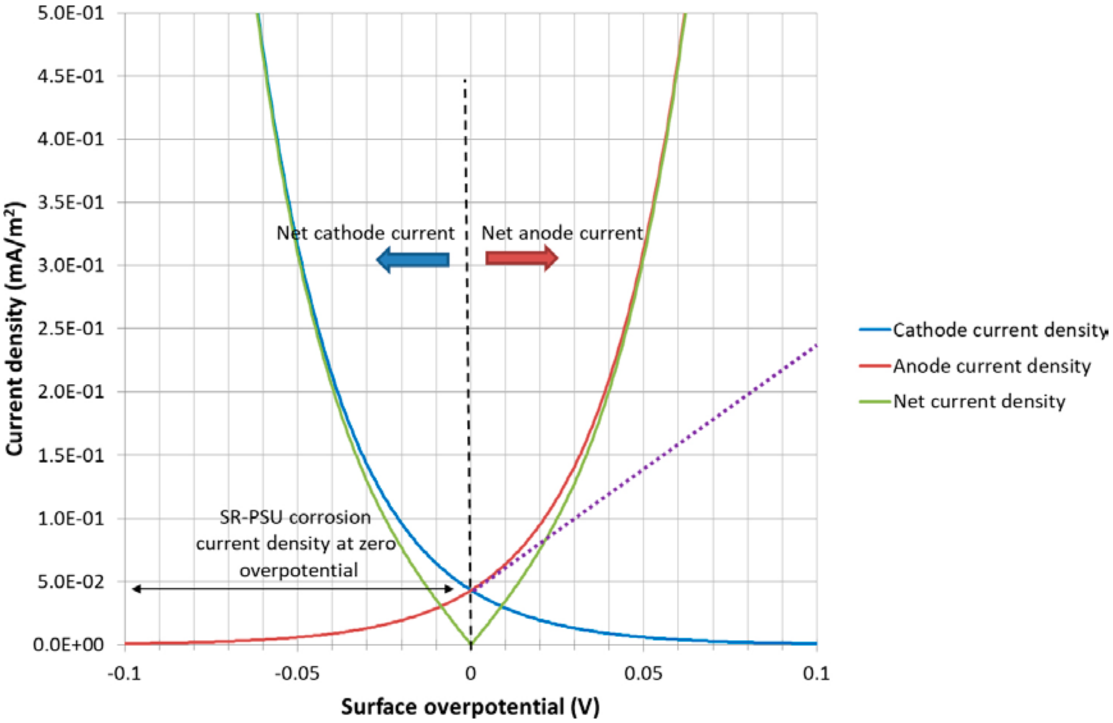

Figure 6-13. *Anode and cathode current density vs. surface overpotential, using the SR-PSU corrosion current density at zero overpotential and Tafel slopes of 59 mV/dec. The dotted purple line marks the slope at which a doubling of the anodic overpotential leads to a doubling of the anodic current density.*

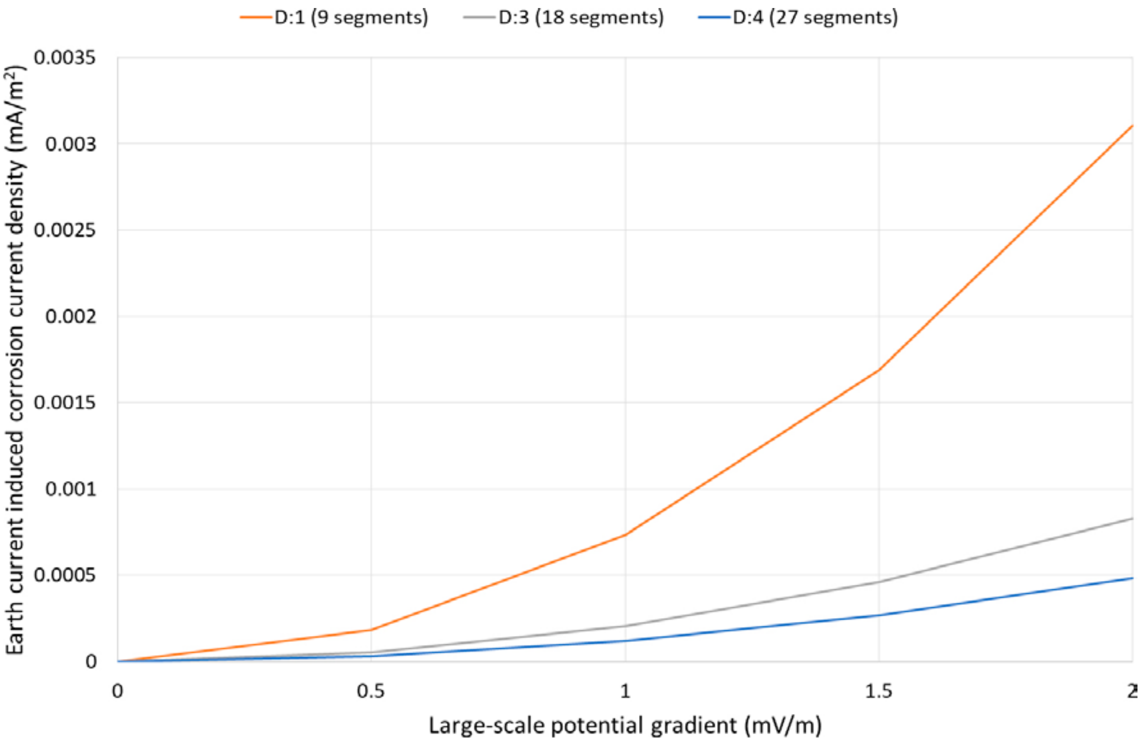

Figure 6-14. *The Earth current induced corrosion current density for calculation case D:1, D:3 and D:4, at different large-scale potential gradients.*

7 3D representation

7.1 Reproducing 2D cylindrical symmetry model in full 3D

In this section, the model of the isolated vault that was set up in 2D in Section 6.2 is reproduced in a full 3D COMSOL Multiphysics model. As such, the charge-balance approach is used and no polarisation resistance is accounted for. This is mainly done to assure that the 3D implementation is adequate. There are therefore no sensitivity calculations done with this model. The electric field and current lines that result from the 3D implementation are illustrated in Figure 7-1. The current leaving each vessel is calculated by surface integration, as described in Section 6.1.1, and the total corrosion current is the sum of each vessel's corrosion current.

In this case, the total corrosion current of the nine vessels becomes:

- 17.5 mA

This can be compared with the corresponding result from Section 6.2, where the total corrosion current was 17.2 mA. Thereby there is a deviation between the two cases of about 1.6 %, which is contributed to numerical issues when going from a 2D to a 3D model. A very similar deviation in the corrosion current is found for each reactor pressure vessel (cf. Table 6-2). In both the 3D and the 2D simulations, the influence radius is ~ 80 m. As comparable results are achieved, these two models are deemed to be sufficiently well implemented for the purpose of this report.

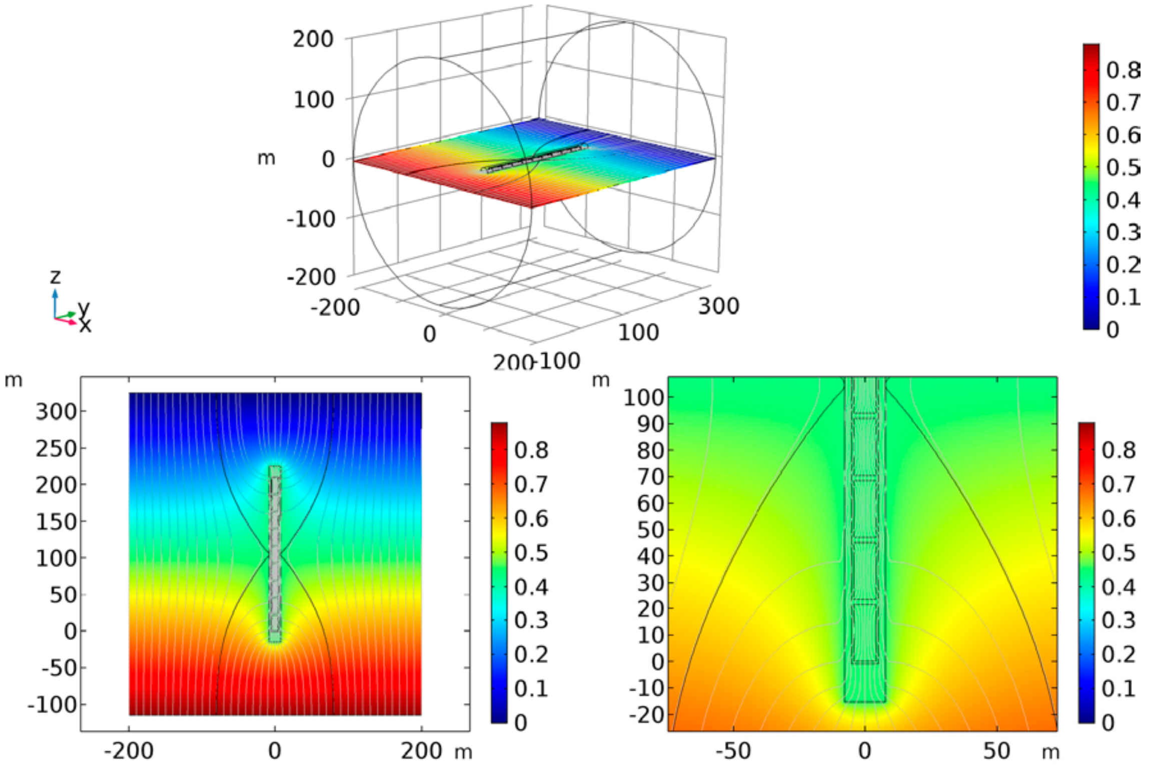

Figure 7-1. *Electric potential (V) and grey current lines for the 3D reproduction. Results are shown in a slice of the model domain. The black current lines indicate an influence radius of ~ 80 m. The 1BRT vault is located at the centre of the cylinder in the 3D representation. A rock resistivity of 10 000 ohm.m and a potential gradient of 2 mV/m are assumed. The bottom row of figures shows the result at 2 different zoom levels.*

7.2 3D repository base case

In the previous 2D cylindrical symmetry cases, and in the 3D implementation of calculation case 2a, the main focus has been on the 1BRT vault and the components within the vault (i.e. gravel backfill, concrete embedment, and steel pressure vessels) and the surrounding rock (with and without heterogeneity in terms of fracture zones). In the SFR repository, several other vaults, access tunnels, ramps, etc. are present. These structures provide parallel paths for the electric current that may lower the contacting current reaching the 1BRT vault and pressure vessels. To evaluate the influence of these structures, a 3D representation of SFR 3 was implemented in COMSOL Multiphysics.

7.2.1 Model setup

The SFR 3 vaults and access tunnels

Dimensions of the SFR 3 structures are based on the design layout version L2 (SKB 2014d), although some simplifications have been made that mainly relate to the access tunnels. The imported layout is shown in Figure 7-2 (left). This can be compared with the more detailed illustration of the vaults of SFR 3 in Figure 7-2 (right), which is a rotated excerpt of Figure 3-3. Note that the NBT tunnel is not directly connected to SFR 3 but is excavated above the vaults.

Except for the 1BRT vault, the extension will feature four BLA vaults and one BMA vault. The dimensions of these vaults, as incorporated in the 3D COMSOL model, can be found in SKB (2014d). When estimating the other vaults characteristic resistivities, very pessimistic assumptions have been made to limit the amount of current that they may carry. This is especially true for the four BLA vaults, which in our model are assumed to be completely backfilled with gravel with a resistivity of 3.75 ohm.m. In reality, the vaults will contain stacks of metallic containers (cf. Figure 7-3) making their total resistances much lower, perhaps even orders of magnitude lower, than what has been assumed. This implies that in reality, more of the total current is diverted through the BLA vaults, thereby reducing the current through the 1BRT vault.

The 2BMA vault will have a large concrete structure that will contain the waste. This concrete structure will be surrounded by macadam backfill, and according to SKB (2014d, Figure 5-2) the backfill should cover about half of the cross-section area of the vault. Despite this, it is assumed that the entire vault is backfilled with concrete of the resistivity 100 ohm.m. With this assumption, the vault's resistance is overestimated by at least one order of magnitude.

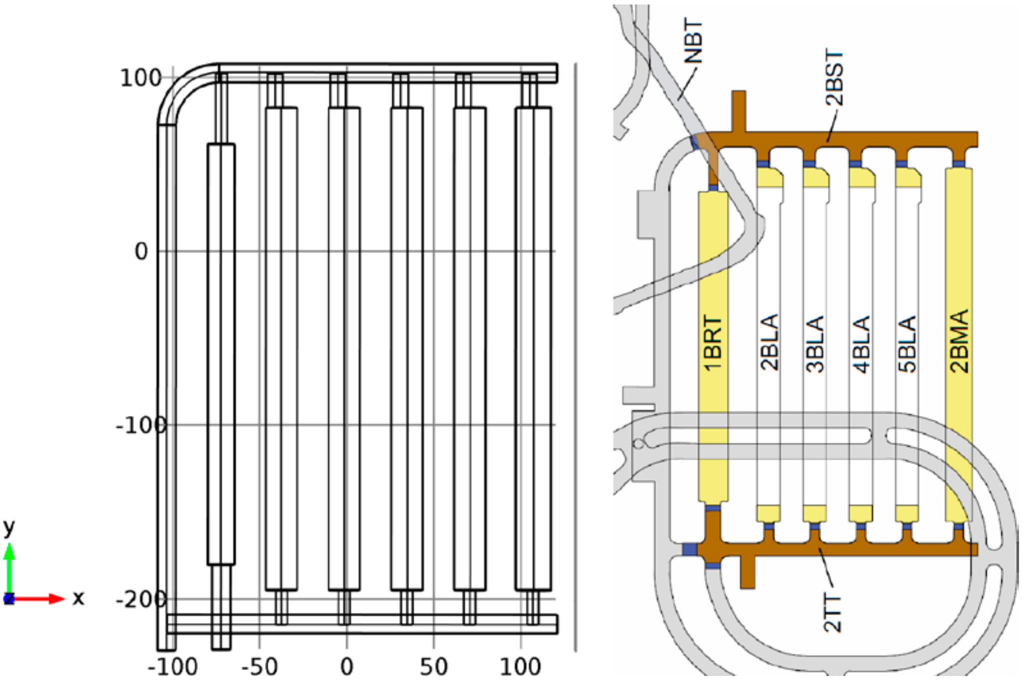

Figure 7-2. *Left: Imported SFR 3 layout version L2 as implemented in the 3D COMSOL model. Right: Excerpt of illustration of the extended SFR from SKB (2014d, Figure 11-1).*

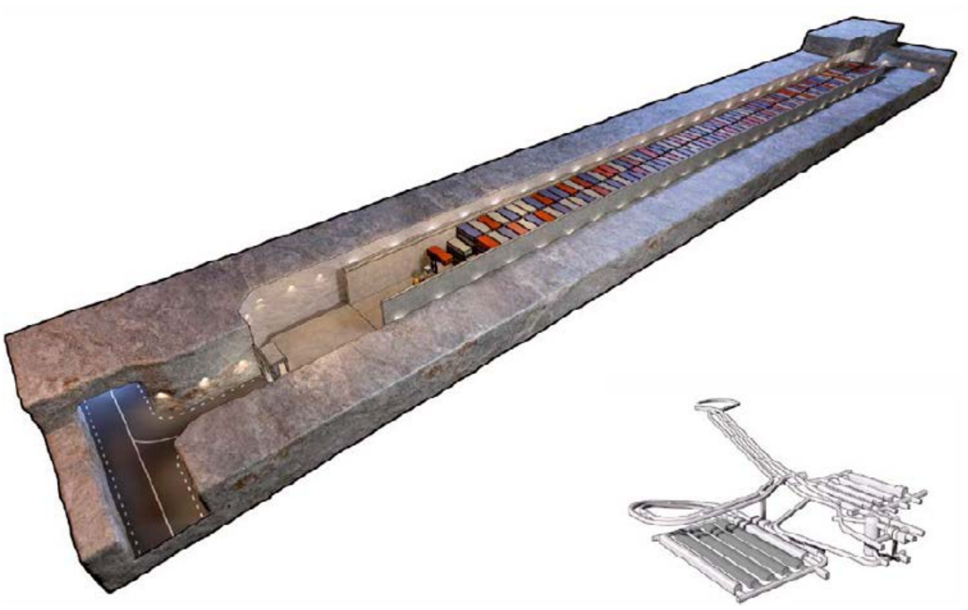

Figure 7-3. Illustration of metallic containers stacked within the 2–5BLA vaults. The vault will not be backfilled at repository closure. Reproduced from SKB (2014d, Figure 9-1).

It is assumed that access tunnels are backfilled with macadam or bentonite of the resistivity 3.75 ohm.m. Furthermore, mechanical plugs of concrete (see blue plugs in Figure 7-2, right) are disregarded. These plugs are more resistive than the macadam backfill and would somewhat decrease the current going through the assembly of vaults, which is pessimistic for the 1BMA vault but (very mildly) non-conservative for the parallel structures. All together the handling of parallel structures is judged to be clearly pessimistic. Even more pessimistic handling of the parallel structures is studied in Section 7.4.

The 1BRT vault

The outer dimensions of the 1BRT vault are provided by the imported design layout version L2. Centred within the vault, the concrete embedment is assumed to be a cuboid of dimensions 8.1 × 8.1 × 207.0 m. This embedment is placed on a concrete floor, with dimensions provided by the design layout version L2. Centred within this cuboid are the reactor pressure vessels, each having the same dimensions as in the 2D cylindrical base case. The vault, surrounding the concrete embedment, is filled with macadam backfill. The following resistivities are used for the different materials within 1BRT:

- Backfill: 3.75 ohm.m
- Concrete: 100 ohm.m
- Metal of pressure vessels: 0.01 ohm.m
- Polarisation resistance at pressure vessel surface: 0 ohm.m^2

The ramp and island

As is shown in Figure 3-3, three interconnected access ramps connect the SFR vaults and silo to ground surface. These ramps are not straight and have different lengths and cross section areas. We have refrained from incorporating their actual geometries in the 3D model, and have instead incorporated a single straight cuboid ramp structure from SFR 3 to ground surface, similarly as in Section 6.3. The same ramp length of 1 500 m is used as in Chapter 6 but in the 3D modelling cross-sectional area does not need to be exactly the same as that of the 1BRT vault. Hence a ramp cross-sectional area of 214 m^2 is assumed, which is the combined cross section areas of the three individual access ramps 1RTT (102 m^2, taken from Carlsson et al. 2014, Table 3-1), BT (48 m^2, estimated from layout summary drawing[9]), and 1DT (64 m^2, estimated from layout summary drawing[9]). The position of the ramp is pessimistically adjusted so that it is aligned with the 1BRT vault in the y-direction of Figure 7-4. However, the ramp has a leaning in the z-direction so that it connects ground surface with the SFR 3 vaults at 120 m depth. The ramp is assumed to be entirely backfilled with macadam and bentonite of the resistivity 3.75 ohm.m. Concrete plugs are pessimistically neglected. The entrance of the ramp is placed on an island of arbitrary shape (a rectangular base of 200 m). This island has the same block-scale rock resistivity as the remaining of the host rock (i.e. 10000 ohm.m). It is surrounded by the Baltic Sea, which is assumed to have uniform depth of 10 m and a resistivity of 1.5 ohm.m (cf. Table 3-5. The impact of the arbitrary shaped island is studied in Section 7.5.

Handling of SFR 1

The vaults and silo of SFR 1 are not included in the model, which is justified as follows. In Chapter 6 it was shown that the influence radius around a conductive structure in the host rock (such as a repository) increases with increasing conductance of the structure. Based on this, one could argue that if also including the SFR 1 part, the influence radius would have increased (especially if also accounting for the physical extension of the SFR 1 part). This should have resulted in an increased current running through the entire SFR facility. If for the sake of simplicity arguing that SFR 1 would have exactly the same properties and layout as SFR 3, the combined effect of the two parts would probably not double the current running through the system. The reason is that the assumed ramp has already incorporated the cross-section areas of all three access ramps. This means that in the model, one may only distribute the current conducting capacity of the ramp on the vaults and access tunnels of SFR 3. Even if increasing the current running through the entire SFR facility, this would mean that there are more vaults to distribute this current on. Based on this, it is judged that disregarding SFR 1 in the model only provokes an insignificant error (at least in the view of the purpose or this modelling).

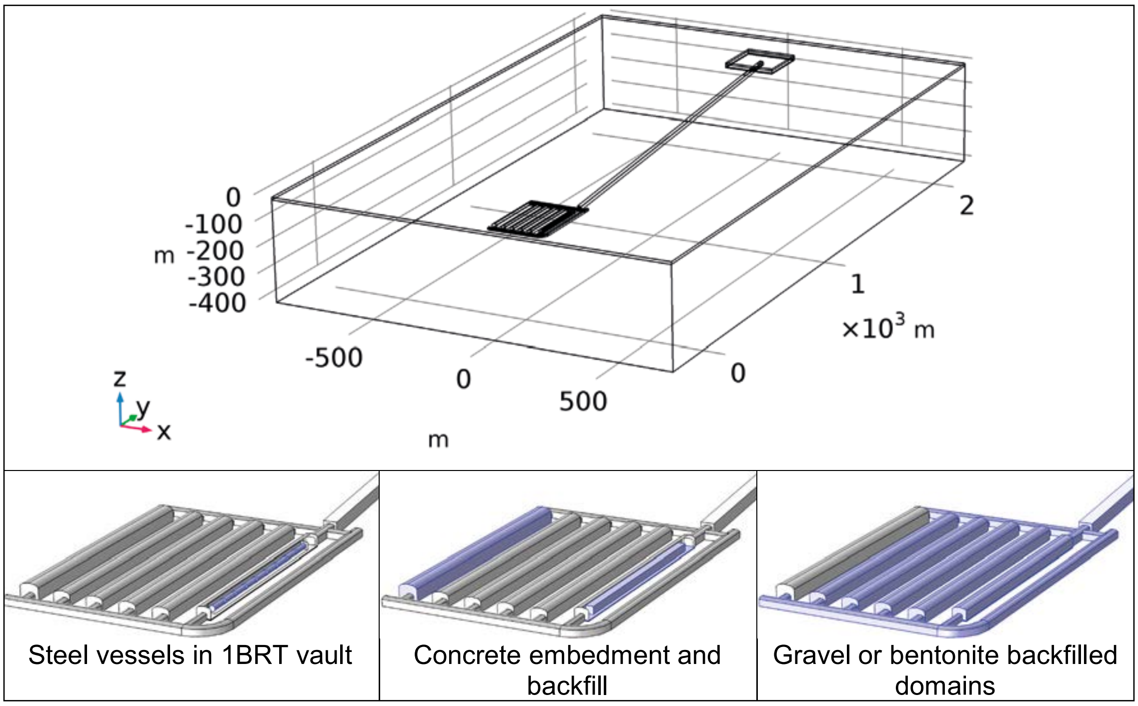

Steel vessels in 1BRT vault

Concrete embedment and backfill

Gravel or bentonite backfilled domains

***Figure 7-4.** COMSOL 3D model layout implementation. The bottom row indicates the different materials (steel vessels, concrete embedment and floor in 1BRT, assumed concrete backfill in BMA and assumed macadam or bentonite backfill in the remaining tunnels and ramp).*

---

[9] SFR 1 i Forsmark, Layoutsammanställning (Forsgren and Aronsson, Stockholm 1987.09.10).

Meshing, host rock and potential gradient

The entire 3D COMSOL model domain is illustrated in Figure 7-4 for the 3D repository base case. The modelled mesh contains a little more than 6.3 million tetrahedral elements and is difficult to illustrate graphically in a meaningful way. The mesh covering part of the SFR 3 domains is illustrated in Figure 7-5. The SFR 3 domain alone is comprised of 1.4 million elements (of which 1.1 million elements in the 1BRT vault).

In the 3D repository base case calculation, a potential gradient is imposed over the modelled domain in the longitudinal direction of the 1BRT vault and ramp (y-direction in Figure 7-6). The boundary conditions are set as fixed potentials at the faces normal to the vault's and ramp's longitudinal direction, so that a horizontal potential gradient of 2 mV/m is obtained. Other boundary faces are electrically insulated (i.e. no current may flow normal to the boundaries). The host rock surrounding the engineered parts of the repository is assumed to be homogenous, with a resistivity of 10 000 ohm.m.

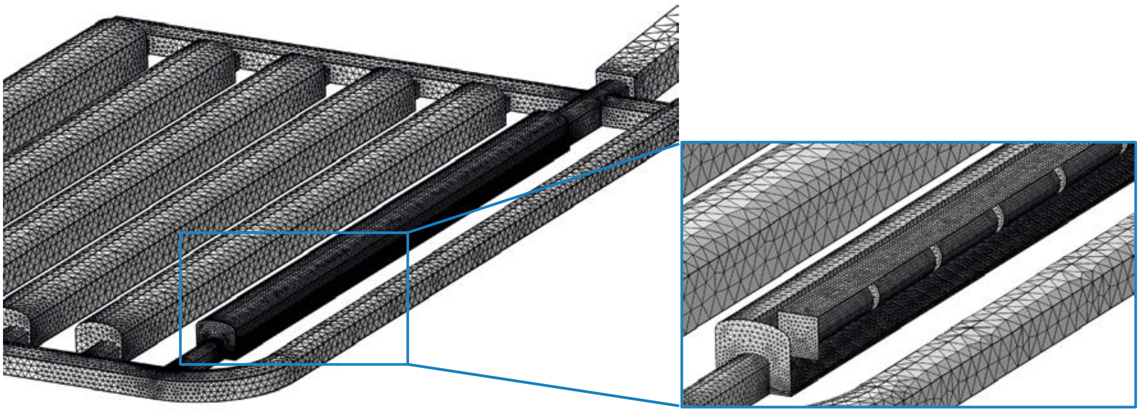

Figure 7-5. *Example of the finite volume mesh showing parts of the SFR 3 domains.*

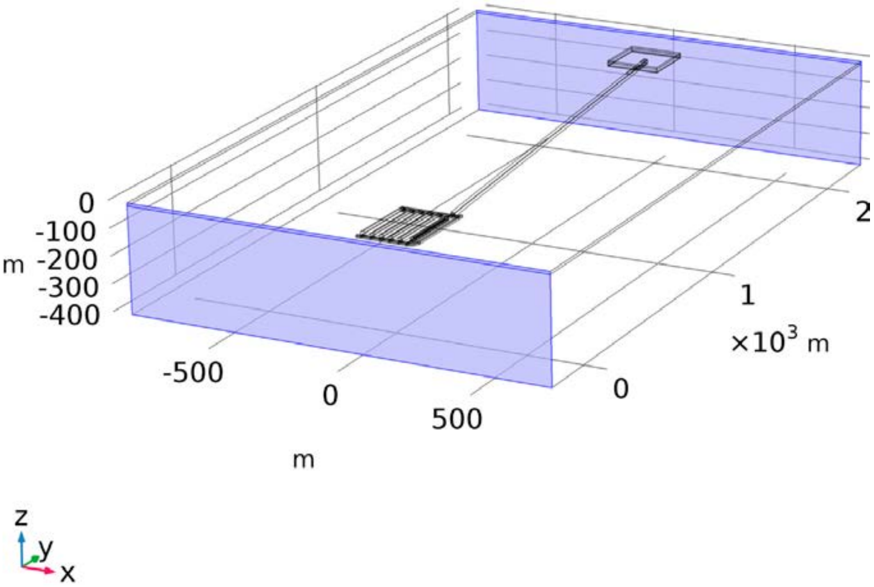

Figure 7-6. *Fixed potential boundary conditions (blue faces) imposing a potential gradient over the model domain.*

7.2.2 Results

Results for the entire 3D model domain are shown for the 3D repository base case in Figure 7-7, as planar slices coloured after electrical potential and with grey current lines. The black current line indicates an approximate influence radius of flowlines that intersects with the SFR 3 repository (i.e. not the 1BRT vault specifically as in previous model cases). Results zoomed in at the repository vaults (Figure 7-8) reveals that most current lines exit through the ramp and tend to follow tunnels and vaults with least resistance (gravel and bentonite backfilled vaults and tunnels). The access tunnels "collect" current from the rock which is distributed to, mainly, the gravel backfilled vaults closest to the ramp. It is again noted that the BMA vault (rightmost vault in Figure 7-8) is assumed to be concrete backfilled. The current entering the vault at some locations is transported against the global potential gradient along the path of least resistance.

Figure 7-9 shows the current density lines in the sea water at the top boundary. The current density lines divert around the assumed location of the island where the entrance of the ramp is located.

The corrosion current leaving each reactor pressure vessel is calculated as described in Section 6.1.1. The total amount of current that leaves the 1BRT vault is estimated by the same approach, i.e. by surface integration over its boundaries. The total amount of current that exits SFR 3 and enters the ramp is estimated by surface integration at the mouth of the ramp. This area is indicated by a red arrow in Figure 7-8. All these currents are reported in Table 7-1.

The results indicate that approximately 25 % of the current entering the mouth of the ramp (75 mA) has passed through the 1BRT vault (19 mA). Thus, the majority (75 %) of the current passing through the repository is conducted through the 1–5BLA and access tunnels, bypassing the 1BRT vault. The results also show that the total corrosion current of 42 mA (for all vessels) is less than it would have been if all current passing through 1BRT also intersects with each vessel. If this was the case, a total corrosion current of 19 mA times 9 vessels, i.e. 171 mA would be observed. This together with the observation that the corrosion current for each vessel increases with decreasing distance to the ramp, suggests that some of the corrosion current for vessel 9 have bypassed all other vessels, some of the corrosion current for vessel 8 has bypassed vessels 1 through 7 etc. A final observation is that the total corrosion current of 42 mA resulting from the base case calculation is only a fraction (14 %) of the benchmark current of 300 mA (corresponding to general corrosion without Earth currents).

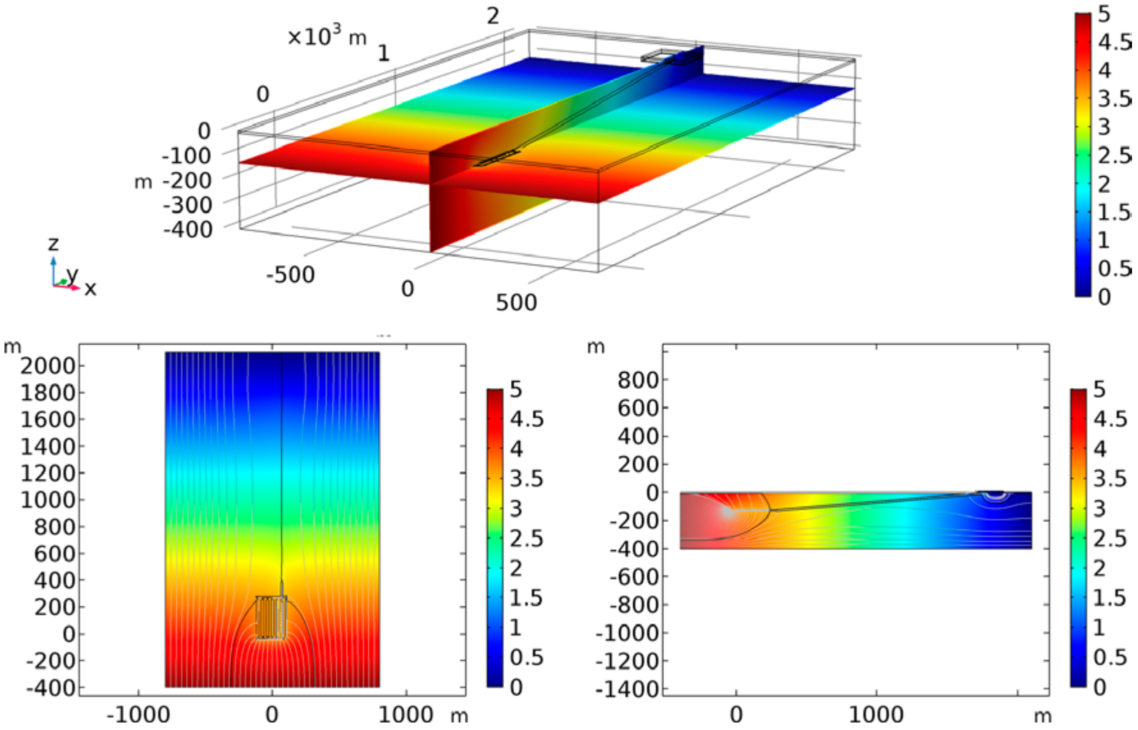

Figure 7-7. *Results for the 3D repository base case. Colour scale indicate the potential (V) in a horizontal and vertical slice that both intersect the 1BRT vault. Grey lines in the bottom figures show current lines.*

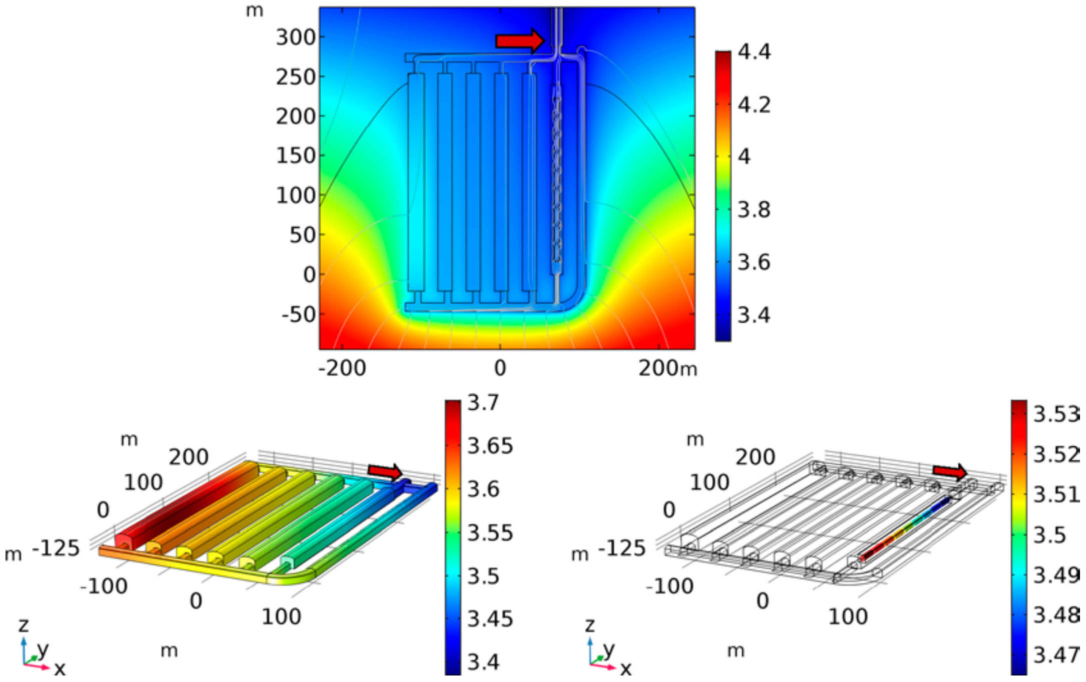

Figure 7-8. *Results zoomed in over the SFR 3 vaults. The red arrows indicate the surface between SFR 3 and the ramp.*

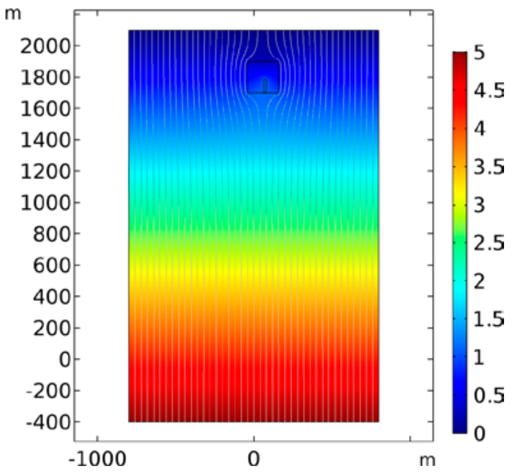

Figure 7-9. *Current lines and potential at the ground surface. Current is diverted around the island.*

Table 7-1. Current leaving SFR 3 and 1BRT; corrosion currents of reactor pressure vessels 1 to 9; and total corrosion current for all vessels in 3D repository base case. The vessels are ordered by distance to the ramp.

Component	Current (mA)
SFR 3	75
1BRT vault	19
Vessel 1 (far end)	3.5
Vessel 2	3.8
Vessel 3	4.2
Vessel 4	4.5
Vessel 5 (middle)	4.8
Vessel 6	5.0
Vessel 7	5.3
Vessel 8	5.5
Vessel 9 (at ramp)	5.9
Total corrosion current	42

7.3 3D repository variation A – field direction and strength

7.3.1 Model setup

The main purpose of this variation case is to study the sensitivity of the results to the direction of the electrical potential field. This is motivated partly by the fact that the present-day potential gradient has both a horizontal and a vertical component, and partly by the possibility of future electrode installations and cable extensions that may induce potential fields that differ from that of the present-day installations. In the 3D base-case calculation, a horizontal potential gradient was assumed with a direction parallel to the 1BRT vault, inducing a main current flow along the vaults and ramp extension. In the variation cases, the field is rotated 90 degrees in two different directions. In 3D variation case A:1 this is done by specifying fixed potentials at the faces parallel to the direction of the 1BRT and ramp extension (blue faces in the left illustration in Figure 7-10). In 3D variation case A:2 this is done by specifying fixed potentials at the top and bottom faces of the model domain imposing a vertical potential field (right illustration in Figure 7-10). For both field rotations, the absolute value of the potential gradient is assumed to be the same as in the 3D repository base case, i.e. 2 mV/m. In all other aspects, apart from the field direction, these variation cases reproduce the 3D repository base case.

By scaling the results from the 3D repository base case, and variation cases A:1 and A:2, the corresponding current for two other fields strengths are obtained. These field strengths are a reasonable future field (30 mV/m) and pessimistic future field (200 mV/m), as justified in Section 3.2.2.

7.3.2 Results

The resulting field and current lines for 3D variation case A:1 are shown in Figure 7-11. It is evident from the figure that the current is, to a large extent, directed along the access tunnels normal to the vaults, and that only a small portion of the current intersects the 1BRT vault and pressure vessels. The small current entering the 1BRT vault exits mainly through the access tunnel 2BST on the opposite side of the ramp, as can be seen from the red arrows in Figure 7-11 indicating the current flow direction. The total corrosion current for the nine vessels is calculated to be 2.7 mA, by the approach described in Section 6.1.1. The current that enters the 1BRT vault is 2.1 mA.

The resulting field and current lines for the vertical potential field in variation case A:2 are shown in Figure 7-12. It is evident from the figure that the current is, to a large extent, directed vertically through the repository. Only a small portion of the vertical current is directed through the 1BRT vault in this case. The current enters the 1BRT vault mainly through the roof of the vault and exits mainly through the floor, as can be seen from the red arrows in Figure 7-12 indicating the current flow direction. Current also enters the vault to some extent from the ramp mainly due to its vertical inclination and relatively low resistivity. The total corrosion current for the nine vessels is calculated to be 2.4 mA, by the approach described in Section 6.1.1. The current that enters the 1BRT vault is 2.3 mA. These currents are tabulated in Table 7-2, as compared to the 3D repository base case.

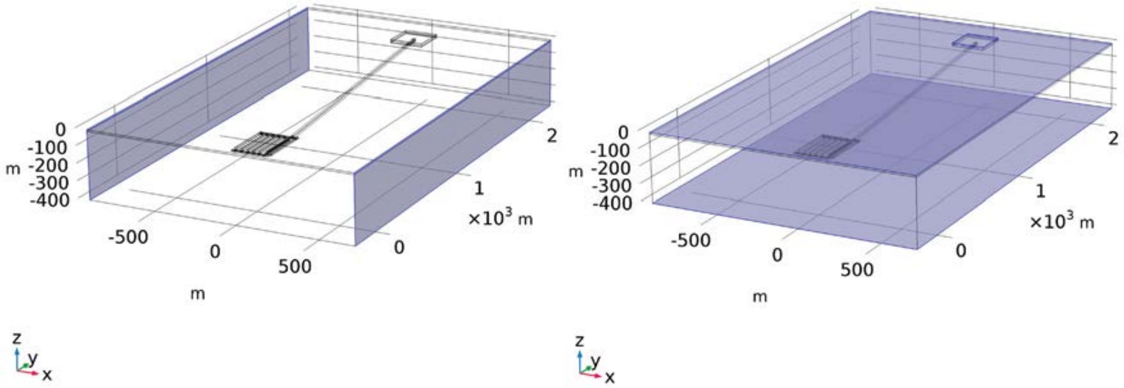

Variation case A:1

Variation case A:2

Figure 7-10. *Fixed potential boundary conditions (blue faces) imposing a potential gradient over the model domain normal to the direction of the 1BRT and ramp extension (left) and a vertical potential gradient (right).*

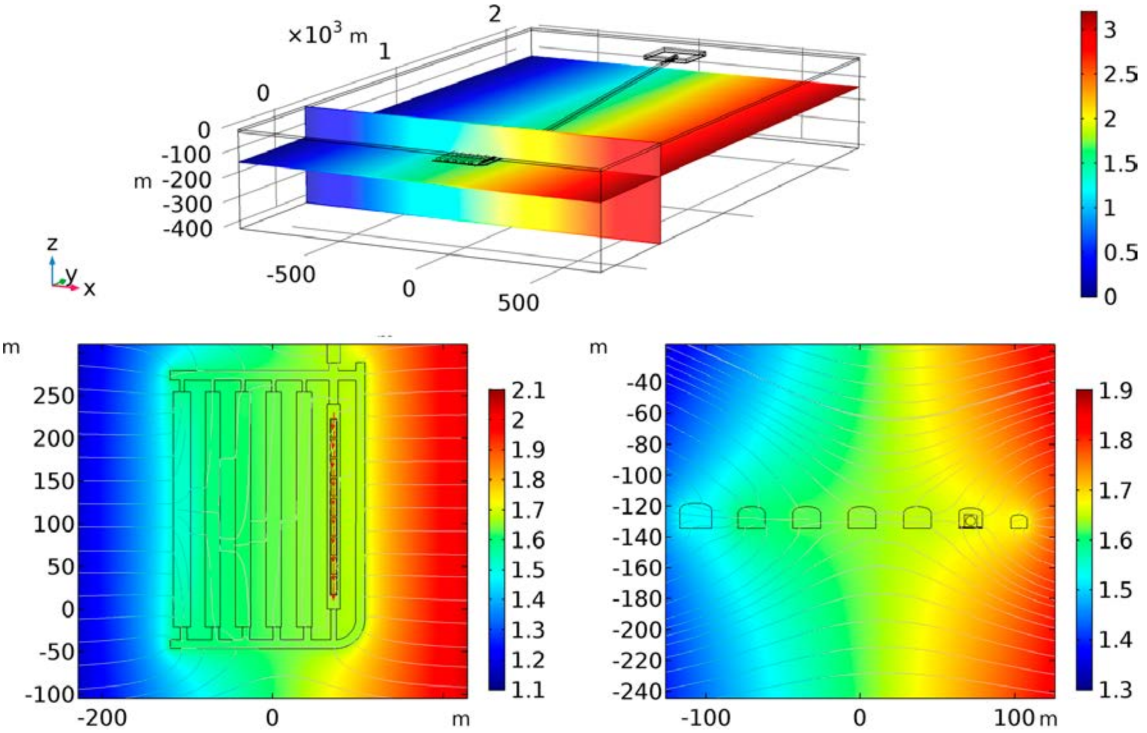

Figure 7-11. *Results for 3D variation case A:1 with an imposed potential field normal to the direction of the 1BRT and ramp extension. Colour indicates potential (V) and current lines are grey. Red arrows indicate current flow direction within 1BRT.*

Table 7-2. Total corrosion current and current leaving the 1BRT vault in 3D repository base case and variation cases A:1 and A:2.

Component	Total corrosion current (mA)	Current entering 1BRT (mA)
3D repository base case	42	19
3D variation case A:1	2.7	2.1
3D variation case A:2	2.4	2.3

In Table 7-3, corrosion currents in Table 7-2 are scaled based on the larges-scale potential gradient, from 2 mV/m at present day conditions to the future field strengths of 30 and 200 mV/m.

Table 7-3. Total corrosion current, as scaled based on the large-scale potential gradient.

Component	Total corrosion current at 30 mV/m (mA)	Total corrosion current at 200 mV/m (mA)
3D repository base case	42 × 15 = 630	42 × 100 = 4200
3D variation case A:1	2.7 × 15 = 40.5	2.7 × 100 = 270
3D variation case A:2	2.4 × 15 = 36	2.4 × 100 = 240

It is evident from the results that the global electrical fields imposed on the boundaries in cases A:1 and A:2 results in much lower total corrosion rates as compared with the base-case. Even for the reasonable future potential gradient of 30 mV/m, the total corrosion is only a small fraction (< 14 %) of the benchmark current of 300 mA. When applying a very pessimistic potential gradient of 200 mV/m the resulting corrosion currents in cases A:1 and A:2 may reach levels corresponding to the benchmark current.

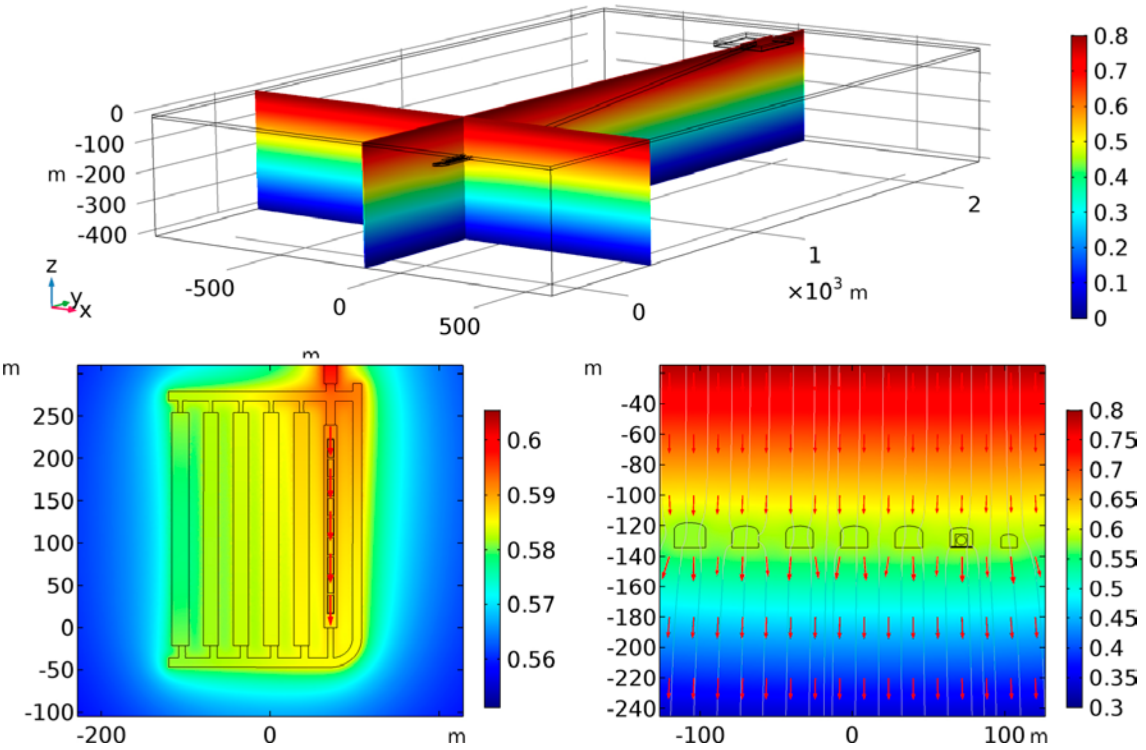

Figure 7-12. *Results for 3D variation case A with an imposed vertical potential field. Colour scales indicate potential (V) and grey streamlines indicate current lines. Note that colour scale ranges differ between the figures. The direction of current flow is indicated by red arrows.*

7.4 3D repository variation B – concrete backfilled vaults

7.4.1 Model setup

The purpose of this variation case is to study the effect of a pessimistic choice of backfill resistivity in other underground openings than the 1BRT vault. In doing this, the 1BRT vault and its components are kept the same as in the 3D repository base case. This should divert more of the current through the 1BRT vault than in the base case. In this variation, conductive gravel backfill or bentonite (with a resistivity of 3.75 ohm.m) is assumed in access tunnels 2TT and 2BST (see Figure 7-13). These structures thereby collect current from a larger rock volume. Gravel backfill is also assumed in the ramp to mediate a conductive current path from SFR 3 to the ground surface. The more resistive concrete (100 ohm.m) is assumed to completely backfill the other vaults (i.e. neglecting the waste) and the access tunnel parallel to the 1BRT vault. This is done to avoid conductive parallel paths where current can flow past the 1BRT vault. This variation case also encompasses, although in an exaggerated manner, the effect of mechanical concrete plugs in parallel vaults (cf. blue compartments of Figure 7-2, right) in terms of reducing the current through these parallel structures. In all other aspects, apart from the backfilling properties, the variation case is a reproduction of the 3D repository base case.

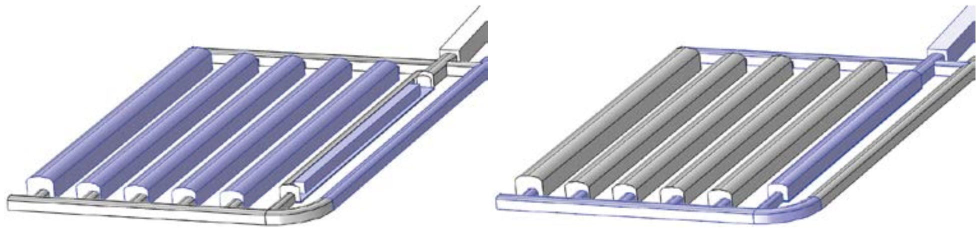
Concrete backfilled domains

Gravel/bentonite backfilled domains

Figure 7-13. *Domains backfilled with concrete (access tunnel parallel to the repository vaults and all vaults except 1BRT) and gravel or bentonite (1BRT, access tunnels normal to the vaults and ramp) are indicated by blue colour for variation case B.*

7.4.2 Results

The resulting potential field and current lines for this case are shown in Figure 7-14. The total corrosion current of the nine reactor pressure vessels, the current leaving 1BRT, and the current leaving the SFR 3 part are calculated in the same manner as in the 3D repository base case. The results are tabulated in Table 7-4, as compared to the corresponding results for the 3D repository base case.

Table 7-4. Total corrosion current and current leaving the 1BRT vault in 3D repository base case and variation case B.

Component	Total corrosion current (mA)	Current leaving 1BRT (mA)	Current leaving SFR-3 (mA)
3D repository base case	42	19	75
3D variation case B	98	41	68

The integrated current density at the 1BRT vault/ramp interface is 41 mA. The current of 19 mA in the 3D repository base case is thus slightly more than doubled. Even with these pessimistic backfill properties, the corrosion current is less (one third) than the benchmark current of 300 mA. It may also be noted that the current passing through the repository/ramp interface is slightly less (68 mA) than in the base case (75 mA).

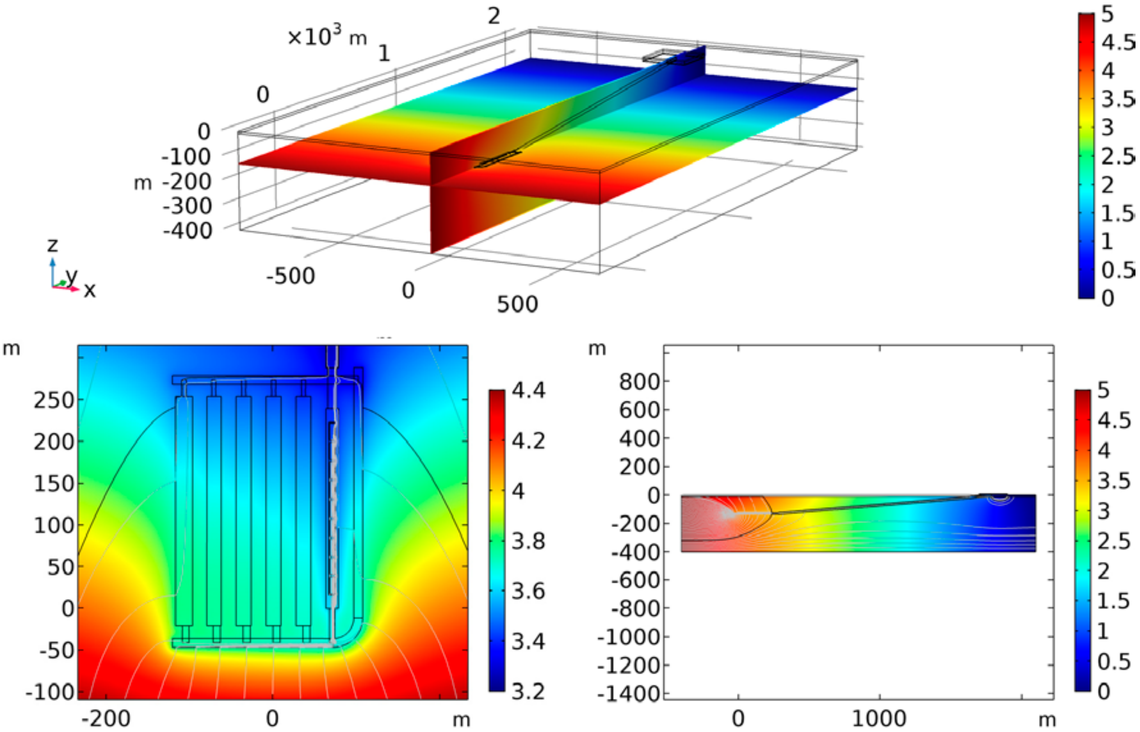

Figure 7-14. Results for the 3D variation case B with concrete backfilled vaults (except for the gravel backfilled 1BRT vault).

7.5 3D repository variation C – no island

7.5.1 Model setup

This variation case, for which no graphical results are presented, investigates the impact of the arbitrarily shaped island hosting the entrance of the access ramp. This is done by removing the rectangular island (in the upper right of Figure 7-4), with the consequence that the entrance of the access ramp is at the bottom of the Baltic Sea. This increases the connectivity between the ramp and the Baltic Sea, in the most extreme fashion. This increased connectivity also encompasses the case where the Singö zone connects the upper part of the ramp with the Baltic Sea (cf. Appendix A).

7.5.2 Results

Allowing the ramp to exit at the bottom of the sea has a relatively limited effect on the total current running through the 1BRT vault. In this case, 20 mA runs through the 1BRT vault while 78 mA runs through all SFR 3 vaults and access tunnel. This is up by ~ 4 % compared to the 3D repository base case. If increasing the connectivity between the ramp and the Baltic Sea in a more moderate fashion, the increase in these current would have been even smaller. This indicates that the arbitrary shape of the island has little impact on the results. It also justifies neglecting the increased connectivity of the ramp to the Baltic Sea, via the Singö zone, in the 3D repository base case.

7.6 3D repository variation D – inland repository location

7.6.1 Model setup

The purpose of this variation case is to study the effect of changed conditions relevant for a future inland location of the SFR repository. The variation case is based on the 3D repository base case but includes a number of deviations. Firstly, the sea at the top of the model domain is neglected. This is done by extending the rock domain all the way to the top boundary. Secondly, the parameterisation is adjusted to illustrate conditions relevant for future inland conditions, mainly relating to a less saline groundwater, as discussed in Section 3.3. The resistivity for the gravel backfill and surrounding rock is assumed to be 170 ohm.m and 30 000 ohm.m respectively (cf. Table 3-5), accounting for an assumed future groundwater composition. In accordance with Section 3.5.1, the concrete resistivity is kept at 100 ohm.m. Thirdly, the regional potential gradient is assumed to be 2 mV/m in variation case D:1 and 30 mV/m in variation case D:2. As in the 3D repository base case it is aligned in parallel with the 1BRT vault, which is achieved by fixating potentials at the model boundary faces (see Figure 7-6).

7.6.2 Results

The resulting field and current lines are shown in Figure 7-15 for variation case D:1. The current in Table 7-5 are calculated in the same manner as in the 3D repository base case, and are compared to the corresponding data in the base case.

Table 7-5. Total corrosion current and current leaving the 1BRT vault and SRF 3, in the 3D repository base case and variation cases D:1 and D:2.

Component	Total corrosion current (mA)	Current leaving 1BRT (mA)	Current leaving SFR-3 (mA)
3D repository base case	42	19	75
3D variation case D:1	15	1.9	2.3
3D variation case D:2	220	28	35

Three main processes, working in different directions, deserve mentioning. In variation case D:2 the electrical potential gradient is increased by a factor of 15 compared to in the base case, which works to increase the current through the repository system. Secondly, in both variation cases the host rock's resistivity is increased by a factor of three, which works to lower the current fed to the

SFR extension. Thirdly, for both variation cases the resistivity of the gravel backfill is increased by a factor of 45. This makes the gravel backfill slightly more resistive than the concrete backfill. As discussed in Section 6.4, this diminishes the Faraday's cage properties of the backfill. Moreover, this decreases the contrast between the rock and backfill resistivities, which decreases the influence radius.

Altogether, this produces corrosion current for future conditions, where the repository has an inland position. With a future field strength of 30 mV/m, the results indicate an increased corrosion current that is about five times higher than in the 3D repository base case. If the field strength is not increased, the lower salinity of the groundwater makes the reactor pressure vessels less sensitive to Earth current induced corrosion as compared to the base case.

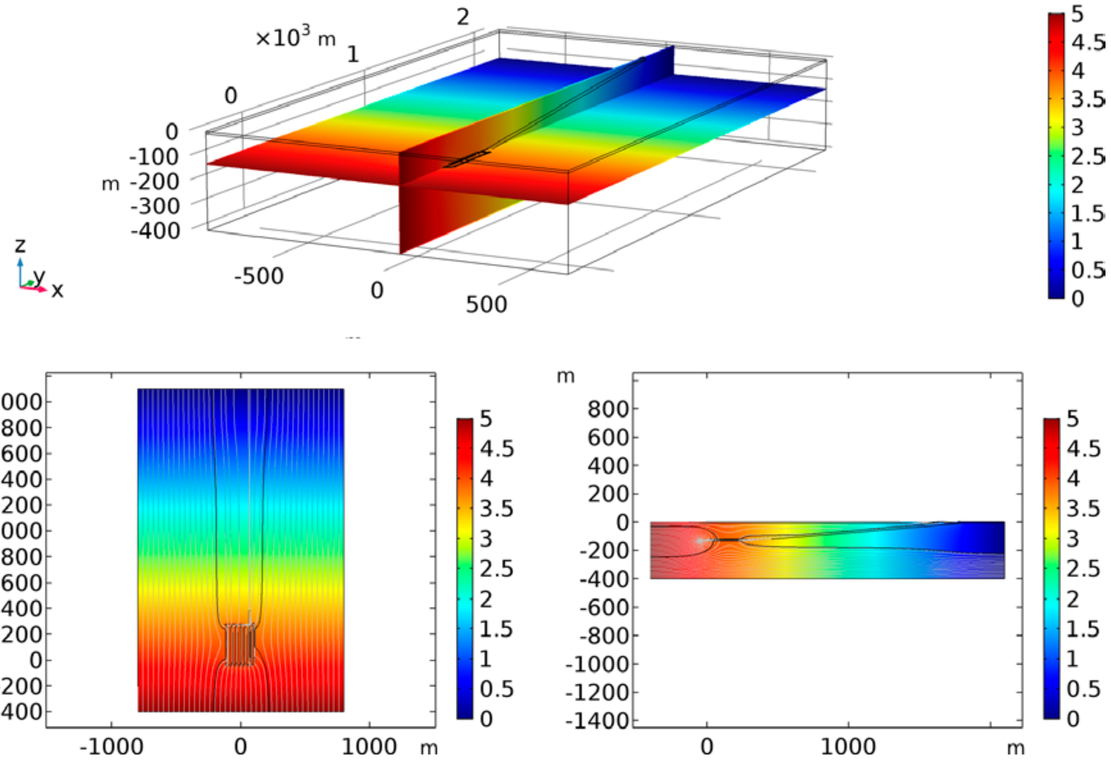

Figure 7-15. *Results for the 3D variation case D:1 with parameterisation relevant for future inland conditions with no sea water at the top of the model domain and backfill and rock resistivities adjusted for presumable inland groundwater composition.*

8 Impact on radiation safety during operation

The operational period of SFR has not been a focus of attention of this work. However, based on the experience from this work and also from basic process understanding, the importance of Earth currents from Fenno-Skan for the radiation safety of SFR, during operation, can be discussed. This is done for two situations, both relating to the enhanced corrosion of metallic waste in SFR. The first situation relates to the enhanced corrosion of reactor pressure vessels; other metallic waste; and metals in general (such as waste packages) that are stored at relatively dry conditions. The second situation relates to the same waste, but stored at moist or even wet conditions. In both cases, the conclusion is that Earth current induced corrosion has a small or even insignificant impact on the total corrosion rate of the waste and waste packages. As such, the impact on the radiation safety of SFR is at the most minor during operation.

It should be noted that the below discussion is not extended to maintenance and other operational safety issues of SFR. Long metallic structures in SFR, such as electric wiring and ventilation, may be the subject to local corrosion due to Earth currents, which may affect their integrity and function.

8.1 Metallic waste stored at dry conditions

As is discussed in Section 2.1, direct Earth currents are to an overwhelming majority propagated by electrolytic conduction, while the amount propagated by electronic conduction is vanishingly small. For all practical purposes this requires a continuous water pathway from the Fågelsundet electrode to the metallic component in SFR in question. If the metallic waste (and other metallic components) is stored at dry conditions, there will be no such continuous water pathway and Earth currents will not contact the metal. The reactor pressure vessels, for example, will be placed on concrete stands where the contacting surface of the stands will have dried out.

8.2 Metallic waste stored at moist or wet conditions

Normal amounts of moisture in the air may locally condense on metallic surfaces, which may cause local corrosion. However, unless the moisture creates a continuous condensation film on the waste and other components of SFR, it will not form a path for Earth currents to contact the metallic waste. Accordingly, even at moist conditions Earth currents will not normally cause additional corrosion of metallic waste.

As a bounding case, Earth current induced corrosion is discussed for locally wet conditions in SFR. This situation may reflect a local inflow from a fracture where water pours down on the waste. The design and maintenance of the SFR repository should prevent this situation from occurring during operation. Accordingly, this should be seen as a what-if discussion where it is assumed that, locally, a continuous water film creates a path for electrolytic conduction from the host rock to the metallic waste. This could create an electrical potential build-up over the metallic waste component, which could corrode at enhanced rates. This is discussed for two cases below.

In a first case this is exemplified by water pouring down on the pressure reactor vessels prior to them being embedded in concrete. As discussed in this report, the pressure vessels feature an induced activity and their corrosion would give rise to a radionuclide source term. This situation could, under specific conditions, create Earth current induced corrosion at similar rates as previously discussed in this report, with corrosion currents on the order of 10 mA per vessel (cf. Section 7.2). This would create a corrosion rate that is small, but not insignificant, compared to the corrosion rate for carbon steel under alkaline anoxic conditions in the absence of Earth currents. The corrosion rate of carbon steel under non-alkaline oxic condition, which would apply in this situation, is however 1 200 times larger than under alkaline anoxic conditions. Accordingly, compared to the general corrosion the Earth current induced corrosion would be insignificant.

If, on the other hand, the reactor pressure vessels are embedded in concrete, the relative impact of Earth current induced corrosion is not necessarily insignificant, although its impact is still smaller than from general corrosion. Under these circumstances, however, the total corrosion rate would probably be too low to be of concern for operational radiation safety.

The second case includes the corrosive penetration of metallic waste packages, which may impact the operational safety if water contacts, and leaches, the waste it contains. This may be consequential if the waste package is not embedded in shielding concrete. In such a case, as above, it would be the general corrosion in the non-alkaline and oxic environment that would be the dominant source for penetrative corrosion, and no Earth current induced corrosion.

9 Conclusions

9.1 Are Earth currents consequential?

The main question to answer in this report is whether or not Earth currents are consequential for the long-term safety of the SFR repository, from the perspective of additional corrosion of reactor pressure vessels. The short answer is that although Earth currents probably will give rise to additional corrosion of reactor pressure vessels, this contribution is very small compared to the corrosion that will occur anyway in their absence.

The 3D repository base case is the most realistic model of this report, although it still uses many pessimistic data and the pessimistic charge-balance approach. The total Earth current induced corrosion current in this model is 42 mA. This corresponds to an additional corrosion rate of 0.4 kg of reactor pressure vessels per year. In the absence of Earth currents the corrosion rate is expected to be 2.8 kg of reactor pressure vessels per year, based on SR-PSU assumptions (Section 3.9.1). Due to the relatively small significance of Earth current induced corrosion, no attempt was made to trim down the pessimism of the 3D repository base case. The most obvious way of trimming down the pessimism would have been to acknowledge that the HVDC electrode does not emit a large electric field constantly, but only during imbalanced operation. Thereafter there is a suite of modifications that would be rather simple to implement in the model, should the need arise.

In this report it is argued that the charge-balance approach overestimates the corrosion current by at least a factor of four (but probably more), as there in reality would be kinetic limitation that restricts the Earth current induced corrosion rate. This adds extra safety margin to the above statement that Earth current induced corrosion is overshadowed by the corrosion that would take place in the absence of an eternal field.

Future HVDC installations may increase the field strength at the SFR site, which may give rise to higher Earth current induced corrosion rates. Due to the presence of Gräsö, making the placement of a HVDC electrode in the Öregrundsgrepen ill-suited, a large but still reasonable future field strength is 30 mV/m. If applying this field strength to the 3D repository base case, the total corrosion current is 630 mA. This gives an additional Earth current induced corrosion rate that is slightly more than twice the corrosion rate expected in the absence of Earth currents.

It is conceivable that the reactor pressure vessels will not be deposited intact, but will be segmented prior to deposition. By accounting for kinetics limitations, it has been shown that segmentation either lowers the Earth current induced corrosion rate, or leaves the rate unchanged (depending on the circumstances). For realistic circumstances, the relative importance of Earth current induced corrosion, compared to the corrosion in the absence of Earth currents, diminishes upon segmentation.

From the above it can be concluded that Earth currents have a very limited impact on the long-term corrosion of reactor pressure vessels, and that this impact can be quantified.

In this report it is also argued for that Earth currents are not consequential for the radiological risk during operation. This is mainly due to the relatively dry conditions under which the waste is stored. At more wet conditions, which should only occur locally, other corrosion processes that are not induced by Earth currents would dominate the corrosion.

9.2 Is there sufficient process understanding?

Substantial effort has been devoted to obtain a valid process understanding of how Earth currents could promote corrosion. We are fairly confident that we have gained sufficient process understanding to achieve the objectives of this report.

Earth current does not primarily promote the corrosion by bringing reducible species from the host rock, or distant parts of the engineered barriers, to the corrosion surface. Instead the primary effect is that the external field facilitate a sustainable polarisation of the pressure reactor vessels, creating an anodic side and a cathodic side. At the anodic side, where there is an anodic overpotential, there is a deficiency of electrons, which promotes the oxidation of metallic iron into ferrous iron. At the same time, this electron deficiency supresses the reduction of water. At the cathode side of the reactor pressure vessel, an electron surplus promotes the reduction of water while it supresses the oxidation of iron. In order to sustain the polarisation, i.e. the surplus of electrons at the cathode side and deficiency at the anode side, despite the fact that redox reactions at the metal surface consumes or produces electrons, an electrical current must propagate in the pressure reactor vessel. At the same time, the charged reaction products must be carried away in the surrounding electrolyte by the external field; essentially making them part of the Earth currents.

Based on this process understanding, it is argued that the charge-balance approach is a pessimistic approach, which assumes very rapid reactions. By using, for example, the Butler-Volmer equation to calculate the anodic corrosion current from a given overpotential, the pessimism can be dialled down. Kinetic limitations are investigated in this report by accounting for the activation polarisation, which can be tied to fundamental principles of reaction kinetics. In the real case, there is also a reduction in the corrosion rate from concentration polarisation. The impact of this type of polarisation is, however, neglected in this report. The reason is that it appears to be very complicated to justify a numerical value by which to implement this limiting process, that is valid for repository conditions.

9.3 Are the input data justifiable, and is there substantial data uncertainty?

In this work, substantial effort has been made to use data that represent the repository concept assumed in SR-PSU. This has been done in the light of repository geometries, material quantities, material properties and external conditions. In many cases, pessimistic assumptions have been made, where the pessimism (that is using values in the high or low end of the spectrum) reflects the aims of this work. In other cases, sensitivity to input data or assumptions has been investigated though setting up variation cases. Therefore, we are confident that we have used justifiable input data. This does not take away from the fact that there is substantial uncertainty in the input data that could have profound effects on the results. For example, if using Tafel slopes of, say, 200 mV/dec, this severely reduces the Earth current induced corrosion rates in the kinetics limitation approach. Another example is that acknowledging the current conducting capacity of the metallic waste and containers in BLA vaults, which are parallel with the 1BRT vault, may significantly reduce the amount to current being transported through the 1BRT vault. Considering the degree of pessimism introduced in the modelling, it is likely that the actual Earth current induced corrosion rates are orders of magnitude lower than suggested here. It is unlikely, however, that the actual Earth current induced corrosion rate supersedes those suggested here.

9.4 Are the models reliable and the calculated results sufficiently pessimistic?

Prior to setting up the more complex models in COMSOL Multiphysics, we used the electrical circuit model for scoping calculations. The electrical circuit model is essentially a “back of the envelope” calculation and is, accordingly, associated with restrictions. However, its simplicity makes it very robust for estimating the upper value of Earth currents that may flow through the 1BRT vault. The fact that we could transfer calculation case 2a of the electrical circuit model to both 2D and 3D models in COMSOL Multiphysics, with understandable results, is reassuring. We have used the electrical circuit model as a tool of understanding the COMSOL Multiphysics results throughout this work and can say that we have confidence in our models. The problem of modelling a stationary electric field in a 3D-domain that includes different compartments, which are all internally homogenous, is very suitable for a finite element tool such as COMSOL Multiphysics. Overall, this means that our models, and especially the more realistic 3D model in COMSOL Multiphysics, work as intended and deliver usable results in relation to our modelling goals.

There are remaining uncertainties in how the large-scale electric field develops around the Fågelsundet electrode, especially at locations close to the shoreline and in the rock beneath the seabed (where SFR is located). There are empirical data on the electrical potential gradient at the site, which we have used. Furthermore, the order of magnitude of these field data can be understood from regional-scale modelling of the electric field. However, there are specifics in how the electric field is skewed due to the presence of the shoreline that are not fully understood. Moreover, the grounding of power lines at the nuclear power plant complicates the matter. Even with these uncertainties we have an understanding of the magnitude of the potential gradient at the site. Thereby, we can use pessimistic values, and also a pessimistic alignment, of the potential gradient, and still achieve only minute Earth currents contacting the pressure vessels.

Due to the many layers of pessimism involved, we judge that the actual corrosion rates of the pressure vessels, caused by Earth currents, will probably be orders of magnitude lower than in our (pessimistic) best estimates. Below we list the most important pessimistic assumptions, although at the end of the list the importance of the pessimism decreases:

- We assume that 100 % of the charge carried by Earth currents to the vessel surfaces is utilised for corrosion.
- We assume that the Fågelsundet electrode is always switched on at a high power output. As the Fenno-Skan transmission uses two cables over the Baltic Sea (transmitting current in opposite directions) one seeks to limit the use of the Fågelsundet electrode.
- In our base cases, we assume a horizontal potential gradient that is perfectly aligned with the 1BRT vault. If this is not the case, modelling shows a considerable drop in the contacting current.
- We assume that the parallel vaults (especially the 2–5BLA vaults filled with metal containers) are much too resistive, forcing too much current through the 1BRT.
- We neglect the shielding effect of a plausible reinforcement bar network in e.g. the floor of the 1BRT vault.
- We have conceptualised the actual ramps by a straight ramp structure having a length that exceeds the Euclidian distance between the entrance at ground surface and exit in the underground facility. Moreover, this modelled structure features no concrete plugs and is perfectly aligned with the 1BRT vault.
- We assume that the macadam backfill is too conductive, increasing the influence radius in the repository host rock.
- We assume, for a plausible future case, a much higher potential gradient than is presently observed, with the prerequisites that a future installation is more powerful and that its electrodes are more closely located.

10 References

SKB's (Svensk Kärnbränslehantering AB) publications can be found at www.skb.com/publications.

Anunti Å, Larsson H, Edelborg M, 2013. Decommissioning study of Forsmark NPP. SKB R-13-03, Svensk Kärnbränslehantering AB.

Archie G E, 1942. The electrical resistivity log as an aid in determining some reservoir characteristics. Transactions of AIME 146, 54–62.

Arps J J, 1953. The effect of temperature on the density and electrical resistivity of sodium chloride solutions. Transactions of AIME 198, 327–330.

Atkins P W, 1994. Physical chemistry. 5th ed. Oxford: Oxford University Press.

Auqué L F, Gimeno M J, Acero P, Gómez J B, 2013. Compositions of groundwater for SFR and its extension, during different climate cases, SR-PSU. SKB R-13-16, Svensk Kärnbränslehantering AB.

Berg C, Nilsson A-C, 2007. Forsmark site investigation. Hydrochemical sampling and analyses in KFM12A. Results from two investigated borehole sections, 343.0–363.0 m and 516.0–536.0 m. SKB P-07-171, Svensk Kärnbränslehantering AB.

Binley A, Kruschwitz S, Lesmes D, Kettridge N, 2010. Exploiting the temperature effects on low frequency electrical spectra of sandstone: a comparison of effective diffusion path lengths. Geophysics 75, A43–A46.

Carlsson A, Martin D, Christiansson R, 2014. Site Engineering Report – SER – Projekt SFR utbyggnad. SKB R-14-17, Svensk Kärnbränslehantering AB.

Crawford J, 2008. Bedrock transport properties Forsmark. Site descriptive modelling, SDM-Site Forsmark. SKB R-08-48, Svensk Kärnbränslehantering AB.

Freeze A R, Cherry J A, 1979. Groundwater. Englewood Cliffs, NJ: Prentice Hall.

Hayashi M, 2004. Temperature–electrical conductivity relation of water for environmental monitoring and geophysical data inversion. Environmental Monitoring and Assessment 96, 119–128.

Hellman H, Winnerstam B, 2014. Teknisk beskrivning av SFR – Befintlig anläggning och planerad utbyggnad. SKBdoc 1341767 ver 2.0, Svensk Kärnbränslehantering AB. (In Swedish.)

Höglund L O, 2014. The impact of concrete degradation on the BMA barrier functions. SKB R-13-40, Svensk Kärnbränslehantering AB.

Jones D A, 1992. Principles and prevention of corrosion. New York: Macmillan.

Keyvani A, 2013. Electrical resistivity of cement types in reinforced concrete structures of electrically powered transit lines. International Journal on "Technical and Physical Problems of Engineering" 5, 96–101.

Lide D R (ed), 2003. CRC handbook of chemistry and physics: a ready-reference book of chemical and physical data. 84th ed. Boca Raton, FL: CRC Press.

Löfgren M, 2004. Diffusive properties of granitic rock as measured by in situ electrical methods. Ph.D. thesis. Royal Institute of Technology, Stockholm, Sweden.

Löfgren M, 2014. Recommendation of rock matrix effective diffusivities for SR-PSU. Based on formation factor logging in situ by electrical methods in KFR102B and KFR105. SKB R-13-39, Svensk Kärnbränslehantering AB.

Löfgren M, 2015. Artefacts associated with electrical measurements of the rock matrix formation factor. With comments on handling in, and potential consequences for, the safety assessment SR-Site. SKB R-14-20, Svensk Kärnbränslehantering AB.

Löfgren M, Večernik P, Havlova V, 2009. Studying the influence of pore water electrical conductivity on the formation factor, as estimated based on electrical methods. SKB R-09-57, Svensk Kärnbränslehantering AB.

Mäntynen M, 2001. Temperature correction coefficients of electrical conductivity and of density measurements for saline groundwater. Posiva WR 2001-15, Posiva Oy.

Neretnieks I, 1980. Diffusion in the rock matrix: an important factor in radionuclide retardation? Journal of Geophysical Research 85, 4379–4397.

Nielsen U T, Ringgaard J, 2007. Forsmark site investigation. Geophysical borehole logging in boreholes KFM11A and KFM90B. SKB P-07-92, Svensk Kärnbränslehantering AB.

Nielsen U T, Ringgaard J, 2009a. Site investigation SFR. Geophysical borehole logging in boreholes KFR105 and HFM07. SKB P-09-76, Svensk Kärnbränslehantering AB.

Nielsen U T, Ringgaard J, 2009b. Site investigation SFR. Geophysical borehole logging in the boreholes KFR27 (0–500 m), KFR102A, KFR102B, KFR103, KFR104 and HFM07. SKB P-09-16, Svensk Kärnbränslehantering AB.

Nilsson K, 2011. Hydrochemical characterisation of groundwater in the SFR repository. Sampling and analysis during 2010. Extended investigations in KFR7A: 48.0 to 74.7 m, KFR08: 63.0 to 104.0 and KFR19: 95.6 to 110.0 m. Site investigation SFR. SKB P-11-14, Svensk Kärnbränslehantering AB.

Ohlsson Y, 2000. Studies of ionic diffusion in crystalline rock. PhD thesis. Royal Institute of Technology, Stockholm, Sweden.

Olin M, Valkiainen M, Aalto H, 1997. Matrix diffusion in crystalline rocks: coupling of anion exclusion, surface diffusion and surface complexation. Posiva 96-25, Posiva Oy, Finland.

Parkhomenko E I, 1967. Electrical properties of rocks. New York: Plenum Press.

Pedersen L B, 2016. Assessment of SKB TR-14-15 "Possible influence from stray currents from high voltage DC power transmission on copper canisters" Technical Note 2016:15, Swedish Radiation Safety Authority.

Penttinen L, Siitari-Kauppi M, Ikonen J, 2006. Determination of porosity and micro facturing using the 14C-PMMA technique in samples taken from Forsmark area. Forsmark site investigation. SKB P-06-60, Svensk Kärnbränslehantering AB.

Petersson J, Nissen J, Curtis P, Bockgård N, Öhman J, Mattsson H, Stråhle A, Winell S, 2010. Site investigation SFR. Geological single-hole interpretation of KFR105. SKB P-10-06, Svensk Kärnbränslehantering AB.

Revil A, Glover P W, 1997. Theory of ionic-surface electrical conduction in porous media. Physical Review B 55, 1757–1773.

Román-Ross G, Trinchero P, Maia F, Molinero J, 2014. Hydrogeochemical modelling and evolution of the groundwater types and processes in geosphere of SFR, SR-PSU. SKB R-13-30, Svensk Kärnbränslehantering AB.

Sandberg B, Ahlström J, Tidblad J, Sederholm B, 2009. Korrosion på stål i betong på kylvattenvägar. Delprojekt 3 – Korrosion på stål i vattenmättad betong. Elforsk rapport 10:84, Elforsk, Sweden. (In Swedish.)

Selnert E, Byegård J, Widestrand H, 2008. Forsmark site investigation. Laboratory measurements within the site investigation programme for the transport properties of the rock. Final report. SKB P-07-139, Svensk Kärnbränslehantering AB.

SKB, 2010. Data report for the safety assessment SR-Site. SKB TR-10-52, Svensk Kärnbränslehantering AB.

SKB, 2013a. Site description of the SFR area at Forsmark at completion of the site investigation phase. SDM-PSU Forsmark. SKB TR-11-04, Svensk Kärnbränslehantering AB.

SKB, 2013b. Låg- och medelaktivt avfall i SFR. Referensinventarium för avfall 2013. SKB R-13-37, Svensk Kärnbränslehantering AB. (In Swedish.)

SKB, 2014a. Svar på Föreläggande om redovisning rörande betydelsen av jordströmmar vid SFR. SKBdoc 1434594 ver 1.0, Svensk Kärnbränslehantering AB. (In Swedish.)

SKB, 2014b. Data report for the safety assessment SR-PSU. SKB TR-14-10, Svensk Kärnbränslehantering AB.

SKB, 2014c. Geosphere process report for the safety assessment SR-PSU. SKB TR-14-05, Svensk Kärnbränslehantering AB.

SKB, 2014d. Initial state report for the safety assessment SR-PSU. SKB TR-14-02, Svensk Kärnbränslehantering AB.

SKB, 2015. Safety analysis for SFR Long-term safety. Main report for the safety assessment SR-PSU. Revised edition. SKB TR-14-01, Svensk Kärnbränslehantering AB.

Smart N R, Blackwook D J, Werme L, 2001. The anaerobic corrosion of carbon steel and cast iron in artificial groundwaters. SKB TR-01-22, Svensk Kärnbränslehantering AB.

Stumm W, Morgan J J, 1996. Aquatic chemistry: chemical equilibria and rates in natural waters. 3rd ed. New York: Wiley.

Taxén C, Sandberg B, Lilja C, 2014. Possible influence from stray currents from high voltage DC power transmission on copper canisters. SKB TR-14-15, Svensk Kärnbränslehantering AB.

Thunehed H, 2017. Compilation and evaluation of earth current measurements in the Forsmark area. SKB R-14-34, Svensk Kärnbränslehantering AB.

Vilks P, Miller N H, Stanchell F W, 2005. Laboratory program supporting SKB's Long Term Diffusion Experiment. Report 06819-REP-01300-10111-R00, Atomic Energy of Canada Limited.

Waxman M H, Smits L J M, 1968. Electrical conductivities in oil-bearing shaly sands. Society of Petroleum Engineering Journal 8, 107–122.

Appendix A

Deformation zone resistivities

A.1 Introduction

This appendix describes the estimate of a representative block-scale rock resistivity of minor and major fracture zones, which could hypothetically contact the 1BRT-vault. Here the term fracture zone denotes the fractured part of a deformation zone. For a fracture zone to affect the current led through the vault it would have to contact, or be in close proximity to, the SFR underground openings. The SFR site has been thoroughly studied in site investigations and the locations of minor and major deformation zones are well known. Figure A-1 (left) shows the known zones (red and green lines) with trace lengths ≥ 300 m within the local modelling area of SDM-site, as indicated by the black rectangle. The extended SFR facility is shown on the right in Figure A-1 for comparison. The zones of the local modelling area are relatively small and the layout is made so that underground openings to the largest possible extent stay clear of the largest zones. One major zone, the so called Singö zone (ZFMWNW0001), intersects the upper part of the ramp outside of the local modelling area (cf. Figure A-5).

Not only the magnitude of the zones, but also their alignment relative to the vault, is of importance. Figure A-2 shows four simplistic examples of the isolated 1BRT vault accompanied by one or two zones. A horizontal potential gradient is assumed in the following discussion. In Figure A-2a, two vertical zones surround the vault but do not contact it. As there are resistive rock volumes upstream and downstream of the vault, shielding it from the presence of the zones, their impact will be limited. In Figure A-2b the two vertical zones touch the ends of the vault. The zones thereby aid the current lines in bending from the surrounding host rock towards the vault, by way of creating vertical conductive pathways. In preliminary testing with COMSOL Multiphysics it was clearly shown that allowing the vertical zones to touch the vault's ends, instead of being at the short distance of 10 m from the vault's ends, clearly increased the current running through the vault. The preliminary testing was made on an isolated vault as shown in Figure A-2a and b. In other aspects, the modelling is represented by that in Section 6.1.

If a zone is parallel with the vault, but does not intersect it, as in Figure A-2c, this provides a parallel conductive path. The presence of such a zone would lower the current running through the vault. A zone that is parallel with the vault, and also intersect it (cf. Figure A-2d), may increase the current through the otherwise isolated vault. Such a zone could be visualised as increasing the length of the vault. In accordance with the discussion in Section 5.4, this would increase the influence radius around the vault from which current lines could bend from the host rock to contact the vault.

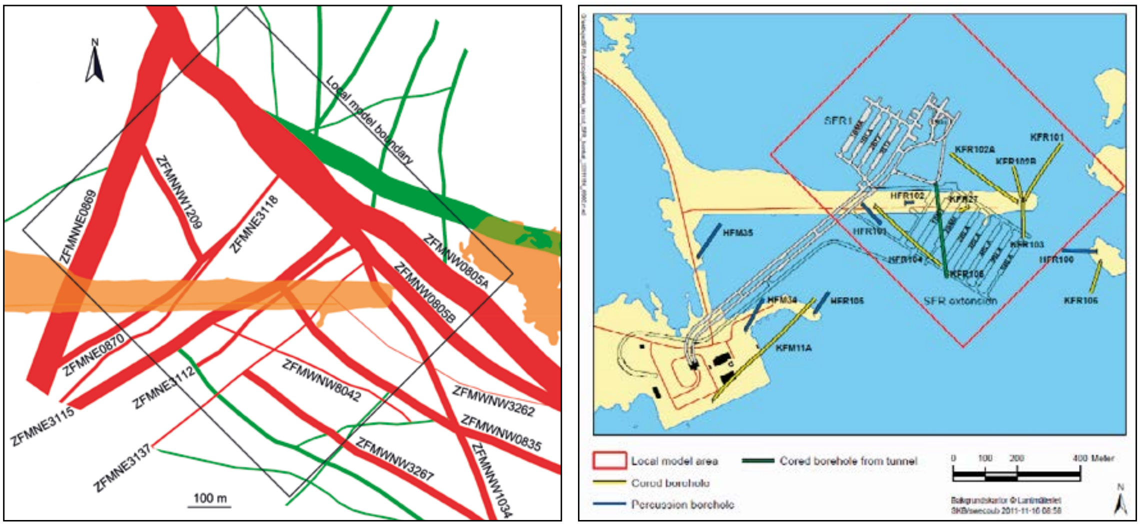

Figure A-1. Left: Deformation zones of the local modelling area with trace lengths ≥ 300 m. Zones are shown in red and green and the pier is in orange. Excerpt from SKB (2013a, Figure 6-11). Right: Preliminary layout of the extended SFR, as well as different boreholes shown by green and yellow tubes. Reproduced from SKB (2013a, Figure 2-10).

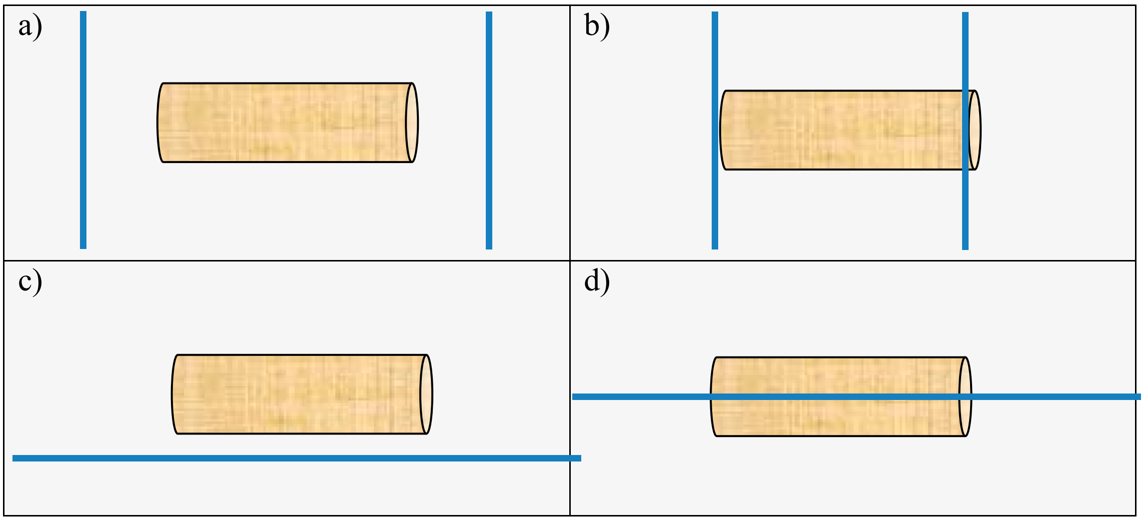

Figure A-2. *Illustrations of the isolated 1BRT vault and different configurations of nearby fracture zones.*

Although this may significantly affect the modelling of an isolated vault, it will have less impact on the results when adding an access ramp to the vault in the model. In modelling in Chapter 6, we have added a 1 500 m long ramp on one side of the vault, as well as an 80 m long extension on the other side of the vault (cf. Figure 6-6) to account for features of the access tunnels, etc. These additional underground openings can be seen as a representation of the case in Figure A-2d. If so, however, they would need to represent major fracture zones, due to their conductive nature. It is unrealistic to assume that such a major fracture zone would intersect the vault, as one of the main objectives of the layout work is to stay clear of such zones.

A.2 Estimation of data

A.2.1 Realistic zone

In this section, a realistic block-scale rock resistivity is estimated, which should represent the zones that actually intersect the SFR local area (cf. Figure A-1). This is done based on apparent rock resistivity data[10] from geophysical downhole logging in borehole KFR105 (Nielsen and Ringgaard 2009a). This borehole is drilled sub-horizontally from the underground part of the existing SFR to intersect the rock volume of the planned extension. The direction of the borehole is shown by the green tube in Figure A-1 (right). The borehole, which is ~ 307 m long, intersects five possible deformation zones according to the single-hole interpretation (Petersson et al. 2010, Chapter 5). The total length of these possible deformation zones is 56 m, or 18 % of the borehole length. These possible deformation zones have been part in constructing the deformation zone model in Figure A-1.

Rock resistivity downhole logging was made in 0.1 m increments along the ~ 307 m long borehole, resulting in 3 012 data points. Figure A-3 shows the downhole log, but the apparent rock resistivities have been converted to rock electrical conductivities.

The most profound anomaly occurs at deformation zone ZFMNE3115 between the borehole lengths 45 – 52 m. An image of the fractured drill core in this section is displayed in SKB (2013a, Figure 5-18). The arithmetic mean of the rock EC in this 7 m long interval is 9.8×10^{-4} S/m (corresponding to the block-scale rock resistivity of 1 016 ohm.m). The highest rock EC obtained in a single data point in the borehole is 6.9×10^{-3} S/m (146 ohm.m), corresponding to a short section of highly fractured cataclastic rock between the borehole lengths 45.59 – 45.75 m (SKB 2013a, Figure 5-18). In Figure A-4, the rock electrical conductivities of the entire borehole are arranged in a cumulative distribution function (CDF). From the CDF one can see that only 1.6 % of the data points have electrical conductivities of above 1×10^{-3} S/m, although deformation zones make up as much as 18 % of the borehole. This indicates that fracture zones only make up a small part of the deformation zones.

---

[10] DATA DELIVERY Sicada_12_091.

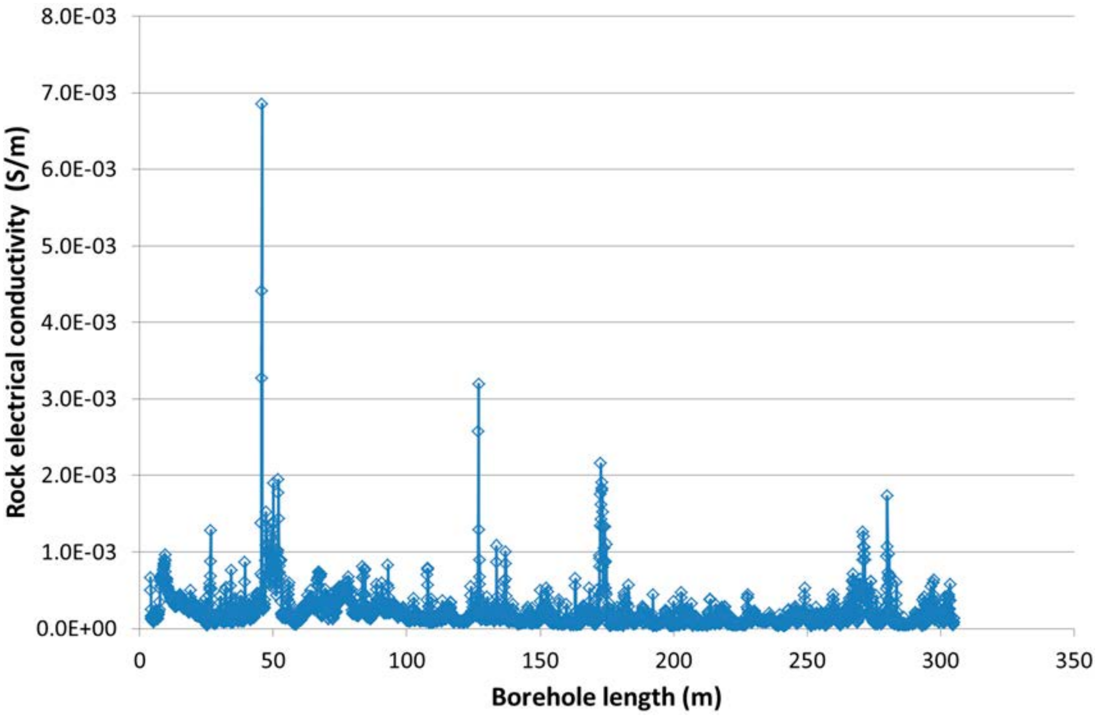

Figure A-3. *Geophysical downhole log in KFR105 where apparent rock resistivities have been converted to rock electrical conductivities.*

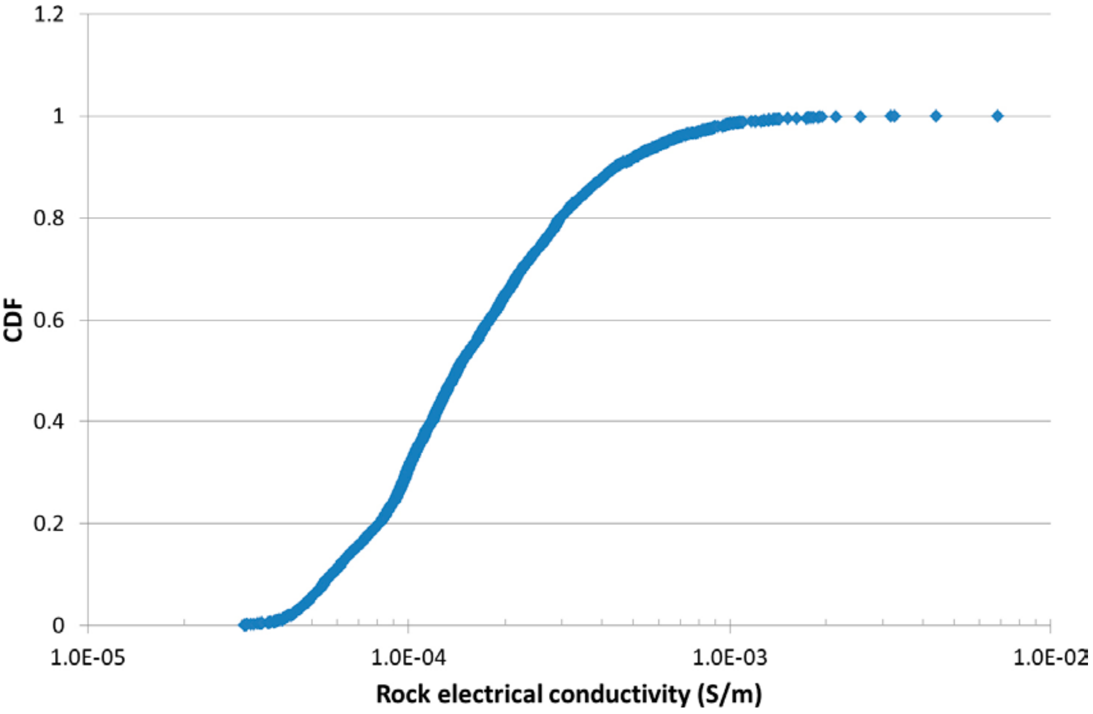

Figure A-4. *CDF of measured rock electrical conductivities in downhole geophysical logging in KFR105.*

Based on the above, the following judgment is made. The rock volume intended to host the extended part of SFR is intersected by a number of minor deformation zones. Without going into details of the deformation zone model and the actual layout, it is possible that the 1BRT-vault is intersected by a number of these minor deformation zones. Such zones may be realistically represented by deformation zone ZFMNE3115 in Figure A-1b. For our model, we propose a realistic zone with the thickness 10 m and the resistivity 1 000 ohm.m.

A.2.2 Intense and extreme zone

We also propose a more intense deformation zone in our model, with the same thickness of 10 m but with the resistivity 100 ohm.m. Such a low apparent resistivity was never measured in borehole KFR105, but the lowest apparent resistivity corresponding to a narrow zone of cataclastic rock came close. Hence, the intense zone can be envisioned as a 10 m thick fracture zone made of cataclastic rock, likely within a much larger deformation zone,

Here comparisons can be made with the Singö zone. The apparent rock resistivity of this zone has been logged in borehole KFM11A (Nielsen and Ringgaard 2007). The upper part of the borehole stays clear of the zone while the lower part intersects the zone. Only within very short borehole intervals apparent rock resistivities drops below 100 ohm.m. The total borehole length demonstrating lower apparent resistivities than 100 ohm.m is on the order of a meter (Nielsen and Ringgaard 2007, Appendix 2). The majority of the apparent resistivities within the zone stay at, or above, 1 000 ohm.m. There are, however, borehole intervals with apparent rock resistivities of a few hundred ohm.m, with a total length on the order of 10 m. Accordingly, one may assume that a combination of the most fractured parts of the Singö zone roughly represents our suggested intense zone.

Finally, for sensitivity studies, we propose an extreme zone with the rock resistivity 10 ohm.m. To achieve such low resistivity (at present day groundwater composition) the porosity would have to be about 15 %. Such high porosity, as result of only fracturing, is highly unlikely. However, at the Forsmark site investigation area there is very sparsely occurring quartz dissoluted episyenite with rock matrix porosities of this magnitude (Selnert et al. 2008, Figure 4-6). For the sake of simplicity, we propose the same thickness of this extreme deformation zone as of the other zones, i.e. 10 m.

This extreme zone could alternatively be envisioned as an extensive network of underground openings (access tunnels, ramps, shaft, etc.) connecting the vault to other parts of the repository and to ground surface. In the following we simplistically assume that the underground openings are excavated in a 10 m thick plane. We further assume they are backfilled with gravel of high porosity and a resistivity of 3.75 ohm.m (cf. Section 3.4). For this plane of underground openings to have the same conductive properties as the extreme zone, about one third of the rock mass would need to be excavated and backfilled. For a repository for radioactive waste, where one aims to minimise access routes down to the repository, this is on the verge of absurd. The suggested data of this appendix are summarised in Table A-1.

Table A-1. Assumed parameters of deformation zones used in modelling.

Description zone	Block scale rock resistivity	Thickness
Realistic zone	1 000 ohm.m	10 m
Intense zone	100 ohm.m	10 m
Extreme zone or highly pessimistic tunnel and shaft system	10 ohm.m	10 m

A.3 Handling of the Singö zone in modelling

The Singö zone will intersect the shallow part of the ramps. This is shown in Figure A-5, where only the existing parts of the SFR are included. Although data indicates that the Singö zone is not very conductive, we include its possible impact in a pessimistic manner in all COMSOL Multiphysics modelling in 2D, in cases where the 1BRT vault is connected to ground surface by a ramp. This is done by extending the ramp to the end of the model boundary (cf. Figure 6-6). This is roughly equivalent to extending the ramp to end in the water mass of the Baltic Sea. An alternative conceptualisation would be that the Singö zone connects the ramp with the water mass of the Baltic Sea.

This pessimistic approach is not taken generally in COMSOL Multiphysics modelling in 3D, where the entire ramp is generally assumed be surrounded by resistive rock and where its entrance is on an island with the same resistivity as the remaining host rock (cf. Section 7.2). This is justified by the data in Nielsen and Ringgaard (2007) indicating that the Singö zone is not very conductive. However, we have also tested the impact of the modelled island by neglecting its presence and by leading the ramp up into the Baltic Sea (cf. Section 7.5).

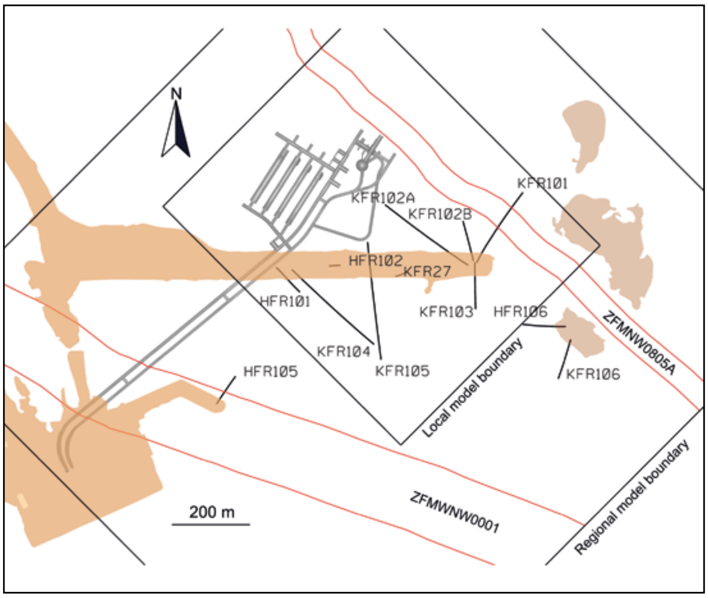

***Figure A-5.** The location of the Singö Zone (ZFMWNW0001), intersecting the upper part of the ramp. Only existing part of SFR is shown in the figure. Excerpt of SKB (2013a, Figure 6-11).*

Appendix B

Preliminary regional-scale field modelling

B.1 Background

In Section 3.2, the local potential gradient in a homogenous medium at a distance from the electrode is expressed assuming a perfectly hemispherical electric field (see Figure 3-12). With this assumption, the modelled potential gradient *dU/dr* at a fixed distance *r* from the current source is linearly correlated with the assumed rock resistivity ρ, providing that the current output *I* remains unchanged:

$$I = -\frac{2\pi r^2}{\rho}\frac{dU}{dr}$$ Equation B-1

In the real case, the Fågelsundet electrode is located in the Baltic Sea that is, at least locally, also the main conductor for current transfer. As there is a major contrast in the resistivities of the rock and seawater, the electric field becomes skewed from the hemispherical shape and only a minor portion of the current is transferred through the local rock. Under these conditions it is less straightforward to express a correlation between the rock resistivity and potential gradient.

B.2 Aim

The aim of this appendix is only to investigate whether there is a strong or weak correlation between the potential gradient and host rock resistivity. The aim is not to investigate the absolute magnitude of the potential gradient. Doing this would have required a more refined model and a more careful choice of the distance between the electrode and the zero potential.

B.3 Model setup

A very simple regional-scale model was set up to illustrate deviations from the hemispherical case. The modelled volume is 5 km deep, 10 km wide, and 10 km long. It mostly consists of homogenous host rock, but half of the model volume is covered by a ten-meter-deep seawater domain (see Figure B-1). The current electrode is assumed to be a 10 × 10 × 10 m metallic cube, having a fixed surface potential of 150 kV. It is located in the seawater, contacting the seabed as well as the shoreline.

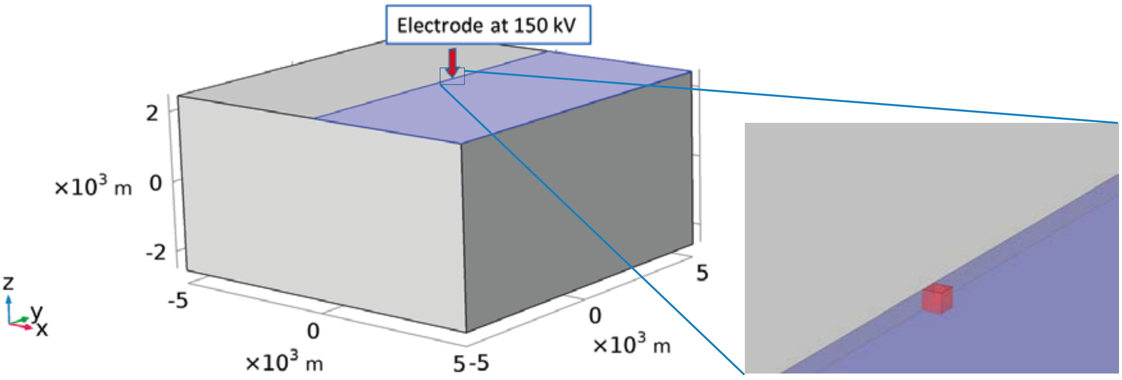

Figure B-1. Model volume with the rock domain (grey) and the 10 m thick water domain (blue). The electrode (red cube) is placed at the shoreline on the seabed, as shown by the zoomed in image.

The top surface of the modelled volume has an isolating boundary condition, prohibiting current from propagate upwards (into the atmosphere). At the other five sides of the model volume, a distributed impedance boundary condition is applied. This condition implies that the current leaving the domain in the direction normal to the boundary faces is calculated analytically assuming a fixed potential U_{ref}, at a far distance d_s, from the boundary. The condition is expressed mathematically in Equation B-2. In the calculations presented below, a zero potential ($U_{ref} = 0$) is assumed at an arbitrarily chosen distance d_s of 50 km normal from the domain boundary.

$$\mathbf{n} \cdot \boldsymbol{J} = \frac{\sigma_i}{d_s}\left(U - U_{ref}\right) \qquad \text{Equation B-2}$$

where **n** denotes the unit vector normal to the boundary face, $\boldsymbol{J}$ (A/m^2) is the current density, σ_i is the electrical conductivity (with index i denoting sea water or rock depending on whether the condition is applied at the sea or rock boundary), and U (V) is the electric potential at the boundary face.

The electric potential gradient in the host rock is investigated at three locations (cf. Figure B-2), all at a depth of 100 m below sea level:

- The shoreline location is directly below the shoreline, with a horizontal distance of 1 km to the electrode.
- The seabed location is straight out in the sea from the electrode, with a horizontal distance of 1 km to the electrode.
- The inland location is straight inland from the electrode, with a horizontal distance of 1 km to the electrode.

The model allows for two domains of different resistivity. Four cases are simulated, in respect of these paired resistivities:

- Case 1: Rock resistivity = 1 000 ohm.m, Water resistivity = 1.5 ohm.m
- Case 2: Rock resistivity = 10 000 ohm.m, Water resistivity = 1.5 ohm.m
- Case 3: Rock resistivity = 100 000 ohm.m, Water resistivity = 1.5 ohm.m
- Case 4: Rock resistivity = 10 000 ohm.m, No water[11]

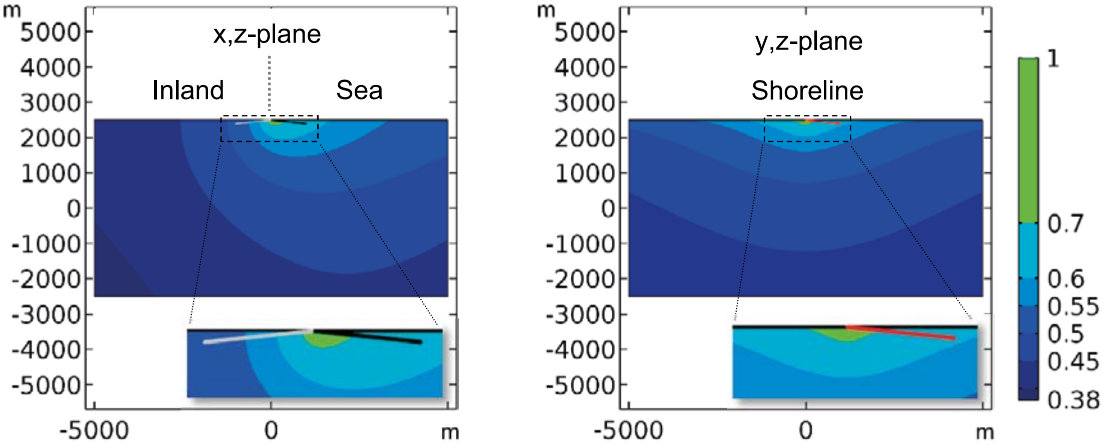

Figure B-2. *Straight lines from the electrode to inland location (grey line), seabed location (black line) and shoreline location (red line). The blue colours indicate the potential, as normalised by the electrode potential, for Case 2.*

---

[11] Simulated by setting the water domain resistivity to 10 000 ohm.m.

B.4 Model results

Figure B-3 shows iso-potentials in the horizontal x,y-plane at 100 m depth, and vertical x,z- and y,z-planes that intersect the electrode, for Case 2. Regarding the horizontal x,y-plane at 100 metres depth, a skewing of the potential field along the shoreline is seen as a consequence of the contrast between the rock and water resistivity at the top of the domain. Regarding the vertical x,z-plane, the field has a hemispherical character on the inland side, while on the sea side, the field is skewed. This is due to the much more conductive seawater, in which much of the current is propagated to the outer model volume boundary.

Figure B-4 shows the decline in electric potential along evaluation lines connecting the electrode with the shoreline, seabed, and inland locations, respectively (cf. Figure B-2). This is shown for the pairs of resistivities in Case 1 to 4. The potential gradients along the lines, at the three locations (i.e. at the end of the lines), are provided in Table B-1 for the four cases. If looking at the three first cases, increasing the rock resistivity from 1 000 to 100 000 decreases the current output from the electrode by approximately 40 %. In all these cases the electrode has the same surface potential of 150 kV and is located in the seawater. This indicates that in the local model volume, the majority of the electrical current leaves through the seawater. The higher the rock resistivity is, the higher does the fraction of current propagated in the seawater become. Moreover, changing the rock resistivity by two orders of magnitude has a limited impact on the potential gradient at the observed locations in the bedrock. Only when disregarding the seawater (Case 4), there are dramatic changes in the current output and host rock's potential gradients at the three locations.

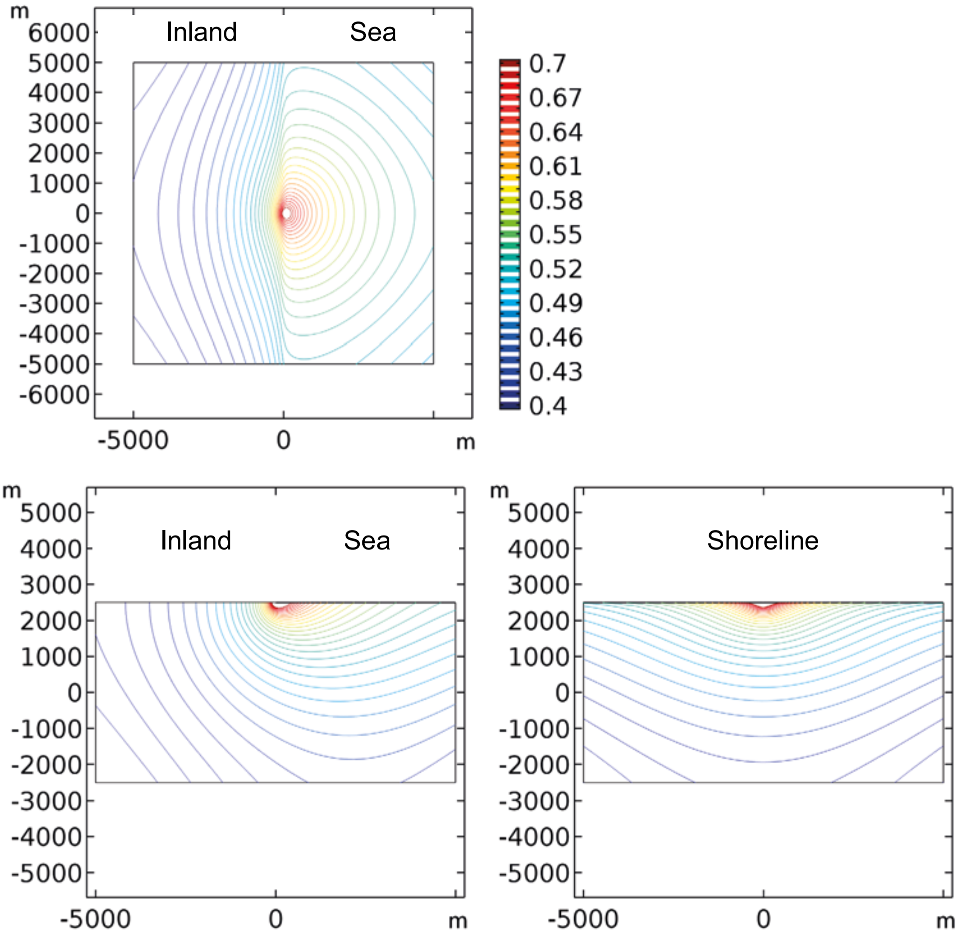

Figure B-3. *Isopotential lines in the horizontal x,y-plane at 100 m depth (top image), and vertical x,z (bottom left image) and y,z (bottom right image) planes, as evaluated for Case 2. All potentials are normalised by the electrode potential.*

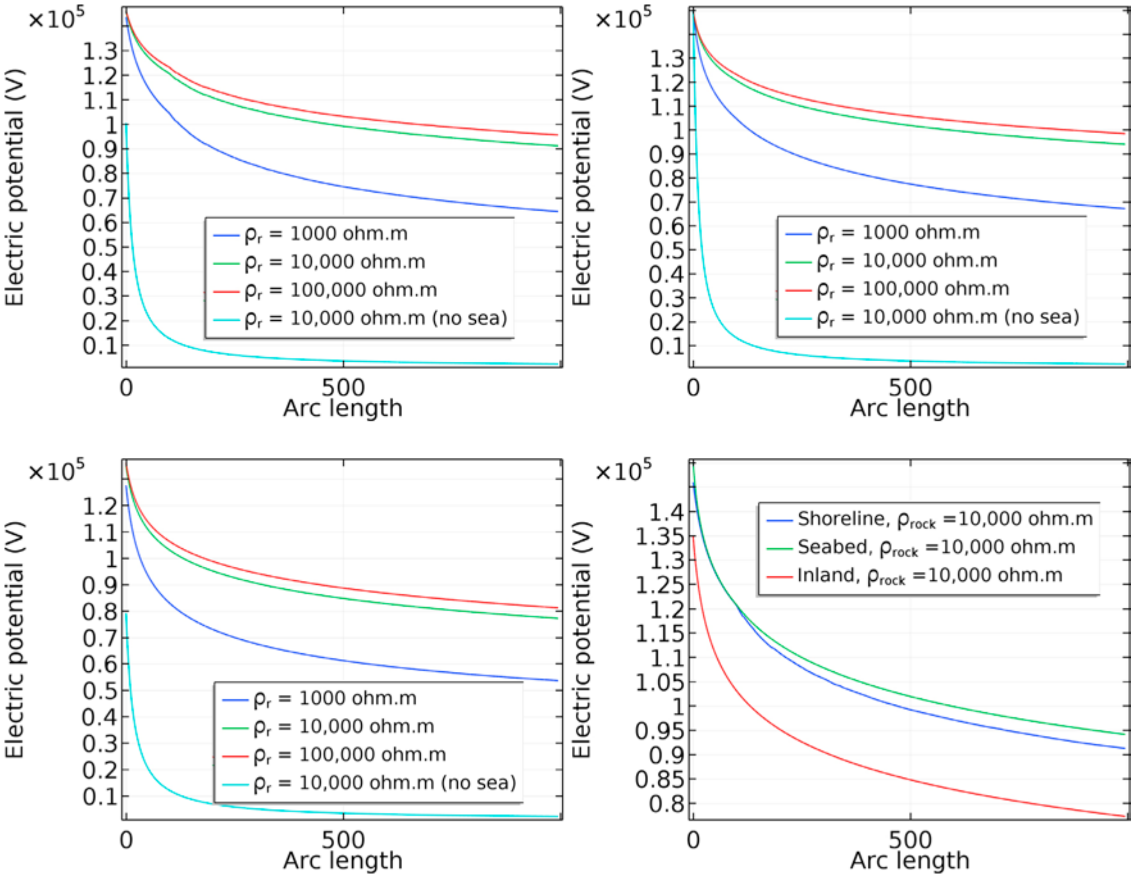

Figure B-4. *Potentials along the lines shown in Figure B-2, from the electrodes to the different locations. Upper left: Case 1–4 for shoreline location. Upper right: Case 1–4 for seabed location. Lower left: Case 1–4 for inland location. Lower right: Case 2 for all locations.*

The above modelling suggests that the hemispherical field formulation (Equation B-1) does not describe the modelled situation well, when the model includes the sea. Using the rock's resistivity as an approximation of the homogenous resistivity in Equation B-1 is apparently a poor choice. This is even as an overwhelming majority of the model volume consists of rock. This indicates a weak correlation between the rock resistivity and potential gradient in the host rock, at repository depth, as result of a sea-based HVDC electrode. This is, perhaps, a controversial result (cf. Thunehed 2017) and we stress that it is obtained by a preliminary model. In fact, the present model is not refined enough to provide the correlation between the rock resistivity and potential gradient, in response to a HVDC electrode, and setting up such a refined model remains as future work. The remaining uncertainty justifies evaluating both the non-correlated and correlated case in Section 6.5.

Table B-1. Electric potential gradients at the inland, seabed and shoreline location for Case 1 to 4.

Case	Rock resistivity (ohm.m)	Sea water presence	Inland location gradient (V/m)	Seabed location gradient (V/m)	Shoreline location gradient (V/m)
Case 1	1 000	Yes	−10	−14	−14
Case 2	10 000	Yes	−11	−11	−11
Case 3	100 000	Yes	−11	−11	−11
Case 4	10 000	No	−1.3	−1.3	−1.3

Arkitektkopia AB, Bromma, 2018

SKB is responsible for managing spent nuclear fuel and radioactive waste produced by the Swedish nuclear power plants such that man and the environment are protected in the near and distant future.

skb.se

SVENSK KÄRNBRÄNSLEHANTERING